TECHNISCHE UNIVERSITÄT MÜNCHEN

TUM School of Natural Sciences

QUANTUM STATISTICAL PROPERTIES OF A SUPERCONDUCTING DUFFING OSCILLATOR

Qiming Chen

Vollständiger Abdruck der von der TUM School of Natural Sciences der Technischen Universität München zur Erlangung des akademischen Grades eines

Doktors der Naturwissenschaften

genehmigten Dissertation.

Vorsitzender:		Prof. Dr. Johannes Knolle
Prüfer der Dissertation:	1.	Prof. Dr. Rudolf Gross
	2.	Prof. Dr. Alexander Holleitner

Die Dissertation wurde am 19.05.2022 bei der Technischen Universität München eingereicht und durch die TUM School of Natural Sciences am 19.10.2022 angenommen.

Walther Meißner Institut

BAdW BAYERISCHE AKADEMIE DER WISSENSCHAFTEN

Technische Universität München

QUANTUM STATISTICAL PROPERTIES OF A SUPERCONDUCTING DUFFING OSCILLATOR

超导杜芬电路的量子统计性质

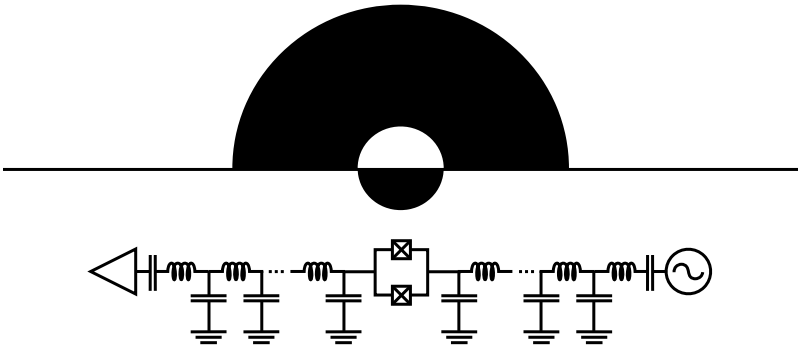

Qi-Ming Chen

陈启明

Fakultät für Physik

Technische Universität München

慕尼黑工业大学物理系

Abstract

Understanding the non-deterministic behavior of deterministic nonlinear systems has been an implicit dream since Lorenz observed the "butterfly effect". A prominent example is the hysteresis and bistability of a Duffing oscillator, which is traditionally attributed to the coexistence of two steady states in a double-well potential. However, this interpretation fails in a quantum-mechanical perspective where a single unique steady state is allowed in the whole parameter space. Here, we measure the non-equilibrium dynamics of a superconducting Duffing oscillator and reconcile the classical and quantum theories in a unified picture. We demonstrate that the steady states regarded as classically are in fact metastable states. They have a remarkably long lifetime in a certain parameter regime but must relax to the single unique steady state allowed by quantum mechanics in the long-time limit. By engineering the lifetime of the metastable states sufficiently large, we observe a first-order dissipative phase transition which mimics a sudden change of the mean field in a 11-site Bose-Hubbard lattice. We also reveal the two distinct phases of the transition by quantum state tomography, i.e., a coherent phase and a squeezed phase separated by a critical point. Our results provide a comprehensive understanding of the Duffing oscillator. They form an essential step towards the understanding of the intriguing non-equilibrium phenomena in driven-dissipative systems.

Ein umfassendes Verständnis des nicht vorhersagbaren Verhaltens von deterministischen nichtlinearen Systemen zu entwickeln ist ein Traum, seit Lorenz den "Schmetterlingseffekt" beobachtet hat. Ein bekanntes Beispiel ist das hysteretische Verhalten und die Bistabilität eines Duffing-Oszillators, die traditionell auf die Koexistenz von zwei stationären Zuständen in einem Doppelmuldenpotenzial zurückgeführt werden. Diese Interpretation versagt jedoch in einer quantenmechanischen Perspektive, in der nur ein einziger stationärer Zustand im gesamten Parameterraum zulässig ist. Hier messen wir die Nicht-Gleichgewichtsdynamik eines supraleitenden Duffing-Oszillators und bringen die klassische und die Quantentheorie in einem einheitlichen Bild zusammen. Wir zeigen, dass die als klassisch betrachteten stationären Zustände metastabil sind. Sie haben eine bemerkenswert lange Lebensdauer, gehen aber schließlich in den einzigen von der Quantenmechanik erlaubten stationären Zustand über. Indem wir die Lebensdauer des metastabilen Zustands genügend groß machen, beobachten wir einen dissipativen Phasenübergang erster Ordnung, der wie die plötzliche Änderung des mittleren Feldes in einem 11-Platz Bose-Hubbard-Gitter aussieht. Mit Hilfe der Quantenzustands-Tomographie können wir auch die beiden Phasen des Übergangs als eine kohärente Phase und eine gequetschte Phase identifizieren. Unsere Ergebnisse liefern ein umfassendes Verständnis des Duffing-Oszillators. Sie stellen ferner einen wesentlichen Schritt auf dem Weg zum Verständnis der faszinierenden Nicht-Gleichgewichtsphänomene in getriebenen dissipativen Systemen dar.

因真理，得自由，以服务

"And you will know the truth, and the truth will set you free." (John 8:32)

Contents

Outline

Nomenclature

I QUANTUM STATISTICAL PROPERTIES OF MICROWAVES

1 Superconducting quantum circuits **3**
1.1 Motivation to go beyond classical circuits . . . 3
1.2 Josephson junctions . . . 4
1.3 Recipe for circuit quantization . . . 5
1.3.1 Generalized Josephson junction . . . 6
1.3.2 DC-SQUID . . . 7
1.3.3 Transmission line resonator . . . 8

2 Microwave quantum optics **11**
2.1 Second quantization of microwaves . . . 11
2.2 Quantum states of photons . . . 12
2.2.1 Fock states . . . 12
2.2.2 Coherent states . . . 12
2.2.3 Squeezed states . . . 13
2.2.4 Thermal states . . . 14
2.2.5 Gaussian states . . . 14
2.3 Quasidistribution functions . . . 15
2.3.1 The Glauber-Sudarshan P representation . . . 15
2.3.2 The Husimi Q representation . . . 16
2.3.3 The Wigner-Ville W representation . . . 17
2.3.4 Transform among different representations . . . 18
2.4 Quantum theory of damping . . . 19
2.4.1 Heisenberg picture: The Langevin-equation approach . . . 19
2.4.2 Schrödinger picture: The master-equation approach . . . 21

II SUPERCONDUCTING OSCILLATOR WITH TUNABLE NONLINEARITY

3 Model: Josephson-junction-embedded transmission line resonator **25**
3.1 Circuit description . . . 25
3.1.1 Equivalent circuits of the external circuitry . . . 25
3.1.2 Josephson junction in an equivalent circuit . . . 28
3.1.3 Scattering responses of the circuit . . . 28
3.2 Quantum description . . . 29
3.2.1 Boundary conditions . . . 29
3.2.2 Normal (spatial) modes . . . 30
3.2.3 Canonical quantization . . . 31
3.3 Design parameters . . . 33
3.3.1 Asymmetric DC-SQUID . . . 33
3.3.2 Sample chip . . . 34
3.4 Cryogenic setup . . . 34
3.4.1 The dilution refrigerator . . . 35
3.4.2 Optimization of heat load . . . 36
3.4.3 Wiring up the system . . . 37

4 Closed-system parameters: Automated sample characterization and tuning 39
4.1 Automated sample characterization . . . 39
4.1.1 Spectroscopy experiment . . . 39
4.1.2 Least square estimation . . . 41
4.2 Characterization results of closed-system parameters . . . 43
4.3 Automated sample tuning . . . 44

5 Open-system parameters: Scattering coefficients of microwave resonators 47
5.1 Circuit perspective: The transfer matrix approach . . . 47
5.1.1 Classification of microwave resonators . . . 47
5.1.2 Ideal scattering coefficients . . . 49
5.1.3 Practical scattering coefficients: Small circuit asymmetry . . . 53
5.1.4 Practical scattering coefficients: Finite-length feedlines . . . 54
5.2 Quantum perspective: The input-output approach . . . 55
5.2.1 Amplitude damping . . . 56
5.2.2 Phase damping . . . 60
5.3 A recipe for Q-factor measurement . . . 60
5.4 Characterization results of open-system parameters . . . 63

III QUANTUM MEASUREMENT IN NON-EQUILIBRIUM

6 Measurement of propagating microwave fields 69
6.1 Theory of quadrature measurements . . . 69
6.1.1 Description of amplification process . . . 69
6.1.2 Description of quadrature measurements . . . 70
6.2 Room-temperature setup . . . 72
6.3 FPGA logic . . . 73
6.3.1 I/Q demodulation . . . 74
6.3.2 Low-pass filter . . . 75
6.3.3 Data storage . . . 76
6.3.4 Virtual-time filtering . . . 78
6.4 Input-output characterization . . . 79
6.4.1 The Planck's law and output channel characterization . . . 79
6.4.2 Input channel characterization . . . 81

7 Quantum state tomography of microwave photons 83
7.1 Tomography based on signal moments . . . 83
7.1.1 Arbitrary state tomography . . . 84
7.1.2 Gaussian state tomography . . . 85
7.2 Tomography based on quadrature histogram . . . 86
7.2.1 Tomography via inverse linear transformation . . . 86
7.2.2 Tomography via maximum likelihood estimation . . . 88
7.3 Other methods for quantum state tomography . . . 90
7.3.1 Tomography with power-law detectors . . . 90
7.3.2 Tomography with a probe qubit . . . 92

IV QUANTUM SIMULATION WITH NONLINEAR OSCILLATORS

8 Quantum behavior of Duffing oscillator at dissipative phase transition 97
8.1 Introduction . . . 97
8.2 Theory . . . 98
8.2.1 Quantum and classical descriptions of a Duffing oscillator . . . 98
8.2.2 Liouvillian spectrum, metastability, and dissipative phase transition . . . 100
8.2.3 Thermodynamic limit and the Bose-Hubbard lattice . . . 101

8.3 Experimental methods . . . 102
8.4 Results and analysis . . . 103
8.4.1 Quantum fluctuations in hysteresis . . . 103
8.4.2 Two-stage relaxation of metastable states . . . 104
8.4.3 A first-order dissipative phase transition . . . 106
8.4.4 Microscopic picture of the phase transition . . . 107
8.4.5 The two phases of phase transition . . . 109
8.4.6 Discussion of dephasing effects . . . 110
8.5 Conclusions . . . 111

9 Towards a superconducting Bose-Hubbard quantum simulator 113
9.1 Unconventional photon blockade . . . 113
9.2 Quantum cups and balls . . . 114
9.3 Boundary time crystal . . . 115

V APPENDICES

A Quasi-distribution functions of Gaussian states 119

B General form of the input-output formalism 123

C The Z-transform and the transfer function 125

D Classical theory of Duffing oscillator 127

Bibliography 129

List of publications (2018.10-2022.04) 155

Acknowledgement 156

Outline

The major goal of this thesis is to use a driven-dissipative superconducting nonlinear resonator to simulate, and eventually understand, the non-equilibrium quantum statistical properties of the Duffing oscillator. With the sample designed and fabricated by M. Fischer, we develop the characterization and measurement techniques, and perform the quantum simulation experiments. Correspondingly, this thesis is split into four parts with different emphases:

Part I reviews the quantum statistical properties of microwaves, which is an interdisciplinary research field between superconducting quantum circuits and quantum optics. In **Chapter 1**, we introduce the elementary building blocks of superconducting quantum circuits, such as the Josephson junction, and describe the standard recipe for circuit quantization. In **Chapter 2**, we reveal the connection between the microwave and optical fields, and introduce the theoretical tools developed in quantum optics, such as the quasidistribution functions, for describing microwave photons.

Part II focuses on the modeling and characterization of our system. In **Chapter 3**, we introduce the classical- and quantum-mechanical models of a nonlinear superconducting resonator, as well as the design parameters of the sample chip and the cryogenic setup [1]. In **Chapter 4**, we report a computer-automated procedure for characterizing and *in-situ* tuning the closed-system parameters [2], such as the Kerr nonlinearity, and summarize the characterization result. In **Chapter 5**, we describe a method to characterize the open-system parameters [3, 4], such as the energy dissipation rate, and summarize the characterization result.

Part III describes the measurement techniques that are necessary for capturing the non-equilibrium dynamics of the system. In **Chapter 6**, we theoretically describe the heterodyne measurement in superconducting quantum circuits, and introduce our control and measurement protocols. In **Chapter 7**, we review several methods for quantum state tomography of microwave photons, and compare their performance with the same data set [5].

Part IV summarizes the major results of quantum simulation experiments and provides an outlook on future researches. In **Chapter 8**, we reveal the quantum behavior of the Duffing oscillator, and report a first-order dissipation phase transition [6]. In **Chapter 9**, we discuss possible phenomena that can be observed in coupled nonlinear superconducting resonators, called the Bose-Hubbard dimer. The ultimate goal is to build a Bose-Hubbard lattice for simulating strongly interacting bosons in a controllable and measurable way, and thus obtaining a deeper understanding of the condensed matter physics.

Related publications:

[1] Michael Fischer, Qi-Ming Chen, Christian Besson, Peter Eder, Jan Goetz, Stefan Pogorzalek, Michael Renger, Edwar Xie, Michael J. Hartmann, Kirill G. Fedorov, Achim Marx, Frank Deppe, and Rudolf Gross, *In situ tunable nonlinearity and competing signal paths in coupled superconducting resonators*, Phys. Rev. B **103**, 094515 (2021)

[2] Qi-Ming Chen, Michael Fischer, Yuki Nojiri, Stefan Pogorzalek, Michael Renger, Matti Partanen, Kirill G. Fedorov, Achim Marx, Frank Deppe, and Rudolf Gross, *Automated calibration and control of superconducting resonators with tunable nonlinearity*, in *WMI Annual Report*, pages 53–54, 2020.

[3] Qi-Ming Chen, Meike Pfeiffer, Matti Partanen, Florian Fesquet, Kedar E. Honasoge, Fabian Kronowetter, Yuki Nojiri, Michael Renger, Kirill G. Fedorov, Achim Marx, Frank Deppe, and Rudolf Gross, *The scattering coefficients of superconducting microwave resonators: I. Transfer-matrix approach*, arXiv:2109.07762 (2021)

[4] Qi-Ming Chen, Matti Partanen, Florian Fesquet, Kedar E. Honasoge, Fabian Kronowetter, Yuki Nojiri, Michael Renger, Kirill G. Fedorov, Achim Marx, Frank Deppe, and Rudolf Gross, *The scattering coefficients of superconducting microwave resonators: II. System-bath approach*, arXiv:2109.07766 (2021)

[5] Qi-Ming Chen, Frank Deppe, Yuki Nojiri, Stefan Pogorzalek, Michael Renger, Matti Partanen, Kirill G. Fedorov, Achim Marx, and Rudolf Gross, *Measurement of the second-order correlation functions under different signal-to-noise ratios*, in *WMI Annual Report*, pages 51–52, 2020.

[6] Qi-Ming Chen, Michael Fischer, Yuki Nojiri, Michael Renger, Edwar Xie, Matti Partanen, Stefan Pogorzalek, Kirill G. Fedorov, Achim Marx, Frank Deppe, and Rudolf Gross, *Quantum behavior of the Duffing oscillator at the dissipative phase transition*, arXiv:2206.06338 (2022)

Nomenclature

Abbreviations:

ADC	Analog-to-digital converter. [Defined on page 69.]
AFG	Arbitrary function generator. [Defined on page 72.]
BBQ	Black-box quantization. [Defined on page 6.]
CIC	Cascaded integrator comb (filter). [Defined on page 75.]
CT	Computer tomography. [Defined on page 91.]
DC	Direct current. [Defined on page 5.]
DPT	Dissipative phase transition. [Defined on page 97.]
DSP	Digital signal processing. [Defined on page 74.]
ENIAC	Electronic numerical integrator and computer. [Defined on page 3.]
EOM	Euler-Lagrange equation of motion. [Defined on page 19.]
FIR	Finite impulse response (filter). [Defined on page 75.]
FPGA	Field programmable gate array. [Defined on page 74.]
FWHM	Full width at half maximum. [Defined on page 47.]
GND	Ground. [Defined on page 3.]
HEMT	High-electron-mobility transistor. [Defined on page 36.]
IF	Intermediate frequency. [Defined on page 72.]
IP	Intellectual property (core). [Defined on page 76.]
IVC	Inner vacuum chamber. [Defined on page 35.]
JPA	Josephson parametric amplifier. [Defined on page 77.]
JPM	Josephson photomultiplier. [Defined on page 92.]
JRM	Josephson ring modulator. [Defined on page 77.]
KCL, KVL	Kirchhoff's current and voltage laws. [Defined on page 3.]
LO	Local oscillator. [Defined on page 72.]
LSE	Least-square estimation. [Defined on page 39.]
MLE	Maximum likelihood estimation. [Defined on page 84.]
MS	Metastable state. [Defined on page 97.]

MXC Mixing chamber. [Defined on page 35.]

POVM Positive operator-valued measure. [Defined on page 89.]

RF Radio frequency. [Defined on page 6.]

RWA Rotating wave approximation. [Defined on page 98.]

SNAIL Superconducting nonlinear asymmetric inductive element. [Defined on page 6.]

SNR Signal-to-noise ratio. [Defined on page 39.]

SQUID Superconducting quantum interference device. [Defined on page 6.]

SS Steady state. [Defined on page 97.]

TMP Turbomolecular pump. [Defined on page 35.]

TWA Truncated Wigner approximation. [Defined on page 116.]

TWPA Traveling wave parametric amplifier. [Defined on page 77.]

VNA Vector network analyzer. [Defined on page 39.]

Symbols:

C Capacitance. [Defined on page 3.]

c Capacitance per unit length. [Defined on page 8.]

L Inductance, in the context of lumped-element circuits. [Defined on page 3.]

Length of transmission line resonator, in the context of distributed-element circuits. [Defined on page 8.]

L_J Josephson inductance. [Defined on page 5.]

l Inductance per unit length. [Defined on page 8.]

Length of transmission line resonator, in the discussion of scattering coefficients. [Defined on page 48.]

ϕ, q Node flux and charge variables. [Defined on page 3.]

I, V Current and voltage variables. [Defined on page 4.]

I_J Critical current of Josephson junction. [Defined on page 5.]

E_C, E_L, E_J Capacitive, inductive, and Josephson energies. [Defined on page 6.]

γ Energy dissipation rate. [Defined on page 19.]

Complex propagating coefficient, if it is defined as $\gamma \equiv \alpha + j\beta$. [Defined on page 26.]

γ_ϕ Dephasing rate. [Defined on page 20.]

$Q_\mathrm{i}, Q_\mathrm{e}, Q_\mathrm{l}$	Internal, external, and loaded quality factors.[Defined on pages 48 and 49.]
v_ph	Phase velocity in waveguide. [Defined on page 9.]
$a^\dagger, a$	Creation, annihilation operators for resonator. [Defined on page 11.]
$b^\dagger, b$	Creation, annihilation operators for reservoir. [Defined on page 19.]
$l^\dagger, l$ $(r^\dagger, r)$	Creation, annihilation operators for left (right) propagating fields. [Defined on page 56.]
G	Output power gain. [Defined on page 69.]
A	Input power attenuation. [Defined on page 81.]
ω_A	Resonant frequency of Kerr nonlinearity resonator. [Defined on page 32.]
U_A	Nonlinearity of Kerr nonlinearity resonator. [Defined on page 32.]
ω_d	Driving frequency. [Defined on page 56.]
ξ	Driving strength. [Defined on page 81.]
ρ	Density operator. [Defined on page 14.]
H	Hamiltonian. [Defined on page 3.]
$\mathcal{D}[\,\cdot\,]$	Lindblad superoperator. [Defined on page 22.]
$\mathcal{L}$	Lagrangian. [Defined on page 6.]
	Liouvillian superoperator, if it is in company with ρ. [Defined on page 22.]
λ_n	Eigenvalues of Liouvillian superoperator. [Defined on page 100.]

Constants:

e	Electron charge. [Defined on page 4.]
$\hbar$	Reduced Planck constant. [Defined on page 3.]
$i \equiv \sqrt{-1}$	Imaginary unit in physics convention. [Defined on page 3.]
$j \equiv -\sqrt{-1}$	Imaginary unit in electrical engineering convention. [Defined on page 47.]
k_B	Boltzmann constant. [Defined on page 4.]
$\phi_0 \equiv \hbar/2e$	Reduced magnetic flux quantum. [Defined on page 4.]

Part I:
QUANTUM STATISTICAL PROPERTIES OF MICROWAVES

*credit Metro-Goldwyn-Mayer

Chapter 1

SUPERCONDUCTING QUANTUM CIRCUITS

1.1 Motivation to go beyond classical circuits

People living in this century have witnessed a dramatic reduction of the size of commercial electronic devices. For example, the first fully-programmable computer, ENIAC (electronic numerical integrator and computer), invented in 1945 occupies a whole room space of around $2.4\,\mathrm{m} \times 0.9\,\mathrm{m} \times 30.0\,\mathrm{m}$, while a 13.3" MacBook Pro, which is the major working horse for writing this thesis, can be easily put on my desk with an even higher computational power. With the development of nanofabrication techniques, electrical circuits are made increasingly small. It is not a news in this decade to integrate billions of transistors on a single $25\,\mathrm{mm} \times 25\,\mathrm{mm}$ silicon wafer. On the one hand, it is remarkable that our traditional understanding of a bulky electrical circuit still applies to such a small physical scale. The size of each transistor is even smaller than a circular Rydberg atom which can only be described by quantum mechanics. On the other hand, it also leads to the famous question: Whether or not one can observe quantum mechanics in electrical circuits [1, 2]?

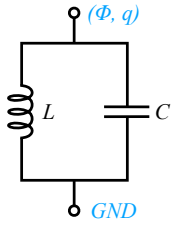

Figure 1.1. Circuit diagram of a LC oscillator. Here, a capacitor, C, and an inductor, L, are connected in parallel, ϕ and q are the flux and charge variables at the top node.

In order to get some intuitions to the potential answer, let us consider a simple lumped-element circuit as shown in Fig. 1.1. Here, a capacitor, C, and an inductor, L, form a so-called LC oscillator, and we define the bottom node as the ground (GND). By defining the node flux, ϕ, and charge, q, as conjugate variables, $\{\phi, q\} = 1$, and applying the Kirchhoff's current and voltage laws (KCL and KVL), the classical Hamiltonian of the system can be readily written as [3] (see Section 1.3 for derivation)

$$H = \frac{q^2}{2C} + \frac{\phi^2}{2L}. \tag{1.1}$$

To quantize such a system, Dirac taught us that one should simply replace the Poisson bracket by a commutator with the following canonical commutation relation [4–6]

$$\frac{1}{i\hbar}[\phi, q] = 1. \tag{1.2}$$

Here, $i \equiv \sqrt{-1}$ is the imaginary unit, $\hbar$ is the reduced Planck constant, ϕ and q are conjugate quantum operators. We note that this quantum-mechanical description of the LC oscillator is always valid and is independent of the size, material, or temperature of the circuit. However, to make the

quantum phenomena measurable and controllable in real experiments, there must be several additional considerations [6]:

Firstly, the circuit should be cooled down to a low temperature, T, where the energy of thermal fluctuations, $k_{\mathrm{B}}T$ with k_{B} being the Boltzmann constant, is much smaller than the energy level separations of the system. In our example, the energy levels are evenly spaced by $\hbar\omega_0$ with $\omega_0 = 1/\sqrt{LC}$ being the resonant frequency of the LC oscillator. With the help of the cryogenic techniques, one can thermally anchor the circuits to the mixing chamber stage of a dilution refrigerator and suppress the thermal noise to approximately 10 mK. Thus, it indicates that the characteristic frequency of the circuits should be designed, at least, in the microwave regime, which is often chosen in the range of $\omega/2\pi = 4 - 8\,\mathrm{GHz}$ in experiments.

Secondly, the energy spreading of each individual energy levels, $\delta\hbar\omega_0$, must also be smaller than their separation, $\hbar\omega_0$. In other words, the decay rate of the circuit, for example, the energy decay rate of the charge-flux oscillation, should be engineered as small as possible. This consideration leads to the use of superconducting materials, such as niobium (Nb) and aluminium (Al), to make an electrical circuit, where the electrons around the fermi level exist in the form of Cooper pairs below the critical temperature of superconductivity (9.3 K and 1.2 K, respectively). The supercurrent carried by the Cooper pairs can propagate in the circuit with, ideally, no energy dissipation. Moreover, one must carefully shield the circuit from the electromagnetic environments and also the external circuitries that are used to manipulate and measure the superconducting circuits. This requires an adequate circuit design as well as the proper arrangement of the microwave components, such as attenuators, filters, and circulators, at different temperature stages of the cryostat.

1.2 Josephson junctions

Usually, there exists a third requirement that the superconducting circuit must contain a certain amount of nonlinearity. This request originates from the observation that the transition frequencies between any two adjacent energy levels are degenerate in a perfectly linear system, which prevents us from accessing an arbitrary quantum state in the system in the sense of both control and readout. To date, the Josephson junction, as shown in Fig. 1.2A, may be the only known non-dissipative and non-linear circuit element which can be integrated into superconducting circuits. The properties of an ideal Josephson junction are summarized by the two Josephson equations

$$I = I_J \sin\varphi, \text{ and } \dot{\varphi} = V/\phi_0. \tag{1.3}$$

Here, $\varphi = \phi/\phi_0$ and V are respectively the gauge invariant phase difference and the voltage drop across the junction, $\phi_0 = \hbar/2e$ is the *reduced* magnetic flux quantum with e being the electron charge, I is the supercurrent flowing through the junction, and I_J is the critical current of the junction.

Taking the time derivative of the first Josephson equation and combining it with the second one, we obtain $V = (L_J/\cos\varphi)\,\dot{I}$, where $L_J = \phi_0/I_J$ is called the effective Josephson inductance. This name can be understood by expanding the first Josephson equation into a Taylor series [7]

$$I \approx (1/L_J)\,\phi - \left[1/\left(6L_J\phi_0^2\right)\right]\phi^3 + \mathcal{O}\left(\phi^5\right), \text{or, } \phi \approx L_J I + \left[L_J^3/\left(6\phi_0^2\right)\right] I^3 + \mathcal{O}\left(I^5\right). \tag{1.4}$$

These two expressions see the junction as a parallel or series circuit, respectively, which consists of an inductor, L_J, and a nonlinear circuit element nicknamed cut-line or spine-line spider, as shown in

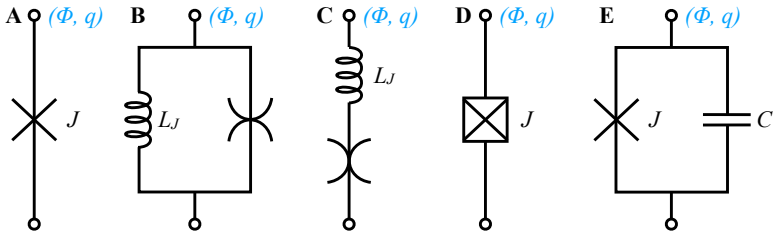

Figure 1.2. Different circuit diagrams of a Josephson junction. **(A)** Circuit symbol of a *zero*-dimensional junction which is fully described by the two Josephson equations. **(B)** – **(C)** By using Taylor series, one may separate the linear and nonlinear parts of a junction and obtain a parallel or series equivalent circuit diagram, respectively. Here, the cut- and spine-line spider symbols indicate two different nonlinear parts. **(D)** – **(E)** Circuit symbol of a practical junction, which is equivalent to a parallel circuit of a *zero*-dimensional junction and a Josephson capacitance.

Fig. 1.2B and C. In this regard, it is common to describe an ideal, or *zero*-dimensional, Josephson junction as a nonlinear inductor. However, for a real junction with a finite junction area, it is more appropriate to model it as a nonlinear inductor in parallel with a small capacitor in the 10^{-15} – 10^{-12} F range [6], as shown in Fig. 1.2D and E. The so-called Josephson capacitance, or shunt capacitance, originates from the finite cross section areas of the two junction electrodes separated by a thin insulating barrier, which form a parallel-plate capacitor in a real circuit.

We note that the value of ϕ is not necessarily small for ultra-small junctions at the size of 10 – 100 nm, where the capacitive energy is comparable to the Josephson energy. In this case, the Coulomb energy of the capacitor can blockade the Josephson tunneling effects [8–10], such that ϕ oscillates in the full-2π interval when biasing the junction by a DC (direct current) source. This phenomenon is known as the Bloch oscillation [11–13], and it is more appropriate to model a Josephson junction here as a nonlinear capacitor but not an inductor. In these regards, one should bear in mind that whether a Josephson junction should be treated as an inductive link or a capacitive break depends on the detailed parameters of the external circuit, for example, the size of the shunt capacitor.

1.3 Recipe for circuit quantization

We have learned from the example of the LC oscillator that the quantization of an electrical circuit consists of two major steps: (1) Write down the classical Hamiltonian, and (2) replace the Poisson bracket by a commutator. In many applications, the step (1) is the the major challenge while (2) is straightforward. To write down the Hamiltonian, one standard approach is to start from KVL and KCL, write down the Lagrangian, and use the Legendre transformation to get the Hamiltonian [3, 6]. Figuratively, we will call this approach the bottom-up approach. There is also a top-down approach, called black-box quantization (BBQ) [14, 15]. Here, one separates the linear and nonlinear parts of the Josephson junction (as we did in Section 1.2), and describes all the linear components of the entire circuit by a series connection of LC circuits. Thus, the linear part of the system Hamiltonian can be conveniently described as a collection of LC oscillators, whilst the nonlinear part is treated as a small perturbation. Here, we focus on the bottom-up approach and illustrate the step (1) of the quantization procedure with three examples.

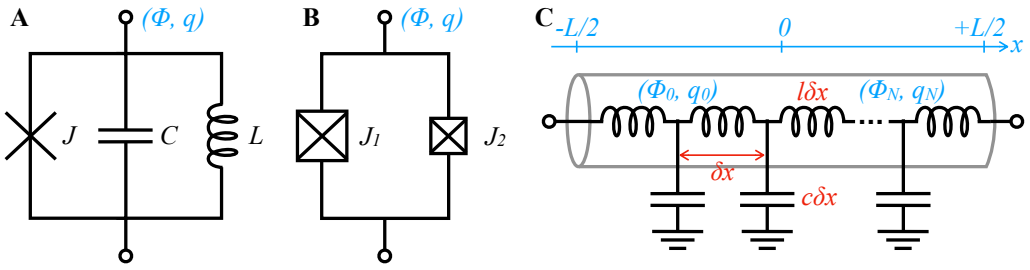

Figure 1.3. Circuit diagrams of three superconducting quantum devices. (A) A generalized Josephson junction, which is a parallel circuit of a *zero*-dimensional junction, J, a capacitor, C, and an inductor, L. **(B)** A DC-SQUID, which consists of two Josephson junctions, J_1 and J_2, in a superconducting loop. Here, we intentionally shrink the size of the second junction to indicate a possible loop asymmetry. **(C)** The distributed-element model of a transmission line resonator with length L and open boundary conditions. Here, c and l are the capacitance and inductance per unit length, δx is the length of a unit cell.

1.3.1 Example #1: Generalized Josephson junction

As introduced in Section 1.2, a Josephson junction is typically modeled as a *zero*-dimensional junction, J, with a shunt capacitor, C. Here, we add also a parallel inductor, L, to the circuit and describe it as a generalized Josephson junction [16, 17], as shown in Fig. 1.3A. Our first step is to define the independent nodes of the circuit and name one as GND. Here, we define the bottom node as the ground, such that the electromagnetic properties of top node is the only degree of freedom. Then, we define node variables, ϕ and q, apply KCL to the nodes and KVL to the circuit loops, and write down the Lagrangian of the circuit.

A shortcut to the Lagrangian is to distinguish first the inductive and capacitive elements of the circuit, which obey the relations $\dot{q} = g(\phi)$ and $\dot{\phi} = f(q)$, respectively. For example, the first Josephson equation indicates that the Josephson junction is an inductive element. Normal inductors and capacitors obey the relations $\dot{q} = \phi/L$ and $\dot{\phi} = q/C$, respectively, such that they are inductive and capacitive elements. Energies of the inductive and capacitive elements can be readily written as an integral of $g(\phi)$ and $f(q)$ over ϕ and q, respectively, and the Lagrangian is obtained by subtracting the total inductive energy from the total capacitive energy [6]. In this example and for *zero* applied current, the Lagrangian is

$$\mathcal{L} = \frac{C}{2}\dot{\phi}^2 - \left[\frac{\phi^2}{2L} - \phi_0 I_J \cos\left(\frac{\phi}{\phi_0}\right)\right], \tag{1.5}$$

where we have used the relation $\dot{\phi} = f(q)$ to change the variables in capacitive elements.

Next, we define the conjugate variable, $q = \partial\mathcal{L}/\partial\dot{\phi}$, and apply the Lagendre transformation, $H = \sum_n \dot{\phi}_n q_n - \mathcal{L}$. In this way, we obtain the Hamiltonian of the generalized Josephson junction as

$$H = 4E_C\left(\frac{q}{2e}\right)^2 + \frac{E_L}{2}\left(\frac{\phi}{\phi_0}\right)^2 - E_J\cos\left(\frac{\phi}{\phi_0}\right), \tag{1.6}$$

where $E_C = e^2/(2C)$, $E_L = \phi_0^2/L$, $E_J = \phi_0 I_J = \phi_0^2/L_J$ are called the capacitive, inductive, and Josephson energies of the circuit.

1.3.2 Example #2: DC-SQUID

A SQUID (superconducting quantum interference device) consists of a superconducting loop which is interrupted by several Josephson junctions [18–20]. For example, the so-called RF (radio frequency)-SQUID contains one junction in the loop while the DC-SQUID has two. When there are many large junctions in one arm and a single smaller one in the other, it is also called the SNAIL (superconducting nonlinear asymmetric inductive element) [21–24]. The Lagrangian of a DC-SQUID, as shown in Fig. 1.3B, can be written in the same way as we did for a single Josephson junction

$$\mathcal{L} = \left[\frac{C_1}{2}\dot{\phi}^2 + E_{\mathrm{J},1}\cos\left(\frac{\phi}{\phi_0}\right)\right] + \left[\frac{C_2}{2}\dot{\phi}^2 + E_{\mathrm{J},2}\cos\left(\frac{\phi}{\phi_0} + \frac{\phi_{\mathrm{ex}}}{\phi_0}\right)\right], \tag{1.7}$$

where ϕ is the node flux, and ϕ_{ex} is the external magnetic flux penetrating the loop. We have neglected the geometric and kinetic inductances of the superconducting loop, which is valid in typical DC-SQUIDs. The above Lagrangian can be readily written in a more compact form

$$\mathcal{L} = \frac{C_1 + C_2}{2}\dot{\phi}^2 + E_{\mathrm{J}}\left(\phi_{\mathrm{ex}}\right)\cos\left(\frac{\phi}{\phi_0} + \varphi'_{\mathrm{ex}}\right), \tag{1.8}$$

where

$$E_J\left(\phi_{\mathrm{ex}}\right) = E_+\sqrt{\cos^2\left(\frac{\phi_{\mathrm{ex}}}{2\phi_0}\right) + d^2\sin^2\left(\frac{\phi_{\mathrm{ex}}}{2\phi_0}\right)}, \tag{1.9}$$

$$\varphi'\left(\phi_{\mathrm{ex}}\right) = -\arctan\left[d\tan\left(\frac{\phi_{\mathrm{ex}}}{2\phi_0}\right)\right] + \left(\frac{\phi_{\mathrm{ex}}}{2\phi_0} + n\pi\right). \tag{1.10}$$

Here, $E_\pm = E_{\mathrm{J},1} \pm E_{\mathrm{J},2}$ is the summation or difference of the two Josephson energies, $d = E_{\mathrm{J},-}/E_{\mathrm{J},+}$ is the SQUID asymmetry. Comparing with the Lagrangian of a single junction in Eq. (1.5), one can readily write down the Hamiltonian as

$$H \approx 4E_{\mathrm{C}}\left(\frac{q}{2e}\right)^2 - E_J\left(\phi_{\mathrm{ex}}\right)\cos\left[\frac{\phi}{\phi_0} + \varphi\left(\phi'_{\mathrm{ex}}\right)\right], \tag{1.11}$$

By definition, the absolute value of the SQUID asymmetry, $|d|$, ranges from 0 to 1. The lower limit corresponds to a perfectly symmetric SQUID with $\phi/\phi_0 + \varphi'\left(\phi_{\mathrm{ex}}\right) = \phi/\phi_0 + \phi_{\mathrm{ex}}/(2\phi_0)$, which is the node flux at the center of the top branch. This observation indicates that a symmetric DC-SQUID can be treated as a single junction with tunable Josephson energy. However, one should be careful with this claim when considering a finite SQUID asymmetry. If the SQUID is coupled to some other circuits, the the phase offset, $\varphi'\left(\phi_{\mathrm{ex}}\right) \neq \phi_{\mathrm{ex}}/(2\phi_0)$, may contribute to the interaction and thus should not be simply omitted by a shift of variable. The other extreme case happens at $|d| = 1$, where there is only one junction in the loop and the flux-tunability of the equivalent Josephson energy vanishes. This circuit is in fact a RF-SQUID if the geometric loop inductance, L, is sufficiently large. The corresponding Hamiltonian is

$$H \approx 4E_{\mathrm{C}}\left(\frac{q_1}{2e}\right)^2 + \frac{E_L}{2}\left(\frac{\phi_1}{\phi_0}\right)^2 - E_{\mathrm{J}_1}\cos\left(\frac{\phi_1}{\phi_0} + \frac{\phi_{\mathrm{ex}}}{\phi_0}\right). \tag{1.12}$$

1.3.3 Example #3: Transmission line resonator

In all the discussions above, we assume that the circuit is composed of a finite number of circuit elements, such as capacitors, inductors, and junctions, which are *zero*-dimensional components without spatial degree of freedom. This assumption is valid when the circuit characteristic wavelength is much larger than its physical scale, called the lumped-element model. However, this condition is usually not fulfilled for typical superconducting quantum circuits, where the two scales are comparable. In this case, it is required to describe the system under investigation by a distributed-element circuit, while the result may be transformed into an equivalent lumped-element model within a small bandwidth.

A transmission line resonator is a typical distributed-element circuit, which is a central element of superconducting quantum circuits. We will meet it again in Chapter 5 when studying the scattering coefficients of superconducting microwave resonators. As shown in Fig. 1.3C, a transmission line resonator can be modeled as a periodic structure with N terms of LC-oscillator cells

$$\mathcal{L} = \sum_{n=0}^{N} \frac{c\delta x}{2}\dot{\phi}_n^2 - \frac{(\phi_{n+1}-\phi_n)^2}{2l\delta x}, \tag{1.13}$$

where c and l are the capacitance and inductance per unit length, respectively, δx is the length of a unit cell, and $L = N\delta x$ is the total length of the resonator. In the continuum limit, $\delta x \to 0$, we have $(\phi_{n+1}-\phi_n)/\delta x \to \phi'(x)$, such that the Lagrangian can be written in an integral form

$$\mathcal{L} = \int_{-L/2}^{+L/2} dx \left[\frac{c}{2}\dot{\phi}(x)^2 - \frac{\phi'(x)^2}{2l}\right]. \tag{1.14}$$

Readers familiar with the quantum field theory may immediately recognize that the mathematical description of a transmission line resonator is identical to that of a one-dimensional linear field, which is nothing but a collection of independent harmonic oscillators [25]. However, let us repeat the major steps of field quantization here to see the correspondance.

There are two steps to quantize a linear field: (1) Describe the system as a collection of harmonic oscillators, and (2) quantize each of them independently. The goal of the first step is to find a mode basis, $\{\phi_m(x,t)\}$, called the normal modes, where the temporal and spatial degrees of freedom are separable

$$\phi_m(x,t) = \phi_m(x)\phi_m(t). \tag{1.15}$$

Moreover, the normal (spatial) modes $\{\phi_m(x)\}$ should be orthonormal

$$\frac{1}{L}\int_{-L/2}^{+L/2} dx\phi_m(x)\phi_n(x) = \delta_{m,n}, \tag{1.16}$$

where $\delta_{m,n}$ is the Kronecker delta. To find the normal modes, we note that the transmission line resonator must obey some special boundary conditions to be called a resonator. Here, we assume an open boundary condition, $\phi'(-L/2) = \phi'(L/2) = 0$, which guarantees that no current is flowing through the two ends of the resonator. In this way, the Lagrangian can be diagonalized in the plane

wave basis

$$\phi(x,t) = \sum_{m=1}^{\infty} \sqrt{2}\cos\left(k_m x\right)\phi_m(t), \tag{1.17}$$

where $k_m = m\pi/L$, $m = 1, 2, \cdots$. By replacing $\phi(x,t)$ in Eq. (1.14) with (1.17), we obtain

$$\mathcal{L} = L\sum_{m=1}^{\infty}\left[\frac{c}{2}\dot{\phi}_m(t)^2 - \frac{k_m^2}{2l}\phi_n(t)^2\right]. \tag{1.18}$$

This result is self-consistent with our assumption of the normal modes. Comparing Eq. (1.18) with the first example of LC oscillator, we demonstrate the firstst half of the claim, that is "a one-dimensional field is nothing but a collection of independent harmonic oscillators".

The next step is to write down the Hamiltonian for each harmonic oscillator, and "quantize them one by one". Following the analysis of the LC oscillator introduced in Section 1.1, one can readily write down the result as

$$H = \sum_{m=1}^{\infty}\frac{q_m^2}{2C} + \frac{\phi_n^2}{2L_m}, \tag{1.19}$$

where $C = Lc$, $L_m = l/\left(k_m^2 L\right)$. We see that there is an infinite number of modes in a transmission line resonator, whose resonant frequencies are separated by $\omega_{m+1} - \omega_m = v_{\mathrm{ph}}(\pi/L)$. Here, $v_{\mathrm{ph}} = 1/\sqrt{lc}$ is the phase velocity of the microwave propagating along the transmission line. However, in practice one may focus only on a single or several modes because of the relatively large separation between the two adjacent eigenfrequencies. Thus, it is reasonable to describe a transmission line resonator as a lumped-element LC circuit with a single resonant frequency of interest.

Chapter 2

MICROWAVE QUANTUM OPTICS

2.1 Second quantization of microwaves

By replacing the node flux, ϕ, and charge, q, with non-commuting operators, we have witnessed a leap from the classical to quantum circuits. In this new regime, dynamics of the system obeys the Schrödinger equation

$$i\hbar\frac{\partial}{\partial t}\psi(\phi,t) = H\psi(\phi,t), \tag{2.1}$$

where H is the system Hamiltonian, $\psi(\phi,t)$ is the wavefunction written in the flux basis. To solve this differential equation, a standard procedure is to find the eigenvalues and eigenstates, E_n and $\psi_n(\phi)$, of the Hamiltonian and write an arbitrary wave function in a linear superposition of them: $\psi(\phi,t) = \sum_{n=0}^{\infty} c_n \exp\left(-iE_n t/\hbar\right)\psi_n(\phi)$, where c_n are probability amplitudes. For example, let us recall the example of an LC oscillator (as introduced in Chapter 1)

$$H = \frac{q^2}{2C} + \frac{\phi^2}{2L}, \text{ where } q = -i\hbar\partial_\phi, \tag{2.2}$$

of which the eigenvalues and eigenstates can be obtained by using the spectral method [26]

$$E_n = \hbar\omega_0\left(n+\frac{1}{2}\right),\ \psi_n(\phi) = \frac{1}{\sqrt{2^n n!}}\left(\frac{C\omega_0}{\pi\hbar}\right)^{1/4}\mathcal{H}_n\left(\sqrt{\frac{C\omega_0}{\hbar}}\phi\right), \tag{2.3}$$

where $\omega_0 = 1/\sqrt{LC}$, $\mathcal{H}_n(\cdot)$ are Hermite polynomials. Thus, an arbitrary wavefunction of an LC oscillator can be expressed by using the superposition principle. One thing we have learned from this example is that to describe a quantum system lots of efforts are required to solve the differential equation. A natural question is that whether there exists an algebraic way to describe a quantum system and simplify the calculation.

The second quantization provides an affirmative answer to the question. The door to the expected simplification is opened by interpreting these evenly spaced energy levels, E_n, as a corresponding numbers of quanta [25]. By defining the following annihilation and creation operators

$$a = \frac{1}{\sqrt{2\hbar}}\left(\sqrt{C\omega_0}\phi + \frac{i}{\sqrt{C\omega_0}}q\right),\ a^\dagger = \frac{1}{\sqrt{2\hbar}}\left(\sqrt{C\omega_0}\phi - \frac{i}{\sqrt{C\omega_0}}q\right), \tag{2.4}$$

the Hamiltonian in Eq. (2.2) can be written in the following form

$$H = \hbar\omega_0\left(n+\frac{1}{2}\right), \tag{2.5}$$

where $n = a^\dagger a$ is called the number operator. By definition, the annihilation and creation operators obey the canonical commutation relation, $\left[a, a^\dagger\right] = 1$. The interpretation of a and $a^\dagger$ is that they annihilate or create a quanta of energy, $\hbar\omega_0$, in the system, which is named as a microwave photon in

superconducting quantum circuits. Thus, the eigenstate, $\psi_n(\phi)$, represents a state with n photons in the system, which will be written as $|n\rangle$ by following Dirac's bra-ket notation. In this way, we avoid the mathematical details of solving the differential equation and describe the microwave radiation in terms of photon numbers in the normal modes. Most importantly, the second quantization procedure provides a common language for describing the optical and microwave radiation. It enables us to apply directly the theoretical tools developed in quantum optics to study a superconducting quantum circuit.

2.2 Quantum states of photons

Having seen that the microwaves can be described in the same way of optical light, we now review several quantum states of photons that are useful to describe the quantum statistical properties of radiation.

2.2.1 Example #1: Fock states

Fock states are eigenstates of the number operator

$$a^\dagger a|n\rangle = n|n\rangle, \tag{2.6}$$

where $n = 0, 1, \cdots$ is the photon number. Sometimes, it is useful to define the Fock state from the vacuum

$$|n\rangle = \frac{a^{\dagger n}}{\sqrt{n!}}|0\rangle, \tag{2.7}$$

where $a|0\rangle = 0$. With this definition, the physical meaning of the creation and annihilation operators can be immediately appreciated from the following relations

$$a^\dagger|n\rangle = \sqrt{n+1}|n+1\rangle,\ a|n\rangle = \sqrt{n}|n-1\rangle, \tag{2.8}$$

which creates or annihilates an extra photon in the system.

2.2.2 Example #2: Coherent states

Coherent states are eigenstates of the annihilation operator [27, 28]

$$a|\alpha\rangle = \alpha|\alpha\rangle, \tag{2.9}$$

where α is an arbitrary complex number. By this definition, one can calculate the average photon number of a coherent state as $\bar{n} = |\alpha|^2$. Similar to Eq. (2.7), one may also define a coherent state from the vacuum

$$|\alpha\rangle = D(\alpha)|0\rangle, \tag{2.10}$$

where $D(\alpha) = \exp\left(\alpha a^\dagger - \alpha^* a\right)$ is called the displacement operator. Alternatively, a coherent state can also be defined in the basis of Fock states

$$|\alpha\rangle = \exp\left(-\frac{|\alpha|^2}{2}\right)\sum_{n=0}^{\infty}\frac{\alpha^n}{\sqrt{n!}}|n\rangle. \tag{2.11}$$

For completeness, we list several useful properties of the displacement operator [29]

$$(1)\, D^\dagger(\alpha) = D^{-1}(\alpha) = D(-\alpha), \tag{2.12}$$

$$(2)\, D(\alpha)D(\beta) = e^{(\alpha\beta^* - \alpha^*\beta)/2}D(\alpha+\beta) = e^{\alpha\beta^* - \alpha^*\beta}D(\beta)D(\alpha), \tag{2.13}$$

$$(3)\, D^\dagger(\alpha)aD(\alpha) = a + \alpha,\ D^\dagger(\alpha)a^\dagger D(\alpha) = a^\dagger + \alpha^*. \tag{2.14}$$

2.2.3 Example #3: Squeezed-coherent and coherent-squeezed states

Squeezed coherent and coherent squeezed states are closely related to each other by the definitions

$$|\alpha,\zeta\rangle = D(\alpha)S(\zeta)|0\rangle,\ |\beta,\zeta\rangle' = S(\zeta)D(\beta)|0\rangle, \tag{2.15}$$

where $D(\alpha)$ is the displacement operator, $S(\zeta) = \exp\left[(\zeta^*/2)\,a^2 - (\zeta/2)\,a^{\dagger 2}\right]$ is called the squeeze operator. In the literature, these states are more often called the *squeezed state* and the *two-photon coherent state*, respectively, which differ in the sequence of applying the displacement and squeeze operators to the vacuum [29]. However, they are equivalent to each other, i.e., $D(\alpha)S(\zeta) = S(\zeta)D(\beta)$, on condition that

$$\alpha = \beta\cosh(r) - e^{i2\varphi}\beta^*\sinh(r),\ \text{or},\ \beta = \alpha\cosh(r) + e^{i2\varphi}\alpha^*\sinh(r), \tag{2.16}$$

where $\zeta = re^{i2\varphi}$. In what follows, we focus only on the squeezed state.

The squeezed state is an eigenstate of the operator, $S(\zeta)aS^\dagger(\zeta)$, that is,

$$\left[S(\zeta)aS^\dagger(\zeta)\right]|\alpha,\zeta\rangle = \beta|\alpha,\zeta\rangle. \tag{2.17}$$

Following this definition and using the property (3) of the squeeze operator listed below, one may calculate the mean photon number as $\bar{n} = |\alpha|^2 + \sinh^2(r)$. In the Fock state basis, the squeezed state reads [30]

$$|\alpha,\zeta\rangle = \mathcal{N}\sum_{n=0}^{\infty}\left\{\sqrt{\frac{[e^{i2\varphi}\tanh(r)/2]^n}{n!\cosh(r)}}\mathcal{H}_n\left[\frac{\beta}{\sqrt{e^{i\varphi}\sinh(2r)}}\right]\right\}|n\rangle \tag{2.18}$$

where $\mathcal{H}_n(\cdot)$ is the Hermite polynomial, $\mathcal{H}$ is a normalization factor.

For completeness, we also list several properties of the squeeze operator [31]

$$(1)\, S^\dagger(\zeta) = S^{-1}(\zeta) = S(-\zeta), \tag{2.19}$$

$$(2)\, S(\zeta_1)S(\zeta_2) = S\left(\frac{\zeta_1+\zeta_2}{1+\zeta_1^*\zeta_2}\right)\exp\left[\frac{1}{2}\ln\left(\frac{1+\xi_1\xi_2^*}{1+\xi_1^*\xi_2}\right)\left(a^\dagger a + \frac{1}{2}\right)\right], \tag{2.20}$$

$$(3)\, S^\dagger(\zeta)aS(\zeta) = a\cosh(r) - a^\dagger e^{i2\varphi}\sinh(r),\ S^\dagger(\zeta)a^\dagger S(\zeta) = a^\dagger\cosh(r) - ae^{-i2\varphi}\sinh(r). \tag{2.21}$$

We note that, to derive the property (2), one needs to write the squeeze operator as $S(\zeta) =$

$\exp(-\tau\sigma_+)\exp\left[\ln\left(1+|\tau|^2\right)\sigma_z/2\right]\exp(\tau^*\sigma_-)$, where $\tau = e^{i\varphi}\tanh(r)$, $\sigma_+ = a^{\dagger 2}/2$, $\sigma_- = a^2/2$, and $\sigma_z = a^\dagger a + 1/2$ [32].

2.2.4 Example #4: Thermal states

The three states we have introduced are called pure states, which are the states a single quantum object can stay at one specific time instance. For an ensemble of identical and non-interacting quantum objects, there are probabilities for each object to be in different pure states. In this situation, we say that the object is in a mixed state in the sense of an ensemble average. To describe a mixed state, it is useful to define a density operator, ρ, which is a weighted summation of the outer products of pure states. The weight, P_n, is the classical probability for one object to be in the corresponding pure state, $|\psi_n\rangle$. To make this definition more clear, here we take the thermal state for illustration.

The density operator of a thermal state at temperature, T, is defined as

$$\rho_T = \sum_{n=0}^{\infty} P_n |n\rangle\langle n|, \tag{2.22}$$

where $P_n = \exp\left[-E_n/(k_\mathrm{B}T)\right] / \sum_{m=0}^{\infty}\exp\left[-E_n/(k_\mathrm{B}T)\right]$ obeys the Boltzmann distribution, which describes the probability for the system to be in the Fock state $|n\rangle$. Recalling that $E_n = \hbar\omega\,(n+1/2)$ for Fock states, one can simplify the distribution function as

$$P_n = \frac{1-\exp\left[-\hbar\omega/(k_\mathrm{B}T)\right]}{\exp\left[n\hbar\omega/(k_\mathrm{B}T)\right]}. \tag{2.23}$$

In this regard, the average photon number of the thermal state is $\bar{n}_T = 1/\left\{\exp\left[\hbar\omega/\left(k_\mathrm{B}T\right)\right]-1\right\}$.

2.2.5 Example #5: Gaussian states

In experiments of quantum optics, the system are often in the so-called Gaussian state, which is relatively easy to prepare, manipulate, and read out [33–36]. The most general definition of a Gaussian state is a rotated, squeezed, and displaced thermal state

$$\rho_\mathrm{G} = D(\alpha)S(\zeta)R(\phi)\rho_T R^\dagger(\phi)S^\dagger(\zeta)D^\dagger(\alpha), \tag{2.24}$$

where $D(\alpha)$ and $S(\zeta)$ are displacement and squeeze operators, respectively, and $R(\phi) = \exp\left(-i\phi a^\dagger a\right)$ is called the rotation operator. We note that the rotation operator plays no role in the expression of a single-mode Gaussian state and thus can be simply omitted. However, we keep it here for completeness. Similar to all the states introduced above, one may also write a Gaussian state in Fock state basis [37–41]. The result is too complicated to display here. In fact, it is more convenient to describe a Gaussian state by the quasidistribution functions that will be introduced shortly in Section 2.3. The mean photon number of a Gaussian state is $\bar{n} = (\bar{n}_T + 1/2)\cosh(2r) - 1/2 + |\alpha|^2$, where $\bar{n}_T$ is the average photon number of a thermal state at temperature T (see Chapter 7 for deviation).

For completeness, we also list several properties of the rotation operator

$$(1)\ R^\dagger(\phi) = R^{-1}(\phi) = R(-\phi), \tag{2.25}$$

$$(2)\ R(\phi_1)R(\phi_2) = R(\phi_1+\phi_2), \tag{2.26}$$

$$(3)\ R^\dagger(\phi)aR(\phi) = ae^{-i\phi},\ R^\dagger(\phi)a^\dagger R(\phi) = a^\dagger e^{i\phi}. \tag{2.27}$$

2.3 Quasidistribution functions

Using Dirac's bra-ket notation, we have seen that an arbitrary quantum state of photons can be written as a linear combination of different Fock states $\{|n\rangle|n = 0, 1, \cdots\}$, which fulfill the requirement of completeness and orthonormality

$$\sum_{n=0}^{\infty} |n\rangle\langle n| = \mathbb{1},\ \langle n|n'\rangle = \delta_{n,n'}. \tag{2.28}$$

These properties ensure that a wavefunction corresponds to a unique linear combination of the basis states, which is a commercial and useful method for describing a quantum state. However, in the experiments of quantum optics it may be more convenient to describe a state in the so-called coherent state basis $\{|\alpha\rangle\}$, which are neither orthonormal nor complete. In fact, the coherent states form an overcomplete basis [42]

$$\langle\alpha|\beta\rangle = e^{-\left(|\alpha|^2+|\beta|^2\right)/2} e^{\alpha^*\beta},\ \int d^2\alpha |\alpha\rangle\langle\alpha| = \pi, \tag{2.29}$$

where the integral covers the entire complex plane. In this regard, a quantum state cannot be uniquely expanded on the coherent state basis. However, the bright side of overcompleteness is that, as was initially revealed by Glauber and Sudarshan [27, 28, 43, 44], one may write the density matrix of an arbitrary state, ρ, as a weighted average over different coherent states, $|\alpha\rangle\langle\alpha|$. Here, the weight for different α is called the P representation. This approach can also be generalized to many other representations such as the Q and W representations, which are named after the mathematicians Husimi and Wigner, respectively. In this section, we introduce the definition of the three representations as well as their basic properties.

2.3.1 The Glauber-Sudarshan P representation

We define the characteristic function as $\chi(z, z^*)$, such that the corresponding quasidistribution function, $F(\alpha, \alpha^*)$, can be written as a two dimensional Fourier transform [42]

$$F(\alpha, \alpha^*) = \frac{1}{\pi^2} \int d^2z \chi(z, z^*) e^{-iz^*\alpha^*} e^{-iz\alpha}, \tag{2.30}$$

$$\chi(z, z^*) = \int d^2\alpha F(\alpha, \alpha^*) e^{iz^*\alpha^*} e^{iz\alpha}. \tag{2.31}$$

For P representation, the characteristic function reads

$$\chi_{\mathrm{N}}(z, z^*) = \mathrm{tr}\left(\rho e^{iz^*a^\dagger} e^{iza}\right), \tag{2.32}$$

such that the P representation is

$$P(\alpha, \alpha^*) = \frac{1}{\pi^2} \int d^2z \chi_{\mathrm{N}}(z, z^*) e^{-iz^*\alpha^*} e^{-iz\alpha}. \tag{2.33}$$

The convenience of P representation is that the normal-ordered operator averages can be readily calculated via the prescription

$$\left\langle a^{\dagger p}a^{q}\right\rangle = \frac{\partial^{p+q}}{\partial\left(iz^{*}\right)^{p}\partial\left(iz\right)^{q}}\chi_{\mathrm{N}}(z,z^{*})\bigg|_{z=z^{*}=0} = \int d^{2}\alpha P(\alpha,\alpha^{*})\alpha^{*p}\alpha^{q}. \tag{2.34}$$

Recalling the overcomplete property of coherence states, i.e., Eq. (2.29), the above equation indicates that

$$\rho = \int d^{2}\alpha P(\alpha,\alpha^{*})|\alpha\rangle\langle\alpha|. \tag{2.35}$$

This is consistent with the previous claim that arbitrary state can be written as a weighted summation over coherent states.

With these notations, let us calculate the P-quasidistribution function of the states introduced in Section 2.2. They are the Fock state $|n\rangle$, coherent state $|\beta\rangle$, squeezed state $|\beta,\zeta\rangle$, thermal state ρ_T, and Gaussian state ρ_{G}. The P representation of the Fock, squeezed, and Gaussian states does not exist in general, since they can be non-classical states [42]. However, they exist in the sense of generalized functions which involves too many mathematical details and is beyond the interest of this thesis. This is also the major drawback of P representation: It is positive and nonsingular only for classical states in the sense that they can be regarded as a distribution function. The P representations for the other two states read

$$\text{Coherent state } |\beta\rangle\text{: } P(\alpha,\alpha^{*}) = \delta(\alpha-\beta), \tag{2.36}$$

$$\text{Thermal state } \rho_T\text{: } P(\alpha,\alpha^{*}) = \frac{e^{-|\alpha|^{2}/\bar{n}_T}}{\pi\bar{n}_T}. \tag{2.37}$$

2.3.2 The Husimi Q representation

Similar to the discussions above, the characteristic function of the Q representation is defined as

$$\chi_{\mathrm{A}}(z,z^{*}) = \mathrm{tr}\left(\rho e^{iza}e^{iz^{*}a^{\dagger}}\right), \tag{2.38}$$

and thus the Q representation is

$$Q(\alpha,\alpha^{*}) = \frac{1}{\pi^{2}}\int d^{2}z\chi_{\mathrm{A}}(z,z^{*})e^{-iz^{*}\alpha^{*}}e^{-iz\alpha}. \tag{2.39}$$

Contrary to the P representation, the convenience of Q representation exists in calculating the antinormal-ordered operator averages

$$\left\langle a^{p}a^{\dagger q}\right\rangle = \frac{\partial^{p+q}}{\partial\left(iz^{*}\right)^{p}\partial\left(iz\right)^{q}}\chi_{\mathrm{A}}(z,z^{*})\bigg|_{z=z^{*}=0} = \int d^{2}\alpha Q(\alpha,\alpha^{*})\alpha^{p}\alpha^{*q}. \tag{2.40}$$

One can also write the Q function as

$$Q(\alpha,\alpha^{*}) = \frac{\langle\alpha|\rho|\alpha\rangle}{\pi}, \tag{2.41}$$

where we have used the overcomplete property of coherent states. In this regard, we may interpret the value of the Q function as the probability density of detecting the field at position $x = \left(\alpha+\alpha^{*}\right)/\sqrt{2}$

and momentum $p = -i(\alpha - \alpha^*)/\sqrt{2}$. We will return to this point again in Chapter 6 in the context of quadrature measurement.

The possible drawbacks of the P-representation, that are the non-positivity and singularity, are expected to be solved in the Q representation, because the value of $\pi Q(\alpha, \alpha^*)$ is strictly the probability of detecting the coherent state $|\alpha\rangle$. The quasidistribution functions of the five states introduced in Section 2.2 are [42, 45]

$$\text{Fock state } |n\rangle\text{: } Q(\alpha,\alpha^*) = \frac{|\alpha|^{2n}\exp\left(-|\alpha|^2\right)}{\pi n!}, \tag{2.42}$$

$$\text{Coherent state } |\beta\rangle\text{: } Q(\alpha,\alpha^*) = \frac{\exp\left[-\left(x^2+y^2\right)\right]}{\pi}, \tag{2.43}$$

$$\text{Squeezed state } |\beta,\zeta\rangle\text{: } Q(\alpha,\alpha^*) = \frac{2\exp\left\{-2\left[\frac{(x\cos\varphi+y\sin\varphi)^2}{1+e^{-2r}} + \frac{(-x\cos\varphi+y\sin\varphi)^2}{1+e^{2r}}\right]\right\}}{\pi\sqrt{\left(1+e^{-2r}\right)\left(1+e^{2r}\right)}}, \tag{2.44}$$

$$\text{Thermal state } \rho_T\text{: } Q(\alpha,\alpha^*) = \frac{\exp\left[-|\alpha|^2/\left(1+\bar{n}_T\right)\right]}{\pi\left(1+\bar{n}_T\right)}, \tag{2.45}$$

$$\begin{aligned}\text{Gaussian state } \rho_{\mathrm{G}}\text{: } Q(\alpha,\alpha^*) = {} & \sqrt{\frac{2}{\pi[1+(2\bar{n}_T+1)e^{-2r}]}}\exp\left\{-2\frac{[x\cos\varphi+y\sin\varphi]^2}{1+(2\bar{n}_T+1)e^{-2r}}\right\} \\ & \times\sqrt{\frac{2}{\pi[1+(2\bar{n}_T+1)e^{2r}]}}\exp\left\{-2\frac{[-x\sin\varphi+y\cos\varphi]^2}{1+(2\bar{n}_T+1)e^{2r}}\right\},\end{aligned} \tag{2.46}$$

where we have defined $x = \mathrm{Re}(\alpha-\beta)$ and $y = \mathrm{Im}(\alpha-\beta)$ to simplify the notation. However, the spread of the Q function in phase space is somewhat wider than that of the P function, as can be readily seen by comparing with the result in Eqs. (2.36) and (2.37). Because of this relatively large uncertainty, one can hardly distinguish a vacuum state from a thermal state without a very careful comparison. This is the major drawback of the Q representation.

2.3.3 The Wigner-Ville W representation

As a compromise between the P and Q representations, we define the characteristic function of the W representation as

$$\chi_{\mathrm{S}}(z,z^*) = \mathrm{tr}\left(\rho e^{iz^*a^\dagger + iza}\right), \tag{2.47}$$

such that the W representation is

$$W(\alpha,\alpha^*) = \frac{1}{\pi^2}\int d^2z\chi_{\mathrm{S}}(z,z^*)e^{-iz^*\alpha^*}e^{-iz\alpha}. \tag{2.48}$$

The W representation is useful to calculate the so called symmetric-ordered operator averages

$$\left\langle\left(a^{\dagger p}a^q\right)_{\mathrm{S}}\right\rangle = \frac{\partial^{p+q}}{\partial(iz^*)^p\,\partial(iz)^q}\chi_{\mathrm{S}}(z,z^*)\bigg|_{z=z^*=0} = \int d^2\alpha W(\alpha,\alpha^*)\alpha^p\alpha^{*q}, \tag{2.49}$$

where $\left(a^{\dagger p}a^q\right)_{\mathrm{S}}$ denotes the average of all possible oderings of p creation and q annihilation operators [45]. For example, $\left(a^{\dagger 2}a^2\right)_{\mathrm{S}} = \left(a^{\dagger 2}a^2 + a^\dagger a a^\dagger a + a^\dagger a^2 a^\dagger + a a^{\dagger 2}a + a a^\dagger a a^\dagger + a^2 a^{\dagger 2}\right)/6$.

Compared to the P and Q representations, the W representation is always a normal function but allows negative values. We note that this negativity originates from the non-commutating relation between the field operators, a and $a^\dagger$, and thus may be a useful indication of the non-classical properties

of radiation. More precisely, it has been shown that the negativity can be observed only if the state is non-Gaussian [46]. For the five states discussed above, we summarize their W quasidistribution functions as [42, 45]

$$\text{Fock state } |n\rangle\colon W(\alpha,\alpha^*) = \frac{2e^{-2|\alpha|^2}}{\pi n!}\sum_{k=0}^{n}(-1)^{n-k}\frac{(n!)^2|2\alpha|^{2k}}{(k!)^2(n-k)!}, \tag{2.50}$$

$$\text{Coherent state } |\beta\rangle\colon W(\alpha,\alpha^*) = \frac{2\exp\left[-2\left(x^2+y^2\right)\right]}{\pi}, \tag{2.51}$$

$$\text{Squeezed state } |\beta,\zeta\rangle\colon W(\alpha,\alpha^*) = \frac{\exp\left\{-2\left[\frac{(x\cos\varphi+y\sin\varphi)^2}{e^{-2r}}+\frac{(-x\cos\varphi+y\sin\varphi)^2}{e^{2r}}\right]\right\}}{\pi}, \tag{2.52}$$

$$\text{Thermal state } \rho_T\colon W(\alpha,\alpha^*) = \frac{2\exp\left[-2|\alpha|^2/\left(1+2\bar{n}_T\right)\right]}{\pi\left(1+2\bar{n}_T\right)}, \tag{2.53}$$

$$\begin{aligned}\text{Gaussian state } \rho_{\mathrm{G}}\colon W(\alpha,\alpha^*) = {}& \sqrt{\frac{2}{\pi(2\bar{n}_T+1)e^{-2r}}}\exp\left\{-2\frac{[x\cos\varphi+y\sin\varphi]^2}{(2\bar{n}_T+1)e^{-2r}}\right\}\\ &\times\sqrt{\frac{2}{\pi(2\bar{n}_T+1)e^{2r}}}\exp\left\{-2\frac{[-x\sin\varphi+y\cos\varphi]^2}{(2\bar{n}_T+1)e^{2r}}\right\}.\end{aligned} \tag{2.54}$$

Although the expressions of the non-classical states, for example, the Fock state $|n\rangle$, seems to be rather complicated, Eq. (2.50) is a well defined function without singularity. In fact, one can always find a well-behaved function to describe an arbitrary state in W representation, which is advantageous over the P representation. On the other hand, the uncertainty of the W quasidistribution function is smaller than that of the Q function for describing the same state. In these regards, the W representation is commonly used to describe a photonic state in the literature compared with the other two representations.

2.3.4 Transform among different representations

Knowing the definitions and properties of the P, Q, and W representations, it is convenient to use different representations for different purposes. These transformations will be useful in Chapter 6, where we describe the theory of quadrature measurement. Here, we summarize the results while referring the readers to Ref. [42] for the detailed derivations. On the characteristic function side, the transformations are straightforward

$$e^{|z|^2/2}\chi_{\mathrm{A}}(z,z^*) = \chi_{\mathrm{S}}(z,z^*) = e^{-|z|^2/2}\chi_{\mathrm{N}}(z,z^*). \tag{2.55}$$

However, the transformation among the quasidistribution functions must be done in a P-W-Q sequence, that is

$$Q(\alpha,\alpha^*) = \frac{2}{\pi}\int d^2\beta W(\beta,\beta^*)e^{-2|\beta-\alpha|^2} = \exp\left(\frac{1}{2}\frac{\partial^2}{\partial\alpha\partial\alpha^*}\right)W(\alpha,\alpha^*), \tag{2.56}$$

$$W(\alpha,\alpha^*) = \frac{2}{\pi}\int d^2\beta P(\beta,\beta^*)e^{-2|\beta-\alpha|^2} = \exp\left(\frac{1}{2}\frac{\partial^2}{\partial\alpha\partial\alpha^*}\right)P(\alpha,\alpha^*). \tag{2.57}$$

Inserting Eq. (2.57) into (2.56), we obtain a direct relation between the P and Q functions

$$Q(\alpha,\alpha^*) = \frac{1}{\pi}\int d^2\beta P(\beta,\beta^*)e^{-|\beta-\alpha|^2} = \exp\left(\frac{\partial^2}{\partial\alpha\partial\alpha^*}\right)P(\alpha,\alpha^*). \tag{2.58}$$

2.4 Quantum theory of damping

So far, our discussions are focused solely on closed systems. To take dissipation into consideration, the usual way in classical mechanics is to add a velocity-dependent term in the Euler-Lagrange equation of motion (EOM) [47]. For example, the EOM of a damped LC oscillator can be written as

$$\ddot{\phi} + \gamma\dot{\phi} + \omega_0^2\phi = 0, \tag{2.59}$$

where γ is the energy damping rate. However, this approach can hardly be used in quantum systems because it necessarily violates the Heisenberg uncertainty relation. The key to incorporate damping into quantum mechanics relies on the fact that the system is damped because of the interaction with the environment, while the latter is large enough to be described as a thermal equilibrium throughout the process [42]. In other words, a dissipation is always accompanied with a fluctuating force acted by the environment, $f(t)$, called the Langevin force. Thus, Eq. (2.59) should be written as a stochastic equation to describe an open quantum system

$$\ddot{\phi} + \gamma\dot{\phi} + \omega_0^2\phi = f(t). \tag{2.60}$$

This is one formulation of the fluctuation-dissipation theorem. In this section, we review the theoretical tools developed in quantum optics to describe an open quantum system.

2.4.1 Heisenberg picture: The Langevin-equation approach

Amplitude damping

We consider a harmonic oscillator, i.e., the system, which interacts with a bosonic bath, i.e., the environment. The Hamiltonian of the composite system reads

$$H_\mathrm{s} = \hbar\omega_0 a^\dagger a, \tag{2.61}$$

$$H_\mathrm{b} = \hbar\int_{-\infty}^{+\infty} d\omega\omega b_\omega^\dagger b_\omega, \tag{2.62}$$

$$H_\mathrm{sb} = \hbar\int_{-\infty}^{+\infty} d\omega\left(\kappa^* a b_\omega^\dagger + \kappa a^\dagger b_\omega\right). \tag{2.63}$$

Following the Heisenberg equation, the time evolution of the intra-resonator field, a, as well as the bath field, b_ω, can be readily written as

$$\dot{a} = -i\omega_0 a - i\int_{-\infty}^{+\infty} d\omega\kappa b_\omega, \tag{2.64}$$

$$\dot{b}_\omega = -i\omega b_\omega - i\kappa^* a. \tag{2.65}$$

Inserting the formal solution of Eq. (2.65) into (2.64), we have

$$\dot{a}(t) = -i\omega_0 a(t) - |\kappa|^2\int_{-\infty}^{+\infty} d\omega\int_{t_0}^{t} dt' e^{-i\omega(t-t')}a(t') + f(t). \tag{2.66}$$

where

$$f(t) = -i\kappa \int_{-\infty}^{+\infty} d\omega e^{-i\omega(t-t_0)} b_\omega(t_0). \tag{2.67}$$

This equation can be further simplified by using the property, $\int_{-\infty}^{+\infty} d\omega e^{-i\omega(t-t_0)} = 2\pi\delta(t-t_0)$. We therefore obtain the so-called quantum Langevin equation

$$\dot{a} = -i\omega_0 a - \frac{\gamma}{2}a + f(t), \tag{2.68}$$

where $\sqrt{\gamma} = i\sqrt{2\pi}\kappa$. For the bath in a thermal state at temperature T, the correlation functions of the Langevin force obey the following relations [48, 49]

$$\langle f \rangle = 0,\ \langle f^\dagger(t) f(t') \rangle = \gamma \bar{n}_T \delta(t-t'). \tag{2.69}$$

Moreover, we have [48]

$$\langle a(t) f(t) \rangle = \langle f^\dagger(t) a^\dagger(t) \rangle = 0,\ \langle f(t) a(t) \rangle = \langle a^\dagger(t) f^\dagger(t) \rangle = 0, \tag{2.70}$$

$$\langle f^\dagger(t) a(t) \rangle = \langle a^\dagger(t) f(t) \rangle = \frac{\gamma}{2}\bar{n}_T,\ \langle a(t) f^\dagger(t) \rangle = \langle f(t) a^\dagger(t) \rangle = \frac{\gamma}{2}\left(\bar{n}_T + 1\right), \tag{2.71}$$

such that

$$\frac{d}{dt}\langle a \rangle = -i\omega_0 \langle a \rangle - \frac{\gamma}{2}\langle a \rangle, \text{ and } \frac{d}{dt}\langle a^\dagger a \rangle = -\gamma \langle a^\dagger a \rangle + \gamma \bar{n}_T. \tag{2.72}$$

Phase damping

The above discussions describe the amplitude damping of the system, where a photon of the system is exchanged with a photon of the bath. Another damping mechanism that is commonly studied in quantum optics is called the dephasing, where a system photon is scattered when it absorbs or emits a bath photon [50]. To describe this effect, one may consider a phase bath with the following system-environment interaction [50–54]

$$H_{\text{sb}} = \hbar \int_{-\infty}^{+\infty} d\omega a^\dagger a \left(\kappa_\phi^* b_\omega^\dagger + \kappa_\phi b_\omega\right). \tag{2.73}$$

Following a similar derivation, we obtain the corresponding Langevin equation

$$\dot{a} = -i\omega_0 a - \frac{\gamma_\phi}{2}a + \left(af - f^\dagger a\right), \tag{2.74}$$

where $\sqrt{\gamma_\phi} = i\sqrt{2\pi}\kappa_\phi$. Similarily, the correlation functions of the Langevin force obey the following relations [49]

$$\langle f \rangle = 0,\ \langle f^\dagger(t) f(t') \rangle = \gamma \bar{n}_\phi \delta(t-t'). \tag{2.75}$$

However, the following averages are slightly different from Eq. (2.71) [48]

$$\langle a(t)f(t)\rangle = -\frac{\gamma_\phi}{2}\bar{n}_\phi\langle a(t)\rangle,\ \langle f^\dagger(t)a^\dagger(t)\rangle = -\frac{\gamma_\phi}{2}\bar{n}_\phi\langle a^\dagger(t)\rangle, \tag{2.76}$$

$$\langle f(t)a(t)\rangle = -\frac{\gamma_\phi}{2}\left(\bar{n}_\phi+1\right)\langle a(t)\rangle,\ \langle a^\dagger(t)f^\dagger(t)\rangle = -\frac{\gamma_\phi}{2}\left(\bar{n}_\phi+1\right)\langle a^\dagger(t)\rangle, \tag{2.77}$$

$$\langle f^\dagger(t)a(t)\rangle = \frac{\gamma_\phi}{2}\bar{n}_\phi\langle a(t)\rangle,\ \langle a^\dagger(t)f(t)\rangle = \frac{\gamma_\phi}{2}\bar{n}_\phi\langle a^\dagger(t)\rangle, \tag{2.78}$$

$$\langle a(t)f^\dagger(t)\rangle = \frac{\gamma_\phi}{2}\left(\bar{n}_\phi+1\right)\langle a(t)\rangle,\ \langle f(t)a^\dagger(t)\rangle = \frac{\gamma_\phi}{2}\left(\bar{n}_\phi+1\right)\langle a^\dagger(t)\rangle. \tag{2.79}$$

Correspondingly, we have

$$\frac{d}{dt}\langle a\rangle = -i\omega_0\langle a\rangle - \frac{\gamma_\phi}{2}\left(2\bar{n}_\phi+1\right)\langle a\rangle, \text{ and } \frac{d}{dt}\langle a^\dagger a\rangle = 0. \tag{2.80}$$

2.4.2 Schrödinger picture: The master-equation approach

Amplitude damping

The so-called master equation is essentially identical to the quantum Langevin equation, while the former describes the system dynamics in the Schrödinger picture. Given the Hamiltonians in Eqs. (2.61)-(2.63), we write the dynamics of the composite system in an integro-differential form in the interaction picture [42]

$$\dot{\tilde{\chi}}(t) = \frac{1}{i\hbar}\left[\tilde{H}_{\rm sb},\tilde{\chi}(0)\right] - \frac{1}{\hbar^2}\int_0^t dt'\mathrm{tr}_{\rm b}\left\{\left[\tilde{H}_{\rm sb}(t),\left[\tilde{H}_{\rm sb}(t'),\tilde{\chi}(t')\right]\right]\right\}. \tag{2.81}$$

Here, we have defined $\tilde{\chi}(t) = \exp\left[it\left(H_{\rm s}+H_{\rm b}\right)/\hbar\right]\chi(t)\exp\left[-it\left(H_{\rm s}+H_{\rm b}\right)/\hbar\right]$, $\tilde{H}_{\rm sb}(t) = \exp\left[it\left(H_{\rm s}+H_{\rm b}\right)/\hbar\right]H_{\rm sb}\exp\left[-it\left(H_{\rm s}+H_{\rm b}\right)/\hbar\right]$. The master equation can be obtained by assuming that the composite system is initially in a product state of the system and the environment, i.e., $\chi(0)=\rho(0)\otimes\rho_{\rm b}$, and that $\mathrm{tr}_{\rm R}\left\{\tilde{H}_{\rm sb}(t)\rho_{\rm b}\right\}=0$. However, in most of the time the name "master equation" denotes the equation in the Born-Markov approximation

$$\dot{\tilde{\rho}}(t) = -\frac{1}{\hbar^2}\int_0^t dt'\mathrm{tr}_{\rm R}\left\{\left[\tilde{H}_{\rm sb}(t),\left[\tilde{H}_{\rm sb}(t'),\tilde{\rho}(t)\otimes\rho_{\rm b}\right]\right]\right\}. \tag{2.82}$$

There are two approximations from Eq. (2.81) to (2.82), which correspond to the names of Born and Markov. The Born approximation assumes that the system and the bath are always in a product state $\rho(t)=\rho(t)\otimes\rho_{\rm b}$, while the bath state is $\rho_{\rm b}=\sum_k\rho_T(\omega_k)$ with ρ_T being a thermal state at temperature T. Physically, it requires a weak system-environment coupling strength and a huge environment. On the other hand, the Markov approximation assumes that the time derivative of the system, $\dot{\tilde{\rho}}(t)$, depends solely on the current state, $\tilde{\rho}(t)$. The Markov approximation relies on the separation of two time scales: a long time scale for the dynamics of the system, and a short time scale that characterizes the decay of the correlation functions of the bath field [42].

Now, let us replace the interaction Hamiltonian, $H_{\rm sb}$, in Eq. (2.82) by (2.63), and calculate the specific form of the master equation for the damped LC oscillator. It is straightforward to write

$$\dot{\tilde{\rho}}(t) = \alpha\left(a\tilde{\rho}(t)a^\dagger - a^\dagger a\tilde{\rho}(t)\right) + \beta\left(a\tilde{\rho}(t)a^\dagger + a^\dagger\tilde{\rho}(t)a - a^\dagger a\tilde{\rho}(t) - \tilde{\rho}(t)aa^\dagger\right) + \text{h.c.}, \tag{2.83}$$

where $\alpha=\int_0^t dt'\sum_k|\kappa_k|^2e^{-i(\omega_k-\omega_0)(t-t')}$, $\beta=\int_0^t dt'\sum_k\bar{n}_T(\omega_k)|\kappa_k|^2e^{-i(\omega_k-\omega_0)(t-t')}$, and $\bar{n}_T(\omega_k)$ is the

mean photon number of the thermal state at frequency ω_k. In the limit where the frequencies of the bath modes are close in spectrum, one can replace the summation in α and β by an integral over frequency, i.e., $\sum_k \to \int_{-\infty}^{+\infty} d\omega g(\omega)$ with $g(\omega)$ being the density of states. The result is $\alpha = \gamma/2 + i\Delta$, $\beta = \bar{n}_T\gamma/2 + i\Delta'$, where $\gamma = 2\pi g(\omega_0)|\kappa(\omega_0)|^2$, $\Delta = \mathcal{P}\int_{-\infty}^{+\infty} d\omega g(\omega)|\kappa(\omega_0)|^2/(\omega_0 - \omega)$, $\Delta' = \mathcal{P}\int_{-\infty}^{+\infty} d\omega \bar{n}_T(\omega) g(\omega)|\kappa(\omega_0)|^2/(\omega_0 - \omega)$, and $\mathcal{P}$ represents the Cauchy principle value [42]. By inserting these values into Eq. (2.83), rotating back to the Schrödinger picture, and rearranging the terms in the so-called Lindblad form, we arrive at the celebrated form of the master equation

$$\dot{\rho} = -i\,(\omega_0 + \Delta)\left[a^\dagger a, \rho\right] + \frac{\gamma}{2}\,(\bar{n}_T + 1)\,\mathcal{D}[a]\rho + \frac{\gamma}{2}\bar{n}_T\mathcal{D}[a^\dagger]\rho, \tag{2.84}$$

where $\mathcal{D}[a]\rho = 2a\rho a^\dagger - a^\dagger a\rho - \rho a^\dagger a$ is called the Lindbladian superoperator. Here, the frequency shift, Δ, is small and often neglected in the literature. However, in the case of a damped two-level system, Δ has a famous name: the Lamb shift, which has been precisely measured in experiments and directly motivates the study of quantum electrodynamics. However, one must note that an accurate calculation of the Lamb shift requires the consideration of the counter rotating terms, which have been neglected in the above derivations [55, 56].

In the context of superconducting quantum circuits, the bath is often assumed to be in the vacuum state. This is because that the circuit is cooled down to a low temperature around 10 mK, which corresponds to a negligibly small photon number, $\bar{n}_T \approx 0.03$, for fields oscillating at 6 GHz. Thus, we write the master equation in a simpler form

$$\dot{\rho} = \mathcal{L}\rho, \tag{2.85}$$

where $\mathcal{L}\,(\,\cdot\,) = -(i/\hbar)\,[H, \cdot\,] + (\gamma/2)\mathcal{D}[a]\,(\,\cdot\,)$ is called the Liouvillian superoperator.

Phase damping

To describe the dephasing effect, we insert Eq. (2.73) into (2.82) and follow the same procedure introduced above. The result is simply [50–54]

$$\dot{\rho} = -i\,(\omega_0 + \Delta)\left[a^\dagger a, \rho\right] + \frac{\gamma_\phi}{2}\,[2\bar{n}_\phi + 1]\,\mathcal{D}[a^\dagger a]\rho. \tag{2.86}$$

One sees that the energy is conserved since $\langle a^\dagger a\rangle$ is a conserved quantity of the system. This result is consistent with the Langevin equation, i.e., Eq. (5.63), derived in the Heisenberg picture.

As a closing remark, we comment that there may exist many other decoherence mechanisms, for example, a cross-Kerr type interaction for describing the dissipation-free decoherence [57] or a fermionic bath for capturing the influence of the possible two-level defects [49, 50], which indicate different forms of the system-bath interaction and also the Hamiltonian of the environment. In certain scenarios, the environment can also be in a non-thermal state [58, 59]. A careful distinction between different mechanisms is crucial to the understanding of the open-system dynamics. However, in most of the cases the amplitude and phase damping reservoirs, as introduced above, capture the major physical process of decoherence in a general quantum system. The results form the major building blocks of the field of quantum optics.

Part II:
SUPERCONDUCTING OSCILLATOR WITH TUNABLE NONLINEARITY

*credit Metro-Goldwyn-Mayer

Chapter 3

MODEL: JOSEPHSON-JUNCTION-EMBEDDED TRANSMISSION LINE RESONATOR

In this chapter, we introduce the system we consider throughout the entire thesis: The superconducting nonlinear resonator. We follow the methods of microwave engineering and quantum optics to obtain the classical and quantum descriptions of the system, respectively. Then, we introduce the design parameters of the sample, which has been fabricated by M. Fischer and reported in Ref. [60]. We also introduce the dilution refrigerator which accommodates the sample, as well as the cryogenic setup which is wired up specifically for this thesis.

3.1 Circuit description

3.1.1 Equivalent circuits of the external circuitry

The superconducting nonlinear resonator used in this thesis is realized by embedding a Josephson junction, or a DC-SQUID with a small asymmetry, in the middle of a $\lambda/2$ transmission line resonator, as shown in Fig. 3.1A. To model the system as a lumped-element circuit, we isolate the junction from the other parts, and use the Thevenin's or Norton's theorem to obtain an equivalent lumped-element circuit for the external circuitry, as shown in Fig. 3.1B and C [7, 61–64]. In the Thevenin's equivalent circuit, the external circuitry is described by a *series* circuit with a voltage source, V_{eff}, and an effective impedance, Z_{eff}. Alternatively, a Norton's equivalent circuit is a *parallel* circuit with a current source, I_{eff}, and the same effective impedance, Z_{eff}.

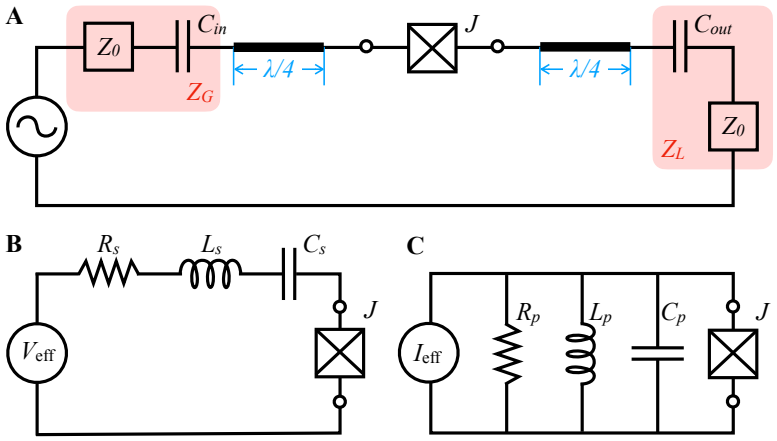

Figure 3.1. Distributed-element and the equivalent lumped-element circuit diagrams of a superconducting nonlinear resonator. (A) Distributed-element model, where a Josephson junction, J, is embedded in the middle of a $\lambda/2$ transmission line resonator. **(B)** The Thevenin's equivalent circuit of (A), where the external circuitry of the Josephson junction is described by a series circuit with a voltage source, V_{eff}, a resistor, R_{s}, an inductor, L_{s}, and a capacitor, C_{s}. **(C)** The Norton's equivalent circuit of (A), where the external circuitry is described by a parallel circuit with a current source, I_{eff}, a resistor, R_{p}, an inductor, L_{p}, and a capacitor, C_{p}.

Thevenin's equivalent series circuit

Let us consider first a Thevenin's equivalent circuit, as shown in Fig. 3.1B. The effective source voltage, $V_{\rm eff}$, should be equal to the voltage at the position $x = 0$ when replacing the Josephson junction by an open circuit element. In this situation, the circuit can be viewed as a $\lambda/4$ transmission line resonator driven by the generator on the left side while being open on the other side, as shown in Fig. 3.2A. The total voltage and current at the position x can be written as [65]

$$V(x) = V_{\rm eff}^{+}\left(e^{-j\beta x} + \Gamma_{\rm L} e^{+j\beta x}\right),\ I(x) = \frac{V_{\rm eff}^{+}}{Z_0}\left(e^{-j\beta x} - \Gamma_{\rm L} e^{+j\beta x}\right), \tag{3.1}$$

where $\beta = 2\pi/\lambda$ is the imaginary part of the complex propagation constant ($\gamma \equiv \alpha + j\beta$), $\Gamma_{\rm L} \approx 1$ is the reflection coefficient of the open-circuited load, $V_{\rm eff}^{+}$ is the amplitude of the right propagating microwave field. On the other hand, we know from KVL that

$$V(-L/2) = \frac{Z_{\rm in}}{Z_{\rm in} + Z_{\rm G}} V_{\rm G}. \tag{3.2}$$

Combining Eqs. (3.1) and (3.2), we obtain

$$V_{\rm eff}^{+} = \frac{Z_{\rm in}}{Z_{\rm in} + Z_{\rm G}} \frac{V_{\rm G}}{e^{j\beta L/2} + \Gamma_{\rm L} e^{-j\beta L/2}}. \tag{3.3}$$

Here, the input impedance is defined as [65]

$$Z_{\rm in} = Z_0 \frac{Z_{\rm L} + jZ_0 \tan(\beta L/2)}{Z_0 + jZ_{\rm L} \tan(\beta L/2)} \approx \frac{Z_0^2}{Z_{\rm L}}, \tag{3.4}$$

where $Z_L = \infty$ for an open circuit, $Z_0 = \sqrt{l/c}$ is the characteristic impedance of the transmission line with l and c being the inductance and capacitance per unit length. In total, we have

$$V_{\rm eff} \equiv V(0) = \frac{2Z_0}{Z_0 + Z_{\rm G}} \frac{V_{\rm G} e^{-j\beta L/2}}{1 - \Gamma_{\rm G} e^{-j\beta L}}, \tag{3.5}$$

where $\Gamma_{\rm G} = (Z_{\rm G} - Z_0)/(Z_{\rm G} + Z_0)$. By inserting $Z_{\rm G} = Z_0 + 1/(j\omega C_{\rm in})$ and $\beta L \approx \pi$ in Eq. (3.5), we have

$$V_{\rm eff} \approx \frac{-jZ_0 V_{\rm G}}{Z_0 + \frac{1}{j\omega_0 C_{\rm in}}} \approx \omega_0 C_{\rm in} Z_0 V_{\rm G}, \tag{3.6}$$

where we have assumed $\omega_0 C_{\rm in} Z_0 \ll 1$ and $\omega_0 = \pi v_{\rm ph}/L$, with $v_{\rm ph} = 1/\sqrt{lc}$ being the phase velocity.

Next, we short-circuit the Josephson junction and calculate the effective current, $I_{\rm eff}$, flowing through the point $x = 0$. The new circuit can be viewed as a loaded $\lambda/2$ transmission line resonator driven by the generator, as shown in Fig. 3.2B. Similar to the open-circuit case, the total voltage and current at the position x are

$$V(x) = V_{\rm eff}^{+}\left(e^{-j\beta(x-L/2)} + \Gamma_{\rm L} e^{+j\beta(x-L/2)}\right),\ I(x) = \frac{V_{\rm eff}^{+}}{Z_0}\left(e^{-j\beta(x-L/2)} - \Gamma_{\rm L} e^{+j\beta(x-L/2)}\right). \tag{3.7}$$

Here, the reflection coefficient, $\Gamma_{\rm L} = (Z_{\rm L} - Z_0)/(Z_{\rm L} + Z_0)$, follows the same definition with the open-

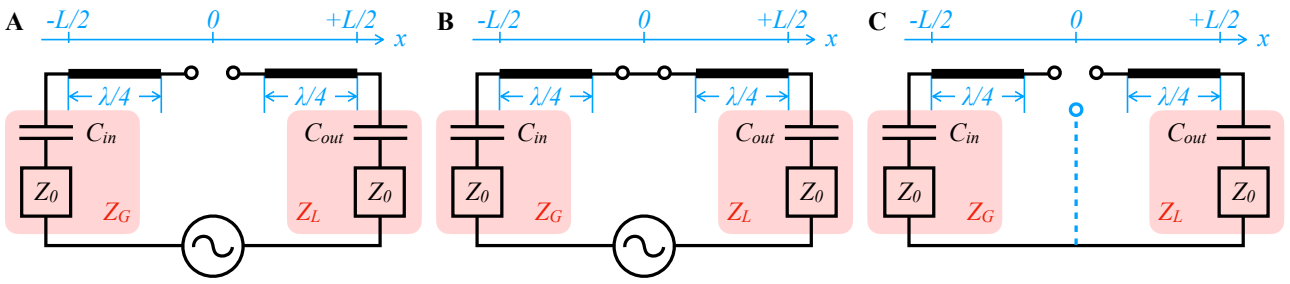

Figure 3.2. Steps for deriving the equivalent lumped-element circuit. **(A)** The effective source voltage, V_{eff}, is determined by the voltage at $x = 0$ when replacing the Josephson junction by an open circuit element. **(B)** The effective source current, I_{eff}, is determined by the current at $x = 0$ when replacing the Josephson junction by a short-circuited circuit element. **(C)** The effective impedance, Z_{eff}, is determined by the input impedance when looking through the two ports of the Josephson junction with the generator being short-circuited.. The input impedance can be regarded as a series combination of two circuits which share the common node colored in blue.

circuit case but has a different value. Combining Eqs. (3.7) with (3.2), we obtain

$$V_{\text{eff}}^{+} = \frac{Z_{\text{in}}}{Z_{\text{in}} + Z_{\text{G}}} \frac{V_{\text{G}}}{e^{j\beta L} + \Gamma_{\text{L}} e^{-j\beta L}}, \tag{3.8}$$

where $Z_{\text{in}} \approx Z_{\text{L}}$ [65]. Thus, the effective current is

$$I_{\text{eff}} \equiv I(0) = \frac{Z_{\text{in}}}{(Z_{\text{in}} + Z_{\text{G}})\, Z_0} \frac{V_{\text{G}} \left(e^{j\beta L/2} - \Gamma_{\text{L}} e^{-j\beta L/2}\right)}{e^{j\beta L} + \Gamma_{\text{L}} e^{-j\beta L}}. \tag{3.9}$$

By replacing $Z_{\text{L}} = Z_0 + 1/\left(j\omega C_{\text{out}}\right)$ and $\beta L/2 \approx \pi/2$ in Eq. (3.9), we have

$$I_{\text{eff}} \approx \frac{-jZ_{\text{L}} V_{\text{G}}}{(Z_{\text{L}} + Z_{\text{G}})\, Z_0} \approx \frac{-jV_{\text{G}}}{\left(1 + \frac{C_{\text{out}}}{C_{\text{in}}}\right) Z_0}. \tag{3.10}$$

Combining Eqs. (3.5) and (3.9), we obtain the effective impedance $Z_{\text{eff}} = V_{\text{eff}}/I_{\text{eff}}$ of the equivalent circuit. However, the result is found to be too coarse to provide a reliable estimation of Z_{eff} in numerical tests, because ω is not exactly equal to the resonant frequency ω_0 [61]. Alternatively, the effective impedance can be obtained by short-circuiting the source, replacing the Josephson junction by an open circuit element, and calculating the input impedance by looking through the two ports of the two open nodes, as shown in Fig. 3.2C. The new circuit can be viewed as a series connection of two circuits which share one common ground. The input impedances for the two circuits are

$$Z_1 = Z_0 \frac{Z_{\text{G}} + jZ_0 \tan(\beta L/2)}{Z_0 + jZ_{\text{G}} \tan(\beta L/2)},\ Z_2 = Z_0 \frac{Z_{\text{L}} + jZ_0 \tan(\beta L/2)}{Z_0 + jZ_{\text{L}} \tan(\beta L/2)}. \tag{3.11}$$

Recalling the relation that $\omega_0 = \pi v_{\text{ph}}/L$ and $\beta = \omega/v_{\text{ph}}$, we have $\beta L/2 = \pi\omega/(2\omega_0)$. Thus, the total impedance can be simplified as

$$Z_{\text{eff}} = Z_1 + Z_2 \approx \omega_0^2 Z_0^3 \left(C_{\text{in}}^2 + C_{\text{out}}^2\right) + j\pi Z_0 \frac{\omega - \omega_0}{\omega_0}, \tag{3.12}$$

which corresponds to the following three circuit elements in a Thevenin's equivalent circuit

$$R_{\text{s}} = \omega_0^2 Z_0^3 \left(C_{\text{in}}^2 + C_{\text{out}}^2\right),\ L_{\text{s}} = \frac{\pi Z_0}{2\omega_0},\ C_{\text{s}} = \frac{2}{\pi Z_0 \omega_0}. \tag{3.13}$$

Norton's equivalent parallel circuit

The procedure for deriving a Norton's equivalent circuit, as shown in Fig. 3.1C is exactly the same as that for a Thevenin's equivalent circuit. Here, the equivalent source current, I_{eff}, and the equivalent impedance, Z_{eff}, are determined by Eqs. (3.10) and (3.12), respectively. We will not repeat the derivations here.

3.1.2 Josephson junction in an equivalent circuit

Having described the external circuitry of the junction with the equivalent circuits, we now consider the dynamics of the junction in a lumped-element circuit configuration. As has been introduced in Chapter 1, one can split the linear and nonlinear parts of an ideal junction as a series combination of the Josephson inductance, L_J, and a spine-line spider, or a parallel combination of L_J and a cut-line spider [7]. In circuit language, these two expressions correspond to the two equations $\phi \approx L_J I + \left[L_J^3/\left(6\phi_0^2\right)\right] I^3$ and $I \approx (1/L_J)\,\phi - \left[1/\left(6L_J\phi_0^2\right)\right]\phi^3$, respectively. We note that the shunt capacitance, C_J, for a practical junction can be attributed to the equivalent circuit, but it is usually negligibly small compared with the total capacitance of the transmission line. Thus, it is straightforward to place the junction in the series and parallel equivalent circuits, and obtain the two EOMs that describe the dynamics of the junction

$$\frac{q}{C_{\text{s}}} + R_{\text{s}}\dot{q} + L_{\text{s}}\ddot{q} + L_J\ddot{q}\left(1 + \frac{L_J^2\dot{q}^2}{2\phi_0^2}\right) = V_{\text{eff}}\cos(\omega t)\,, \tag{3.14}$$

$$C_{\text{p}}\ddot{\phi} + \frac{\dot{\phi}}{R_{\text{p}}} + \frac{\phi}{L_{\text{p}}} + \frac{\phi}{L_J}\left(1 - \frac{\phi^2}{6\phi_0^2}\right) = I_{\text{eff}}\cos(\omega t)\,. \tag{3.15}$$

As will be discussed in detail in Chapter 8 and Appendix D, the above equations describe a so-called Duffing oscillator which is the focus of this thesis work.

3.1.3 Scattering responses of the circuit

In experiments with superconducting quantum circuits, it is straightforward to measure the scattering responses, S_{ij}, of the circuit, which compares the amplitude and phase of the output field at port i to the input field at port j. The calculation of the scattering responses can be performed by using the standard transfer matrix method without deriving the lumped-element equivalent circuit [65], if the junction can be fairly described as a linear inductor, L_J. However, the derivations of the equivalent lumped circuits are necessary if one must take the junction nonlinearity into account. Instead of approximating the junction by a linear inductor, we describe it strictly as an unconventional inductance [63]

$$L(\delta) = \frac{\delta}{2\mathcal{J}_1(\delta)}L_J, \tag{3.16}$$

where $\mathcal{J}_1$ is the Bessel function of the first kind, δ is the phase oscillation amplitude across the junction. Recalling the second Josephson equation as introduced in Chapter 1, we have $\delta = V/(j\omega\phi_0)$ in the phasor notation, while V can be calculated by using the equivalent circuits. In total, the transfer

matrix of the system is $A = A_{C_{\text{in}}} A_{\lambda/4} A_J A_{\lambda/4} A_{C_{\text{out}}}$, where

$$A_{C_{\text{in/out}}} = \begin{pmatrix} 1 & 1/\left(j\omega C_{\text{in/out}}\right) \\ 0 & 1 \end{pmatrix}, \; A_{\lambda/4} = \begin{pmatrix} \cosh\left(\gamma L\right) & Z_0 \sinh\left(\gamma L\right) \\ \sinh\left(\gamma L\right)/Z_0 & \cosh\left(\gamma L\right) \end{pmatrix}, \; A_J = \begin{pmatrix} 1 & j\omega L\left(\delta\right) \\ 0 & 1 \end{pmatrix}. \tag{3.17}$$

Here, $\gamma \equiv \alpha + j\beta$ is the propagation constant of the field in the transmission line, $\beta = \omega/v_{\text{ph}}$, and we have neglected the shunt capacitance of the junction. The scattering responses can be readily obtained from the following formulae [65]

$$S_{11} = \frac{A_{11} + A_{12}/Z_0 - A_{21}Z_0 - A_{22}}{A_{11} + A_{12}/Z_0 + A_{21}Z_0 + A_{22}}, \qquad S_{12} = \frac{2(A_{11}A_{22} - A_{12}A_{21})}{A_{11} + A_{12}/Z_0 + A_{21}Z_0 + A_{22}}, \tag{3.18}$$

$$S_{21} = \frac{2}{A_{11} + A_{12}/Z_0 + A_{21}Z_0 + A_{22}}, \qquad S_{22} = \frac{-A_{11} + A_{12}/Z_0 - A_{21}Z_0 + A_{22}}{A_{11} + A_{12}/Z_0 + A_{21}Z_0 + A_{22}}. \tag{3.19}$$

3.2 Quantum description

We have introduced in Chapter 1 that there are two major steps for quantizing a transmission line resonator: (1) Describe the system as a collection of harmonic oscillators, and (2) quantize each of them. Here, we follow this convenient recipe to derive the quantum mechanical description of a junction-embedded transmission line resonator [66–73], as shown in Fig. 3.3.

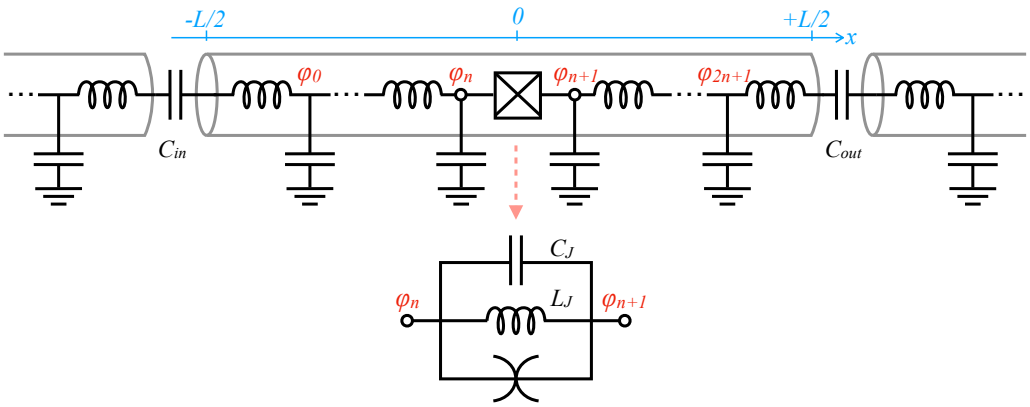

Figure 3.3. Distributed-element model of a junction-embedded transmission line resonator. The transmission line resonator has a length, L, with open boundary conditions. The Josephson junction is embedded in the middle of the resonator and can be described as a parallel circuit with shunt capacitance, C_J, Josephson inductance, L_J, and a spine-line spider.

3.2.1 Boundary conditions

We first determine the boundary conditions of the transmission line such that it can be properly defined as a microwave resonator. Assuming that the resonator is well separated from the external circuitry with the two gaps at the ends, there is no current flowing through the two gaps. This assumption gives the first two boundary conditions of the system

$$\frac{1}{l\delta x}\left(\phi_0 - \phi_1\right) + c\delta x\ddot{\phi}_0 = 0, \tag{3.20}$$

$$\frac{1}{l\delta x}\left(\phi_{2n} - \phi_{2n+1}\right) - c\delta x\ddot{\phi}_{2n+1} = 0, \tag{3.21}$$

Here, we have assumed that there are $2n+2$ nodes in the transmission line resonator. Besides, l and c are the inductance and capacitance of the transmission line per unit length, and δx is the length of a unit cell. These parameters have been introduced in Chapter 1, where we have quantized a transmission line resonator. The other two boundary conditions describe the role of the junction in the circuit. By using KCL at the nth and $(n+1)$th nodes, we obtain

$$C_J\left(\ddot{\phi}_n-\ddot{\phi}_{n+1}\right)+\frac{\phi_0}{L_J}\sin\left(\frac{\phi_n-\phi_{n+1}}{\phi_0}\right)=\frac{1}{l\delta x}\left(\phi_{n-1}-\phi_n\right)-c\delta x\ddot{\phi}_n, \tag{3.22}$$

$$C_J\left(\ddot{\phi}_n-\ddot{\phi}_{n+1}\right)+\frac{\phi_0}{L_J}\sin\left(\frac{\phi_n-\phi_{n+1}}{\phi_0}\right)=\frac{1}{l\delta x}\left(\phi_{n+1}-\phi_{n+2}\right)+c\delta x\ddot{\phi}_{n+1}. \tag{3.23}$$

In the continuous limit, $\delta x\to 0$, the four boundary conditions can be rewritten in a more compact form

$$\frac{\phi'\left(x=\pm\frac{L}{2}\right)}{l}=0,\ -\frac{\phi'\left(x=0^{\pm}\right)}{l}=C_J\ddot{\delta}+\frac{\phi_0}{L_J}\sin\left(\frac{\delta}{\phi_0}\right). \tag{3.24}$$

Here, $\delta=\phi(0^-)-\phi(0^+)$ is the flux drop across the junction, and we have neglected the size of the junction because it is much smaller than the characteristic wavelength of the resonator mode (recall the result of Chapter 1 that the resonant frequencies of a transmission line resonator of length L are $\omega_n=n\pi v_{\mathrm{ph}}/L$ for $n=1,2,\cdots$).

3.2.2 Normal (spatial) modes

The electromagnetic field inside the transmission line resonator can have multiple degrees of freedom, which correspond to the various modes of light, such as polarization, spatial, and temporal modes [36]. The usage of different modes provides different perspectives to describe the same field. For example, a given quantum state can be entangled in one basis but factorized in another. However, this flexibility also requires one to find the normal modes, or called principal modes, of the system that simplify the expression of the quantum state and makes it suitable for experimental characterization [74]. Our basic strategy towards this goal is to separate the spatial and temporal degrees of freedom. We first look for the normal spatial modes of the system which fulfills the orthonormal relation, and then relate a unique temporal mode to each normal spatial mode. With the knowledge of the normal spatial modes, the field will be determined by only the temporal degree of freedom. Most importantly, because of the orthonormality of the former, the result is nothing but a collection of harmonic oscillators as we have introduced in Chapter 1. This one-to-one combination between the spatial and temporal modes forms the so-called normal modes of the system.

Because of the discontinuity of ϕ at $x=0^{\pm}$, we split the normal modes into the left and right parts as $\phi_l(x,t)$ and $\phi_r(x,t)$, respectively. Considering also the first two boundary conditions in Eq. (3.24), we write the spatial degree of freedom by a summation of plane waves

$$\phi_l(x,t)=\sum_{m=1}^{\infty}\phi_{l,m}(t)\cos\left[k_m\left(x+\frac{L}{2}\right)\right],\ x\in\left[-\frac{L}{2},0\right); \tag{3.25}$$

$$\phi_r(x,t)=\sum_{m=1}^{\infty}\phi_{r,m}(t)\cos\left[k_m\left(x-\frac{L}{2}\right)\right],\ x\in\left(0,+\frac{L}{2}\right]. \tag{3.26}$$

Inserting Eqs. (3.25)-(3.26) into the last two boundary conditions in Eq. (3.24), we obtain

$$\frac{k_m}{l}\phi_{l,m}(t)\sin\left(k_m\frac{L}{2}\right) = -\frac{k_m}{l}\phi_{r,m}(t)\sin\left(k_m\frac{L}{2}\right), \tag{3.27}$$

$$\begin{aligned}\frac{k_m}{l}\phi_{l,m}(t)\sin\left(k_m\frac{L}{2}\right) &= C_J\left[\ddot{\phi}_{l,m}(t)-\ddot{\phi}_{r,m}(t)\right]\cos\left(k_m\frac{L}{2}\right)\\ &\quad+\frac{\phi_0}{L_J}\sin\left(\sum_m\frac{[\phi_{l,m}(t)-\phi_{r,m}(t)]\cos\left(k_m\frac{L}{2}\right)}{\phi_0}\right).\end{aligned} \tag{3.28}$$

One obvious set of solutions are $\phi_{l,m}(t)=\phi_{\mathrm{r,m}}(t)$ and $k_mL=2m\pi$, which are also the normal modes of a linear transmission line resonator with length L. However, we are mostly interested in those solutions where the junction plays a significant role. Strictly speaking, these solutions may have a rather complex form if it is derived in a mathematical rigorous way. However, our strategy is to use a Taylor expansion of the last term of Eq. (3.28) and consider only the leading terms up to the second order. In this way, we obtain a set of approximate solutions that fulfill the assumption of separability. This simplification leads to a self-consistent formula for the wave vector

$$k_m\tan\left(k_m\frac{L}{2}\right)=2\left(\frac{l}{L_J}-\frac{C_J}{c}k_m^2\right). \tag{3.29}$$

By solving k_m in the above equation and inserting the solution into Eqs. (3.25) and (3.26), we obtain the normal (spatial) modes of the system with the following orthonormal relations

$$c\int_{-L/2}^{+L/2}\cos\left[k_m\left(x\pm\frac{L}{2}\right)\right]\cos\left[k_n\left(x\pm\frac{L}{2}\right)\right]dx+4C_J\cos\left(k_m\frac{L}{2}\right)\cos\left(k_n\frac{L}{2}\right)=\delta_{mn}C_\Sigma, \tag{3.30}$$

$$\frac{k_mk_n}{l}\int_{-L/2}^{+L/2}\sin\left[k_m\left(x\pm\frac{L}{2}\right)\right]\sin\left[k_n\left(x\pm\frac{L}{2}\right)\right]dx+\frac{4}{L_J}\left(k_m\frac{L}{2}\right)\cos\left(k_n\frac{L}{2}\right)=\frac{\delta_{mn}}{L_\Sigma}. \tag{3.31}$$

where $C_\Sigma=\frac{Lc}{2}+2\cos^2\left(k_m\frac{L}{2}\right)\left(C_J+\frac{lc}{k_m^2L_J}\right)$, $L_\Sigma=\frac{lc}{k_m^2C_\Sigma}$ are generally attributed to the total capacitance and inductance of the linear part of the circuit.

3.2.3 Canonical quantization

Following the recipe of circuit quantization as introduced in Chapter 1, we write the Lagrangian of the system as

$$\mathcal{L}=\frac{1}{2}\int_{-L/2}^{+L/2}\left(l\dot{q}(x)^2+\frac{\phi'(q)^2}{c}\right)dx+\frac{C_J}{2}\dot{\delta}_J^2+E_J\cos\left(\frac{\delta}{\phi_0}\right). \tag{3.32}$$

This formula can be greatly simplified by using the orthonormal relations of the normal spatial modes, i.e., Eqs. (3.30) and (3.31). The result is

$$\mathcal{L}=\sum_{m=1}^{\infty}\overbrace{\frac{C_\Sigma}{2}\dot{\phi}_m^2-\frac{1}{2L_\Sigma}\phi_m^2}^{\text{linear part}}+\overbrace{\sum_{n=2}^{\infty}\frac{E_J}{(2n)!}\left(\frac{\sum_m 2\phi_m\cos(k_ml)}{\phi_0}\right)^{2n}}^{\text{nonlinear part}}. \tag{3.33}$$

Quantization of the linear part

Let us assume a relatively small nonlinearity in the system and consider first the linear part. The Hamiltonian of the linear part can be readily written in analogy to a linear transmission line resonator

$$H^{(\mathrm{l})} = \sum_{m=1}^{\infty} \frac{q_m^2}{2C_\Sigma} + \frac{\phi_m^2}{2L_\Sigma}. \tag{3.34}$$

Here, $q_m = C_\Sigma \dot{\phi}_m$ is the conjugate variable of ϕ_m, which obey the standard commutation relation $[\phi, q] = i\hbar$ [75]. The eigenstates of the linear Hamiltonian, i.e., the temporal degree of freedom for the normal mode, have been derived in Chapter 1. Here, it is more convenient to use the second quantization form of the Hamiltonian (as introduced in Chapter 2)

$$H^{(l)} = \sum_{m=1}^{\infty} \hbar\omega_m \left(a_m^\dagger a_m + \frac{1}{2} \right), \tag{3.35}$$

with the annihilation and creation operators

$$a_m = \sqrt{\frac{C_\Sigma \omega_m}{2\hbar}} \left(\phi_m + \frac{i}{C_\Sigma \omega_m} q_m \right), \quad a_m^\dagger = \sqrt{\frac{C_\Sigma \omega_m}{2\hbar}} \left(\phi_m - \frac{i}{C_\Sigma \omega_m} q_m \right). \tag{3.36}$$

Here, $\omega_m = k_m v_{\mathrm{ph}}$ with $v_{\mathrm{ph}} = 1/\sqrt{lc}$ being the phase velocity of the transmission line.

Nonlinear perturbations

Next, we consider the nonlinear part as a perturbation of the linear system to the second order of a_m and $a_m^\dagger$

$$H^{(\mathrm{nl})} \approx \sum_{m=1}^{\infty} -\frac{\hbar^2 E_J \cos^4(k_1 l)}{\phi_0^4 C_\Sigma^2 \omega_1^2} \left({a_m^\dagger}^2 a_m^2 + 2 a_m^\dagger a_m \right). \tag{3.37}$$

Here, we have used the following relation [68]

$$\frac{\left(a^\dagger + a\right)^{2n}}{(2n)!} = \sum_{k=0}^{n} \sum_{i=0}^{2(n-k)} \frac{a^{\dagger i} a^{2(n-k)-i}}{2^k k! i! [2(n-k)-i]!}, \tag{3.38}$$

and omitted the counter rotating terms. By combing the linear and nonlinear parts and restricting ourselves to the fundamental mode with $m = 1$, we obtain the Hamiltonian of a junction-embedded transmission line resonator [68, 69]

$$H/\hbar \approx \omega_{\mathrm{A}} a^\dagger a + U_{\mathrm{A}} a^{\dagger 2} a^2, \tag{3.39}$$

where $\omega_{\mathrm{A}} = \omega_1 + 2U_{\mathrm{A}}$ and $U_{\mathrm{A}} = -\hbar \cos^4(k_1 l) / \phi_0^2 L_J C_\Sigma^2 \omega_1^2$. This result shows that a junction-embedded transmission line resonator can be seen as a Kerr-nonlinear resonator with a negative nonlinearity. The nonlinearity originates from the deviation between the sinusoidal-like potential of the junction and the parabolic potential of a harmonic oscillator, which can be readily seen from the Lagrangian in Eq. (3.32).

3.3 Design parameters

3.3.1 Asymmetric DC-SQUID

So far, we have derived both the classical and quantum descriptions of a superconducting nonlinear resonator. However, one may also consider replacing the junction by a DC-SQUID, which provides a flux-tunable Josephson energy, and consequently, a tunable resonant frequency and nonlinearity [60]. As discussed in Chapter 1, a DC-SQUID with a small asymmetry can be equivalently regarded as a single junction with the following Josephson energy

$$E_J\left(\phi_{\mathrm{ex}}\right) = E_+\sqrt{\cos^2\left(\frac{\phi_{\mathrm{ex}}}{2\phi_0}\right) + d^2\sin^2\left(\frac{\phi_{\mathrm{ex}}}{2\phi_0}\right)}, \tag{3.40}$$

where $|d| \ll 1$. To get a figurative understanding of how the magnetic flux would influence the properties of the nonlinear resonator, we numerically calculate ω_{A} and U_{A} with the following parameters: $L = 7.4\times10^{-3}\,\mathrm{m}$, $l = 4.6\times10^{-7}\,\mathrm{H/m}$, $c = 1.8\times10^{-10}\,\mathrm{F/m}$, and $C_J = 1\times10^{-12}\,\mathrm{F}$. These parameters indicate a phase velocity $v_{\mathrm{ph}} = 1/\sqrt{lc} = 1.1\times10^{8}\,\mathrm{m/s}$, and a characteristic impedance $Z_0 = \sqrt{l/c} = 50.5\,\Omega$. We plot in Fig. 3.4A the relation between the effective critical current, $I_J\left(\phi_{\mathrm{ex}}\right)$, or equivalently the effective Josephson energy $E_J\left(\phi_{\mathrm{ex}}\right) = \phi_0 I_J\left(\phi_{\mathrm{ex}}\right)$, and the resonant frequencies of the nonlinear resonator. The inset shows the transmission response of the resonator, S_{21}, that is calculated by using the circuit theory, with $C_{\mathrm{in}} = C_{\mathrm{out}} = 5\times10^{-15}\,\mathrm{F}$, $\alpha = 2.5\times10^{-4}\,/\mathrm{m}$, and $\beta = \omega/v_{\mathrm{ph}}$.

On the one hand, the classical and quantum descriptions perfectly agree with each other. At every resonant frequency, we observe a strong peak in S_{21} with a sharp phase change. On the other hand, we observe a relatively large tuning range of the resonant frequency, saying 7.4 GHz for the fundamental mode and 14.9 GHz for higher harmonic modes. For the mth mode, the resonant frequency achieves the minimum, $\omega_m^{\mathrm{min}}/2\pi \approx (m-3/2)v_{\mathrm{ph}}/L$ (we define $\omega_m^{\mathrm{min}}/2\pi \approx 0$ for $m = 1$), at a sufficiently small Josephson energy where the plasma frequency, $\omega_J/2\pi = 1/\left(2\pi\cdot\sqrt{L_J C_J}\right)$, is close to the $(2m-3)$th resonant frequency of a linear resonator (or, 0 for $m = 1$). In comparison, it reaches a maximum, $\omega_m^{\mathrm{max}}/2\pi \approx (m-1/2)v_{\mathrm{ph}}/L$, at a sufficiently large Josephson energy where the plasma frequency, $\omega_J/2\pi$, is close to the $(2m-1)$th resonant frequency of a linear resonator. The frequency tunability takes place mainly in the range $\omega_m^{\mathrm{min}} \le \omega_J \le \omega_m^{\mathrm{max}}$. We note also that the even mode of the linear resonator is not influenced by the embedded junction, which is consistent with our theoretical expectation (see Section 3.2 for detail).

We also plot in Fig. 3.4B the relation between the effective critical current, $I_J\left(\phi_{\mathrm{ex}}\right)$, and the negative nonlinearity, $-U_{\mathrm{A}}/2\pi$. The latter can be tuned in a relatively large range from *zero* to an upper bound of 7.2 MHz that is limited by $e^2/\left(2\pi\cdot4\hbar C_J\right)$. Moreover, the effective tuning range of the nonlinearity corresponds roughly to that for the resonant frequency, such that both of them can be tuned *in-situ* with an external magnetic field [60]. These observations set up the basic principles of the sample design: We aim to fabricate a DC-SQUID with asymmetry $d = 0.13$ in the middle of a 7.4 mm-long transmission line resonator, which corresponds to a tunable critical current in the 10^{-7} A – 10^{-6} A range. Here, the length L is the electromagnetic length of the transmission line resonator, which may be different from the physical length of the resonator by a few percent.

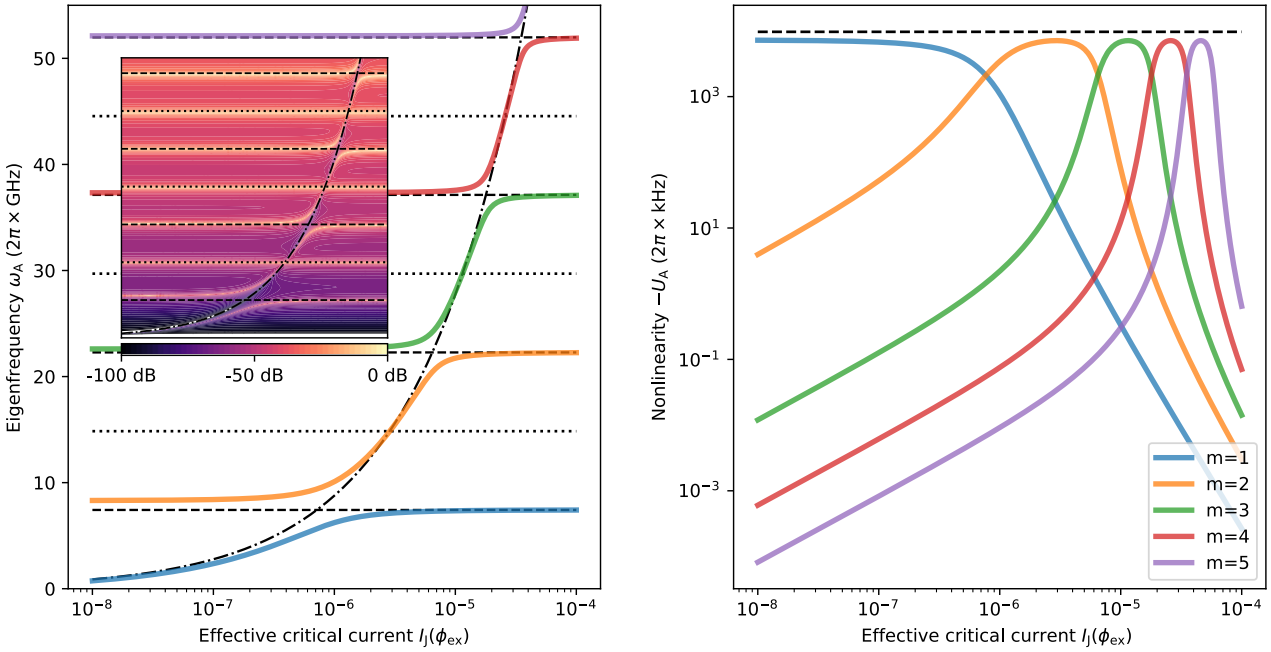

Figure 3.4. Resonant frequency ω_A and negative nonlinearity $-U_A$ of the nonlinear resonator at different critical current $I_J(\phi_{ex})$. **(A)** With the increase of $E_J(\phi_{ex})$, the value of $\omega_A/2\pi$ increases monotonically in a 7.4 GHz range for the fundamental mode, and 14.9 GHz for higher harmonic modes. Here, the dashed and dotted lines distinguish the *odd* and *even* resonant frequency, $\omega_m/2\pi$, of a linear transmission line resonator, while the dash-dotted curve indicates the plasma frequency, $\omega_J/2\pi$, of the junction. The inset shows the transmission coefficient, S_{21}, of the circuit calculated by the classical theory. **(B)** With the increase of $I_J(\phi_{ex})$, the value of $-U_A/2\pi$ varies in a 7.2 MHz range which goes across several orders of magnitude. The dashed line indicates the upper bound of the nonlinearity that is predicted in quantum theory.

3.3.2 Sample chip

In the entire thesis, we perform experiments on a sample with two tunable superconducting nonlinear resonators, as shown in Fig. 3.5. The sample has been designed and fabricated by M. Fischer on a 10 mm × 6 mm-large and 525 μm-thick silicon chip with double-angle shadow evaporation and lift-off procedures. The superconductor layer is made of Al with a thickness of 140 nm. The major part of the sample consists of two 7.2 mm-long 13.2 μm-wide transmission line resonators with two DC-SDUIDs embedded in the middle, respectively. The areas of the two SQUIDs are designed to be 10.5 μm × 24.5 μm, in which the two junctions differ in size with an estimated SQUID asymmetry of approximately 0.13. In addition, two T-shaped on-chip antennae are placed close to the two SQUIDs, respectively, to control the magnetic fluxes threading the SQUID loops. All of these described features result into two nonlinear resonators with tunable frequency and nonlinearity [60]. The two resonators are coupled by a 20 μm-long finger capacitor, which is treated perturbatively as a photon-conserving type interaction, $\left(a^\dagger b + a b^\dagger\right)$. They couple to the outside fields, respectively, by two 40 μm-long finger capacitors at the two ends, and also to the microwave fields in the flux lines through the two antennae.

3.4 Cryogenic setup

As we have discussed in Chapter 1, experiments with superconducting quantum circuits require a careful design of the cryogenic setup. On the one hand, the microwave signals should be routed in a

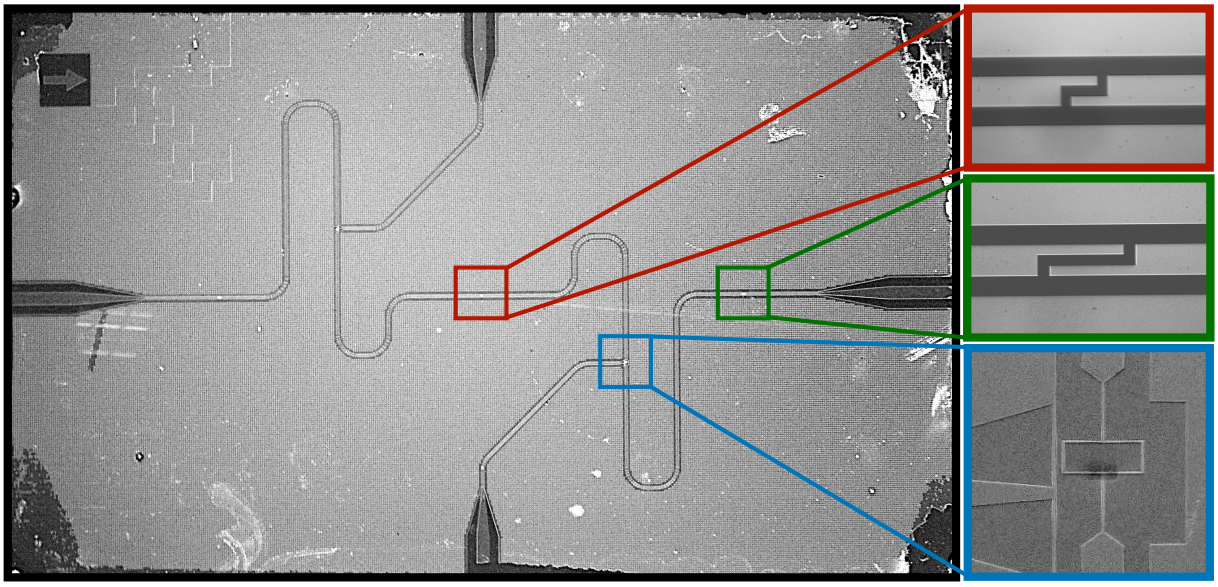

Figure 3.5. Optical photograph of the sample chip. The sample consists of two DC-SQUID-embedded stripline resonators, which are coupled with each other by a 20 μm-long finger capacitor shown in the red box. The two external fields couple to the two resonators, respectively, by two 40 μm-long finger capacitors, as shown in the green box. The resonant frequency and the nonlinearity of the resonators are controlled by two T-shape antennae, as shown in the blue box. The photograph is taken by M. Fischer.

proper way such that one can control and measure the quantum phenomenon that happens inside the sample box. On the other hand, the sample should also be well separated from the external circuitry in order to minimize the various noises that can easily wash out the quantum statistical properties of radiation. Moreover, it is also technically important to reach a balance between the heat loads and the cooling power of the cryostat.

3.4.1 The dilution refrigerator

Our experiments are performed in a homemade wet-type dilution refrigerator, as shown in Fig. 3.6. The refrigerator contains a 93.3 L helium reservoir and a 85.6 L nitrogen reservoir, which provide a 4 K environment for the inner vacuum chamber (IVC). The 1K pot is located inside the IVC, where the liquid helium is fed by the helium reservoir and evaporated with an oil-sealed pump. The relatively warm ^{3}He/^{4}He mixture from the cold trap is pre-cooled by the nitrogen and helium reservoirs before entering the IVC. It is further cooled by the 1K pot, still, continuous and step heat exchangers, before entering the mixing chamber (MXC). Here, two phases of the mixture, i.e., the concentrated phase with pure ^{3}He and the dilute phase with 6.6% ^{3}He and 93.4% ^{4}He, coexist and are separated by a physical boundary because of the different densities. A tube in the bottom of MXC connects the dilute-phase mixture with the still, which cools down the incoming concentrated mixture by the heat exchangers. The still is stabilized at a temperature of around 600 mK and is strongly pumped by the combination of a turbomolecular pump (TMP) and a dry vacuum pump (PRE). Here, the ^{3}He evaporates much faster than the ^{4}He in the dilution phase and dilutes the mixture. Consequently, more ^{3}He in the concentrated phase in the MXC has to be resolved in the diluted phase in order to keep the balance between the two phases. In other words, a transition from the concentrated phase to the dilute phase happens in MXC during this process, which continuously absorbs heat from the local environment and cools down the sample plate to approximately 30 mK. The evaporated mixture

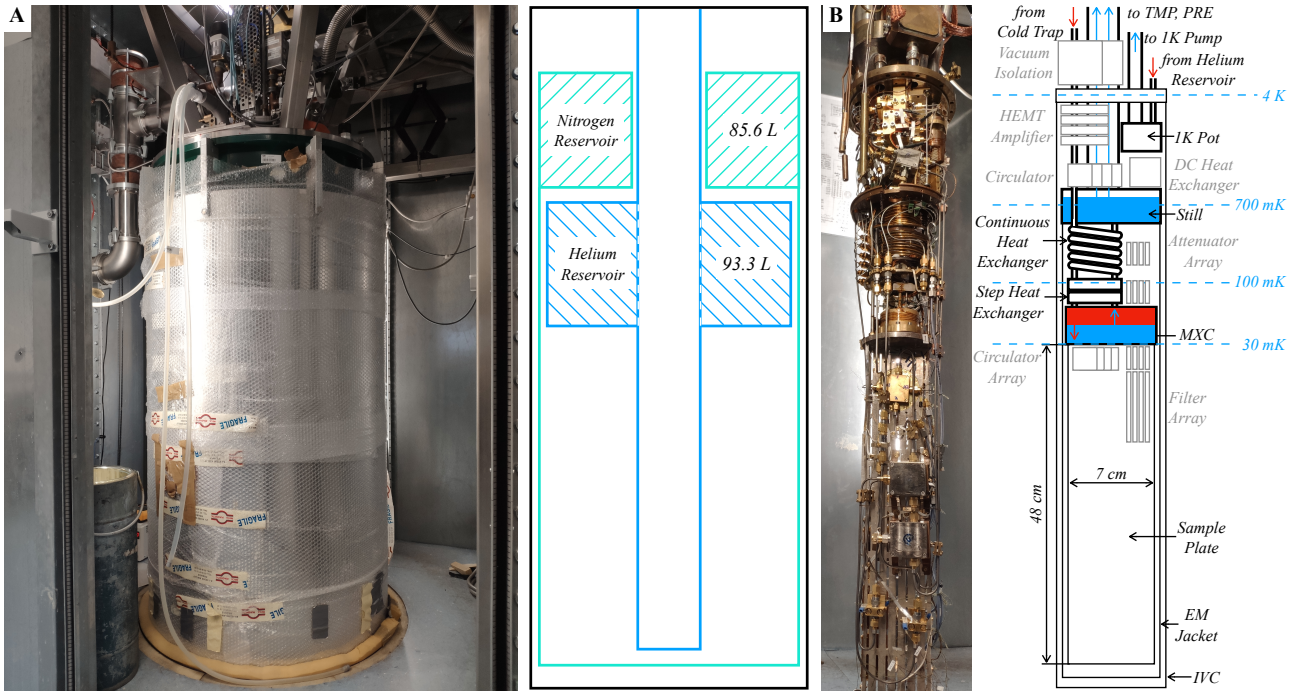

Figure 3.6. Photographs and schematic figures of the homemade dilution refrigerator. **(A)** The stainless steel liquid helium cryostat purchased from *Cryogenic Ltd.*, which contains a 93.3 L helium reservoir (blue) accompanied with a 85.6 L nitrogen reservoir (cyan) for reducing the rate of helium boil-off. **(B)** The central part of the refrigerator, where the process of dilution refrigeration happens. A number of microwave devices are mounted in different temperature stages of refrigerator, which route the microwave signals and balance the cooling power and the heating load in the meanwhile.

is purified by liquid nitrogen in the cold trap and recycled as mentioned before.

3.4.2 Optimization of heat load

To ensure that the refrigerator works in a stable condition during experiments, one needs to engineer the heat loads inside the cryostat. Generally speaking, there are mainly three sources of the heat loads one should consider, i.e., the passive, active, and blackbody radiative loads [76]. Whilst the last one is determined by the design of the refrigerator, one can optimize the first two by choosing the right cable materials and distributing attenuators and circulators wisely among the different temperature stages.

The passive load originates from the heat conducted through the microwave cables from the higher to the lower temperature stages [76]. In this regard, we use cables with low thermal conductivity to minimize the passive heat load. However, the virtue of low thermal conductivity usually comes at a price of a low electrical conductivity, which is undesired in our experiments. Moreover, one should also consider the temperature dependance of the thermal and electrical conductivities, and the prices of the materials. Table 3.1 summarizes the properties of several commercial cables materials. In our experiments, we use stainless still (SS) cables for all the input lines, from the room temperature to the 30 mK stage, because of their low thermal conductivity. On the output side, the niobium-titanium (NbTi) cables are used below 4 K before the high-electron-mobility transistor (HEMT) amplifier, in order to maximize the electrical conductivity while maintaining a low thermal conductivity. Above 4 K, we use cupronickel (CuNi) cables for their low thermal conductivity and the relatively low price.

The active load arises due to the dissipation of the microwave signals that are propagating in the

coaxial cable	thermal conductivity	electrical conductivity	typical usage
SS	low	low	RF input
CuNi	low	low	RF output above 4 K
NbTi	low	high (below 10 K)	RF output below 4 K

twisted wire	thermal conductivity	electrical conductivity	typical usage
Cu	high	high	DC line above 4 K
PhBr	low	high	
NbTi	low	high (below 10 K)	DC line below 4 K

Table 3.1. Properties of several commercial cable materials and their usage in our setup. Here, the abbreviations correspond to stainless still (SS), cupronickel (CuNi), niobium-titanium (NbTi), Copper (Cu), phosphor-bronze (PhBr). The data is extracted from Ref. [76].

cable [76]. It has been demonstrated that one can engineer the thermal photon number at the sample stage to a value of 10^{-3} by mounting three 20 dB attenuators at the 3 K, 100 mK, and 10 mK stages, respectively, in the context that the MXC temperature is around 10 mK. However, the described homemade dilution refrigerator can hardly achieve a MXC temperature of around 30 mK. Moreover, we would also like to make the total attenuation relatively large to reach a low driving strength in several measurement, where the nonlinearity of the resonator can be fairly neglected (see Chapter 5 for a more detailed discussion). In these regards and for other practical considerations, such as the very limited space of the cryostat, we distribute a total amount of 70 dB attenuation among the 4 K, 1 K, 700 mK, 100 mK, and 30 mK temperature stages, as shown in Fig. 3.7. By modeling the attenuators as beam splitters, one can verify that the thermal photon number is kept below 10^{-3}.

3.4.3 Wiring up the system

The schematic of the cryogenic setup that is placed inside, or integrated on top of the dilution refrigerator is shown in Fig. 3.7. From the top to the bottom, the temperature decreases from approximately 290 K, which is stabilized by using the Peltier cooler (Laird Hi-Pot tested 750VOC) and the temperature stabilizer (Telemeter TR12-PI-2Q2), to a minimum value of 30 mK at the sample stage. The input and output microwave lines, labelled as MW 1/2, FLX 1/2, and OUT 1/2, are coupled to the two nonlinear resonators through on-chip finger capacitors and the T-shaped antennae, as shown in Fig. 3.5. Here, the fields in MW 1/2 and OUT 1/2, are separated by using the cryogenic circulators (QuinStar QCY-060400CM00). We add also a 5.5-10 GHz high-pass filter in each of the input paths to isolate the sample from higher-frequency harmonics of the driving fields. In each of the the output paths, we add two circulators (QuinStar CTH1184-KS18, Pamtech CTH1368-K18-A) at 30 mK and 700 mK, respectively, to isolate the sample from the high-temperature thermal radiations and the possible back propagating fields coming from the HEMT amplifiers (LNC4_8A). At the top of the cryostat, we place a 5.5-10 GHz high-pass filter and amplify the coming signal by a low-noise room-temperature amplifier (MITEQ JS2-0200080-08-0A) in each of the output line. These amplifiers are tightly integrated with the Peltier cooler, such that they operate at a stable temperature of around 17 °C. We place all of the described microwave components in an electromagnetically shielded room, while the temperature of the entire laboratory is stabilized at 27 °C by using the air conditioner.

For the DC part, we combine the output of the DC current sources (ADCMT 6241A) with the microwaves in FLX 1/2 by using the bias-tee (UMCC BT-S00-HS), which are further connected to the T-shaped antennae on chip. In addition, two pairs of homemade cryogenic thermometers and heaters

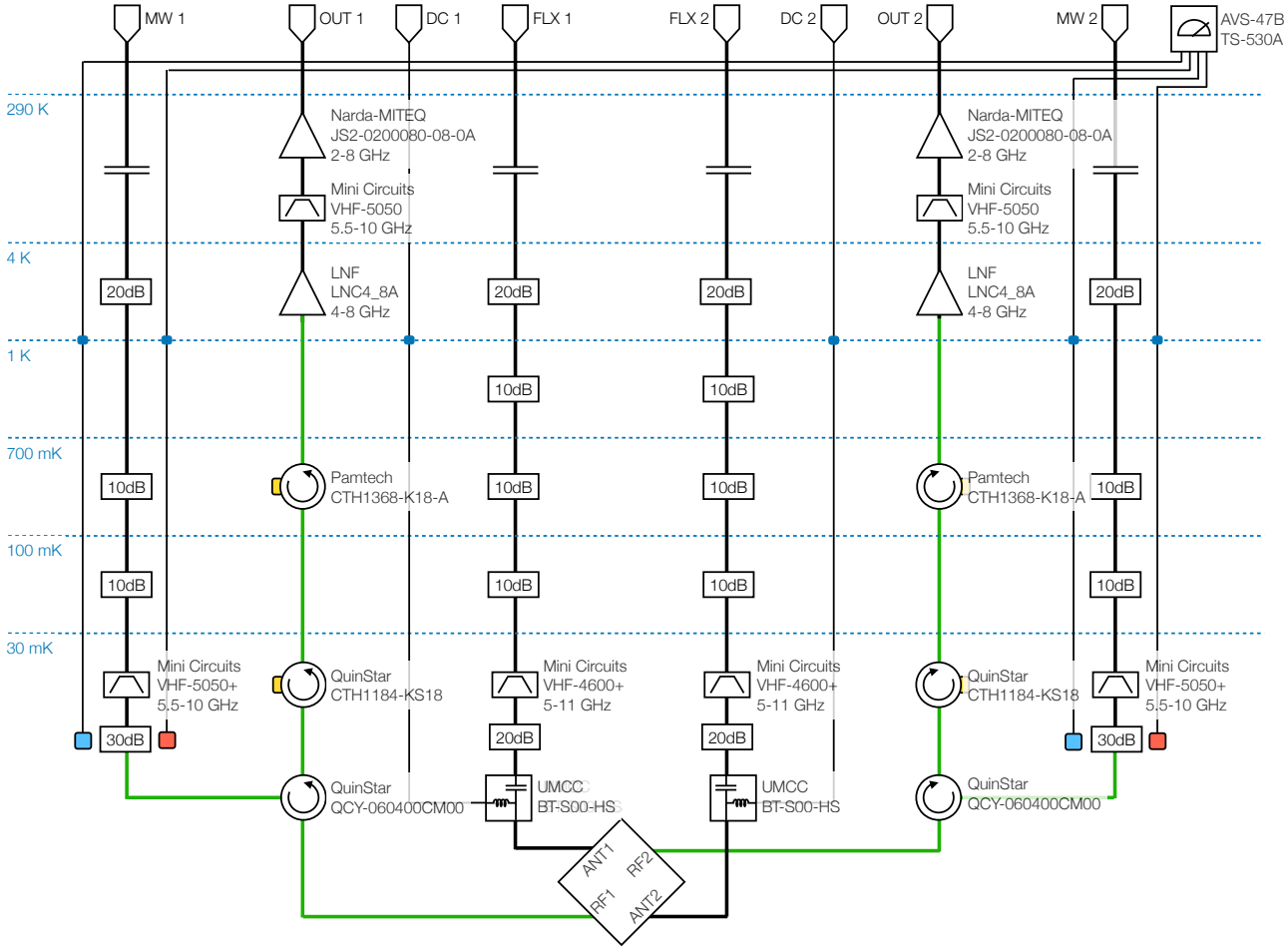

Figure 3.7. Schematic of the cryogenic setup. The sample is placed at the mixing chamber stage of a homemade wet dilution refrigerator, to which four microwave coaxial cables and two pairs of DC wires are connected. We also anchor two pairs of homemade cryogenic thermometers (blue box) and heaters (red box) to the two 30 dB attenuators at 30 mK to realize active and independent control of the local temperatures. Here, the blue dashed lines indicate the temperature stages of the cryostat, the blue dots indicate a thermal interface between the DC wires at two temperatures. The green lines indicate NbTi cables.

are clamped tightly to the two 30 dB attenuators located at 30 mK. They are connected to a AC resistance bridge (Picowatt AVS-47B) and the corresponding PID temperature controller (Picowatt TS-530A), in order to control the local temperatures of the two attenuators (see Appendix C for an introduction of the PID controller). This configuration is used to characterize the amplification gain and the noise temperature of the output paths, as will be introduced in Chapter 6.

Chapter 4

CLOSED-SYSTEM PARAMETERS: AUTOMATED SAMPLE CHARACTERIZATION AND TUNING

The tunability of our sample provides an access to different parameter regimes where fundamentally different properties of the nonlinear resonator exist. However, it also leads to a practical challenge to characterize the control parameters. In this chapter, we describe a computer-automated characterization and tuning procedure to alleviate the human workload. More importantly, this automation not only provides the possibility to find the optimal estimation of the sample parameter, not matter the local or global optimum, in the huge parameter space, but also avoids possible biases in manual characterizations and keeps a relatively objective criteria among different experiments [77].

4.1 Automated sample characterization

4.1.1 Spectroscopy experiment

Generally speaking, the automated characterization procedure can be split into two steps: (1) Spectroscopy experiment and (2) least-square estimation (LSE). In the first step, we slowly sweep the magnetic fields threading into the two SQUID loops, ϕ_1 and ϕ_2, and measure the scattering coefficients of the system. This is achieved by slowly sweeping the DC current, I_1 and I_2, that are applied to the two antennae on chip (see Chapter 3 for detail). Considering also the crosstalk between the two antennae, we assume a linear relation between the flux and the applied currents [78–81]

$$\begin{pmatrix}\phi_1\\ \phi_2\end{pmatrix} = \begin{pmatrix}A_{11} & A_{12}\\ A_{21} & A_{22}\end{pmatrix}\begin{pmatrix}I_1\\ I_2\end{pmatrix} + \begin{pmatrix}\phi_{1,\mathrm{off}}\\ \phi_{2,\mathrm{off}}\end{pmatrix}, \tag{4.1}$$

where A is the crosstalk matrix, $\phi_{1,\mathrm{off}}$ and $\phi_{2,\mathrm{off}}$ are the offset flux threading into the two SQUID loops.

Fig. 4.1 shows a typical result of the spectroscopy experiment, where the resonant frequency of the two resonators are plotted as a function of the applied currents. We label the input and out fields of the first resonator as 1 and 2, while those of the second resonator are labelled as 3 and 4, respectively. Thus, for example, S_{21} denotes the reflection response of the first resonator. Here, we sweep respectively the two antenna currents from $-600\,\mathrm{mA}$ to $600\,\mathrm{mA}$ with 80 intermediate steps, and measure the scattering responses of the system by using a VNA (vector network analyzer, Keysight PNA-N5222A). The sweeping speed is set as $1\,\mathrm{mA/s}$. The intermediate frequency (IF) bandwidth of the VNA is set as $1\,\mathrm{kHz}$, and we average each data point over 100 times with an *point-average* mode. In principle, the output power of VNA should be set as low as possible in order to minimize the contribution of the resonator nonlinearity to the scattering responses [63]. However, considering the practical compromise between the signal-to-noise ratio (SNR) and the measurement time, we set the out power as $0\,\mathrm{dBm}$ with an additional $30\,\mathrm{dB}$ attenuation at room temperature. The cables inside the cryostat contribute to an $\sim 130\,\mathrm{dB}$ attenuation, which will be characterized in Chapter 6. This configuration corresponds to an approximately $10\,\mathrm{h}$ measurement time for each characterization.

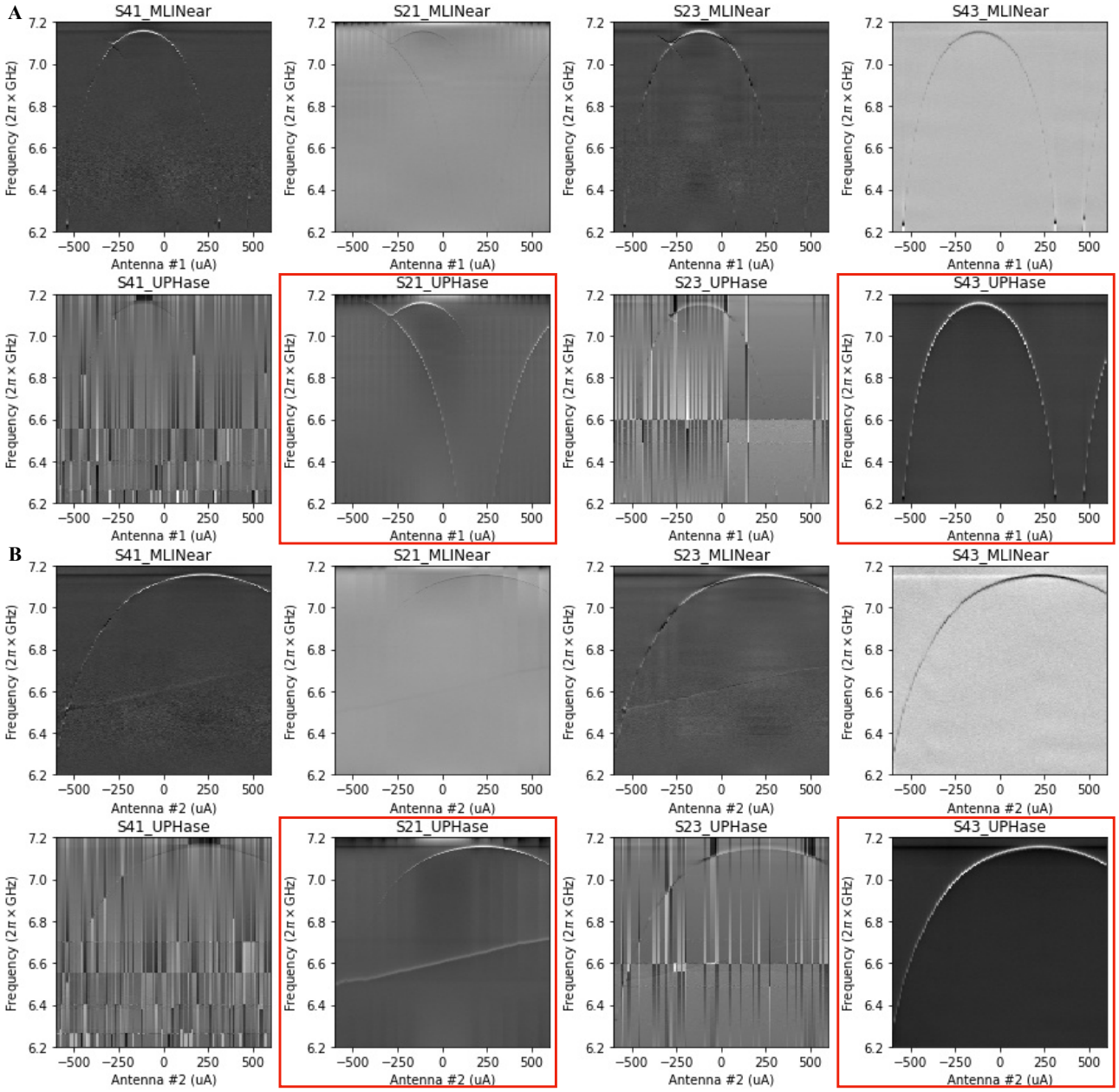

Figure 4.1. Results of a typical flux-sweep experiment. (A) The amplitude and unwrapped phase of the four scattering responses in a two-resonator system. The current applied to the first antenna is swept from −600 mA to +600 mA with 80 intermediate steps, while the second antenna current is kept at *zero*. **(B)** The same experiment but with the second antenna current varying from −600 mA to +600 mA and the first antenna current being *zero*. The four red boxes indicate the phase of the reflection responses, which show the best SNR over all the measurement results and thus will be used for sample characterization. In all the experiments, we set the output power of VNA as 0 dBm, the IF bandwidth 1 kHz, and the average number 100.

4.1.2 Least square estimation

After getting the measurement results, we use the optimization method to find the LSE of the 9 closed-system parameters of the sample, as introduced in Chapter 3, as well as the 6 parameters defined in Eq. (4.1) for controlling the external flux. The basic procedure of the estimation can be further split into two steps: (1) Generate a map that relates each pixel of the measured scattering response to a certain score, and (2) adjust the unknown parameters to achieve a score as high as possible. Generally speaking, the resonant frequencies can be easily identified by searching for the dips (peaks) in the spectroscopy results. However, it is difficult to keep tract of the dips (peaks) individually throughout the flux-tuning process, because of the crosstalk between the two antennae, the relatively poor SNR, and the uneven background signal. As can be already seen in Fig. 4.1, it is very often that one sees only one or even *zero* resonant dip (peak) in certain parameter regimes. It requires a sophisticated design of the algorithm to circumvent these practical issues and distinguish the individual peaks (dips). Alternatively, our algorithm treats the characterization task as an image recognition problem [82–87]. The basic idea is to treat the spectroscopy results as pure images and estimate the parameters by comparing them with the simulated images.

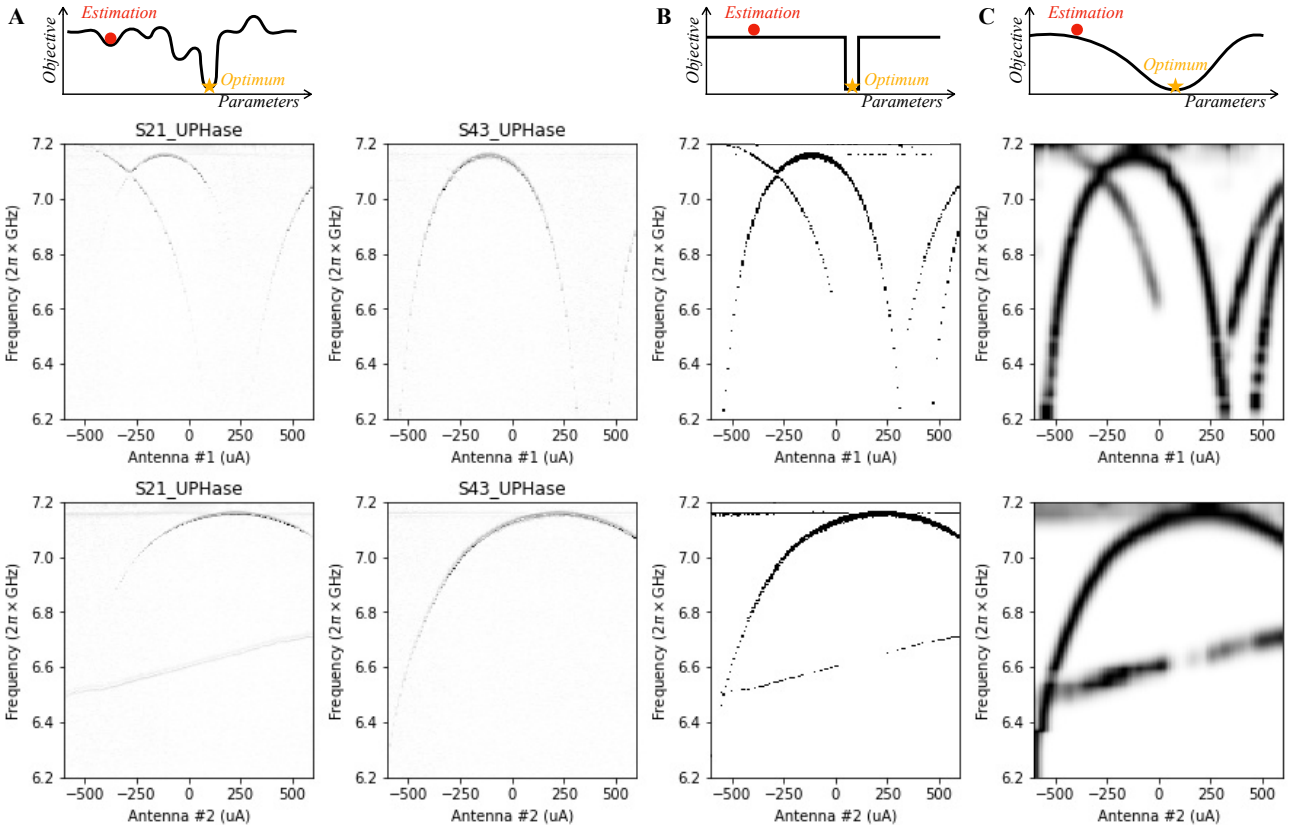

Figure 4.2. Generation of the score table for automated sample characterization. (A) The gradient of the measured scattering response over the y-axis, i.e., the probe frequency. The four panels correspond to the four red boxes shown in Fig. 4.1. **(B)** The binary truth table which indicates the resonant frequencies at different antenna currents and probe frequency. We select the pixels of which the z value is larger than 8 times of the average value at each specific antenna current, and assign their z values as 1 while 0 otherwise. Moreover, we combine the images with the same x-axis, i.e., I_1 or I_2, respectively. **(C)** We transform the binary-valued truth table into a continuous-valued score table by applying a 2D Gaussian filter to (B) with standard deviations 2 and 25 pixels in the x and y directions, respectively. The exact resonant frequency corresponds to the bottom of the Gaussian valley.

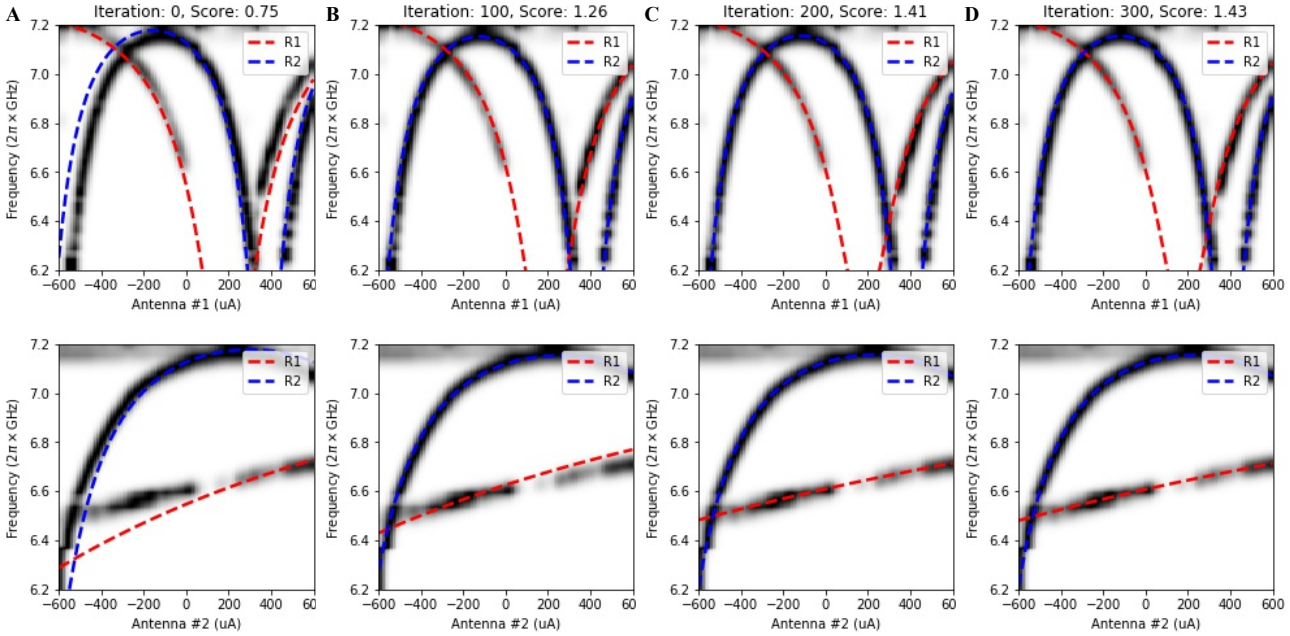

Figure 4.3. The optimization procedure for characterizing the closed-system parameters. **(A)-(D)** The snap shots of the result for several intermediate steps. The dashed curves are the simulated resonant frequencies with estimated parameters, and the gray map is identical to the score table shown in Fig. 4.2C. With the increase of the iteration number, the fitting score increases moronically and saturates at 1.43 after 300 iterations. In principle, it can reach a maximum value of 2 for perfect parameter estimation in perfect experimental conditions.

Ideally, the best estimation of the parameters can be achieved when the simulation results are identical to the measurement results. However, because of the unavoidable experimental imperfections one must restrict the comparison to the key information of them, i.e., the position of the resonant frequencies. We have learned from Fig. 4.1 that the phase of the reflection coefficients contains relatively smaller noises, such that we extract the resonant frequencies from those four corresponding images. We first calculate the absolute gradient of the images with respect to the y-axis, i.e., the probe frequency, as shown in Fig. 4.2A. Then, we combine the images with the same x-axis, i.e., I_1 or I_2. Recalling the fact that the phase undergoes a sharp transition with respect to frequency at the resonant frequency, one may identify the resonant frequencies by simply looking for the large values in the gradient image. Here, we normalize the z values of the gradient image for each x, and label a resonance if the z value is larger than 8 times of the average value. Correspondingly, we obtain a truth table where the z value is 1 for positions we identify as a resonance and 0 elsewhere, as shown in Fig. 4.2B. In principle, the binary table contains all the information we need to characterize the system parameters. With an initial estimation of the parameters, one generate two curves of the resonant frequency which we also see as a 2-dimensional truth table. The estimation result can be quantitively evaluated by multiplying the two truth tables pixel by pixel, and we obtain a reward 1 at each pixel if both of the truth tables are 1. The optimal estimation is thus obtained by optimizing the scores, which corresponds to the best match between the measured and simulated results. The maximum score can be achieved if the range of the probe frequency covers the entire tuning range of the two resonators and the corresponding two resonant peaks are successfully identified for each value of the antenna current.

However, one technical problem in the optimization procedure is that the objective function contains a large number of plateaus, which provide no gradient information of the objective function

CPW resonator	
length L	$7.395 \times 10^{-3}\,\mathrm{m}$
inductance per meter l	$4.598 \times 10^{-7}\,\mathrm{H}$
capacitance per meter c	$1.697 \times 10^{-10}\,\mathrm{F}$
SQUID #1, #2	
critical current I_{J_1}, I_{J_2}	$1.566 \times 10^{-6}\,\mathrm{A}$, $1.416 \times 10^{-6}\,\mathrm{A}$
shunting capacitance C_{J_1}, C_{J_2}	$9.394 \times 10^{-16}\,\mathrm{F}$, $1.168 \times 10^{-15}\,\mathrm{F}$
asymmetry d_{J_1}, d_{J_2}	2.136×10^{-1}, 1.937×10^{-1}
Antenna #1, #2	
flux offset $\phi_{1,\mathrm{off}}$, $\phi_{2,\mathrm{off}}$	$-3.902 \times 10^{-1}\,\phi_0$, $-1.149 \times 10^{-1}\,\phi_0$
flux change per current $d\phi_1/dI_1$, $d\phi_2/dI_1$	$6.088 \times 10^{-4}\,\phi_0/\mathrm{A}$, $9.927 \times 10^{-4}\,\phi_0/\mathrm{A}$
flux change per current $d\phi_1/dI_2$, $d\phi_2/dI_2$	$-3.715 \times 10^{-5}\,\phi_0/\mathrm{A}$, $-5.054 \times 10^{-4}\,\phi_0/\mathrm{A}$

Table 4.1. Characterized closed-system parameters of the two resonators.

and make the numerical algorithm difficult to achieve a reasonably high score in an acceptable amount of time. To overcome this issue, we transform the binary-valued truth table into a continuous-valued score table while maintaining the optimal solution of the objective function unchanged. In specific, we use a Gaussian filter, with standard deviations 2 and 25 pixels in the x- and y-axis of the Gaussian kernel, respectively, to blur the truth table. The result is shown in Fig. 4.2C. With this score table, the highest score is achieved when the simulated curves of the resonant frequency lie in the bottom of the Gaussian-shaped valleys. They correspond to the same positions in the binary truth table where $z = 1$. However, the valleys eliminate plateaus in the original objective function and provide the gradient information to speed up the optimization process.

4.2 Characterization results of closed-system parameters

Figure 4.3 shows several intermediate steps during the optimization process, where the score converges monotonically to the best estimation. Here, we normalized the maximum score as 2, since there are 2 resonators to be characterized. We observe that the optimization algorithm has achieved a total score of 1.43 after approximately 300 steps of iterations. This deviation from the maximum value is mainly caused by the finite range of the probe frequency and the relatively poor SNR, as analyzed in Section 4.1, but not the algorithm itself. In fact, one can hardly achieve a better characterization result by using human force. The estimated sample parameters are summarized in Table 4.1, which is consistent with the design parameters as introduced in Chapter 3. The simulation results with the characterized sample parameters shows a good consistency with the experimental results, as shown in Fig. 4.3D. The estimated parameters are float numbers in Python with 8 bits exponent and 23 bits mantissa [88], which correspond to a numerical precision that cannot be reached by human force. Considering also the greatly reduced human effort and the linear scaling of the algorithm complexity with the system size, we conclude that the described computer-automated characterization technique shows a significantly advantage over the manual characterization procedures.

We note that the 0 dBm output power of VNA may still induce noticeable nonlinear effects in the system. In certain regimes, we observe a difference of the resonant frequency of around 5 MHz when using a lower driving strength (approximately, -30 dBm). However, we can hardly keep the out power of VNA that small for system characterization because of the poor SNR. To make a reasonable compromise, we use the 0 dBm spectroscopy results to find an estimation of the closed-

system parameters, but use an −30 dBm input power to identify the exact resonant frequencies at several working points. We note also that the current version of the automated characterization algorithm still relies on an initial guess of the system parameters that is reasonably close to the optimal solution, as shown in Fig. 4.3A. An arbitrary initial guess may lead to a very long optimization time, or, very often, an obviously incorrect estimation of the system parameters. An improved algorithm with no human intervention at all will be the task of next version.

4.3 Automated sample tuning

With the characterized sample parameters as shown in Table 4.1, especially the characterization of the crosstalk between the two antennae, one can tune the frequency, or nonlinearity, of the two resonators independently to an arbitrary value in the parameter regime in an automated fashion. Fig. 4.4 shows the result of a typical automated tuning experiment, where we tune the two resonators on-resonance in the range of 6.3 GHz – 7.1 GHz. We observe that the resonant dips in the two measured reflection responses, S_{21} and S_{43}, are symmetric to the desired resonant frequency. This is because of the avoid crossing in the energy diagram of the two resonators, and is thus an important indication of the resonance between the two resonators. The frequency difference between the two dips corresponds to two times of the resonator-resonator coupling strength, which is approximately 5 MHz for frequencies higher than 6.8 GHz but increases monotonically with the decrease of the resonant frequency. At the resonant frequency, 6.4 GHz, the coupling strength seems to reach 100 MHz.

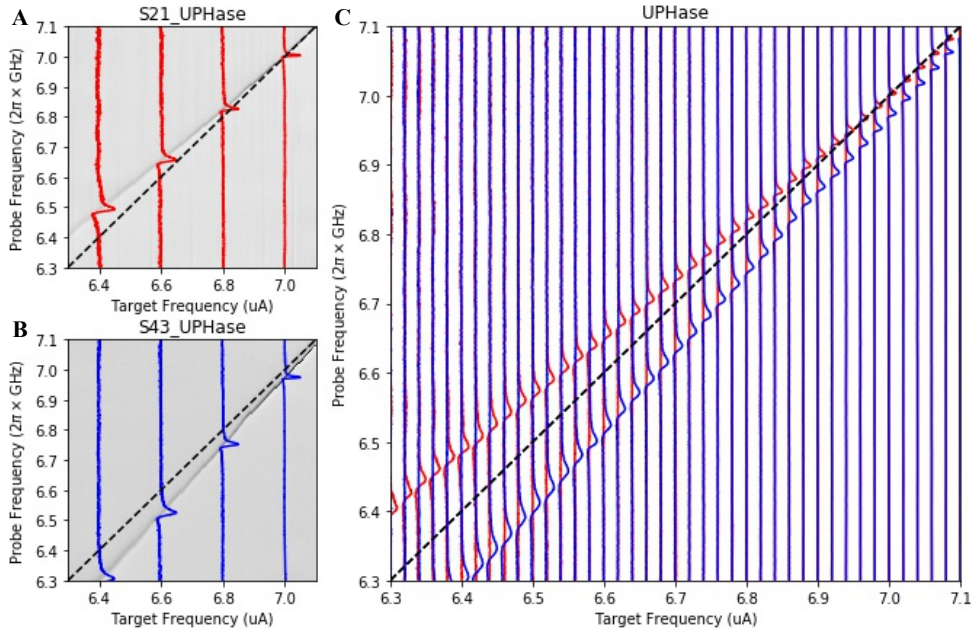

Figure 4.4. Results of automated sample tuning. (A)-(B) Phase of the measured reflection responses, S_{21} and S_{43}, respectively, where the sharp change indicates the resonant frequencies of the resonators. **(C)** A combination of (A) and (B), where the resonant frequencies of the two resonators are approximately symmetric to the anti-diagonal line. In all the panels, the dashed lines indicate the desired resonant frequency.

We note that this frequency-dependent change of the coupling strength is not expected from our perturbative model, as introduced in Chapter 3. However, we suspect that the two resonators may not be resonant below 6.8 GHz, due to the possible imperfection of the characterization results. An improved automated-tuning procedure with a feedback loop may provide an affirmative answer to this

suspect. Here, the basic idea is to add a small perturbation to the calculated antenna currents, and use the measured new resonant frequencies as a feedback to check the resonance condition. Unfortunately, we did not continue in this direction during the thesis, nor verify the resonance condition by a local spectroscopy experiment. A more precise tuning of the resonant frequency and the nonlinearity with feedback techniques should be studied elsewhere in the future.

Chapter 5

OPEN-SYSTEM PARAMETERS: SCATTERING COEFFICIENTS OF MICROWAVE RESONATORS

Besides the the closed-system parameters, such as the resonant frequency and nonlinearity, it is equally important to characterize the open-system parameters, such as the energy decay and the dephasing rates. These parameters are closely related to the concept of the quality factor, Q, of the system. Generally speaking, the Q factor can be phenomenally defined as the ratio between the resonant frequency and the full width at half maximum (FWHM) of the resonance spectrum. The higher the Q factor is the longer the quantum information can be maintained in the system. As we will see later in Chapter 6, the characterization of several other system parameters, such as the driving strength, relies also on the knowledge of the Q factor. In this chapter, we provide a systematic study on the scattering coefficients of superconducting microwave resonators and develop a computer-automatic characterization procedure for Q factor measurements [89, 90].

5.1 Circuit perspective: The transfer matrix approach

5.1.1 Classification of microwave resonators

There are two fundamental types of lumped-element circuits that can used to model a *zero*-dimensional microwave resonator, as shown in Fig. 5.1A. The first one is called the series RLC resonator, which has an input impedance of

$$Z_{\mathrm{s}} = R + j\omega L + \frac{1}{j\omega C}. \tag{5.1}$$

Here, R, L, and C are the resistance, inductance, and capacitance of the circuit, j is the imaginary unit that follows the convention of electrical engineering, $j = -\sqrt{-1}$ [75]. The resonance occurs at $\mathrm{Im}\,(Z_{\mathrm{s}}) = 0$, which corresponds to a resonant frequency $\omega_0 = 1/\sqrt{LC}$ and a (internal) Q factor $Q_{\mathrm{i}} = \omega_0 L/R = 1/\left(\omega_0 RC\right)$ [65]. The second one is called the parallel RLC resonator with the following input impedance

$$Z_{\mathrm{p}} = \left(\frac{1}{R} + \frac{1}{j\omega L} + j\omega C\right)^{-1}. \tag{5.2}$$

Similarly, one can calculate the resonance frequency and the (internal) Q factor as $\omega_0 = 1/\sqrt{LC}$ and $Q_{\mathrm{i}} = R/\left(\omega_0 L\right) = \omega_0 RC$, respectively [65].

Besides, a finite piece of transmission line with proper boundary conditions can also be described as a 1D microwave resonator, as shown in Fig. 5.1B. Depending on the load impedance, Z_{L}, and the length, l, the input impedance of the transmission line resonator, when looking towards one end, can be written as [65]

$$Z(l) = Z_0 \frac{Z_{\mathrm{L}} + Z_0 \tanh \gamma l}{Z_0 + Z_{\mathrm{L}} \tanh \gamma l}. \tag{5.3}$$

Here, $\gamma = \alpha + j\beta$ is the complex propagation constant of the microwave field which we have introduced in Chapter 3, and Z_0 is the characteristic impedance of the transmission line. By assuming a small damping rate of the transmission line, i.e., $\alpha l \ll 1$, and restricting our discussion to a small frequency

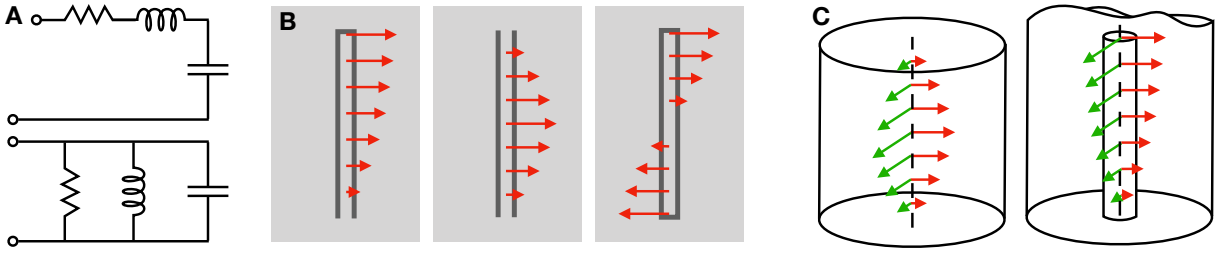

Figure 5.1. Schematics of several different microwave resonators from *zero*- to 3D. (A) The series (top) and parallel (bottom) RLC circuits are the two fundamental types of lumped-element resonators. **(B)** A finite length of transmission line with short-circuited $\lambda/4$ (left), short-circuited $\lambda/2$ (middle), and open-circuited $\lambda/2$ (right) boundary conditions form the three fundamental types of distributed-element resonators. **(C)** Two typical types of 3D resonators, which can be modeled by a short-circuited $\lambda/2$ (left) or a short-circuited $\lambda/4$ (right) transmission line resonator, respectively. In all the panels, red and green vectors depict the special modes of the resonator that are determined by the boundary conditions.

range around the resonant frequency, i.e., $|\Delta| \ll \omega_0$ with $\Delta = \omega - \omega_0$, we obtain three types of microwave resonators for three different boundary conditions. They are (i) the short-circuited $\lambda/4$ resonator with

$$Z_{\lambda/4} = \frac{Z_0}{\alpha l + j\pi\Delta/2\omega_0} \text{ and } \omega_0 = \frac{\pi v_{\text{ph}}}{2l}, \tag{5.4}$$

(ii) the short-circuited $\lambda/2$ resonator with

$$Z_{\lambda/2}^{(\text{short})} = Z_0 \left(\alpha l + j\pi\Delta/\omega_0\right) \text{ and } \omega_0 = \frac{\pi v_{\text{ph}}}{l}, \tag{5.5}$$

and (iii) the open-circuited $\lambda/2$ resonator with

$$Z_{\lambda/2}^{(\text{open})} = \frac{Z_0}{\alpha l + j\pi\Delta/\omega_0} \text{ and } \omega_0 = \frac{\pi v_{\text{ph}}}{l}. \tag{5.6}$$

Here, $v_{\text{ph}} = \omega/\beta$ is the phase velocity of the propagating microwave field in the transmission line. We note that we have discussed the open-circuited $\lambda/2$ resonator, (iii), in Chapter 1.

Comparing these results with the two lumped-element resonators, we observe that the short-circuited $\lambda/4$ resonator and the open-circuited $\lambda/2$ resonator are equivalent to a parallel RLC resonator with $R = Z_0/(\alpha l)$, $L = 1/\left(\omega_0^2 C\right)$, and $C = \pi/(4\omega_0 Z_0)$ or $C = \pi/(2\omega_0 Z_0)$, respectively. The short-circuited $\lambda/2$ resonator is equivalent to a series RLC resonator with $R = Z_0\alpha l$, $L = \pi Z_0/(2\omega_0)$, and $C = 1/(\omega_0^2 L)$. However, the (internal) Q factor has the same definition for all the three resonators: $Q_i = \beta/(2\alpha)$, where $\beta = 2\pi/\lambda$ [65].

The above discussions apply also to 3D microwave resonators, as shown in Fig. 5.1C, which attract an increasing amount of interests during the past decades due to their superior quality factors. The inner surface of a 3D resonator naturally defines the nodes of the spacial modes of an electrical field, while the anti-nodes are located either at the anti-nodes of the standing waves inside the cavity [91–101], or at the top of a $\lambda/4$-long waveguide pillar standing inside the inner space [102–105]. If the electrical fields can be fairly described by one-dimensional functions of the coordinates, the two types of 3D resonators can be equivalently described as a shorted-circuited $\lambda/2$ or a shorted-circuited $\lambda/4$ transmission line resonator, respectively. In this regard, we do not distinguish coplanar and 3D resonators in our study. A careful distinction may be necessary when studying exotic resonator designs, for example, the whispering gallery mode resonators in 2D [106, 107].

5.1.2 Ideal scattering coefficients

To measure the electrical properties of a microwave resonator, such as the resonant frequency and the Q factor, one has to couple it to an external circuitry, called the load, and measure the scattering coefficients. However, this coupling may also lead to an inevitable change of the electric properties to be measured. By convention, we define the loaded quality factor, Q_l, as a combination of two terms [65]

$$\frac{1}{Q_\mathrm{l}} = \frac{1}{Q_\mathrm{i}} + \frac{1}{Q_\mathrm{c}}. \tag{5.7}$$

Here, Q_c is defined as the coupling quality factor which describes the power-loss ratio induced by the external circuity, Q_i is the internal quality factor that characterizes the bare resonator loss. In this section, we study the ideal scattering coefficients of three types of resonators, which contain the information of the Q factors. We neglect the finite length of the feedlines and the circuit asymmetries for now, which will be discussed shortly.

The hanger-type $\lambda/4$ resonator

The hanger-type $\lambda/4$ resonator is a short-circuited $\lambda/4$ resonator with one end short-circuited to GND and the other side-coupled to a one-dimensional waveguide. The schematic of this resonator is shown in Fig. 5.2A, where we denote the coupling capacitance as C_1 and label the left and right ports as 1 and 2, respectively. The transfer matrix of a hanger-type $\lambda/4$ resonator can be written as [65]

$$T = \begin{bmatrix} 1 & 0 \\ 1/\left(\frac{1}{j\omega C_1} + Z_{\lambda/4}\right) & 1 \end{bmatrix}, \tag{5.8}$$

Following the standard procedure, we obtain the scattering coefficients as [89]

$$S_{11} = S_{22} \approx -\frac{Q_\mathrm{l}/Q_\mathrm{c}}{1 + j2Q_\mathrm{l}\delta},\ S_{21} = S_{12} \approx 1 - \frac{Q_\mathrm{l}/Q_\mathrm{c}}{1 + j2Q_\mathrm{l}\delta}, \tag{5.9}$$

where

$$Q_\mathrm{c} = \frac{\pi}{2\omega_\mathrm{r}^2 Z_0^2 C_1^2},\ \delta = (\omega - \omega_\mathrm{r})/\omega_\mathrm{r}. \tag{5.10}$$

The resonant frequency of the composite circuit is

$$\omega_\mathrm{r} \approx \omega_0 - \frac{2Z_0 C_1 \omega_0^2}{\pi}. \tag{5.11}$$

The physical meaning of the parameter, Q_c, can be understood in the perspective of the Norton's equivalent lumped-element circuit [108–110], as introduced in Chapter 3. Assuming that $\omega_0 C_1 Z_0 \ll 1$, the loaded quality factor can be written as

$$Q_\mathrm{l} = \omega_\mathrm{r} C \left(\frac{1}{R} + \frac{\omega_\mathrm{r}^2 Z_0 C_1^2}{2}\right)^{-1}. \tag{5.12}$$

Here, we have $\omega_\mathrm{r} C \approx \pi/4Z_0$ for $\lambda/4$ resonators, such that the coupling quality factor is $Q_\mathrm{c} = \pi/\left(2Z_0^2\omega_r^2 C_1^2\right)$. In this regard, we conclude that the parameter Q_c defined in Eq. (5.10) can be interpreted as the coupling quality factor of a hanger-type $\lambda/4$ resonator.

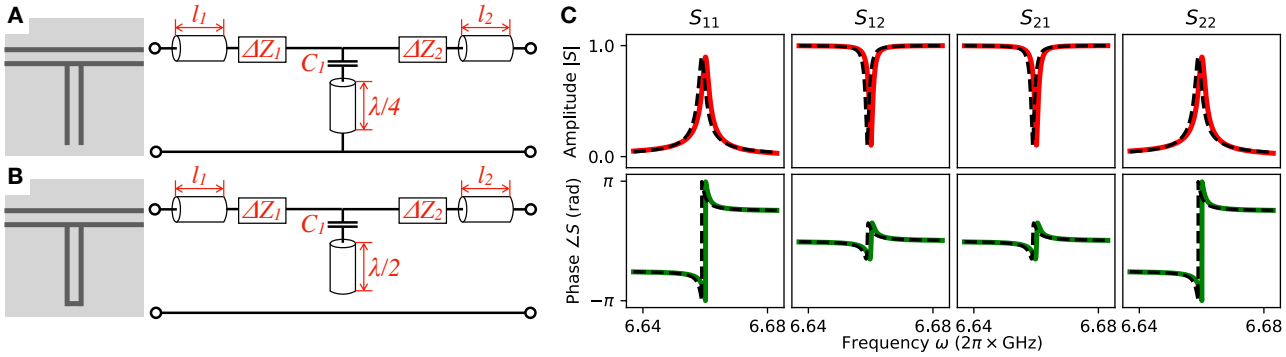

Figure 5.2. Schematics of hanger-type resonators and the corresponding scattering coefficients. (A) A hanger-type $\lambda/4$ resonator, where the open end of a short-circuited $\lambda/4$ resonator is side coupled to a transmission line waveguide. **(B)** A hanger-type $\lambda/2$ resonator, where one of the two open ends of an open-circuited $\lambda/2$ resonator is side coupled to the waveguide. **(C)** The scattering coefficients of a hanger-type $\lambda/4$ resonator as shown in (A). Here, we label the left and right ports of the waveguide by 1 and 2, respectively. The solid and dashed lines distinguish the numerical and analytical results. In all the panels, we denote $l_{1/2}$ as the length of the feedlines that are coupled to the resonator, $C_{1/2}$ the coupling capacitors, and $\Delta Z_{1/2}$ the circuit asymmetries.

The above discussion can also be generalized to a hanger-type $\lambda/2$ resonator, as shown in Fig. 5.2B. Here, we have neglected the coupling capacitance between the open end of the resonator and the ground plane. The corresponding scattering coefficients are exactly the same with that of a hanger-type $\lambda/4$ resonator but with a different definition of the resonant frequency, $\omega_\mathrm{r} \approx \omega_0 - Z_0 C_1 \omega_0^2/\pi$, and the coupling Q factor, $Q_\mathrm{c} = \pi/\left(\omega_\mathrm{r}^2 Z_0^2 C_1^2\right)$. Fig. 5.2C compares the numerically simulated scattering coefficients of a hanger-type $\lambda/4$ resonator with the analytical formulae provided in Eq. (5.9). Here, the parameters are chosen such that $\omega_0/2\pi = 6.75\,\mathrm{GHz}$, $Q_\mathrm{i} = 31416$ for a bare resonator. In the presence of a finite coupling, the analytical expressions predict the resonant frequency, $\omega_\mathrm{r}/2\pi = 6.659\,\mathrm{GHz}$, and the Q factors, $Q_\mathrm{c} = 3589$ and $Q_\mathrm{l} = 3221$, which exhibit an excellent fit to the numerical simulation results.

The necklace-type $\lambda/2$ resonator

The necklace-type $\lambda/2$ resonator, as schematically shown in Fig. 5.3A, consists of an open-circuited $\lambda/2$ resonator which is capacitively coupled to two feedlines through two capacitors, C_1 and C_2, at the two ends, respectively. The transfer matrix, $T = T_{C_1} T_{\lambda/2} T_{C_2}$, can be written as [65]

$$T_{C_{1/2}} = \begin{bmatrix} 1 & 1/j\omega C_{1/2} \\ 0 & 1 \end{bmatrix}, \; T_{\lambda/2} = \begin{bmatrix} \cosh(\gamma l) & Z_0 \sinh(\gamma l) \\ \sinh(\gamma l)/Z_0 & \cosh(\gamma l) \end{bmatrix}. \tag{5.13}$$

Following a similar treatment for the hanger-type resonators, we obtain the scattering coefficients as [89]

$$S_{11} \approx 1 - \frac{2Q_\mathrm{l}/Q_{\mathrm{c},1}}{1 + j2Q_\mathrm{l}\delta}, \; S_{21} = S_{12} \approx \frac{2Q_\mathrm{l}/\sqrt{Q_{\mathrm{c},1}Q_{\mathrm{c},2}}}{1 + j2Q_\mathrm{l}\delta}, \; S_{22} \approx 1 - \frac{2Q_\mathrm{l}/Q_{\mathrm{c},2}}{1 + j2Q_\mathrm{l}\delta}. \tag{5.14}$$

Here, $1/Q_\mathrm{c} = 1/Q_{\mathrm{c},1} + 1/Q_{\mathrm{c},2}$, with

$$Q_{\mathrm{c,k}} = \frac{\pi}{2\omega_r^2 Z_0^2 C_k^2}, \; \text{and}\, \omega_\mathrm{r} = \omega_0 - \frac{Z_0 (C_1 + C_2)\omega_0^2}{\pi}. \tag{5.15}$$

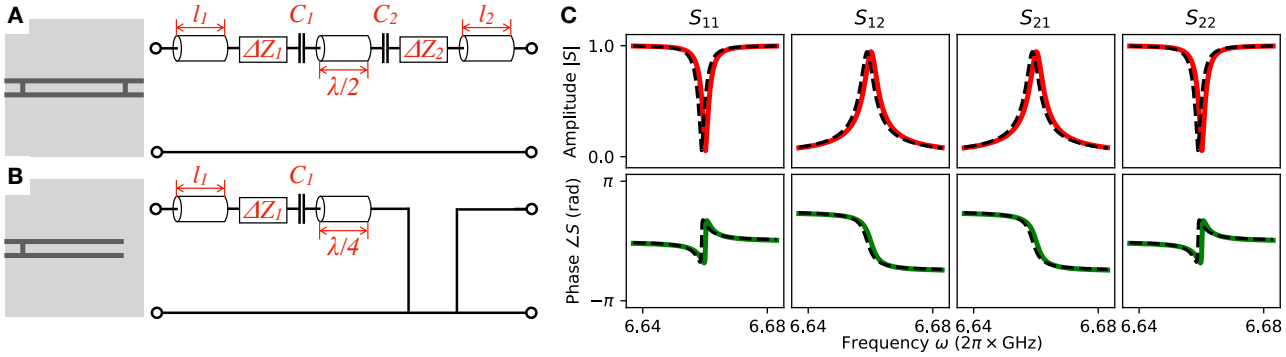

Figure 5.3. Schematics of necklace-type resonators and the corresponding scattering coefficients. (A) A necklace-type $\lambda/2$ resonator, where the two open ends of a open-circuited $\lambda/2$ resonator is end-to-end coupled to two feedlines. **(B)** A necklace-type $\lambda/4$ resonator, where the open end of a short-circuited $\lambda/4$ resonator is end-to-end coupled to one feedline. **(C)** The scattering coefficients of a necklace-type $\lambda/2$ resonator as shown in (A). Here, we label the left and right ports of the waveguide by 1 and 2, respectively. The solid and dashed lines distinguish the numerical and analytical results. In all the panels, we denote $l_{1/2}$ as the length of the feedlines that are coupled to the resonator, $C_{1/2}$ the coupling capacitors, and $\Delta Z_{1/2}$ the circuit asymmetries.

The physical meaning of the parameter, Q_c, can also be understood in the perspective of the Norton's equivalent lumped-element circuit [111–113]. Assuming that $\omega_0 C_1 Z_0, \omega_0 C_2 Z_0 \ll 1$, the loaded quality factor reads

$$Q_\mathrm{l} = \omega_\mathrm{r} C \left(\frac{1}{R} + \omega_\mathrm{r}^2 Z_0 C_1^2 + \omega_\mathrm{r}^2 Z_0 C_2^2 \right)^{-1}, \tag{5.16}$$

where $\omega_\mathrm{r} C = \pi / 2 Z_0$ for a $\lambda/2$ resonator. In this regard, the coupling quality factor can be written as

$$\frac{1}{Q_\mathrm{c}} = \frac{2\omega_\mathrm{r}^2 Z_0^2 C_1^2}{\pi} + \frac{2\omega_\mathrm{r}^2 Z_0^2 C_2^2}{\pi}, \tag{5.17}$$

which is exactly the sum of the two parameters $1/Q_{\mathrm{c},1}$ and $1/Q_{\mathrm{c},2}$ as defined in Eq. (5.15).

The above discussion can also be generalized to a necklace-type $\lambda/4$ resonator, which is a single-port device with only the reflection response shown in Fig. 5.3B. The resonant frequency and the coupling Q factor are $\omega_\mathrm{r} \approx \omega_0 - 2 Z_0 C_1 \omega_0^2 / \pi$ and $Q_\mathrm{c} = \pi / \left(4 \omega_\mathrm{r}^2 Z_0^2 C_1^2\right)$, respectively. We also compare the numerically simulated scattering coefficients of a necklace-type $\lambda/2$ resonator with the analytical formulae provided in Eq. (5.14), as shown in Fig. 5.3C. Here, the parameters are set identical to that in Fig. 5.2C except that the length of the transmission line is doubled. We note also that there are two coupling capacitors, C_1 and C_2, which connect the bare resonator to the external circuity, such that the coupling Q factor should decrease by approximately a factor of two compared with the aforementioned results. In the presence of a finite coupling, the analytical expressions predict the resonant frequency, $\omega_\mathrm{r}/2\pi = 6.659\,\mathrm{GHz}$, and the Q factors, $Q_\mathrm{c} = 1795$ and $Q_\mathrm{l} = 1698$, which are consistent with our exception and fit excellently to the numerical simulation results.

We note that the transmission coefficient, S_{21}, is consistent with the results reported in the literature, which are derived with an equivalent lumped-element circuit [111–113]. However, to the best of our knowledge, the reflection responses, S_{11} and S_{22}, are reported for the first time. Surprisingly, the reflection responses of a necklace-type $\lambda/2$ resonator have a similar form as the transmission response of a hanger-type $\lambda/4$ resonator. In both cases, the complex scattering coefficients form a circle which intersects the real axis at a fixed point, $(1 + j0)$. The circle radius, r_c, equals to $Q_\mathrm{l} / (2Q_\mathrm{c})$ for $C_1 = C_2$.

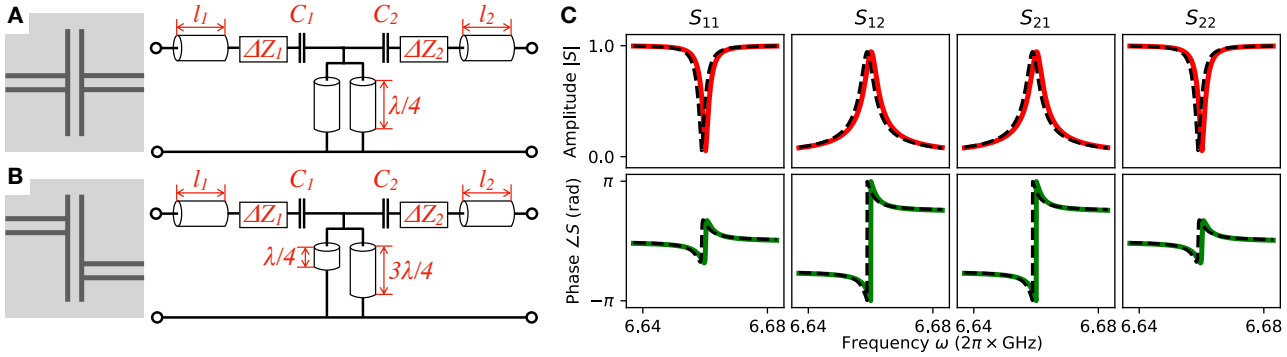

Figure 5.4. Schematics of bridge-type resonators and the corresponding scattering coefficients. (A) A bridge-type $\lambda/2$ resonator, where two feedlines are coupled to the same anti-node of a short-circuited $\lambda/2$ resonator. **(B)** A bridge-type $\lambda/2$ resonator, where two feedlines are coupled to different anti-nodes of the resonator. **(C)** The scattering coefficients of a bridge-type $\lambda/2$ resonator as shown in (A). Here, we label the left and right ports of the waveguide by 1 and 2, respectively. The solid and dashed lines distinguish the numerical and analytical results. In all the panels, we denote $l_{1/2}$ as the length of the feedlines that are coupled to the resonator, $C_{1/2}$ the coupling capacitors, and $\Delta Z_{1/2}$ the circuit asymmetries.

For $C_1 \neq C_2$, the circle radii should be $Q_l/Q_{c,1}$ and $Q_l/Q_{c,2}$, respectively, for the two coefficients, S_{11} and S_{22}. In these regards, the internal quality factor can be directly obtained with the knowledge of the loaded quality factor, Q_l, and the circle radius, r_c. It requires no priori knowledge of the cable calibration results nor the finite-element simulations [112–117].

The bridge-type $\lambda/2$ resonator

Besides, there is a third type of microwave resonator which is often seen in 3D structures. The schematicsare shown in Fig. 5.4A, B, where several feedlines are side-coupled to the anti-nodes of a $\lambda/2$ resonator. Here, we constrain our discussion to the circuit where the two feedlines are coupled to the middle of the resonator, and figuratively name it the bridge-type $\lambda/2$ resonator. The circuit diagram is a combination of the hanger- and necklace-type resonators, which consists of two coupling capacitors, C_1 and C_2, and also two parallel short-circuited $\lambda/4$ resonators in the vertical branch. The transfer matrix, $T = T_{C_1} T_{\lambda/2} T_{C_2}$, can be written as [65]

$$T_{C_{1/2}} = \begin{bmatrix} 1 & 1/j\omega C_{1/2} \\ 0 & 1 \end{bmatrix}, \; T_{\lambda/2} = \begin{bmatrix} 1 & 0 \\ 2/Z_{\lambda/4} & 1 \end{bmatrix}. \tag{5.18}$$

The scattering coefficients can be readily obtained by following the standard procedure [89]

$$S_{11} \approx 1 - \frac{2Q_l/Q_{c,1}}{1 + j2Q_l\delta}, \; S_{21} = S_{12} \approx -\frac{2Q_l/\sqrt{Q_{c,1}Q_{c,2}}}{1 + j2Q_l\delta}, \; S_{22} \approx 1 - \frac{2Q_l/Q_{c,2}}{1 + j2Q_l\delta}, \tag{5.19}$$

where, $1/Q_c = 1/Q_{c,1} + 1/Q_{c,2}$, with

$$Q_{c,k} = \frac{\pi}{2\omega_r^2 Z_0^2 C_k^2}, \text{ and } \omega_r = \omega_0 - \frac{Z_0\omega_0^2\,(C_1 + C_2)}{\pi}. \tag{5.20}$$

Comparing with the scattering coefficients of a necklace-type $\lambda/2$ resonator, as shown in Eq. (5.14), the scattering coefficients of a bridge-type $\lambda/2$ resonator have an almost identical form. However, there is a π phase difference in the transmission response, S_{21} and S_{12}, between Eqs. (5.14) and (5.19),

which distinguishes the two types of resonators. We also compare the numerically simulated scattering coefficients of a bridge-type $\lambda/2$ resonator with the analytical formulae provided in Eq. (5.19), as shown in Fig. 5.4C. Here, the parameters are set identical to Fig. 5.3C. In the presence of a finite coupling, the analytical expressions predict the resonant frequency, $\omega_\mathrm{r}/2\pi = 6.659\,\mathrm{GHz}$, and the quality factors $Q_\mathrm{c} = 1795$, $Q_\mathrm{l} = 1698$. These values are identical to those of a necklace-type $\lambda/2$ resonator and are consistent with the design values.

5.1.3 Practical scattering coefficients: Small circuit asymmetry

In contrast to the ideal circuits we have described above, asymmetries often exist in real circuits in the form of mutual inductance [118], finite impedance mismatch [119, 120], etc. In this section, we keep the *zero*-length feedline assumption but study the influence of a small circuit asymmetry on the scattering coefficients.

Hanger-type resonators

As schematically shown in Fig. 5.2A, we consider small circuit asymmetries, $\Delta Z_1, \Delta Z_2 \ll Z_0$, on both sides of the ideal system. The transfer matrix with asymmetry can be written as

$$T = \begin{bmatrix} 1 + \frac{\Delta Z_1}{Z} & \Delta Z_1 + \Delta Z_2 + \frac{\Delta Z_1 \Delta Z_2}{Z} \\ \frac{1}{Z} & 1 + \frac{\Delta Z_2}{Z} \end{bmatrix}, \tag{5.21}$$

where $Z = 1/(j\omega C_1) + Z_{\lambda/4}$ is the impedance of the vertical branch. Following the derivation in Ref. [89], we obtain the scattering coefficients as

$$S_{11} \approx -\frac{Q_\mathrm{l}'/Q_\mathrm{c}'}{1 + j2Q_\mathrm{l}\delta},\ S_{21} = S_{12} \approx 1 - \frac{Q_\mathrm{l}'/Q_\mathrm{c}'}{1 + j2Q_\mathrm{l}'\delta},\ S_{22} \approx -\frac{Q_\mathrm{l}'/Q_\mathrm{c}'}{1 + j2Q_\mathrm{l}\delta}, \tag{5.22}$$

where we have assumed $\Delta Z_1, \Delta Z_2 \ll Z_0$. Because of the asymmetry, the loaded quality factor becomes $1/Q_\mathrm{l}' = 1/Q_\mathrm{i} + 1/Q_\mathrm{c}'$, where $Q_\mathrm{c}' = Q_\mathrm{c} Z_0 (1/Z_1 + 1/Z_2)/2$ with $Z_1 = Z_0 + \Delta Z_1$ and $Z_2 = Z_0 + \Delta Z_2$. In this regard, both Q_l' and Q_c' can take complex values which indicate a loss mechanism different from a simple exponential energy decay. However, for small circuit asymmetries the real parts of Z_1 and Z_2 should still be dominant. We follow the convention and redefine the loaded quality factor as $1/Q_\mathrm{l}' = 1/Q_\mathrm{i} + \mathrm{Re}\,(1/Q_\mathrm{c}')$ [118, 119]. The information of the imaginary part, $\mathrm{Im}\,(1/Q_\mathrm{c}')$, is interpreted as a small phase factor $\phi = -\arctan[\mathrm{Im}\,(Q_\mathrm{c}')/\mathrm{Re}\,(Q_\mathrm{c}')]$, which rotates the ideal circle in the complex plane. With this definition, we obtain the following scattering coefficients in the presence of a small circuit asymmetry

$$S_{11} \approx -\frac{e^{j\phi} Q_\mathrm{l}'/|Q_\mathrm{c}'|}{1 + j2Q_\mathrm{l}'\delta},\ S_{21} = S_{12} \approx 1 - \frac{e^{j\phi} Q_\mathrm{l}'/|Q_\mathrm{c}'|}{1 + j2Q_\mathrm{l}'\delta},\ S_{22} \approx -\frac{e^{j\phi} Q_\mathrm{l}'/|Q_\mathrm{c}'|}{1 + j2Q_\mathrm{l}'\delta}. \tag{5.23}$$

Necklace-type resonators

For the necklace-type resonator, as shown in Fig. 5.3A, the transfer matrix with asymmetry can be written as

$$T = \begin{bmatrix} A_0 + \sinh(\gamma l)\left(\frac{\Delta Z_1}{Z_0}\right) & B_0 + \sinh(\gamma l)\left(\frac{\Delta Z_1 \Delta Z_2}{Z_0} + \frac{\Delta Z_1}{j\omega C_2 Z_0} + \frac{\Delta Z_2}{j\omega C_1 Z_0}\right) + \cosh(\gamma l)(\Delta Z_1 + \Delta Z_2) \\ C_0 & D_0 + \sinh(\gamma l)\left(\frac{\Delta Z_2}{Z_0}\right) \end{bmatrix}, \tag{5.24}$$

where we denote the matrix elements of the symmetric necklace-type resonator as A_0, B_0, C_0, and D_0. Following the derivation in Ref. [89] and using the conventional notation $1/Q_\mathrm{l}' = 1/Q_\mathrm{i} + \mathrm{Re}\,(1/Q_\mathrm{c}')$, we obtain the scattering coefficients as

$$S_{11} \approx 1 - e^{j\phi_1}\frac{2Q_\mathrm{l}'/\left|Q_{\mathrm{c},1}'\right|}{1 + j2Q_\mathrm{l}'\delta},\ S_{21} = S_{12} \approx e^{j\phi}\frac{2Q_\mathrm{l}'/\sqrt{\left|Q_{\mathrm{c},1}'\right|\left|Q_{\mathrm{c},2}'\right|}}{1 + j2Q_\mathrm{l}'\delta},\ S_{22} \approx 1 - e^{j\phi_2}\frac{2Q_\mathrm{l}'/\left|Q_{\mathrm{c},2}'\right|}{1 + j2Q_\mathrm{l}'\delta}. \tag{5.25}$$

Here, the coupling quality factor is defined as $1/Q_\mathrm{c}' = 1/Q_{\mathrm{c},1}' + 1/Q_{\mathrm{c},2}'$ with $Q_{\mathrm{c},1}' = Q_{\mathrm{c},1}Z_0/Z_1$ and $Q_{\mathrm{c},2}' = Q_{\mathrm{c},2}Z_0/Z_2$. The corresponding phases are $\phi = (\phi_1 + \phi_2)/2$, $\phi_1 = -\arctan\left[\mathrm{Im}\left(Q_{\mathrm{c},1}'\right)/\mathrm{Re}\left(Q_{\mathrm{c},1}'\right)\right]$, and $\phi_2 = -\arctan\left[\mathrm{Im}\left(Q_{\mathrm{c},2}'\right)/\mathrm{Re}\left(Q_{\mathrm{c},2}'\right)\right]$.

Bridge-type resonators

The above results apply also to a bridge-type resonator, as shown in Fig. 5.4A, but with a π phase difference in the transmission coefficients. The scattering coefficients read [89]

$$S_{11} \approx 1 - e^{j\phi_1}\frac{2Q_\mathrm{l}'/\left|Q_{\mathrm{c},1}'\right|}{1 + j2Q_\mathrm{l}'\delta},\ S_{21} = S_{12} \approx -e^{j\phi}\frac{2Q_\mathrm{l}'/\sqrt{\left|Q_{\mathrm{c},1}'\right|\left|Q_{\mathrm{c},2}'\right|}}{1 + j2Q_\mathrm{l}'\delta},\ S_{22} \approx 1 - e^{j\phi_2}\frac{2Q_\mathrm{l}'/\left|Q_{\mathrm{c},2}'\right|}{1 + j2Q_\mathrm{l}'\delta}. \tag{5.26}$$

In these regards, we conclude that a small circuit asymmetry leads to a small rotation of the ideal scattering-response circle in the complex plane. For the transmission coefficients of a hanger-type resonator or the reflection coefficients of a necklace- or bridge-type resonator, this rotation is centered at the reference point $(1 + j0)$ with an angle ϕ. This observation will be used to correct the distortions caused by the circuit asymmetry in the measured scattering coefficients, as will be described in detail in Section 5.3.

5.1.4 Practical scattering coefficients: Finite-length feedlines

Besides the circuit asymmetry, a finite length of the microwave feedlines can also distort the measured scattering coefficients. We recall the expression of the incident and reflected voltages at the position x of a transmission line as [65]

$$V^{\pm}(x) = V_0^{\pm} e^{\mp\gamma x}, \tag{5.27}$$

where the $\pm$ sign distinguishes the incident and reflected wave propagations, and $V_0^{\pm}$ are the corresponding voltage amplitudes at $x = 0$. For finite values of l_1 and l_2, the incident and reflected

voltage signals transferring through the feedlines, $V_1^{\pm\prime}$ and $V_2^{\pm\prime}$, can be described as

$$V_1^{\pm\prime} = e^{\pm\gamma l_1} V_1^{\pm},\ V_2^{\pm\prime} = e^{\pm\gamma l_2} V_2^{\pm}. \tag{5.28}$$

Here, we denote $V_1^{\pm}$ and $V_2^{\pm}$ as the voltage amplitudes at the sample input and output. The scattering coefficients measured through the feedlines are thus

$$S_{11}' = e^{-2\gamma_{\mathrm{c},1} l_1} S_{11},\ S_{21}' = e^{-(\gamma_{\mathrm{c},1} l_1 + \gamma_{\mathrm{c},2} l_2)} S_{21},\ S_{12}' = e^{-(\gamma_{\mathrm{c},1} l_1 + \gamma_{\mathrm{c},2} l_2)} S_{12},\ S_{22}' = e^{-2\gamma_{\mathrm{c},2} l_2} S_{22}, \tag{5.29}$$

where we have assumed a perfect impedance match between the feedlines and the sample. A mismatched feedline causes a small circuit asymmetry, which has already been discussed in the previous section.

Under the high-frequency and low-loss approximations of the transmission feedlines, α is a constant and $\beta = \omega v_{\mathrm{ph}}$ [65]. This observation indicates that the finite-length feedlines can cause a damping coefficient, A, and a frequency-dependent phase shift, $e^{-j\omega\tau}$, in the scattering coefficients. Here, τ is a constant. In addition, there may also exist a constant phase delay, $e^{-j\varphi}$, because of the time difference between the input and output fields captured by VNA. It can also be attributed to the circuit asymmetry, where a global phase factor was neglected in the previous section under the small asymmetry assumption. In total, we obtain a general model that describes the transmission coefficient of a hanger-type resonator or the reflection coefficient of a necklace- or bridge-type resonator

$$S(\omega) \approx A e^{-j(\omega\tau+\varphi)} \left(1 - \frac{e^{j\phi} Q_{\mathrm{l}}/Q_{\mathrm{c}}}{1 + 2jQ_{\mathrm{l}}(\omega/\omega_{\mathrm{r}} - 1)}\right). \tag{5.30}$$

This formula describes the scattering coefficients of a single resonator that is to be measured in real experiments. Here, the global factor, $Ae^{-j(\omega\tau+\varphi)}$, originates from the finite length of the feedlines, while the local phase, $e^{j\phi}$, from small circuit asymmetries. In the complex plane, the former rotates the circle of the ideal scattering coefficients around the original point, $(0 + j0)$, which is accompanied with a shrink of the circle radius. The latter causes a rotation around the reference point, $(1 + j0)$.

5.2 Quantum perspective: The input-output approach

So far, we have developed a classical theory for Q-factor measurement of different types of microwave resonators. In this section, we employ the so-called input-output formalism [48, 121] to develop a quantum theory and compare it with the results of the classical treatment. One clear advantage of the quantum description is that it directly relates the measurement quantities, such as the FWHM of the spectrum, to the open-system parameters, such as the energy dissipation rate, as requested in the master equation (as introduced in Chapter 2).

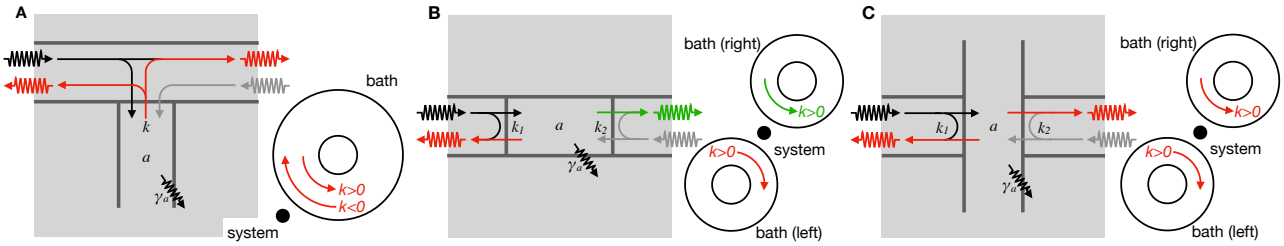

Figure 5.5. Schematics of different types of transmission line resonators. (A) A hanger-type $\lambda/4$ resonator, where a short-circuited $\lambda/4$ resonator, i.e., the system, is side-coupled to a transmission line waveguide, i.e., the bath, which accommodates both left- and right-propagating fields. **(B)** A necklace-type $\lambda/2$ resonator, where an open-circuited $\lambda/2$ is directly coupled to two transmission-line waveguides at the two ends, respectively. Each of the baths accommodates only one unidirectional propagating field. **(C)** A bridge-type $\lambda/2$ resonator, where a short-circuited $\lambda/2$ resonator is coupled to the ends of two transmission line waveguides at the same anti-node. Each of the baths accommodates only one unidirectional propagating field.

5.2.1 Amplitude damping

The hanger-type $\lambda/4$ resonator

The hanger-type $\lambda/4$ resonator is schematically shown in Fig. 5.5A, where the intra-resonator field, a, is coupled to a waveguide, b, with a coupling strength κ. We describe the whole system as

$$H_{\mathrm{s}} = \hbar\omega_0 a^\dagger a, \tag{5.31}$$

$$H_{\mathrm{b}} = \sum_{k=-\infty}^{+\infty} \hbar\omega_k b_k^\dagger b_k, \tag{5.32}$$

$$H_{\mathrm{sb}} = \sum_{k=-\infty}^{+\infty} \hbar\left(\kappa_{\mathrm{c}}^* a b_k^\dagger + \kappa_{\mathrm{c}} a^\dagger b_k\right). \tag{5.33}$$

Following derivations in Appendix B, one can derive a set of linear equations that relate the dynamics of the intra-resonator field, a, to the input and output fields of the bath, b. However, the input and output fields defined in this way are not directly related to the fields measured in experiments. To calculate the scattering coefficients of the system, one must distinguish the left and the right propagating fields, which we denote as l and r, from the bath b.

Keeping this in mind, we restrict our discussion to a small frequency interval around the central driving frequency, ω_{d}. Within this small interval we can approximate the dispersion by a linear relation [122]

$$\omega_k = \omega_{\mathrm{d}} \mp v_{\mathrm{g}}\delta_k. \tag{5.34}$$

Here, v_{g} is the group velocity of the waveguide, $\delta_k = k \pm k_{\mathrm{d}}$ with k and $k_{\mathrm{d}} > 0$ being the wave vectors that correspond to the frequencies ω_k and ω_{d}, respectively. In the rotating frame at ω_{d}, we obtain an

equivalent description of the coupled system

$$H_{\mathrm{s}} = \hbar\left(\omega_0 - \omega_{\mathrm{d}}\right) a^{\dagger} a, \tag{5.35}$$

$$H_{\mathrm{b}} = \sum_{\Delta_k=-\infty}^{+\infty} \hbar v_{\mathrm{g}} \Delta_k \left(-l_{k_{\mathrm{r}}-\Delta_k}^{\dagger} l_{k_{\mathrm{r}}-\Delta_k} + r_{k_{\mathrm{r}}+\Delta_k}^{\dagger} r_{k_{\mathrm{r}}+\Delta_k}\right), \tag{5.36}$$

$$H_{\mathrm{sb}} = \sum_{\Delta_k=-\infty}^{+\infty} \hbar \left(\kappa_{\mathrm{c}}^{*} a l_{k_{\mathrm{r}}-\Delta_k}^{\dagger} + \kappa_{\mathrm{c}} a^{\dagger} l_{k_{\mathrm{r}}-\Delta_k} + \kappa_{\mathrm{c}}^{*} a r_{k_{\mathrm{r}}+\Delta_k}^{\dagger} + \kappa_{\mathrm{c}} a^{\dagger} r_{k_{\mathrm{r}}+\Delta_k}\right). \tag{5.37}$$

Here, we have extended the upper and lower limits of the summation to infinity for mathematical convenience, which is valid as long as ω_{d} is much larger than the typical bandwidth of interest [123, 124]. Finally, we complete our transformation by defining $\omega = v_{\mathrm{g}}\delta_k$, $\Delta_{\mathrm{A}} = \omega_0 - \omega_{\mathrm{d}}$, and replacing the discrete field operators by a continuum: $l_{k_{\mathrm{r}}-\Delta_{\mathrm{k}}} \to l_{\omega}$, $r_{k_{\mathrm{r}}+\Delta_{\mathrm{k}}} \to r_{\omega}$. The result is

$$H_{\mathrm{s}} = \hbar\Delta_{\mathrm{A}} a^{\dagger} a, \tag{5.38}$$

$$H_{\mathrm{b}} = \int_{-\infty}^{+\infty} d\omega \hbar\omega \left(-l_{\omega}^{\dagger} l_{\omega} + r_{\omega}^{\dagger} r_{\omega}\right), \tag{5.39}$$

$$H_{\mathrm{sb}} = \int_{-\infty}^{+\infty} d\omega \hbar \left(\kappa_{\mathrm{c}}^{*} a l_{\omega}^{\dagger} + \kappa_{\mathrm{c}} a^{\dagger} l_{\omega} + \kappa_{\mathrm{c}}^{*} a r_{\omega}^{\dagger} + \kappa_{\mathrm{c}} a^{\dagger} r_{\omega}\right). \tag{5.40}$$

By separating the left- and right-propagating fields in the waveguide, we split the original bath, b, into two independent baths, l and r, representing the different directions of field propagation in the 1D waveguide. In this way, we obtain

$$\dot{a} = -i\Delta_{\mathrm{A}} a - \left(\gamma_{\mathrm{c}} + \frac{\gamma_{\mathrm{A}}}{2}\right) a - \sqrt{\gamma_{\mathrm{c}}}\left(l_{\mathrm{in}} + r_{\mathrm{in}}\right). \tag{5.41}$$

Here, $\sqrt{\gamma_{\mathrm{c}}} = i\sqrt{2\pi}\kappa_{\mathrm{c}}$, $l_{\mathrm{in/out}}$ and $r_{\mathrm{in/out}}$ are the input and output fields of the left- and right-propagating bath fields, respectively, of which the formal definition can be found in Appendix B. Moreover, we have added the intrinsic damping of the resonator, $\gamma_{\mathrm{A}}/2$, by hand.

The scattering coefficients of the resonator can be readily obtained by following the standard input-output formulae

$$S_{11} = \frac{\langle l_{\mathrm{out}}\rangle}{\langle r_{\mathrm{in}}\rangle},\ S_{21} = \frac{\langle r_{\mathrm{out}}\rangle}{\langle r_{\mathrm{in}}\rangle} \text{ with } \langle l_{\mathrm{in}}\rangle = 0, \tag{5.42}$$

$$S_{12} = \frac{\langle l_{\mathrm{out}}\rangle}{\langle l_{\mathrm{in}}\rangle},\ S_{22} = \frac{\langle r_{\mathrm{out}}\rangle}{\langle l_{\mathrm{in}}\rangle} \text{ with } \langle r_{\mathrm{in}}\rangle = 0. \tag{5.43}$$

That is [90],

$$S_{11} = S_{22} = -\frac{\gamma_{\mathrm{c}}}{i\Delta_a + \left(\gamma_{\mathrm{c}} + \frac{\gamma_a}{2}\right)},\ S_{21} = S_{12} = 1 - \frac{\gamma_{\mathrm{c}}}{i\Delta_a + \left(\gamma_{\mathrm{c}} + \frac{\gamma_a}{2}\right)}. \tag{5.44}$$

Here, the imaginary unit $i = \sqrt{-1}$ follows the convention in physics, which is related to the imaginary unit in electrical engineering by $i = -j$ [75].

Comparing with the scattering coefficients of a hanger-type $\lambda/4$ resonator as derived in Section 5.1, we obtain the following relations between the damping rates and the quality factors:

$$\gamma_{\mathrm{A}} = \frac{\omega_{\mathrm{A}}}{Q_{\mathrm{i}}},\ \gamma_{\mathrm{c}} = \frac{\omega_{\mathrm{A}}}{2Q_{\mathrm{c}}}. \tag{5.45}$$

The above relation also holds for a hanger-type $\lambda/2$ resonator, but with different definitions of the resonant frequency and the Q factors. We note that the factor of two in the expression of γ_{c} originates from the fact that both the left- and right-propagating fields in the waveguide couple to the intra-resonator field.

The necklace-type $\lambda/2$ resonator

The necklace-type $\lambda/2$ resonator is schematically shown in Fig. 5.5B, where the intra-resonator field, a, is coupled to two independent baths, b_1 and b_2, on the left and right sides, respectively. We describe the whole system as

$$H_{\mathrm{s}} = \hbar\omega_d a^\dagger a, \tag{5.46}$$

$$H_{\mathrm{b}} = \sum_{m=1}^{2}\sum_{k=0}^{+\infty} \hbar\omega_k b_{m,k}^\dagger b_{m,k}, \tag{5.47}$$

$$H_{\mathrm{sb}} = \sum_{m=1}^{2} (-1)^{m-1} \sum_{k=0}^{+\infty} \hbar\left(\kappa_{\mathrm{c},m}^* a b_{m,k}^\dagger + \kappa_{\mathrm{c},m} a^\dagger b_{m,k}\right). \tag{5.48}$$

Here, the wave vector, k, takes only positive values that defines a unidirectional propagation of the microwave fields in the two feedlines. The phase factor -1 in the system-bath interaction takes into account the π phase difference of the spatial modes with $(2m+1)\lambda/2 = l$ at the two ends of the resonator, whereas there is no phase difference for the modes with $2m\lambda/2 = l$.

Following a similar procedure as before, we linearize the dispersion relation around the central driving frequency as

$$\omega_k = \omega_d + v_{\mathrm{g}}\Delta_k. \tag{5.49}$$

Eventually, we obtain the Hamiltonian in terms of photon frequencies

$$H_{\mathrm{s}} = \hbar\Delta_{\mathrm{A}} a^\dagger a, \tag{5.50}$$

$$H_{\mathrm{b}} = \sum_{m=1}^{2}\int_{-\infty}^{+\infty} d\omega \hbar\omega b_{m,\omega}^\dagger b_{m,\omega}, \tag{5.51}$$

$$H_{\mathrm{sb}} = \sum_{m=1}^{2} (-1)^{m-1} \int_{-\infty}^{+\infty} d\omega \hbar\left(\kappa_{\mathrm{c},m}^* a b_{m,\omega}^\dagger + \kappa_{\mathrm{c},m} a^\dagger b_{m,\omega}\right), \tag{5.52}$$

which leads to the following input-output relation

$$\dot{a} = -i\Delta_{\mathrm{A}} a - \left(\frac{\gamma_{\mathrm{c},1}+\gamma_{\mathrm{c},2}}{2} + \frac{\gamma_{\mathrm{A}}}{2}\right) a + \sum_{m=1}^{2} (-1)^m \sqrt{\gamma_{\mathrm{c},m}} b_{m,\mathrm{in}}. \tag{5.53}$$

Here, $\sqrt{\gamma_{\mathrm{c},m}} = i\sqrt{2\pi}\kappa_{\mathrm{c},m}$ and we have also added the intrinsic damping of the resonator, $\gamma_{\mathrm{A}}/2$, by hand. Because the existence of two baths, the definition of the scattering coefficients is slightly different

from that in Eqs. (5.42)-(5.43). They are

$$S_{11} = \frac{\langle b_{1,\mathrm{out}}\rangle}{\langle b_{1,\mathrm{in}}\rangle},\ S_{21} = \frac{\langle b_{2,\mathrm{out}}\rangle}{\langle b_{1,\mathrm{in}}\rangle} \text{ with } \langle b_{2,\mathrm{in}}\rangle = 0, \tag{5.54}$$

$$S_{12} = \frac{\langle b_{1,\mathrm{out}}\rangle}{\langle b_{2,\mathrm{in}}\rangle},\ S_{22} = \frac{\langle b_{2,\mathrm{out}}\rangle}{\langle b_{2,\mathrm{in}}\rangle} \text{ with }, \langle b_{1,\mathrm{in}}\rangle = 0. \tag{5.55}$$

In total, we have

$$S_{11/22} = 1 - \frac{\gamma_{\mathrm{c},1/2}}{i\Delta + \left(\frac{\gamma_{\mathrm{c},1}+\gamma_{\mathrm{c},2}}{2} + \frac{\gamma_{\mathrm{A}}}{2}\right)},\ S_{21} = S_{12} = \frac{+\sqrt{\gamma_{\mathrm{c},1}\gamma_{\mathrm{c},2}}}{i\Delta + \left(\frac{\gamma_{\mathrm{c},l}+\gamma_{\mathrm{c},2}}{2} + \frac{\gamma_{\mathrm{A}}}{2}\right)}. \tag{5.56}$$

Comparing with the scattering coefficients of a necklace-type $\lambda/2$ resonator as derived in Section 5.1, we obtain the following relations for a necklace-type $\lambda/2$ resonator

$$\gamma_{\mathrm{A}} = \frac{\omega_{\mathrm{A}}}{Q_i},\ \gamma_{\mathrm{c},1} = \frac{\omega_{\mathrm{A}}}{Q_{\mathrm{c},1}},\ \gamma_{\mathrm{c},2} = \frac{\omega_{\mathrm{A}}}{Q_{\mathrm{c},2}}, \tag{5.57}$$

which also hold for a necklace-type $\lambda/4$ resonator but with different definitions of the resonant frequency and the Q factors.

The bridge-type $\lambda/2$ resonators

The bridge-type $\lambda/2$ resonator is schematically shown in Fig. 5.5C, where the intra-resonator field, a, is coupled to two independent baths, b_1 and b_2, on the left and right sides, respectively. Compared with the Hamiltonian of a necklace-type $\lambda/2$ resonator, the major difference lies in the system-bath interaction term

$$H_{\mathrm{sb}} = \sum_{m=1}^{2}\sum_{k=0}^{+\infty} \hbar\left(\kappa^*_{\mathrm{c},m} a b^\dagger_{m,k} + \kappa_{\mathrm{c},m} a^\dagger b_{m,k}\right). \tag{5.58}$$

That is, we assume no phase difference in the system-bath interaction as the two baths are coupled to the resonator mode at the same voltage anti-node. Consequently, the input-output relations are also similar to those of the necklace-type $\lambda/2$ resonator

$$\dot{a} = -i\Delta_{\mathrm{A}} a - \left(\frac{\gamma_{\mathrm{c},1}+\gamma_{\mathrm{c},2}}{2} + \frac{\gamma_{\mathrm{A}}}{2}\right) a - \sum_{m=1}^{2}\sqrt{\gamma_{\mathrm{c},m}} b_{m,\mathrm{in}}. \tag{5.59}$$

As before, we have added the intrinsic damping of the resonator, $\gamma_{\mathrm{A}}/2$, by hand. Following Eqs. (5.54)-(5.55), we obtain the scattering coefficients as

$$S_{11/22} = 1 - \frac{\gamma_{\mathrm{c},1/2}}{i\Delta + \left(\frac{\gamma_{\mathrm{c},1}+\gamma_{\mathrm{c},2}}{2} + \frac{\gamma_a}{2}\right)},\ S_{21} = S_{12} = \frac{-\sqrt{\gamma_{\mathrm{c},1}\gamma_{\mathrm{c},2}}}{i\Delta + \left(\frac{\gamma_{\mathrm{c},1}+\gamma_{\mathrm{c},2}}{2} + \frac{\gamma_a}{2}\right)}. \tag{5.60}$$

Comparing with the scattering coefficients of a bridge-type $\lambda/2$ resonator as derived in Section 5.1, we obtain the following relations for a bridge-type $\lambda/2$ resonator

$$\gamma_a = \frac{2\omega_{\mathrm{A}}}{Q_i},\ \gamma_1 = \frac{2\omega_{\mathrm{A}}}{Q_{\mathrm{c},1}},\ \gamma_2 = \frac{2\omega_{\mathrm{A}}}{Q_{\mathrm{c},2}}. \tag{5.61}$$

As a closing remark, we emphasize that the system-bath method provides an elegant and unified

approach for deriving the scattering coefficients of a general microwave resonator. Here, the key idea is to linearize the dispersion relation of the waveguide and transform the Hamiltonian from the wave vector space to the frequency space. This separation is natural for necklace- and bridge-type resonators with two spatially separated baths, and has been reported in the literature [120, 125]. However, it is not a trivial task to apply the method to a hanger-type resonator. Here, we artificially split the single physical bath into two baths with opposite signs of the wave vectors [122], and relate the scattering coefficients to these two new baths. Depending on the specific geometry of the system, the scattering coefficients can be readily obtained by taking the mean value of the field operators in Eqs. (5.42)-(5.43) for hanger-type resonators, or in Eqs. (5.54)-(5.55) for necklace- or bridge-type resonators.

5.2.2 Phase damping

Besides the energy dissipation, dephasing of microwave resonators can also be incorporated in this theoretical frame. We write the system-bath interaction in the following form [50–54]

$$H_{\mathrm{sb}} = \sum_{m=1}^{2} (-1)^{m-1} \int_{-\infty}^{+\infty} d\omega \hbar a^{\dagger} a \left(\kappa_{\phi}^{*} b_{m,\omega}^{\dagger} + \kappa_{\phi} b_{m,\omega} \right). \tag{5.62}$$

The input-output relation can be readily derived by following the same procedure as described above. The result is

$$\dot{a} = -i\Delta_{\mathrm{A}} a - \frac{\gamma_{\phi}}{2} a - \sqrt{\gamma_{\phi}} \left(a b_{\mathrm{in}} - b_{\mathrm{in}}^{\dagger} a \right), \tag{5.63}$$

where $\sqrt{\gamma_{\phi}} = i\sqrt{2\pi}\kappa_{\phi}$. We note that the input field, $b_{\mathrm{in}} = \int_{-\infty}^{+\infty} d\omega e^{+i\omega t} b_{\omega}(0)/\sqrt{2\pi}$, does not commute with the intra-resonator field. However, the combined operator $b_{\mathrm{in}} + \left(\sqrt{\gamma_{\phi}}\right)^{*} a^{\dagger} a/2$ and $b_{\mathrm{in}}^{\dagger} + \sqrt{\gamma_{\phi}} a^{\dagger} a/2$ commute with all the system operators [50], such that we rewrite Eq. (5.63) as

$$\dot{a} = -i\Delta_{\mathrm{A}} a - \sqrt{\gamma_{\phi}} a \left(b_{\mathrm{in}} - b_{\mathrm{in}}^{\dagger} \right). \tag{5.64}$$

This result indicates that the input field, b, causes a random jittering to the frequency of the intra-resonator field, a. Even though it conserves the energy of the system, the dephasing effect broadens the line shape of the scattering coefficients such that one may not simply obtain the energy dissipation rate of the intra-resonator field by measuring the FWHM of the line shape. In this regard, one should resort to an extra measurement, for example, Ramsey interferometry, to distinguish the contributions of energy decay and dephasing in the FWHM. A careful distinction of the different decoherence mechanisms in a superconducting microwave resonator should be paid enough attention in experiments.

5.3 A recipe for Q-factor measurement

With the detailed understandings of the scattering coefficients in either a classical and quantum perspective, we now study how to correct the distortions in the spectrum and characterize the Q factors. In this section, we take the necklace-type $\lambda/2$ resonator as an example and describe a circle-fitting procedure that corrects the reflection response, S_{11}, automatically. Here, the test data is generated by using a distributed-element circuit model, where the parameters can be fully controlled as a crosscheck of our results. We choose $\alpha = 5.0 \times 10^{-3}\,/\mathrm{m}$, $v_{\mathrm{ph}} = 1.35 \times 10^{8}\,\mathrm{m/s}$, $C_1, C_2 = 1.0 \times 10^{-14}\,\mathrm{F}$, and $l = 1 \times 10^{-2}\,\mathrm{m}$ for the necklace-type $\lambda/2$ resonator. We also assume a small circuit asymmetry,

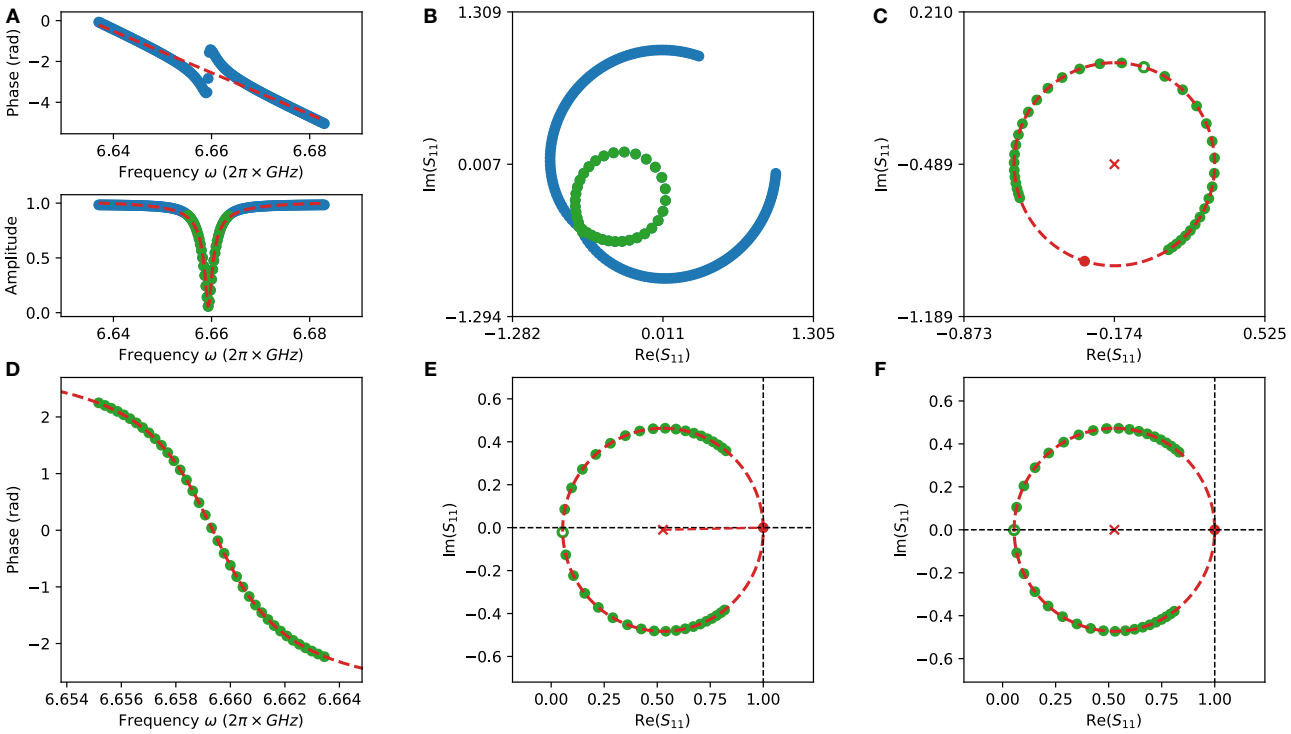

Figure 5.6. The step by step correction of the reflection coefficient S_{11} for a necklace-type $\lambda/2$ resonator. **(A)** Rough phase correction with linear fit and data selection with Lorentzian fit. **(B)** The raw data and the selected data shown in the complex plane. **(C)** Fine phase correction with circle fit. **(D)** Resonant frequency determination with phase-versus-frequency fit. **(E)** Correction of cable attenuation and frequency-independent phase. **(F)** Correction of asymmetry. In all the panels, the blue dots denote raw data and the green dots the selected data within a $\pm 3\Delta_{3\mathrm{dB}}$ bandwidth. The fitting results are colored in red, where the red cross and dot represent the circle center and the far off-resonant point on the circle, respectively.

$\Delta Z_1 = j\omega L_1$ with $L_1 = 1 \times 10^{-9}\,\mathrm{H}$, $\Delta Z_2 = 2\,\Omega$, and consider two finite-length feedlines with $l_1 = l_2 = 1.2\,\mathrm{m}$ with a perfect $50\,\Omega$ impedance match. In these regards, one can simulate the reflection coefficient as shown in Fig. 5.6A-B. The resonant frequency is estimated to be $\omega_\mathrm{r}/2\pi = 6.659\,\mathrm{GHz}$, and the loaded, internal, and coupling quality factors are $Q_\mathrm{l} = 1666$, $Q_\mathrm{i} = 31416$, and $Q_\mathrm{c} = 1759$, respectively.

Correction of frequency-dependent phase shift

The correction procedure consists of three major steps. In the first step, we eliminate the frequency-dependent phase shift $e^{-j(\omega\tau+\varphi_1)}$ with φ_1 being an arbitrary phase offset. This phase shift can be directly seen in Fig. 5.6B, where an expected circle of the scattering coefficient is distorted into a knot in the complex plane. The elimination process can be implemented as follows:

First, we use a linear function to fit τ and φ_1, which serve as an initial guess for a more precise fitting procedure. The objective function is

$$J_1 = \{-(\omega\tau + \varphi_1) - \arg[S(\omega)]\}^2, \tag{5.65}$$

where $\arg[S(\omega)]$ is the unwrapped phase of the complex signal. The fit result is shown as the red dashed line in Fig. 5.6A, where $\tau = 16.18\,\mathrm{s}$.

Next, we use a Lorentzian function to determine the FWHM of the line shape, $\Delta_{3\mathrm{dB}}$, which is used

to select the data that are close to the resonant frequency. The objective function is [126]

$$J_2 = \left[\left(A_1 + A_2 f + \frac{A_3 + A_4 f}{\sqrt{1 + 4\left(\frac{\omega - \omega_\mathrm{r}}{\Delta_\mathrm{3dB}}\right)^2}} \right) - |S(\omega)| \right]^2 . \tag{5.66}$$

Here, ω_r, Δ_3dB, and $A_1, \cdots, A_4$ are fitting parameters. Because the data within the FWHM can form a half circle in the ideal case, to minimize the influence of the background signal we keep only the data within 3 – 5 times of the FWHM in the following analyses. The fit result is shown as the green dots in Fig. 5.6A-B, where $\omega_\mathrm{r}/2\pi = 6.659\,\mathrm{GHz}$ and $\Delta_\mathrm{3dB}/2\pi = 1.41\,\mathrm{MHz}$.

Having obtained the initial guess of the parameters τ, φ_1 and removed the far off-resonant data points beyond $3\Delta_\mathrm{3dB}$ – $5\Delta_\mathrm{3dB}$, we correct the frequency-dependent phase shift by using the circle-fitting technique [127]. On the one hand, we use an algebraic method to fit a circle to the scattering coefficients[128], and determine the circle center S_c and the radius r_c. On the other hand, we optimize the parameter τ with the following objective function

$$J_3 = \left(r_\mathrm{c} - \left| e^{j\omega\tau} S(\omega) - S_\mathrm{c1} \right| \right)^2 , \tag{5.67}$$

in order to make the corrected data $S_1(\omega) = e^{j\omega\tau} S(\omega)$ more likely to be a circle. The corrected data $S_1(\omega)$ and the fitted circle is shown in Fig. 5.6C, where $\tau = 17.58\,\mathrm{s}$, $S_\mathrm{c1} = -0.218 - j0.471$.

Correction of frequency-independent phase shift and cable attenuation

After having corrected the phase shift, $e^{-j(\omega\tau+\varphi_1)}$, the next step is to eliminate the attenuation and the frequency-independent phase shift, $Ae^{-j\varphi_2}$, with $\varphi_2 = \varphi - \varphi_1$. We recall the fact that, without the influence of the finite feedline, the reflection coefficient of a necklace-type resonator intersects the real axis at the reference point $(1 + j0)$ at a far-detuned probe frequency $\omega \to \infty$. We use this property to correct the attenuation and frequency-independent phase shift.

First, we determine the resonant frequency, ω_r, by using a phase-versus-frequency fit, which is proven to be the most precise and robust fitting method for characterizing a microwave resonator [126]. The objective function is

$$J_4 = \left\{ \varphi_2 + 2\arctan\left[2Q_\mathrm{l}\left(1 - \frac{\omega}{\omega_\mathrm{r}}\right)\right] - \arg\left[S_1(\omega)\right] \right\}^2 , \tag{5.68}$$

where $\varphi_2 \equiv (\varphi - \varphi_1) + (2n+1)\pi$, ω_r, and Q_l are fitting parameters. The fitting results are shown in Fig. 5.6D, from which we determine the resonant frequency, $\omega_\mathrm{r}/2\pi = 6.659\,\mathrm{GHz}$, and the loaded quality factor, $Q_\mathrm{l} = 1655$.

Knowing the value of ω_r, one can locate the resonant data point in the fitted circle at $S_\mathrm{r} = -0.041 - j0.040$. Correspondingly, the far off-resonant point, $S_\mathrm{off} = -0.395 - j0.902$, is determined according to the geometry of a circle, i.e., $S_\mathrm{off} = S_\mathrm{c1} + (S_\mathrm{c1} - S_\mathrm{r})$. Then, one can correct the attenuation and the frequency-independent phase shift according to the following relation

$$S_2(\omega) = S_1(\omega)/S_\mathrm{off}. \tag{5.69}$$

The corrected data, $S_2(\omega)$, is shown in Fig. 5.6E, where $S_\mathrm{r} = 0.054 - j0.021$, $S_\mathrm{off} = 1.000$, $S_\mathrm{c2} = S_\mathrm{c1}/S_\mathrm{off} = 0.527 - j0.011$, $r_\mathrm{c2} = r_\mathrm{c1}/|S_\mathrm{off}| = 0.473$.

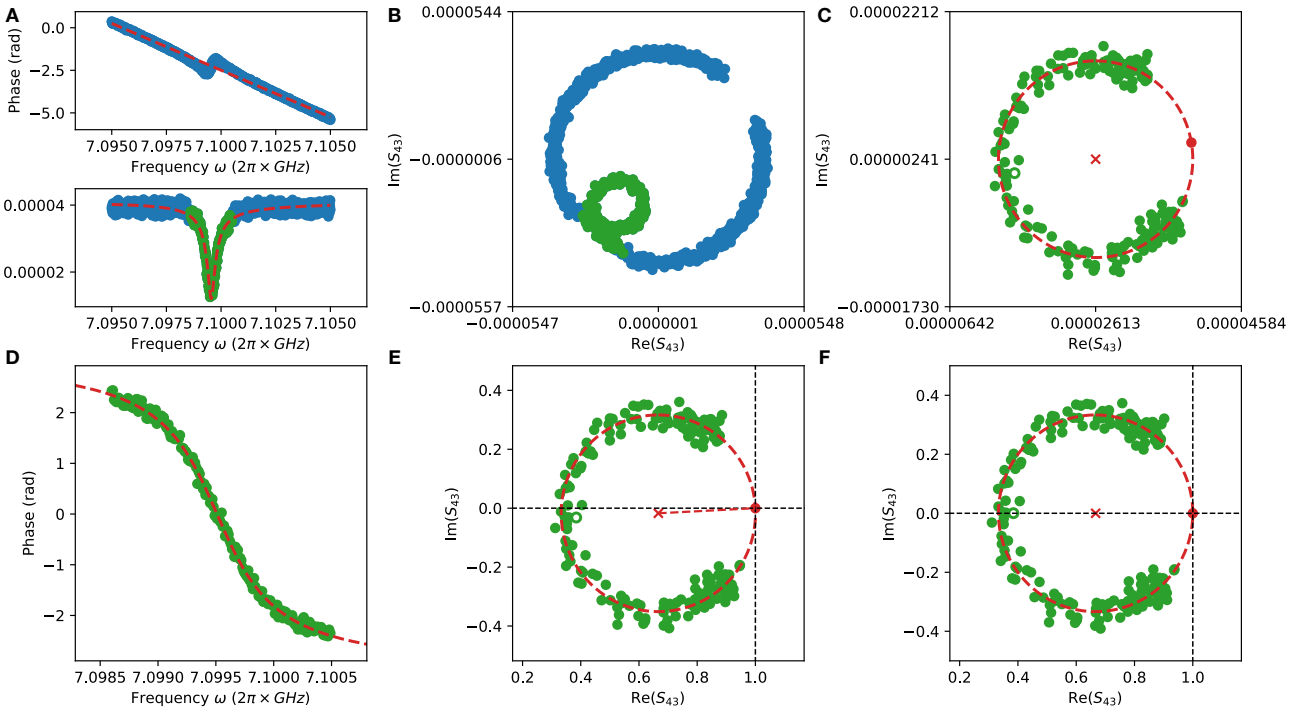

Figure 5.7. The typical procedure for Q-factor measurement. Here, we tune the second resonator to $\omega_r/2\pi = 7.100\,\mathrm{GHz}$, and perform analyzation on the data within $\pm 3\Delta_{3dB}$ bandwidth around the resonant frequency. The panels show the step-by-step circle-fitting procedure, which correspond to Fig. 5.6A-F with the same color code.

Correction of circuit asymmetry

After the first two steps, we have removed the influence of the finite feedlines. The last step is to correct the circuit asymmetry. Here, we use the property that the circle center should be located at the real axis without asymmetry. We identify the asymmetry caused phase shift, ϕ, from the following relation

$$\phi = \arg\left(S_{c2} - S_{off}\right) - \pi, \tag{5.70}$$

and rotate the circle by $-\phi$ around the reference point $(1 + j0)$. In the meantime, we also rescale the circle radius by a factor of $|\cos\phi|$ to account for the difference between $|Q_c|$ and $\mathrm{Re}\,(Q_c)$ [118]. In total, the transformation is described by

$$S_3(\omega) = \cos\phi\,[S_2(\omega) - 1]\,e^{-j\phi} + 1. \tag{5.71}$$

The corrected reflection coefficient, $S_3(\omega)$, is shown in Fig. 5.6F. In this example, we determine $\phi = 0.023$ and thus $S_{c3} = 0.527$, $r_{c3} = 0.473$. The internal quality factor can be calculated as $Q_i = Q_l(1 - 2r_{c3}) = 30530$, while $Q_c = Q_l/(2r_{c3}) = 1750$. The loaded quality factor $Q_l = 1655$ is obtained in the phase-versus-frequency fit. Comparing the fitted Q factors with the estimated values, we obtain the relative errors of the calibration results to be 0.6%, 2.8%, 0.5%, respectively.

5.4 Characterization results of open-system parameters

Using the automated sample tuning procedure described in Chapter 4, we tune either of the two resonators, as introduced in Chapter 3, to different frequencies between 6.8 GHz and 7.2 GHz and measure the reflection coefficient for characterizing the open-system parameters, such as the total

energy dissipation rate, $\gamma = \gamma_A + \gamma_c$. The other resonator is detuned by at least 100 MHz during the measurement, which is much larger than the coupling strength between the two resonators such that its influence on the scattering spectrum can be fairly omitted. The measurement data is processed by the recipe described in Section 5.3, where the experimental imperfections, such as acquisition noise and circuit asymmetries, are corrected automatically. We note that the reflection coefficient of the effective one-resonator system is slightly different from a typical necklace-type $\lambda/2$ resonator as derived in Sections 5.1 and 5.2, because the input and output fields are only coupled to the one resonator end. In other words, we attribute all the photon-loss mechanisms, which includes the resonator intrinsic loss as well as the loss through the flux line and the resonator-resonator coupling capacitor, into the internal quality factor, Q_i. Considering also the practical distortions of the spectrum, we write [60]

$$S_{21/43}(\omega) \approx Ae^{-j(\tau\omega+\varphi)}\left(1 - \frac{e^{j\phi}2Q_l/|Q_c|}{1+2jQ_l(\omega/\omega_r - 1)}\right), \tag{5.72}$$

which shows a factor of two difference in the numerator compared with the general relation given in Section 5.1. Here, we define the reflection coefficient of the first and the second resonators as S_{21} and S_{43}, respectively, where the label correspond to the four ports of the VNA, as defined in Chapter 3. Fig. 5.7A-F shows the result of a typical Q-factor measurement. Here, we tune the second resonator to 7.100 GHz and record the data in a 10 MHz bandwidth of the probe frequency. Because of the nonlinearity, U_A, we observe that different input power, P_{in}, can lead to different scattering spectra and thus different characterization results [63]. To minimize the influence of U_A and obtain a faithful characterization, we keep P_{in} sufficiently small. We set the power at the VNA output to -30 dBm and add 30 – 50 dB room-temperature attenuations depending on the SNR at different frequencies. In this way, the spectrum is kept approximately Lorentzian such that the contribution of U_A in the scattering coefficient can be fairly neglected.

Fig. 5.8A-B summarizes the characterization results of the two resonators in the measurement range. Although the coupling Q factor is approximately a constant for different ω_A, the internal Q factor decreases with the decrease of the resonant frequency. Similar observations are also reported in the literature [129, 130]. Following the discussions in Section 5.2, we attribute the change of Q_i to the dephasing effect. Because the flux noise may perturb the resonant frequency, the dephasing rate must depend on the derivative, $\gamma_\phi(\omega_A) = \eta d\omega_A/d\phi_{ex}$, which can be derived from the effective Josephson energy. Here, ϕ_{ex} is the flux bias and η is a constant to be determined. This phenomenon is consistent with our observation, because $d\omega_A/d\phi_{ex}$ is getting larger at lower frequency. By comparison, the coupling Q factor should not depend on ω_A, which is also consistent with our observation. In these regards, we separate the energy dissipation and dephasing rate from the measured internal loss rate as $\gamma_i(\omega_A) = \gamma_A + \gamma_\phi(\omega_A)$. The exact formula of the derivative $d\omega_A/d\phi_{ex}$ can be derived from the results in Chapter 3, which read

$$\frac{d\omega_A}{d\phi_{ex}} = \frac{\frac{2lv_{ph}}{\phi_0^2}}{\tan(k_mL) + \frac{k_mL}{\cos^2(k_mL)} + 4\frac{C_J}{c}k_m}\frac{dE_J(\phi_{ex})}{d\phi_{ex}}, \tag{5.73}$$

$$\frac{dE_J(\phi_{ex})}{d\phi_{ex}} = \frac{E_{J,+}\sin\left(\frac{\phi_{ex}}{2\phi_0}\right)\cos\left(\frac{\phi_{ex}}{2\phi_0}\right)}{\sqrt{\cos^2\left(\frac{\phi_{ex}}{2\phi_0}\right) + d^2\sin^2\left(\frac{\phi_{ex}}{2\phi_0}\right)}}\frac{d^2-1}{2\phi_0}. \tag{5.74}$$

Even though the expression seems to be rather complicated, the measured results fit very well with

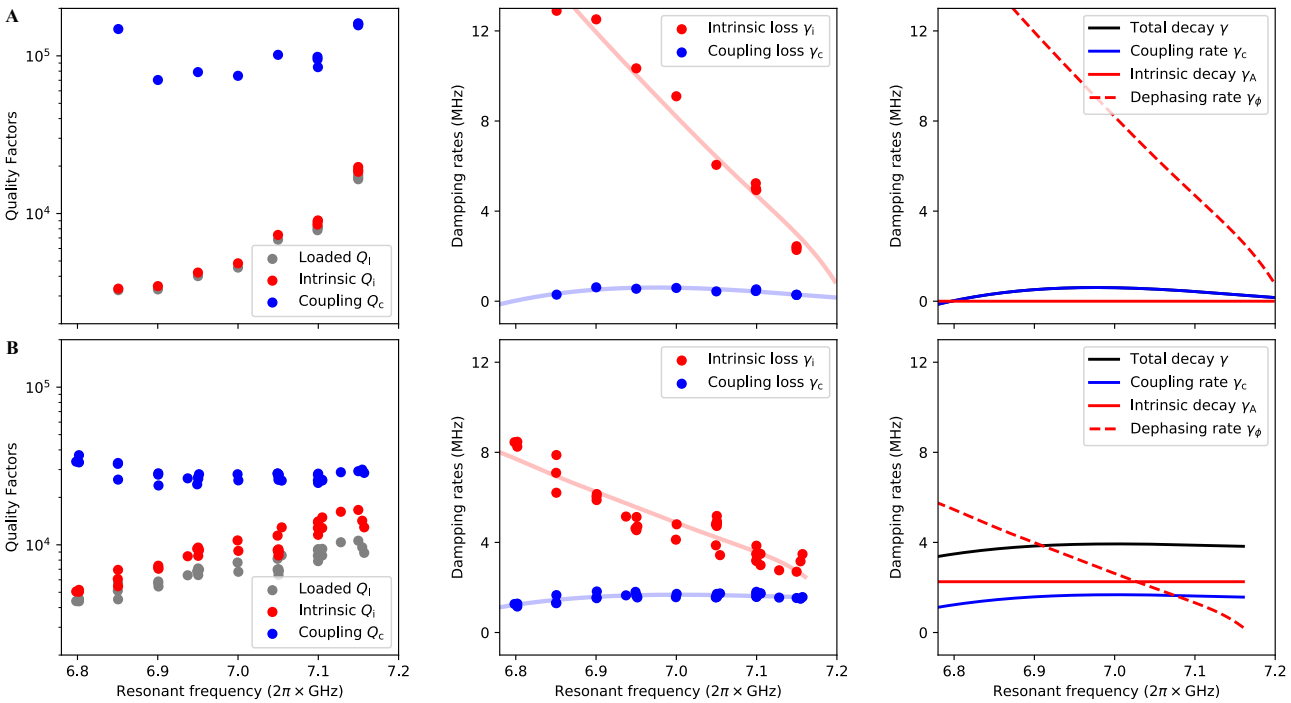

Figure 5.8. Characterized open-system parameters of the two resonators. (A) We tune the first resonator to different frequencies in the 6.8 – 7.2 GHz range, and characterize the intrinsic, coupling, and loaded Q factors (left). The result is transformed into the intrinsic and coupling loss rates, γ_i and γ_c, respectively (middle), and we separate the frequency-dependent and independent parts of γ_i into the intrinsic energy decay, γ_A, and dephasing, γ_ϕ (right). The former can be further split into γ_s and γ_f with two different physical origins. **(B)** Results of the second resonator, which are measured in the same way.

these relations, which indicates a good understanding of the dissipation mechanisms of our system. Besides, we also use a third-order polynomial to fit the weak dependance of the coupling rate on the frequency, $\gamma_c(\omega_A)$. In total, we obtain the total energy dissipation rate $\gamma(\omega_A) = \gamma_A + \gamma_c(\omega_A)$ and the dephasing rate $\gamma_\phi(\omega_A)$. Our detailed characterization shows that the first resonator is overcoupled with $\gamma_A \approx 0.36\,\text{MHz}$ and $\gamma_c \approx 2.67\,\text{MHz}$, while the second one is undercoupled with $\gamma_A \approx 2.26\,\text{MHz}$ and $\gamma_c \approx 1.59\,\text{MHz}$. However, the dephasing rate of the first resonator dominates the total energy decay rate throughout the tuning range, which may easily wash out the dynamic equilibrium between the drive and dissipation. By comparison, the total energy dissipation rate of the second resonator, γ, dominates the dephasing rate, γ_ϕ, in the frequency range $\omega_A/2\pi \geq 6.9\,\text{GHz}$, which indicates that the dephasing effect may be fairly neglected in this frequency range. We are thus prefer to use the second resonator for quantum simulation experiment (see Chapter 8). We note that γ_A can be further attributed to two origins: One is the truly intrinsic damping, γ_s, and the other the coupling induced damping, γ_f, due to the flux line. We assume that $\gamma_s = \gamma_f = \gamma_A/2$ for the rest of the discussions, which will be confirmed by the consistency between the simulation and our experimental results.

Part III:
QUANTUM MEASUREMENT IN NON-EQUILIBRIUM

*credit Metro-Goldwyn-Mayer

Chapter 6

MEASUREMENT OF PROPAGATING MICROWAVE FIELDS

With the knowledge of the system itself, we now move on to control and measure the quantum statistical properties of the microwave fields in the system. In this chapter, we develop the theory of quadrature measurements in superconducting quantum circuits, and describe the room-temperature setup of our experiment. Besides, we introduce the virtual-time filtering technique and the pulsed heterodyne measurement setup which play a key role in revealing the non-equilibrium dynamics of a driven-dissipative system. We also introduce the methods to characterize the intra-resonator photon number and the driving strength of the system, which fill in the final piece of the puzzle for system characterization.

6.1 Theory of quadrature measurements

6.1.1 Description of amplification process

We model the output signal path, from the sample at the MXC stage up to the ADC (analog-to-digital converter) at room temperature, as an effective amplifier with power gain G. The input and output fields of the amplifier are related as [131, 132]

$$b_{\mathrm{s,out}} = \sqrt{G} b_{\mathrm{s,in}} + \sqrt{G-1} b^{\dagger}_{\mathrm{n,in}}, \tag{6.1}$$

where $b_{\mathrm{s,in}}$ and $b_{\mathrm{s,out}}$ represent the input and output fields of the amplifier, respectively, and $b_{\mathrm{n,in}}$ is the amplification noise field. Here, we have assumed that the signal and noise fields are statistically independent from each other. This equation is also known as the Caves formula [132], which describes a phase-insensitive linear amplifier that amplifies the two quadratures in the same way.

To understand the amplification process, we look for a unitary operator which acts on the input fields, $b_{\mathrm{s,in}}$ and $b_{\mathrm{n,in}}$, and results into the output field, $b_{\mathrm{s,out}}$, described by the Caves formula. Strictly speaking, this process must be understood in an open system, where three resonator modes are coupled to one or two baths. Inside the resonator, a three-wave mixing process, or a two-mode squeezing process if we treat the pump field classically, happens and leads to an exponential growth of the amplitude of one resonator modes with time. On the other hand, the finite damping rate of the resonator, which couples the intra-resonator field to the input and output fields, compensates this exponential growth, and results in a finite gain from of input to the output fields [133]. Here, we phenomenally describe the amplification process as a two-mode squeezing operator for simplicity [134–136]

$$S(\zeta) = \exp\left(\zeta^* b_{\mathrm{s,in}} b_{\mathrm{n,in}} - \zeta b^{\dagger}_{\mathrm{s,in}} b^{\dagger}_{\mathrm{n,in}}\right), \tag{6.2}$$

where $\zeta = r\exp(i\theta)$. The input and output fields are related by the unitary evolution $\vec{A}(\zeta) = S^{\dagger}(\zeta)\vec{A}(0)S(\zeta)$, where $\vec{A}(0) = \left[b_{\mathrm{s,in}}, b^{\dagger}_{\mathrm{s,in}}, b_{\mathrm{n,in}}, b^{\dagger}_{\mathrm{n,in}}\right]^{\mathrm{T}}$ and $\vec{A}(\zeta) = \left[b_{\mathrm{s,out}}, b^{\dagger}_{\mathrm{s,out}}, b_{\mathrm{n,out}}, b^{\dagger}_{\mathrm{n,out}}\right]^{\mathrm{T}}$ [137, 138]. Using the *ansatz* of the Heisenberg equation, we obtain $d\vec{A}(\zeta)/d\zeta = J\vec{A}(\zeta)$ with $J_{j,k} = \delta_{j,5-k}$.

This equation has the formal solution

$$\begin{pmatrix} b_{\mathrm{s,out}} \\ b^{\dagger}_{\mathrm{s,out}} \\ b_{\mathrm{n,out}} \\ b^{\dagger}_{\mathrm{n,out}} \end{pmatrix} = \begin{pmatrix} \cosh r & & & -e^{i\theta}\sinh r \\ & \cosh r & -e^{i\theta}\sinh r & \\ & -e^{i\theta}\sinh r & \cosh r & \\ -e^{i\theta}\sinh r & & & \cosh r \end{pmatrix} \begin{pmatrix} b_{\mathrm{s,in}} \\ b^{\dagger}_{\mathrm{s,in}} \\ b_{\mathrm{n,in}} \\ b^{\dagger}_{\mathrm{n,in}} \end{pmatrix}, \tag{6.3}$$

which is a linear map between the input and output fields. When $\cosh r = \sqrt{G}$ and $e^{i\theta}\sinh r = -\sqrt{G-1}$, we resume the result of Eq. (6.1), i.e., the Caves formula.

6.1.2 Description of quadrature measurements

The purpose of using a unitary operator, $S(\zeta)$, to describe the amplification process is to transform our perspective from the Heisenberg to the Schrödinger picture. Here, one measurement record of the field quadratures, $\gamma \equiv (s_I + is_Q)/\sqrt{2}$, can be understood as the outcome of applying the measurement operator, $|\gamma\rangle\langle\gamma|$, to the signal output field, $\rho_{\mathrm{s,out}}$. Consequently, the histogram of the field quadratures forms the Q representation of $\rho_{\mathrm{s,out}}$ [139], as introduced in Chapter 2. We now derive the relation between the measurement histogram and the quasi-distribution functions of the signal field at the input.

In the Schrödinger picture, the signal and the noise fields at the input can be respectively written as

$$\rho_{\mathrm{s,in}} = \int d\alpha^2 P_{\mathrm{s,in}}(\alpha,\alpha^*)|\alpha\rangle\langle\alpha|, \text{ and } \rho_{\mathrm{n,in}} = \int d\beta^2 P_{\mathrm{n,in}}(\beta,\beta^*)|\beta\rangle\langle\beta|. \tag{6.4}$$

Because the two fields are statistically independent from each other, we write the total input field as $\rho_{\mathrm{in}} = \rho_{\mathrm{s,in}} \otimes \rho_{\mathrm{n,in}}$, i.e.,

$$\rho_{\mathrm{in}} = \int d\alpha^2 \int d\beta^2 P_{\mathrm{s,in}}(\alpha,\alpha^*) P_{\mathrm{n,in}}(\beta,\beta^*)|\alpha,\beta\rangle\langle\alpha,\beta|. \tag{6.5}$$

With the unitary operator defined in Eq. (6.2), we write the total output field as $\rho_{\mathrm{out}} = S(\zeta)\rho_{\mathrm{in}}S^{\dagger}(\zeta)$. That is

$$\begin{aligned}
\rho_{\mathrm{out}} &= \int d\alpha^2 \int d\beta^2 P_{\mathrm{s,in}}(\alpha,\alpha^*) P_{\mathrm{n,in}}(\beta,\beta^*) S(\zeta) D(\alpha,\beta)\,|0\rangle\langle 0| D^{\dagger}(\alpha,\beta)\, S^{\dagger}(\zeta) \\
&= \int d\alpha^2 \int d\beta^2 P_{\mathrm{s,in}}(\alpha,\alpha^*) P_{\mathrm{n,in}}(\beta,\beta^*) D\left(\sqrt{G}\alpha + \sqrt{G-1}\beta^*, \sqrt{G}\beta + \sqrt{G-1}\alpha^*\right) S(\zeta)|0\rangle\langle 0| \\
&\times S^{\dagger}(\zeta) D^{\dagger}\left(\sqrt{G}\alpha + \sqrt{G-1}\beta^*, \sqrt{G}\beta + \sqrt{G-1}\alpha^*\right) \\
&= \int d\alpha^2 \int d\beta^2 P_{\mathrm{s,in}}(\alpha,\alpha^*) P_{\mathrm{n,in}}(\beta,\beta^*) D\left(\sqrt{G}\alpha + \sqrt{G-1}\beta^*, \sqrt{G}\beta + \sqrt{G-1}\alpha^*\right) \\
&\times \left[\sum_{n=0}^{\infty} \frac{(G-1)^n}{G^{n+1}} |n,n\rangle\langle n,n|\right] D^{\dagger}\left(\sqrt{G}\alpha + \sqrt{G-1}\beta^*, \sqrt{G}\beta + \sqrt{G-1}\alpha^*\right).
\end{aligned} \tag{6.6}$$

Here, we have defined the two-mode displacement operator as $D(\alpha,\beta) = D(\alpha) \otimes D(\beta)$ and used the

properties of the displacement and squeeze operators [134–136] (see Chapter 2)

$$S(\zeta)D(\alpha,\beta) = D(\alpha\cosh r - e^{i\theta}\beta^*\sinh r, \beta\cosh r - e^{i\theta}\alpha^*\sinh r)S(\zeta), \tag{6.7}$$

$$S(\zeta)|0\rangle = \sum_{n=0}^{\infty}\frac{\left(-e^{i\theta}\sinh r\right)^n}{(\cosh r)^{n+1}}|n,n\rangle. \tag{6.8}$$

The signal part of the output field is obtained by taking a partial trace over the noise part, i.e., $\rho_{\mathrm{s,out}} = \mathrm{tr}_{\mathrm{n,out}}\left(\rho_{\mathrm{out}}\right)$. Using the property that the trace of a density operator equals *one*, we have

$$\begin{aligned}\rho_{\mathrm{s,out}} &= \int d\alpha^2\int d\beta^2 P_{\mathrm{s,in}}(\alpha,\alpha^*)P_{\mathrm{s,in}}(\beta,\beta^*)D\left(\sqrt{G}\alpha+\sqrt{G-1}\beta^*\right)\rho_T D^\dagger\left(\sqrt{G}\alpha+\sqrt{G-1}\beta^*\right),\\ &= \int d\alpha^2\int d\beta^2 P_{\mathrm{s,in}}(\alpha,\alpha^*)P_{\mathrm{n,in}}(\beta,\beta^*)\\ &\times\int d\zeta^2 P_T\left(\zeta,\zeta^*\right)|\zeta+\sqrt{G}\alpha+\sqrt{G-1}\beta^*\rangle\langle\zeta+\sqrt{G}\alpha+\sqrt{G-1}\beta^*|\end{aligned} \tag{6.9}$$

where $P_T(\zeta,\zeta^*) = e^{-|\zeta|^2/(G-1)}/[\pi(G-1)]$ is the P function of a thermal state at temperature T, which has a mean photon number of $\bar{n}_T = G-1$. With this result, we calculate the P function of the signal output field as

$$\begin{aligned}P_{\mathrm{s,out}}(\gamma,\gamma^*) &= \int d\alpha^2\int d\beta^2 P_{\mathrm{s,in}}(\alpha,\alpha^*)P_{\mathrm{n,in}}\left(\beta,\beta^*\right)\\ &\times P_T\left[\gamma-\left(\sqrt{G}\alpha+\sqrt{G-1}\beta^*\right),\gamma^*-\left(\sqrt{G}\alpha^*+\sqrt{G-1}\beta\right)\right].\end{aligned} \tag{6.10}$$

This formula allows us to calculate the normal-ordered characteristic function

$$\begin{aligned}\chi^{(\mathrm{N})}_{\mathrm{s,out}}(z,z^*) &= \int d\gamma^2 P_{\mathrm{s,out}}(\gamma,\gamma^*)e^{iz\gamma}e^{iz^*\gamma^*}\\ &= \chi^{(\mathrm{N})}_{\mathrm{s,in}}\left(\sqrt{G}z,\sqrt{G}z^*\right)\chi^{(\mathrm{N})}_{\mathrm{n,in}}\left(\sqrt{G-1}z^*,\sqrt{G-1}z\right)\chi^{(\mathrm{N})}_T(z,z^*).\end{aligned} \tag{6.11}$$

Because $\chi^{(\mathrm{N})}_T(z,z^*) = \exp\left[-(G-1)\left|z\right|^2\right]$, we have

$$\chi^{(\mathrm{N})}_{\mathrm{s,out}}(z,z^*) = \chi^{(\mathrm{N})}_{\mathrm{s,in}}\left(\sqrt{G}z,\sqrt{G}z^*\right)\chi^{(\mathrm{A})}_{\mathrm{n,in}}\left(\sqrt{G-1}z^*,\sqrt{G-1}z\right), \tag{6.12}$$

and consequently,

$$\chi^{(\mathrm{A})}_{\mathrm{s,out}}(z,z^*) = \chi^{(\mathrm{A})}_{\mathrm{s,in}}\left(\sqrt{G}z,\sqrt{G}z^*\right)\chi^{(\mathrm{N})}_{\mathrm{n,in}}\left(\sqrt{G-1}z^*,\sqrt{G-1}z\right), \tag{6.13}$$

$$\chi^{(\mathrm{S})}_{\mathrm{s,out}}(z,z^*) = \chi^{(\mathrm{S})}_{\mathrm{s,in}}\left(\sqrt{G}z,\sqrt{G}z^*\right)\chi^{(\mathrm{S})}_{\mathrm{n,in}}\left(\sqrt{G-1}z^*,\sqrt{G-1}z\right). \tag{6.14}$$

Then, according to the convolution theorem of Fourier transform, we obtain the corresponding quasi-distribution functions

$$P_{\mathrm{s,out}}(\gamma,\gamma^*) = \frac{1}{G-1}\int d\alpha^2 P_{\mathrm{s,in}}(\alpha,\alpha^*)Q_{\mathrm{n,in}}\left(\frac{\gamma^*-\sqrt{G}\alpha^*}{\sqrt{G-1}},\frac{\gamma-\sqrt{G}\alpha}{\sqrt{G-1}}\right), \tag{6.15}$$

$$Q_{\mathrm{s,out}}(\gamma,\gamma^*) = \frac{1}{G-1}\int d\alpha^2 Q_{\mathrm{s,in}}(\alpha,\alpha^*)P_{\mathrm{n,in}}\left(\frac{\gamma^*-\sqrt{G}\alpha^*}{\sqrt{G-1}},\frac{\gamma-\sqrt{G}\alpha}{\sqrt{G-1}}\right), \tag{6.16}$$

$$W_{\mathrm{s,out}}(\gamma,\gamma^*)=\frac{1}{G-1}\int d\alpha^2 W_{\mathrm{s,in}}(\alpha,\alpha^*)W_{\mathrm{n,in}}\left(\frac{\gamma^*-\sqrt{G}\alpha^*}{\sqrt{G-1}},\frac{\gamma-\sqrt{G}\alpha}{\sqrt{G-1}}\right). \tag{6.17}$$

These results are called the convolution laws in the literature [137, 138], which relate the input and output fields of a phase-insensitive linear amplifier described by the Caves formula.

6.2 Room-temperature setup

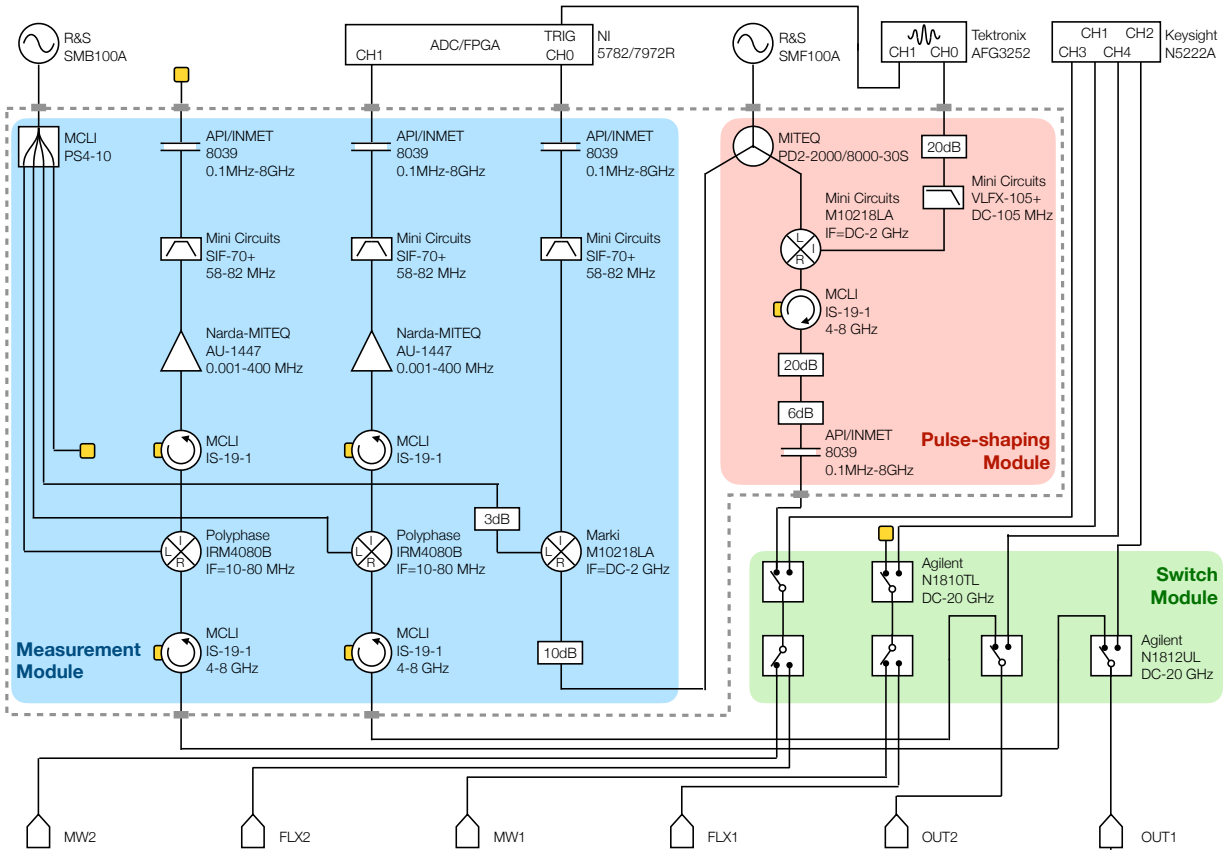

Figure 6.1. Schematic of the room-temperature setup. It contains the measurement module (blue), the pulse-shaping module (red), and the switch module (green) for control and measurement purposes. The components surrounded by the grey dashed lines are sealed in a homemade copper box, as shown in Fig. 6.2.

Figure 6.1 shows the schematic of the room-temperature setup for control and measurement, which consists of three modules. The pulse-shaping module is designed to control the initial state of the nonlinear resonator and also to drive the system. We use a microwave signal generator (R&S SMF100A) to generate the radio frequency (RF) carrier wave. The field envelope is modulated by a double balanced mixer (Marki M1-0218LA) with its local oscillator (LO) port connected to the carrier wave and the intermediate frequency (IF) port to the first channel of an AFG(arbitrary function generator, Tektronix AFG3252). The RF port of the mixer is connected to the switch module for further signal routing. The second channel of the AFG is synchronized with the first one, which is used to trigger the measurement process of the ADC (NI FlexRIO 5782). In addition, we place several attenuators, circulators, and filters in the configuration for the compatibility of different microwave devices.

The measurement module is designed to down-convert the RF signal to an IF frequency of

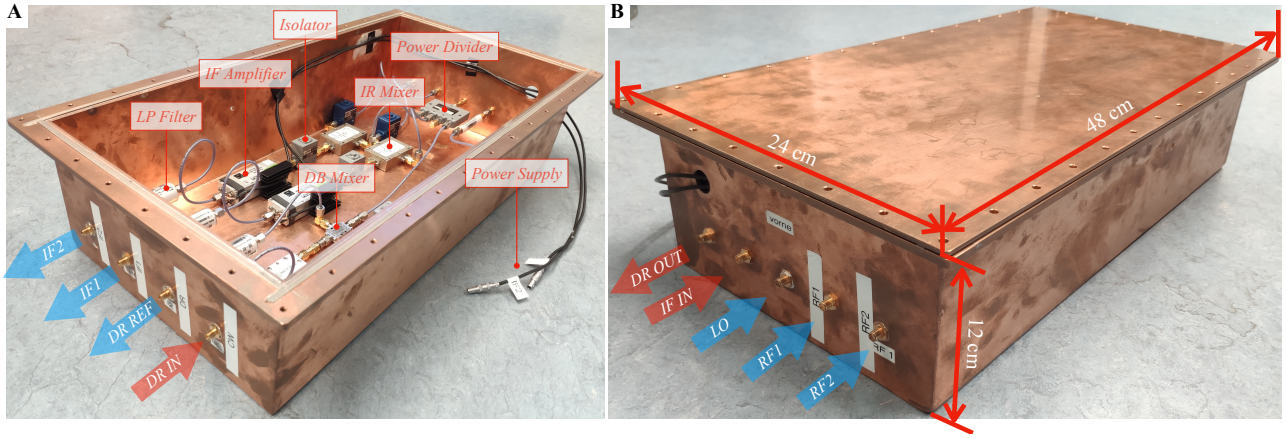

Figure 6.2. The homemade copper box for electromagnetic shielding (A) The front panel without cover. The visible microwave components inside the box and the input-output ports outside the box are labelled with the corresponding names. **(B)** The rear panel with cover, which seals the pulse-shaping and measurement modules as indicated by the grey dashed lines in Fig. 6.1. This box has a dimension of 48 cm × 24 cm × 12 cm.

$f_{\mathrm{IF}} = 62.5\,\mathrm{MHz}$ for heterodyne measurements. This choice of frequency avoids the possible beating between the signal and the higher order harmonics of the Rb frequency standard (SRS FS725), which synchronizes all the instruments in the lab. We use image rejection mixers (Polyphase IRM4080B) in the first two lines, OUT 1/2, to achieve a better SNR, while a double balanced mixer (Marki M1-0218LA) is used in the third line for its relatively low price. However, we use the same LO field, which is generated by the microwave signal generator (R&S SMB100A), to drive all the three mixers for reaching a phase consensus. We also amplify the two channels, OUT 1/2, by low-noise room-temperature amplifiers (MITEQ AU1447R), and place several attenuators, filters, isolators, power dividers to improve the SNR.

Besides, we use several microwave coaxial switches (Agilent N1810TL, N1812UL) in the switch module to control the connectivity of different signal paths for different experimental purposes. The switches are controlled by a commercial controller (Agilent L4445A) with a home made remote-control panel. For typical characterization experiments, where only the scattering coefficients are measured, we connect the two input ports, MW 1/2, and the two output ports, OUT 1/2, to the four channels of the VNA (Keysight PNA N5222A). However, for quadrature measurements we connect one of OUT 1/2 and the driving field to the two channels of the ADC with a sampling frequency of $f_{\mathrm{S}} = 250\,\mathrm{MHz}$. The driving field is connected to either MW 1 or 2 for reflection-type measurements. It is connected to FLX 1 or 2 for transmission-type measurements.

As shown in Fig. 6.2, we seal the pulse-shaping and measurement modules in a 48 cm × 24 cm × 12 cm homemade shielding box for a better electromagnetic isolation and thermalization. The microwave switches are placed outside the box to avoid potential stray magnetic field that may influence the other microwave devices.

6.3 FPGA logic

To reveal the quantum statistical properties of microwaves, one requires a tremendous amount of sampling at the scale of 10^6 – 10^9 in our experiment. However, only a small amount of information, for example, the average of the field quadratures, $\overline{s_I}$ and $\overline{s_Q}$, is extracted from this large amount of

data. This sharp contrast of data volume calls for an efficient way to process the data before flushing them to the computer memory. Our solution is to tightly combine an FPGA (field programmable gate array) card (NI PXIe-7972) with the ADC, where DSP (digital signal processing) can be performed without the host computer. Comparing with our previous setup that uses an ADC (Gage PCIE Gen3 EON Express) only, we observe a more than 25 times acceleration in the measurement efficiency. This improvement provides the opportunity to reveal various statistical properties of microwaves in a reasonable amount of time. In this section, we introduce the detailed FPGA logic for DSP and also the virtual-time filtering technique, which plays a fundamental role in revealing the non-equilibrium dynamics of the system.

6.3.1 I/Q demodulation

The first procedure of DSP is to extract the field quadratures, s_I and s_Q, from the RF signal. Generally speaking, there are three typical ways to achieve this goal, as shown in Fig. 6.3. The first method splits the amplitude and phase information of the field with different analogue components and measures them in parallel, see, for example, Refs. [140–145]. However, the second method separates the I and Q quadratures of the field by using a IQ mixer [146–162]. In both cases, the complete information of the RF signal is encoded in two analogue signal paths which are digitized simultaneously by using two ADCs. By comparison, the third method simply down-converts the RF signal to an IF signal and performs a measurement with a single ADC. The separation of the I/Q quadratures is delayed in the DSP process, which, in our case, is performed on a FPGA card. This approach is free from possible technical issues in building two analogue signal paths, such as the unavoidable imbalance between the two channels of an IQ mixer.

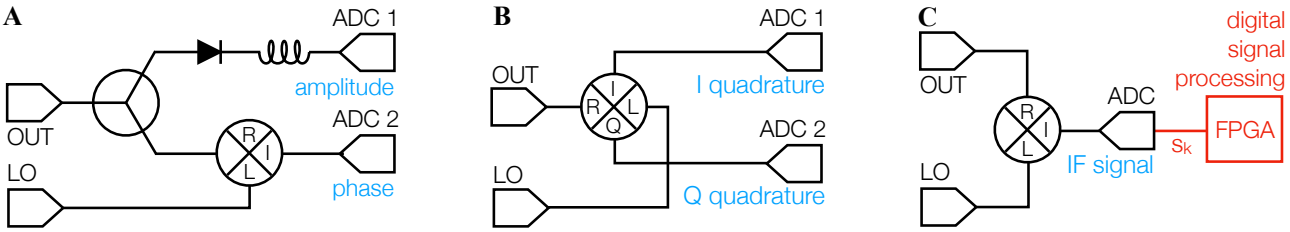

Figure 6.3. Different schemes for quadrature measurement. **(A)** The RF signal is split by a power divider, such that the amplitude and phase information are measured separately by using a Schottky diode combined with a low-pass filter, or a mixer with a resonant LO field, respectively. **(B)** The I/Q quadratures of the RF signal are obtained by mixing the signal with a resonant LO signal in a IQ mixer. When the two fields are off-resonant, the output signal beats at the detuning frequency. **(C)** Instead of splitting the quadratures in the analogue circuit, one can use a normal mixer and sample the IF signal directly by a single ADC. The field quadratures are separated in the following DSP process.

The basic idea of digital I/Q demodulation is similar to the analogue counterpart. That is, we multiply the sampled data by either a sine or cosine function at the IF frequency, f_{IF}, and filter out the side-product frequency components at $2f_{\mathrm{IF}}$. In practice, the filtering process can be achieved by integrating the result over one period [111, 163]. However, one may also use the least-square fitting method to find the best fit between the signal and the sinusoidal functions (see, for example, Ref. [164]). It is proven that, when the the sampling and the IF frequencies satisfy $f_{\mathrm{S}}/f_{\mathrm{IF}} = N/M$, the best fit of

the field quadratures can be obtained analytically as [165]

$$s_I = \frac{2}{N}\sum_{k=0}^{N-1} s_k \sin(k\theta), \text{ and } s_Q = \frac{2}{N}\sum_{k=0}^{N-1} s_k \cos(k\theta), \tag{6.18}$$

where $\theta = 2\pi M/N$, s_k is the kth sampling point of the IF signal within every M periods. According to the description in Section 6.2, we have $M = 1$ and $N = 4$ in our experiments such that the above equation can be written in an even more compact form, $s_I = (s_1 - s_3)/2$ and $s_Q = (s_0 - s_2)/2$. This choice of f_{IF} and f_{S} requires no floating-point multiplication on the FPGA card, and thus reduces the required gate resources and time latencies in DSP.

6.3.2 Low-pass filter

The above discussion considers an ideal classical signal with a single frequency. In reality, the measured field quadratures must have a finite bandwidth, which originates from the practical frequency spread of the coherent signal and the incoherent quantum fluctuations. To reveal the quantum statistical properties of the field, we are interested only in the latter. A finite bandwidth is usually not an issue in quantum optics because the coherent component is much smaller than the quantum fluctuations. The quantum statistical properties of the optical field thus dominates the measurement results [166, 167]. However, in superconducting quantum circuits the measured signal often includes an huge additional amplification noise, as described in Section 6.1. Besides eliminating the amplification noise from the measured field quadratures by using the convolution laws as discussed in Section 6.1, a narrow-band low-pass filter is often necessary to suppress the coherent part. Depending on the required bandwidth in experiments, we use either a FIR (finite impulse response) filter or a combination of CIC (cascaded integrator comb) and FIR filters to reveal the quantum fluctuations of the input signal field.

FIR filter

The concept of FIR filter is closely related to the idea of performing a moving average which smoothes the discontinuities of the input signal and allows only the low-frequency parts to go through. The input and output signals, x and y, of a TYPE-II FIR filter of length M obey the following linear relation

$$y_n = \sum_{m=0}^{M-1} b_m x_{n-m}, \tag{6.19}$$

where $b_m = b_{M-m-1}$, b_m is the mth coefficient of the FIR filter, and x_m and y_m are the mth sampling of the input and output signals, respectively. In the Z-domain, the transfer function of the FIR filter can be written as (see Appendix C for an introduction to the Z-domain)

$$H_{\mathrm{FIR}}(z, z^*) = \sum_{m=0}^{T} b_m z^{-m}, \tag{6.20}$$

which leads to the following frequency response

$$H(e^{j\omega}) = e^{-jM\omega/2}\left\{ b_{\frac{M}{2}} + 2\sum_{m=0}^{M/2-1} b_m \cos\left[\omega\left(\frac{M}{2} - m\right)\right]\right\}. \tag{6.21}$$

This equation benchmarks the low-pass property of a FIR filter.

Benefiting from the commercial toolbox in *Matlab* or the open-source packages in *Python*, design of the coefficients, b_m, can be realized by using numerical methods. In our experiments, we use the *Filter Designer* toolbox in *Matlab* to design the FIR filter with a bandwidth from $B/2\pi = 100\,\mathrm{Hz}$ to 5 MHz with 128 coefficients. The resulting design file is directly compatible with the *Xilinx FIR Compiler* intellectual property (IP) core in the *Vivado Design Suite*. In earlier experiments with only an ADC card, we also used the *scipy.signal* package in *Python* to design the filter. We note that the designed bandwidth, B, corresponds to $2B$ bandwidth of the IF or RF signal. This is because that the frequency components on the both sides of $f_{\mathrm{IF/RF}}$ are folded into the positive frequency range during the I/Q demodulation process [163, 168].

CIC filter

In principle, one can design an arbitrarily narrow-band FIR filter by extending the number of coefficients, M, in the design file. However, a clear drawback of this approach is that one requires a huge amount of FPGA resources and also a large time latency to implement a narrow-band filter. In our experiment, we combine a CIC with a FIR filter to implement a narrow-band filter with $B/2\pi \leq 500\,\mathrm{kHz}$, which is a standard technique in DSP.

Similar to the idea of moving average, a single-stage CIC filter works in a recursive manner

$$y_n = y_{n-1} + (x_n + x_{n-D})/D, \tag{6.22}$$

which corresponds to the following transfer function

$$H(z, z^*) = \frac{1}{D}\frac{1 - z^{-D}}{1 - z^{-1}}. \tag{6.23}$$

Here, D is the latency number, which indicates that one output data is obtained after every D input data. In this regard, one can down-convert the sampling rate by a factor of R to save the FPGA resources, which is often the same as D for designing a single-stage CIC filter but not necessarily equal. If the input frequency is concentrated in a small frequency range, i.e., $\omega \ll 2\pi/D$, the corresponding frequency response can be approximated as

$$H_{\mathrm{CIC}}(e^{j\omega}) = e^{-j(D-1)\omega/2}\frac{\sin(D\omega/2)}{D\omega/2}, \tag{6.24}$$

which behaves as a low-pass filter with a cut-off bandwidth of ω/D.

In practice, one often cascades several single-stage CIC filters into a multi-stage one to achieve a better attenuation at the cut-off frequency, ω/D, and to save FPGA resources [165]. In our experiment, we use the *Xilinx CIC Compiler* IP core in the *Vivado Design Suite* to design the CIC filter, with 6 stages, 1 differential delay, and a down-sampling rate of 128. In this way, we down-convert the sampling frequency from $f_{\mathrm{S}}/N = 62.5\,\mathrm{MHz}$ to $488.281,25\,\mathrm{kHz}$, which makes it possible to design a narrow-band FIR filter with only 128 coefficients.

6.3.3 Data storage

The last step of on-board DSP is to transfer the filtered quadrature signals to the host computer. In our experiment, the data is saved in either of the two forms:

Quadrature Histogram Because the I/Q quadratures are closely related to the real and imaginary parts of the microwave field operator, it is straightforward to save the result in a 2D histogram. In detail, we convert the two quadratures into two 8-digit unsigned integers, respectively, such that 0 – 127 corresponds to a negative value and 128 – 255 a positive value. Then, we concatenate each I/Q pair into a 16-digit unsigned number and transfer it to the computer memory with a 128-length 16-bit data buffer. By repeating this procedure millions of times, one obtains the histogram of the field quadratures, i.e., the Q function of the output field $b_{\mathrm{s,out}}$, which contains all the information of the field. We note that this method works not only for a single mode, but also for multiple modes. For example, two-mode squeezing can be observed by saving 6 histograms with coordinates $(s_{I,1}, s_{Q,1})$, $(s_{I,1}, s_{I,2}), \cdots, (s_{I,2}, s_{Q,2})$. This convenience makes the histogram method readily scalable and suitable for measuring the photon correlations among different fields.

We comment that a more efficient way for data storage is to construct the histogram on the FPGA and transfer it directly to the computer after the entire measurement process. However, we did not realize this design goal due to the limited on-board memory and the gate-time competing issues. Moreover, the above description does not consider the possible drift of the amplification noise, which may play an important role if the experiment is performed at the single-photon level. One possible solution is to use the so-called reference-state method which measures the signal and the noise fields alternatively. Here, each measurement lasts for a shorter time but should generate a histogram with an enough amount of data to reveal the statistical properties [169]. However, one technical issue is to find a compromise between the data amount and the measurement time. A more efficient solution is to use a parametric amplifier before the HEMT, such as a JPA (Josephson parametric amplifier) [170–177], TWPA (traveling wave parametric amplifier) [178–182], and JRM (Josephson ring modulator) [183–186], which significantly increases the SNR and decreases the measurement repetition by orders of magnitude [157–160, 187–189].

Signal Moments Besides recording the histogram of the I/Q quadratures, an alternative way for data storage is to save the average results of the signal moments, for example, $\overline{s_I}$, $\overline{s_Q}$, $\overline{s_I s_I}$, $\overline{s_I s_Q}$, $\overline{s_Q s_Q}$, etc. [147–162]. These signal moments also provide a complete information of the field, assuming that all the orders of moments are stored. This assumption can be relaxed to the first $2(N-1)$ orders, i.e., to measure the moments $\overline{s_I^m s_Q^n}$ up to $m \leq N-1$ and $n \leq N-1$, if the Hilbert space of the intra-resonator field can be fairly truncated to a N-dimensional Fock space [139], or to the first 2 orders if it is in a Gaussian state [147–153]. In this regard, this method requires a much smaller space for data storage and is more convenient for further data processing, such as quantum state tomography as will be introduced in Chapter 7.

However, the challenge is to calculate the signal moments to the required order with the limited on-board resources, which indicates a tremendous work to optimize the gate resources and the timing issues in the FPGA programming. The method itself is also not scalable due to the computational complexity. For example, if we restrict the moments to the fourth-order, there are 14 moments to be calculated for one mode but 69 for two modes. Nevertheless, this computational process can be significantly reduced if one is interested in only certain orders of the signal moments, for example, the second and fourth moments for calculating the second-order correlation function [156–160].

6.3.4 Virtual-time filtering

In the above discussion, we assume that a steady microwave field has to be measured. Except for some special cases, it indicates that the system is in an equilibrium state. Here, the time information is partially lost when extracting the field quadratures from the IF signal, which converts 4 data points within every 16 ns into one pair of the I/Q quadratures. Correspondingly, the time resolution of our measurement is decreased from 4 ns to 16 ns. Then, by applying the low-pass filters we decrease the time resolution further to the inverse of the cut-off frequency, which ranges from 200 ns to 10 ms in our setup. Finally, the time information is completely lost when accumulating millions of data to form a histogram. However, in this thesis we are mainly interested in the non-equilibrium dynamics of the nonlinear resonator, where the field quadratures constantly change with time. To achieve a relatively high time-resolution, we developed the so-called virtual-time filtering technique, as schematically illustrated in Fig. 6.4.

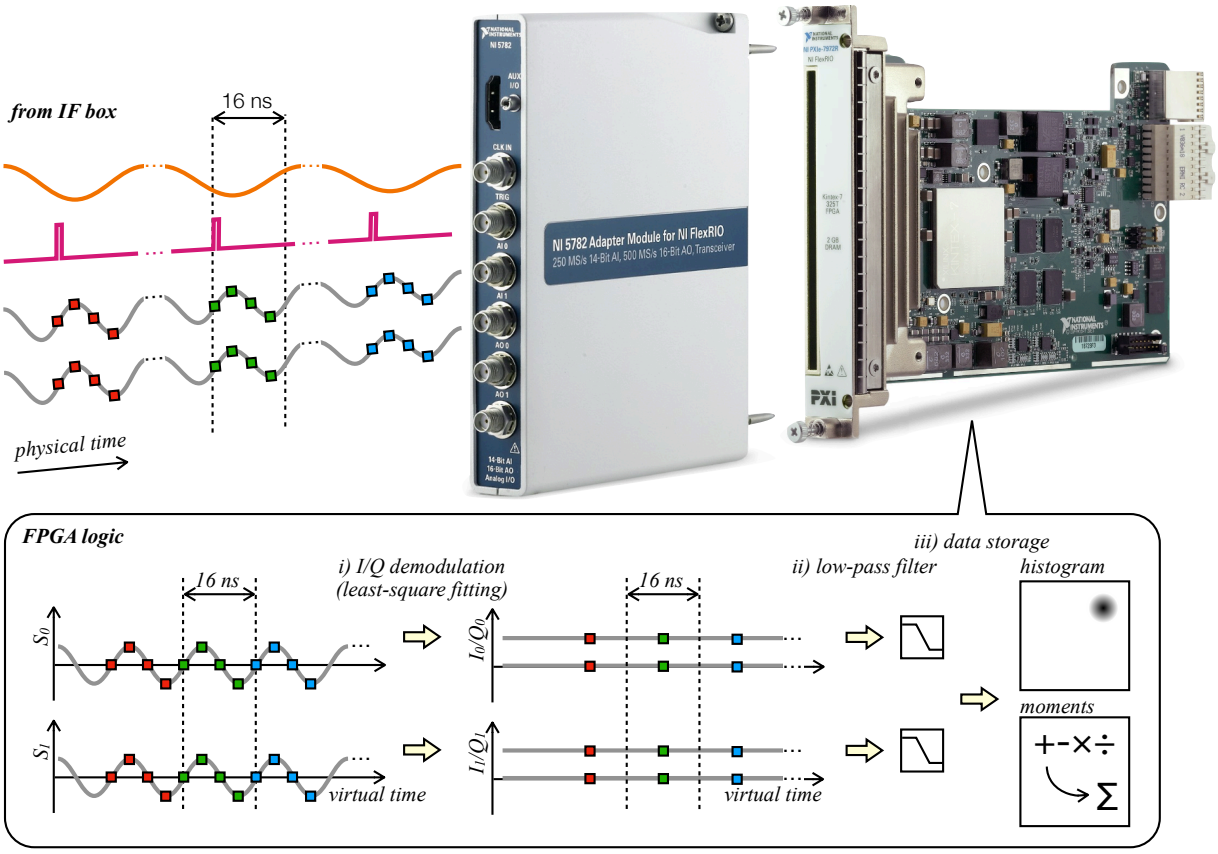

Figure 6.4. Schematic of the FPGA logic and the process of virtual-time filtering. We periodically trigger the ADC to start a measurement at the same relative phase of the IF signal, while each measurement lasts for 16 ns and contains 4 data points. The measurement results are concatenated into a long trace, over which we perform DSP. Depending on the specific experiment, we save the data either in the form of a quadrature histogram or signal moments up to the second order. Photographs of the ADC (NI 5782) and the FPGA (NI PXIe-7972R) are downloaded from the official website of National Instruments (`https://www.ni.com/`).

Instead of performing the measurement over a long and continuous time interval, we use a pulsed measurement setup which measures only a single period of the IF signal. In this regard, only 4 data points are recorded in each measurement event, which ensures one data point of the I/Q quadratures, $s_I + is_Q$, with a time resolution of 16 ns. Then, we initialize the system and repeat the same measurement procedure by millions of times, each of which is triggered at the same relatively time

after initialization. Because the experimental conditions are kept the same in different repetitions, the measurement results should also be the same within the uncertainty range defined by the quantum fluctuations. Figuratively, one can imagine that the measurement is achieved by using millions of ADCs that measure the system at the same time. Then, we concatenate the data recorded by the different virtual ADCs into a long trace and apply a low-pass filter to increase the SNR. Here, one clear difference from the conventional filtering process is that the signal is not sequenced in real time such that the cut-off frequency, or the ring-up time, of the filter does not influence the time resolution of the measurement result, which is kept as 16 ns. The accumulation of the field histogram should also not influence this time resolution, because the repeated measurements are always triggered at the same relative time after initialization. These observations are the essence of the virtual-time filtering technique, which plays an indispensable role in revealing the non-equilibrium photon statistics of the system.

6.4 Input-output characterization

We have constructed the relation between the input signal field at cryogenic temperature, $b_{\mathrm{s,in}}$, and the measured output fields at room temperature, $b_{\mathrm{s,out}}$, which obey the Caves formula (see Section 6.1 for derivation)

$$b_{\mathrm{s,out}} \approx \sqrt{G}\left(b_{\mathrm{s,in}} + b_{\mathrm{n,in}}^{\dagger}\right), \tag{6.25}$$

where $b_{\mathrm{n,in}}$ is the amplification noise field and G is the power gain of the amplification chain. Here, we have neglected the difference between G and $G-1$ for a sufficiently large gain $G \gg 1$, which is valid in common experiments of superconducting quantum circuits [139]. Moreover, we know from the input-output formalism that $b_{\mathrm{s,in}}$ is proportional to the intra-resonator field, a, as (see Chapter 5 for derivation)

$$b_{\mathrm{s,in}} = \sqrt{\gamma_{\mathrm{c}}}a, \tag{6.26}$$

where γ_{c} is the coupling induced energy dissipation rate of the system, and we have assumed that the system is not driven at the same port. These relations indicate one way to reconstruct the quantum statistical properties of the intra-resonator field. The parameter γ_{c} has been characterized in the scattering responses as introduced in Chapter 5. Here, we use the thermal noise as a resource to obtain a precise knowledge of G and $b_{\mathrm{n,in}}$ [146].

6.4.1 The Planck's law and output channel characterization

The Planck's law describes the energy density of a field emitted by a blackbody thermalized at temperature T. A straightforward derivation of Planck's law can be obtained by recalling the properties of a single-mode thermal state at temperature T, as introduced in Chapter 2, where the average photon number is

$$\bar{n}_T(\omega) = \frac{1}{\exp\left[\hbar\omega/(k_{\mathrm{B}}T)\right] - 1}. \tag{6.27}$$

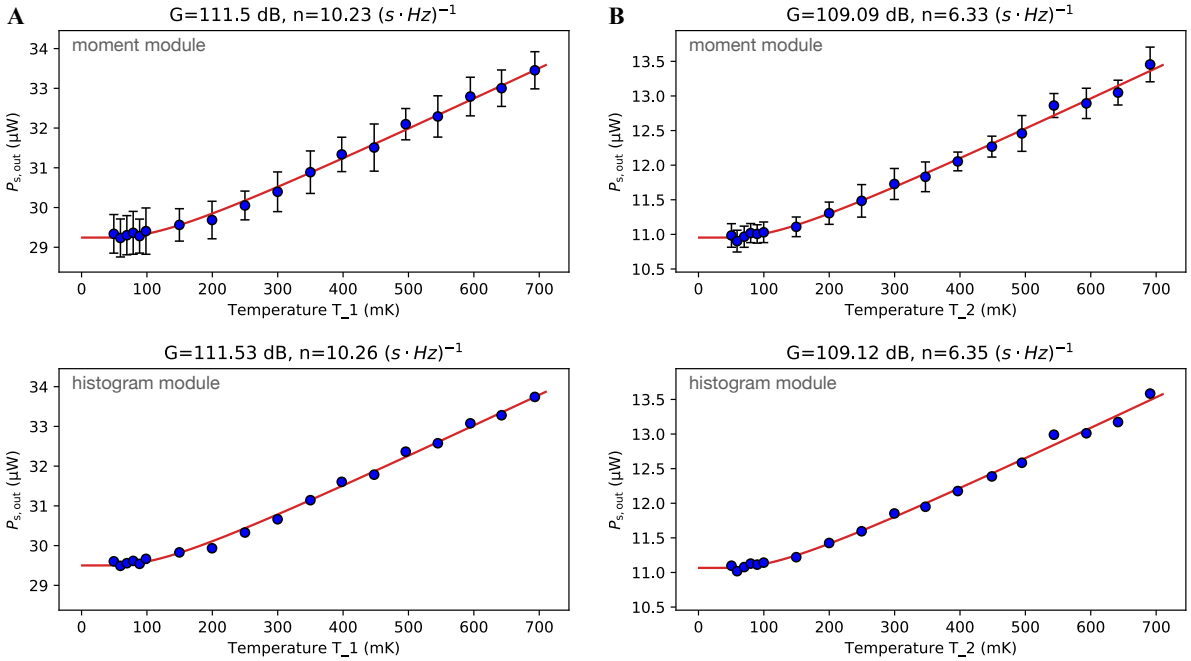

Figure 6.5. Characterized parameters of the two output channels, OUT 1/2. (A) We tune the two resonators to approximately 7.10 GHz and measure the blackbody radiation from the signal path, OUT 1, within ±2 MHz around the central frequency 6.95 GHz (blue dots). The blackbody radiation is generated by a 30 dB heatable attenuator which is mounted just at the sample input, as introduced in Chapter 3. The error bar represents the standard deviation among 16 repetitions, and the red solid curve is the numerical result with optimally estimated parameters G and n. The upper panel is the result obtained from the measured signal moments, while the lower from the quadrature histogram. **(B)** Characterization results of the output path, OUT 2, which are measured in the same way as described above.

Here, $\bar{n}_T(\omega)$ has the unit of 1, or, more strictly, the photon number per second per bandwidth [75]. Straightforwardly, the power of thermal radiation in a narrow band, $2B$, can be obtained as

$$P = \frac{B\hbar\omega}{\pi}\bar{n}_T(\omega). \tag{6.28}$$

The value of P can be calculated from the measured I/Q quadratures, as introduced in Section 6.3. In detail, we have $P = \left(\overline{s_I^2} + \overline{s_Q^2}\right)/(2Z_0)$, where we have assumed a perfect impedance match at the ADC input $Z_0 = 50\Omega$. The factor of 2 originates from the sinusoidal nature of the microwave field. We note that this factor should be omitted when using an analogue IQ mixer for quadrature measurement, because of the energy conservation before and after the mixer [163].

To characterize the parameters G and $\langle b_{\mathrm{n,in}}^\dagger b_{\mathrm{n,in}}\rangle$, we tightly clamp a homemade cryogenic heater and a homemade cryogenic thermometer to a 30 dB attenuator at the sample input to generate the thermal noise (see Chapter 3 for the cryogenic setup). The heater is a 100 Ω resistor (Vishay MCT 0603), of which the temperature, T, is measured and controlled by the AC resistance bridge (Picowatt AVS-47B) and the PID temperature controller (Picowatt TS-530A). The 30 dB attenuator can be modeled as a beam splitter which transmits 0.1% of its input signal and 99.9% of the thermal radiation from the environment at temperature T [76]. Assuming that the measurement bandwidth is largely detuned from the resonant frequency of the resonator, ω_{A}, this thermal radiation can be fully reflected at the sample input, and then amplified and measured as a finite power $P_{\mathrm{out}} \equiv B\hbar\omega_{\mathrm{A}}\langle b_{\mathrm{s,out}}^\dagger b_{\mathrm{s,out}}\rangle/\pi$.

In the form of the Caves formula, we have

$$P_{\mathrm{s,out}} \approx \frac{GB\hbar\omega_{\mathrm{A}}}{\pi}\left[\bar{n}_T(\omega_{\mathrm{A}}) + n + 1\right]. \tag{6.29}$$

Here, we have defined $n \equiv \langle b^{\dagger}_{\mathrm{n,in}} b_{\mathrm{n,in}}\rangle$, and the constant 1 comes from the commutation relation, $b^{\dagger}_{\mathrm{n,in}} b_{\mathrm{n,in}} = b_{\mathrm{n,in}} b^{\dagger}_{\mathrm{n,in}} - 1$. In our experiment, we calibrate G and n by sweeping the temperature T from $30\,mK$ to 700 mK.

Figure 6.5 shows the measured power, $P_{\mathrm{s,out}}$, as a function of the the temperature, T, for the two output channels OUT 1 and 2. The resonant frequencies of the two resonators are tuned to approximately 7.10 GHz, while we measure the microwave signal at 6.95 GHz with a bandwidth of ± 2 MHz. The local temperature of the heatable attenuator is varied from approximately 50 to 700 mK with a precision of ± 2.5 mK during the measurement time. At each temperature, we average the measured signal power by approximately 5×10^4 times, where the error bar is obtained by repeating this procedure 16 times. We use the LSE method to fit the measurement averages according to the relation in Eq. (6.29). We observe a power gain of $G = 111.5$ dB and 109.1 dB for the two output paths, respectively, with the mean photon number of the amplification noise $n = 10.2\,(\mathrm{s}\cdot\mathrm{Hz})^{-1}$ and $6.3\,(\mathrm{s}\cdot\mathrm{Hz})^{-1}$ (corresponding to the noise temperature 3.4 K and 2.1 K, respectively). Comparing with the design parameters of the cryogenic and room-temperature setup, as described in Chapter 3 and Section 6.2, respectively, we conclude that the characterization result is consistent with our expectation. We note that the characterization result may drift with time at a time scale of several weeks and change in different cool-downs. However, for each cool-down we repeat the characterization several times and observe that the variances of the results are smaller than 1 dB and 0.5 K, respectively.

6.4.2 Input channel characterization

Having the knowledge of the gain, G, and noise photon number, n, in the output paths, OUT 1/2, we move on to characterize the attenuation, A, of the input paths, MW 1/2. Assuming that the power of a signal generator is set as P_{d}, we relate the measured signal power, $P_{\mathrm{s,out}}$, and P_{d} in a similar form of the Caves formula

$$P_{\mathrm{s,out}} \approx G\left[AP_{\mathrm{d}} + \frac{B\hbar\omega_{\mathrm{A}}}{\pi}(n+1)\right]. \tag{6.30}$$

The aim of determining A is to establish a relation between P_{d} and the driving strength, ξ, in the system Hamiltonian, as will be formally defined in Chapter 8, that is [190]

$$\xi = -i\sqrt{\gamma_{\mathrm{c}} A P_{\mathrm{d}}/\hbar\omega_{\mathrm{d}}}. \tag{6.31}$$

Here, ω_{d} is the driving frequency, and we have assumed the driving field to be a coherent state [191]. In our experiment, we drive the system via a homemade pulse-shaping module, where the carrier wave generated by the signal generator (R&S SMF100A) is modulated by a voltage signal, V_{d}, generated by the AFG (Tektronix AFG3252), as described in Section 6.2. We assume a simple relation between P_{d} and the pulse amplitude V_{d} as follows

$$P_{\mathrm{d}} = \frac{1}{2}\frac{(V_{\mathrm{d}} - V_{\mathrm{off}})^2}{Z_0}, \tag{6.32}$$

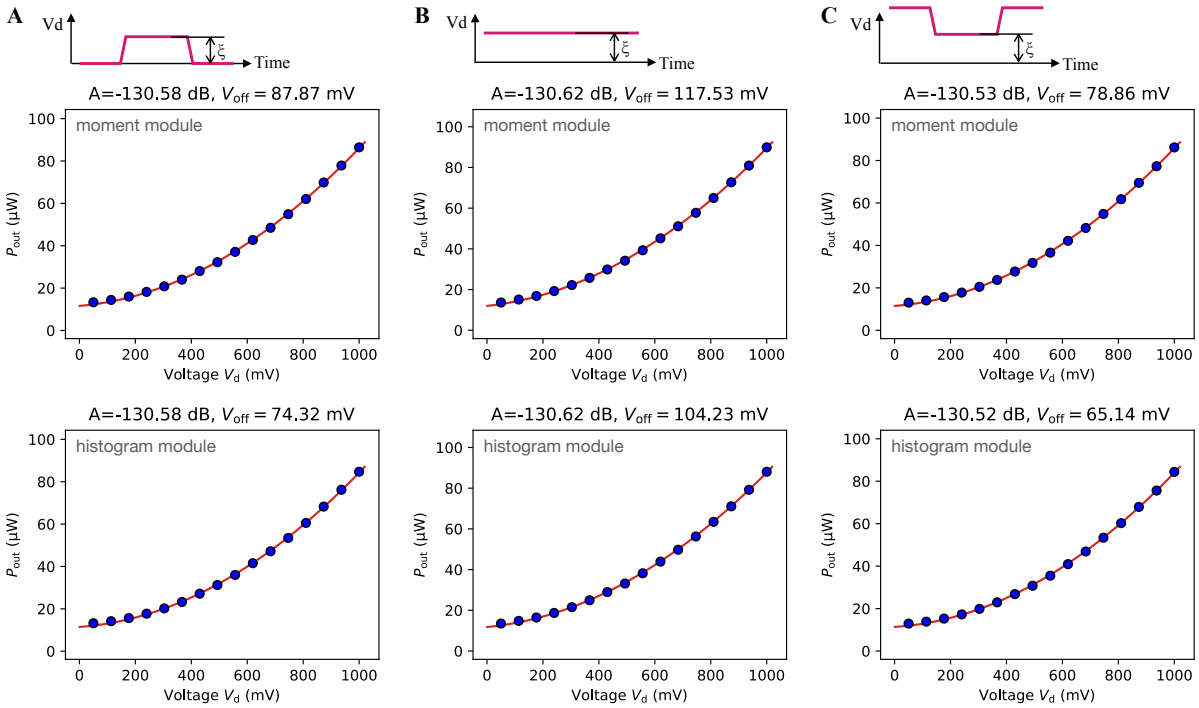

Figure 6.6. Characterized parameters of the second input channel, MW 2. In the same setup of Fig. 6.5, we drive the system through the input path, MW 2, and measure the reflected signal from the path, OUT 2, within ±2 MHz around the central frequency 7.00 GHz (blue dots). The error bar represents the standard deviation among 16 repetitions, which is smaller than the size of the dots, and the red solid curve is the numerical fit. Panels (A)-(C) correspond to different pulse shapes. The upper and lower panels correspond to the results obtained from the measured signal moments and the quadrature histogram, respectively.

where V_{off} is the offset voltage in the setup, which originates from the imperfect grounding of mixers in the pulse-shaping module. Besides, we have assumed a perfect $Z_0 = 50\,\Omega$ match. The goal of the input characterization experiment is to determine the values of A and V_{off}.

Figure 6.6 shows the measured signal power, $P_{\text{s,in}}$, as a function of the pulse amplitude, V_{d}, for the input channel, MW 2. The MW 1 channel is not characterized because the corresponding resonator is not suitable for our experiments, as discussed in Chapter 5. Here, we set the carrier frequency of the input field as 7.0 GHz and vary the pulse amplitude from 50 mV to 1000 mV. The other parameters are set to be exactly the same as for the output characterization experiments. We employ three different pulse shapes for characterization, which will be used in the quantum simulation experiment in Chapter 8. Correspondingly, the characterized attenuations are $A = -130.6$ dB, -130.6 dB, and -130.5 dB, respectively, which are are approximately the same. This result is also consistent with the design parameters as introduced in Chapter 3 and Section 6.2. However, the offset voltage shows a clear dependance on the pulse shape. The results are $V_{\text{off}} = 74 - 88$ mV, $104 - 118$ mV, and $65 - 79$ mV, which vary by approximately 50 mV for the three different pulse shapes, as shown in Fig. 6.6. This is because of the finite on and off ratio of the mixer, which mixes the carrier wave with the voltage signal in the pulse-shaping module, as discussed in Section 6.2. However, we note that a 50 mV difference in V_{d} corresponds to an inaccuracy of $\xi/2\pi$ being less than 5 kHz, which is negligibly small in all of our experiments.

Chapter 7

QUANTUM STATE TOMOGRAPHY OF MICROWAVE PHOTONS

After having introduced the method of quadrature measurement in superconducting quantum circuits, we now move on to methods revealing the quantum statistical properties of the microwave fields. Based on the two forms of the recorded experimental data, i.e., the quadrature histogram and the signal moments, we review several different methods for quantum state tomography, and compare them with the same set of simulation data. We also introduce two other tomography methods, either using a power-law detector or a probe qubit. These methods may be potentially used in our future experiments. In fact, we have already experimentally tested several of these methods in a test setup [192], which is not discussed in this thesis.

7.1 Tomography based on signal moments

Following the discussions in Chapter 6, we model each of the two output signal paths, OUT 1/2, as an effective amplifier which is described by the Caves formula ($G \gg 1$)

$$b_{\mathrm{s,out}} \approx \sqrt{G}\,(b_{\mathrm{s,in}} + b_{\mathrm{n,in}})\,. \tag{7.1}$$

Here, $b_{\mathrm{s,in}}$, $b_{\mathrm{n,in}}$, and $b_{\mathrm{s,out}}$ are the input, noise, and output fields of the amplifier. Assuming that the signal and noise fields are statistically independent from each other, the normal-ordered moments of the output field can be formulated as

$$\langle b^{\dagger k}_{\mathrm{s,out}} b^{l}_{\mathrm{s,out}} \rangle = G^{\frac{k+l}{2}} \sum_{k'=0}^{k} \sum_{l'=0}^{l} C^{k'}_{k} C^{l'}_{l} \langle b^{\dagger k'}_{\mathrm{s,in}} b^{l'}_{\mathrm{s,in}} \rangle \langle b^{k-k'}_{\mathrm{n,in}} b^{\dagger l-l'}_{\mathrm{n,in}} \rangle, \tag{7.2}$$

where $C^{k'}_{k}$ and $C^{l'}_{l}$ are the binomial coefficients. For vacuum as the signal input, which we call the reference state, the moments read

$$\langle b^{\dagger k}_{\mathrm{r,out}} b^{l}_{\mathrm{r,out}} \rangle = G^{\frac{k+l}{2}} \langle b^{k}_{\mathrm{n,in}} b^{\dagger l}_{\mathrm{n,in}} \rangle. \tag{7.3}$$

Here, the subscript r distinguishes the data corresponding to the reference state from those to an arbitrary state. By combining Eqs. (7.2) and (7.3), one can calculate the signal moments of the input fields, $\langle b^{\dagger k}_{\mathrm{s,in}} b^{l}_{\mathrm{s,in}} \rangle$, to an arbitrary order according to the following formula

$$\langle b^{\dagger k}_{\mathrm{s,out}} b^{l}_{\mathrm{s,out}} \rangle = G^{\frac{k'+l'}{2}} \sum_{k'=0}^{k} \sum_{l'=0}^{l} C^{k'}_{k} C^{l'} \langle b^{\dagger k'}_{\mathrm{s,in}} b^{l'}_{\mathrm{s,in}} \rangle \langle b^{\dagger k-k'}_{\mathrm{r,out}} b^{l-l'}_{\mathrm{r,out}} \rangle, \tag{7.4}$$

Recalling also the input-output formalism, $b_{\mathrm{s,in}} = \sqrt{\gamma_{\mathrm{c}}} a$, as discussed in Chapter 6, we obtain a convenient recipe for calculating the optical moments of the intra-resonator field to arbitrary order. The parameters, γ_{c} and G, have been discussed and determined in Chapters 5 and 6, respectively. In what follows, we rescale the power gain as $G \to \gamma_{\mathrm{c}} G$ and simply treat the intra-resonator field, a, as

the signal field at the amplifier input, $b_{\mathrm{s,in}}$.

7.1.1 Arbitrary state tomography

With the knowledge of signal moments, one may employ an optimization algorithm to find the density matrix, $\rho_{\mathrm{s,in}}$, of the input signal field. Because a physically meaningful density matrix must be Hermitian and positive semi-definite, we employ the Cholesky decomposition method and write an arbitrary $N \times N$ density matrix as $\rho = LL^{\dagger}$ [193], where

$$L = \begin{bmatrix} x_{1,1} & 0 & \cdots & 0 \\ x_{2,1} + iy_{2,1} & x_{2,2} & \cdots & 0 \\ \vdots & \vdots & \ddots & \vdots \\ x_{n,1} + iy_{n,1} & x_{n,2} + iy_{n,2} & \cdots & x_{n,n} \end{bmatrix} \tag{7.5}$$

is a complex lower triangular matrix. This formula indicates that there are N^2 real numbers to be determined to obtain a complete tomography of the system. Considering also the requirement of a unitary trace, we add an equality constraint $\mathrm{Tr}\left(L^{\dagger}L\right) = 1$. We define $\{M_1^{(k)}\}, \cdots, \{M_{N'}^{(k)}\}$ as N' different signal moments obtained in different repetitions, where $k = 1, \cdots, K$ is the repetition time of the measurement. We assume that the measurement values obey a Gaussian distribution with standard variances $\sigma_1, \cdots, \sigma_{N'}$, and that they are centered around the ideal values, $\langle M_1 \rangle, \cdots, \langle M_{N'} \rangle$. Here, the variance of the measurement result originates from the classical (technical) noise in experiments but not the quantum fluctuations. Thus, the probability for obtaining the specific values $M_1^{(k)}, \cdots, M_{N'}^{(k)}$ in the kth repetition is

$$P\left(M_1^{(k)}, \cdots, M_{N'}^{(k)}\right) = \prod_{n=1}^{N'} \frac{1}{\sqrt{2\pi\sigma_n^2}} \exp\left(-\frac{\left|M_n^{(k)} - \langle M_n \rangle\right|^2}{2\sigma_n^2}\right). \tag{7.6}$$

It is a 2D Gaussian distribution function with two independent variables, i.e., the real and imaginary parts of $M_n^{(k)}$. In total, the probability for obtaining all the measurement data in K repetitions is

$$\begin{aligned} \prod_{k=1}^{K} P\left(M_1^{(k)}, \cdots, M_{N'}^{(k)}\right) &= \prod_{k=1}^{K} \left[\prod_{n=1}^{N'} \frac{1}{\sqrt{2\pi\sigma_n^2}} \exp\left(-\frac{\left|M_n^{(k)} - \langle M_n \rangle\right|^2}{2\sigma_n^2}\right)\right] \\ &= \prod_{n=1}^{N'} \frac{1}{(2\pi\sigma_n^2)^{K/2}} \exp\left(-K^2 \frac{\left|\overline{M}_n - \langle M_n \rangle\right|^2}{2\sigma_n^2}\right). \end{aligned} \tag{7.7}$$

where $\overline{M}_n = \sum_{k=1}^{K} M_n^{(k)}/K$ are the averaged moments.

The MLE (maximum likelihood estimation) algorithm aims at finding the density matrix, $\rho_{\mathrm{s,in}}$, that maximizes the above probability. This optimization task can be written in the following standard form with a simplified but equivalent objective function

$$\text{minimize: } J = \sum_{n=1}^{N'} \frac{\left|\overline{M}_n - \mathrm{Tr}\left(M_n L^{\dagger} L\right)\right|^2}{\sigma_n^2}, \tag{7.8}$$

$$\text{subject to: } \mathrm{Tr}\left(L^{\dagger}L\right) = 1. \tag{7.9}$$

Because the density matrix has the freedom of N^2, one needs to measure at least N^2 variables to determine $\rho_{\mathrm{s,in}}$ without ambiguity, which correspond to $\langle a^{\dagger m} a^n \rangle$ with $n \leq N-1$ and $m \leq n$. This observation indicates a technical challenge to reconstruct an arbitrary photonic state with more than two photons. On the one hand, a successful measurement of the higher-order moments relies highly on a fairly small amplification noise [157–160, 187–189]. A parametric amplifier is often needed to suppress the noise, ideally, to a photon number of 0.5 [157–160, 187–189]. On the other hand, the MLE algorithm for state reconstruction usually requires a huge amount of computational resources. For example, it took several weeks of computation for reconstructing a 8-qubit state as reported in Ref. [194]. We refer the readers to Refs. [195–197] for the recent progresses of this approach, mostly on the MLE of the qubit states.

7.1.2 Gaussian state tomography

However, the reconstruction process can be significantly accelerated if one already has some information of the state to be reconstructed. The Gaussian state, as introduced in Chapter 2, is a prominent example which is involved in many experiments [36]. Recalling that a Gaussian state is defined as a rotated, squeezed, and displaced thermal state

$$\rho_{\mathrm{G}} = D(\beta)S(\zeta)R(\phi)\rho_{\mathrm{T}}R^{\dagger}(\phi)S^{\dagger}(\zeta)D^{\dagger}(\beta), \tag{7.10}$$

where $R(\phi)$, $S(\zeta)$, and $D(\beta)$ are the rotation, squeeze, and displacement operators, respectively, and ρ_T is a thermal state at temperature T with a mean photon number of $\bar{n}_T = 1/\left\{\exp\left[\hbar\omega/\left(k_{\mathrm{B}}T\right)\right]-1\right\}$. The Wigner function of a Gaussian state reads (see Appendix A for derivation)

$$W(\alpha,\alpha^*) = \frac{1}{\pi(\bar{n}_T+\frac{1}{2})}\exp\left\{-\frac{\left[(x-x_0)\cos\varphi+(y-y_0)\sin\varphi\right]^2}{(\bar{n}_T+\frac{1}{2})e^{-2r}} - \frac{\left[-(x-x_0)\sin\varphi+(y-y_0)\cos\varphi\right]^2}{(\bar{n}_T+\frac{1}{2})e^{2r}}\right\}. \tag{7.11}$$

Here, we have defined $\beta = x_0 + iy_0$, $\zeta = re^{i2\varphi}$. This result indicates that there are only 5 real numbers to be determined to reconstruct a Gaussian state. Recalling also the Q-representation of a Gaussian state, one can verify that [41]

$$\langle a\rangle = \beta,\ \langle a^2\rangle = -\left(\bar{n}_T+\frac{1}{2}\right)\sinh(2r)e^{i2\varphi}+\beta^2,\ \langle a^{\dagger}a\rangle = \left(\bar{n}_{\mathrm{T}}+\frac{1}{2}\right)\cosh(2r)-\frac{1}{2}+|\beta|^2. \tag{7.12}$$

such that a Gaussian state can be equivalently described as

$$W(\alpha,\alpha^*) = \frac{1}{\pi\sqrt{\left(\nu+\frac{1}{2}\right)^2-|\mu|^2}}\exp\left(-\frac{\left(\nu+\frac{1}{2}\right)|\alpha-\langle a\rangle|^2-\frac{\mu^*}{2}\left(\alpha-\langle a\rangle\right)^2-\frac{\mu}{2}\left(\alpha^*-\langle a^{\dagger}\rangle\right)^2}{\left(\nu+\frac{1}{2}\right)^2-|\mu|^2}\right), \tag{7.13}$$

where $\mu = \langle a^2\rangle - \langle a\rangle^2$ and $\nu = \langle a^{\dagger}a\rangle - |\langle a\rangle|^2$. In other words, one only needs to measure the first three lowest-order signal moments, $\langle a\rangle$, $\langle a^{\dagger}a\rangle$, and $\langle a^2\rangle$, in order to fully characterize a Gaussian state in an experiment.

To verify the method described above, we numerically simulate the amplification process and reconstruct the input signal field. In our simulation, the input signal field is a Gaussian state with $\bar{n}_T = 2$, $\beta = 1+1j$, and $\zeta = 0.3\exp(j\pi/2)$. One can calculate the first two orders of signal moments as $\langle a\rangle = 0.998+0.998j$, $\langle a^2\rangle = 0.420j$, $\langle a^{\dagger}a\rangle = 4.455$. The input signal field is amplified with a power

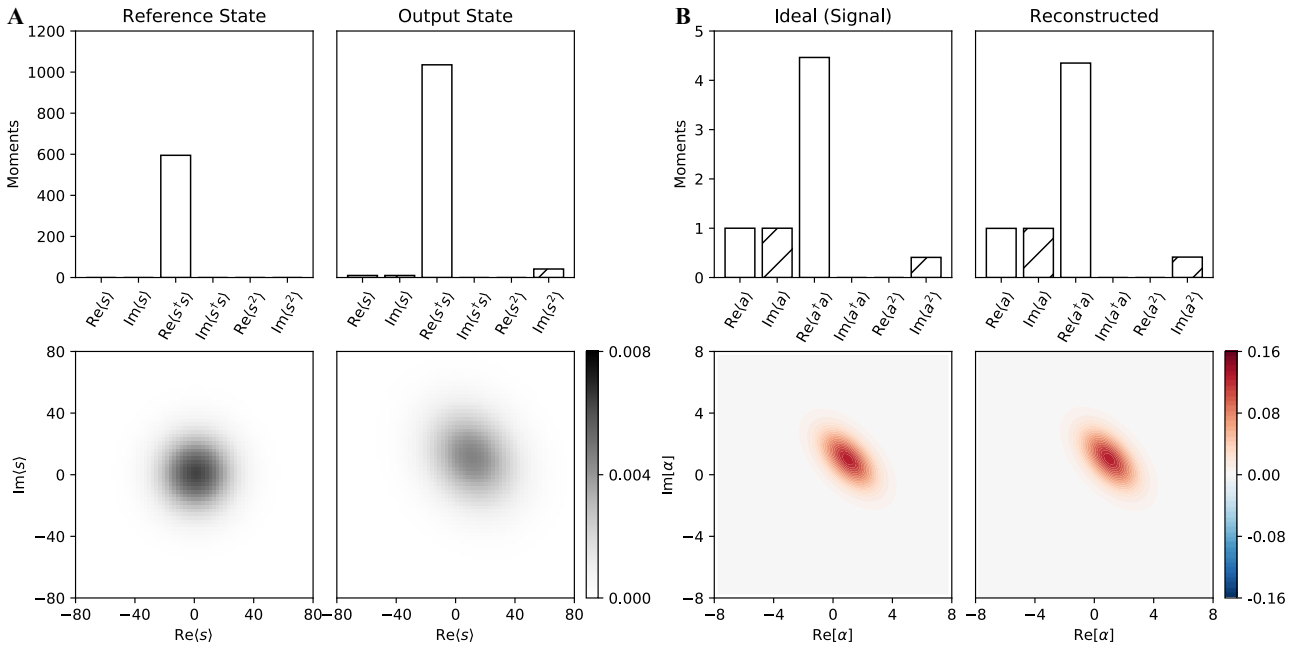

Figure 7.1. Tomography of a Gaussian state with signal moments. **(A)** The signal moments and histogram of the reference state and the output state. Here, the histogram is divided into 65×65 pixels. **(B)** The ideal signal moments and Wigner function of the input signal field and the reconstructed results. The reconstructed state and the ideal input signal state are almost indistinguishable with respect to their Wigner functions.

gain of $G = 20\,\mathrm{dB}$, which induces a thermal noise field with an average photon number of 5.0. The signal moments of the reference state and the output state are shown in Fig. 7.1A. Using the relation in Eq. (7.4), we extract the following signal moments, $\langle a \rangle = 0.995 + 0.995j$, $\langle a^2 \rangle = 0.425j$, $\langle a^\dagger a \rangle = 4.345$, as shown in Fig. 7.1B. The Wigner function and the density matrix of the input signal field can also be obtained accordingly by using the properties of Gaussian states, which are almost indistinguishable from the exact results.

7.2 Tomography based on quadrature histogram

7.2.1 Tomography via inverse linear transformation

Besides signal moments, the measured histogram of the field quadratures contains also all the information that is required to reconstruct an arbitrary quantum state. On the one hand, one can calculate the signal moments from the histogram to the desired order and apply the same method, as introduced in Section 7.1, for state tomography. On the other hand, one can also reconstruct the quantum state directly from the histogram. Recalling the results in Chapter 6, the measured quadrature histogram is identical to the Q-function of the output field. For $G \gg 1$, we have

$$\begin{aligned} Q_{\mathrm{s,out}}(\gamma, \gamma^*) &\approx \frac{1}{G} \int d\alpha^2 Q_{\mathrm{s,in}}(\alpha, \alpha^*) P_{\mathrm{n,in}} \left(\frac{\gamma^*}{\sqrt{G}} - \alpha^*, \frac{\gamma}{\sqrt{G}} - \alpha \right) \\ &= \frac{1}{G} \int d\beta^2 P_{\mathrm{s,in}}(\beta, \beta^*) \frac{1}{\pi} \int d\alpha^2 e^{-|\beta - \alpha|^2} P'_{\mathrm{n,in}} \left(\alpha - \frac{\gamma}{\sqrt{G}}, \alpha^* - \frac{\gamma^*}{\sqrt{G}} \right) \\ &= \frac{1}{G} \int d\beta^2 P_{\mathrm{s,in}}(\beta, \beta^*) Q'_{\mathrm{n,in}} \left(\beta - \frac{\gamma}{\sqrt{G}}, \beta^* - \frac{\gamma^*}{\sqrt{G}} \right) \end{aligned} \tag{7.14}$$

Here, $Q'_{\mathrm{n,in}}(\alpha,\alpha^*)$ is a particular notation of $Q_{\mathrm{n,in}}(-\alpha^*,-\alpha)$, which is obtained by reflecting the original quasi-distribution function, $Q_{\mathrm{n,in}}(\alpha,\alpha^*)$, over the real and imaginary axes.

For a vacuum input state, we have $P_{\mathrm{s,in}}(\beta,\beta^*)=\delta(\beta)$ as derived in Chapter 2, such that Eq. (7.14) becomes

$$Q^{(\mathrm{r})}_{\mathrm{s,out}}(\gamma,\gamma^*)\approx\frac{1}{G}Q'_{\mathrm{n,in}}\left(\frac{\gamma}{\sqrt{G}},\frac{\gamma^*}{\sqrt{G}}\right)=\frac{1}{G}Q_{\mathrm{n,in}}\left(\frac{\gamma^*}{\sqrt{G}},\frac{\gamma}{\sqrt{G}}\right). \tag{7.15}$$

It indicates that the histogram of the reference state is equivalent to the Q-function of the noise field. In fact, by integration we obtain

$$\langle s^m s^{\dagger n}\rangle=\int d\gamma^2\gamma^m\gamma^{*n}Q^{(\mathrm{r})}_{\mathrm{s,out}}(\gamma,\gamma^*)\approx\frac{1}{G}\int d\gamma^2\gamma^{*n}\gamma^m Q^{(\mathrm{r})}_{\mathrm{n,in}}(\frac{\gamma^*}{\sqrt{G}},\frac{\gamma}{\sqrt{G}})=G^{\frac{m+n}{2}}\langle h^n h^{\dagger m}\rangle, \tag{7.16}$$

which is consistent with the result in Section 7.1. In total, the P-function of the input signal field can be obtained by combining Eqs. (7.14) and (7.15), i.e.,

$$Q_{\mathrm{s,out}}(\gamma,\gamma^*)\approx\int d\alpha^2 P_{\mathrm{s,in}}(\alpha,\alpha^*)Q^{(\mathrm{r})}_{\mathrm{s,out}}\left(\frac{\gamma}{\sqrt{G}}-\alpha,\frac{\gamma^*}{\sqrt{G}}-\alpha^*\right). \tag{7.17}$$

In real experiments, one must discretize the complex plane of the histogram into $N\times N$ pixels, and use a pair of integer numbers, $[n_1,n_2]$, to label each pixel. Assuming that the real and imaginary parts of α ranges from $-A$ to $+A$, we can build the relation between each pair of the index and a point in the complex plane: $[n_1,n_2]\leftrightarrow(n_1/N-1/2)A+i(n_2/N-1/2)A$. This discretization leads to a more useful formula for state reconstruction

$$Q_{\mathrm{s,out}}[n_1,n_2]\approx d\alpha^2\sum_{m_1,m_2}P_{\mathrm{s,in}}[m_1,m_2]Q^{(\mathrm{r})}_{\mathrm{s,out}}[n_1-(m_1-N/2),n_2-(m_2-N/2)], \tag{7.18}$$

where $d\alpha^2\equiv(A/N)^2$ is a normalization factor. This result indicates that the state reconstruction problem can be solved by solving a set of linear equations with N^2 dimensions.

We apply this method to the same example introduced in Section 7.1, and obtain the tomography results as shown in Fig. 7.2. Here, the histogram is discretize into 65×65 pixels. The Q function of the noise field, $Q_{\mathrm{n,in}}[n_1,n_2]$, is obtained by simply reflecting the histogram of the reference state by the real axis, and the P function of the input signal field, $P_{\mathrm{s,in}}[m_1,m_2]$, is obtained by solving a 65^2-dimensional linear equation. The Wigner function, $W_{\mathrm{s,in}}[m_1,m_2]$, is obtained from the P-function by a standard transformation as introduced in Chapter 2, which also obeys a linear relation with 65^2 dimensions. The reconstructed Wigner function is almost indistinguishable from the exact state. However, we made no Gaussian-state assumption in the reconstruction process nor did we use any fitting parameters. These are the major advantages of the described method. As a closing remark, we comment that solving a linear equation may not be a trivial task as it may sound when the size of the histogram becomes relatively large. Besides the burden of large computational resources, one must also take care of the numerical precision and the possible singular points in the transfer matrix, which can easily lead to strange results by changing slightly the parameters of the solver itself. The described method relies highly on the efficiency, accuracy, and robustness of the linear equation solver, which are yet to be improved in the future.

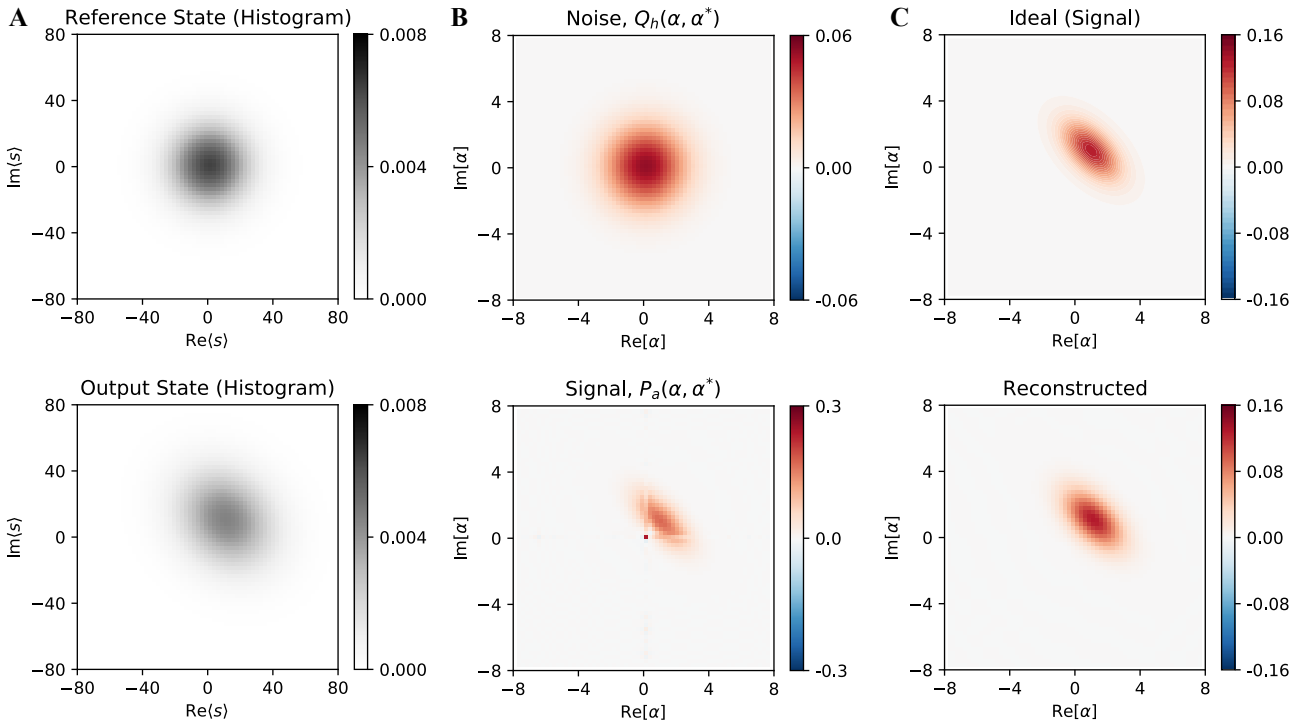

Figure 7.2. Tomography results via inverse linear transformation. **(A)** Histogram of the reference state and the output state. **(B)** From the two histograms, one can calculate the Q function of the noise field and then the P function of the input signal field. We note that the latter in this example may not be a properly behaved function because it is a non-classical state. However, it behaves reasonably well in numerics and does not destroy the following reconstruction process. **(C)** Finally, one can transform the obtained P function into the Wigner function, which is almost indistinguishable from that of the ideal input signal state.

7.2.2 Tomography via maximum likelihood estimation

Besides calculating the quasidistribution functions by solving a linear equation, one may also reconstruct the density matrix by using an optimization method. The key idea is to relate the measured histogram with a measurement operator, Π, such that the density operator can be obtained by using a similar MLE algorithm as introduced in Section 7.1. With this aim, we rewrite Eq. (7.14) as

$$\begin{aligned} Q_{\mathrm{s,out}}(\gamma,\gamma^*) &\approx \frac{1}{G}\mathrm{Tr}\left\{\frac{\rho_{\mathrm{s,in}}}{\pi}\int d\alpha^2 P_{\mathrm{n,in}}\left(\frac{\gamma^*}{\sqrt{G}}-\alpha^*,\frac{\gamma}{\sqrt{G}}-\alpha\right)|\alpha\rangle\langle\alpha|\right\} \\ &= \frac{1}{G}\mathrm{Tr}\left\{\frac{\rho_{\mathrm{s,in}}}{\pi}\int d\alpha^2 P'_{\mathrm{n,in}}\left(-\frac{\gamma}{\sqrt{G}}+\alpha,-\frac{\gamma^*}{\sqrt{G}}+\alpha^*\right)|\alpha\rangle\langle\alpha|\right\} \\ &= \frac{1}{G}\mathrm{Tr}\left\{\frac{\rho_{\mathrm{s,in}}}{\pi}D\left(\frac{\gamma}{\sqrt{G}}\right)\int d\beta^2 P'_{\mathrm{n,in}}(\beta,\beta^*)|\beta\rangle\langle\beta|D^\dagger\left(\frac{\gamma}{\sqrt{G}}\right)\right\} \\ &= \frac{1}{G}\mathrm{Tr}\left\{\frac{\rho_{\mathrm{s,in}}}{\pi}D\left(\frac{\gamma}{\sqrt{G}}\right)\rho'_{\mathrm{n,in}}D^\dagger\left(\frac{\gamma}{\sqrt{G}}\right)\right\}. \end{aligned} \tag{7.19}$$

Here, $\rho'_{\mathrm{n,in}}$ indicates the density matrix reconstructed from the histogram $Q^{(\mathrm{r})}_{\mathrm{s,out}}(-\gamma^*,-\gamma)$ [169]. Thus, the measurement operator can be written as

$$\Pi_\gamma = \frac{1}{G\pi}D\left(\frac{\gamma}{\sqrt{G}}\right)\rho'_{\mathrm{n,in}}D^\dagger\left(\frac{\gamma}{\sqrt{G}}\right). \tag{7.20}$$

One can prove that $\int d\gamma^2 \Pi_\gamma = \mathbb{1}$ [169, 198], which indicates that all the measurement operators, Π_γ, form a complete POVM (positive operator-valued measure) set. In the discrete case, the measurement operator can be written as

$$\Pi[n_1, n_2] = \frac{d\alpha^2}{\pi} D\left[n_1, n_2\right] \rho'_{\mathrm{n,in}} D\left[N - n_1, N - n_2\right], \tag{7.21}$$

with $d\alpha^2 \equiv (A/N)^2$. In this regard, the summation of the probability to record a measurement in each pixel, $p[n_1, n_2] = \sum_{n_1,n_2} \mathrm{tr}\left(\rho_{\mathrm{s,in}} \Pi[n_1, n_2]\right)$, is equal to the unity, i.e., $\sum_{n_1,n_2} p[n_1, n_2] = 1$. The summation of the discretized measurement operators, $T \equiv \sum_{n_1,n_2} \Pi[n_1, n_2]$, is not strictly identical to the identity operator, $\mathbb{1}$, for any finite N, but is close to $\mathbb{1}$ for a reasonably large N. In these regards, the iterative method for reconstructing the state can be described as [139, 199–204]

$$\rho_{\mathrm{s,in}}^{(k+1)} = T^{-1} R \rho_{\mathrm{s,in}}^{(k)} R T^{-1}, \tag{7.22}$$

where $\rho_{\mathrm{s,in}}^{(k)}$ is the kth MLE estimation of the input signal state, and

$$R = \sum_{n_1,n_2} \frac{d\alpha^2 Q_{\mathrm{s,out}}[n_1, n_2]}{p[n_1, n_2]} \Pi[n_1, n_2]. \tag{7.23}$$

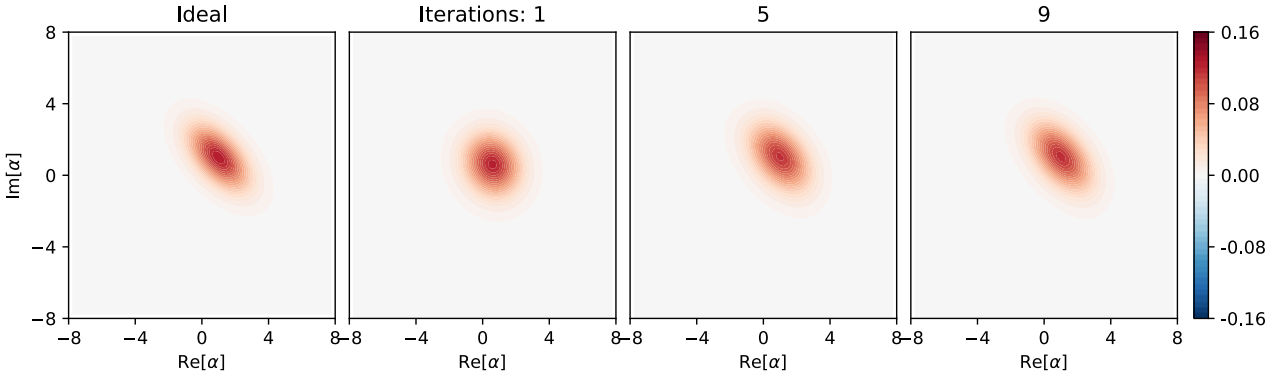

Figure 7.3. Tomography results via iterative MLE. With the increase of the iteration number, the MLE result converges to the exact state. At iteration steps 1, 5, and 9, the fidelities between the exact and the reconstructed state are 0.925, 0.994, and 0.998, respectively.

We also apply this iterative method to the same example introduced in Section 7.1. The initial guess, $\rho_{\mathrm{s,in}}^{(0)}$, is chosen as a thermal state with an average photon number of 2. The difference between the operator, T, and the identity operator, $\mathbb{1}$, is omitted for simplicity. As shown in Fig. 7.3, the prediction converges to the exact state with increasing number of iteration steps. A reasonably good estimation is obtained after 9 iteration steps, where the reconstructed state overlaps with the exact one with a fidelity of 0.998. However, we observe that the fidelity does not increase monotonically with the iteration number. It reaches a maximum of 0.999 after 12 iteration steps and decreases to 0.970 at the 30th iteration. This behavior may originate from the difference between T and $\mathbb{1}$, and the finite numerical accuracy of the algorithm. However, we should also comment that the method itself does not guarantee the convergence to the exact state [200–204]. In addition, the Hilbert space should be made large enough to ensure a successful reconstruction. Here, we truncate the maximum photon number to 100 for reconstructing the state with a mean photon number of 4.5. These observations indicate a tedious computation process and a fragile tomography result in real experiments. However,

the clear advantage is that the method requires no prior knowledge of the state to be constructed. Furthermore, the required computational resources are still significantly smaller than those for making a MLE of an arbitrary state with the measured signal moments (see Section 7.1).

7.3 Other methods for quantum state tomography

Besides, there are several other methods for quantum state tomography. We introduce two methods that are commonly seen in superconducting quantum circuits and also quantum optics. These methods may find useful applications in our future experiments.

7.3.1 Tomography with power-law detectors

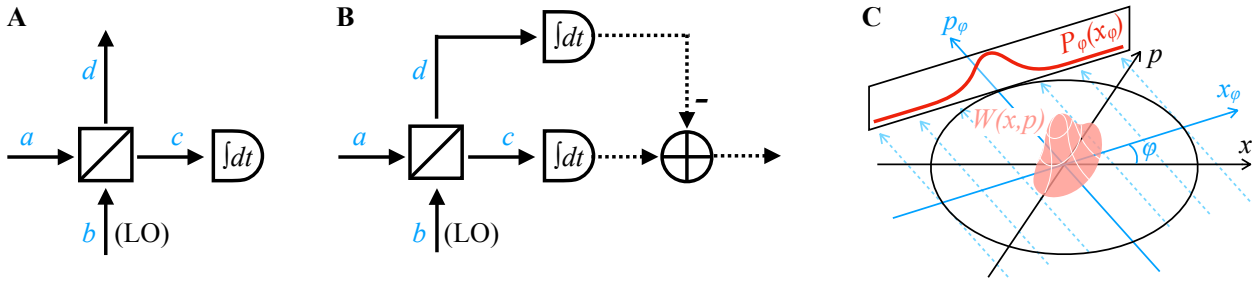

Figure 7.4. Schematic of the tomography process with power-law detectors. (A) The homodyne detection scheme, where a beam splitter with an almost unitary transmissivity ($t \to 1$) is used to measure the field quadrature, x_ϕ, at different angles ϕ. **(B)** The balanced homodyne detection scheme, which is in the same spirit as (A) but uses a 50 : 50 beam splitter. **(C)** The tomography process with power-law detectors. The measured probability distribution at different angles, ϕ, corresponds to the marginal probability distribution of the Wigner function projected along the orthogonal direction, $\phi + \pi/2$.

Instead of using linear detectors for heterodyne detection, it is more often in quantum optics to perform homodyne measurements with power-law detectors. The central component for the homodyne measurement is the beam splitter, as shown in Fig. 7.4A, which has the following input-output relation [49]

$$\begin{bmatrix} c \\ d \end{bmatrix} = \begin{bmatrix} \sqrt{t} & i\sqrt{1-t} \\ i\sqrt{1-t} & \sqrt{t} \end{bmatrix} \begin{bmatrix} a \\ b \end{bmatrix}, \tag{7.24}$$

where t is the power transmission coefficient of the beam splitter, a, b, c, and d describe the modes at the four different ports. The signal obtained by the power-law detector is proportional to the photon number, which is

$$\langle c^\dagger c \rangle = t\langle a^\dagger a \rangle + (1-t)\langle b^\dagger b \rangle + i\sqrt{t(1-t)}\langle a^\dagger b - b^\dagger a \rangle. \tag{7.25}$$

In ordinary homodyne detection, the transmission coefficient is close to the unity and the amplitude of LO signal is large enough to be described by a complex number β. Thus, we have [49]

$$\langle c^\dagger c \rangle \approx (1-t)\,|\beta|^2 - 2\sqrt{t(1-t)}\,|\beta|\,\langle X\,(\phi + \pi/2)\rangle, \tag{7.26}$$

where $X\,(\phi) = \left[a\exp(-i\phi) + a^\dagger \exp(i\phi)\right]/2$ and $\phi = \arg(\beta)$. Besides, we have assumed that the LO

reaching the detector dominates the signal field, i.e., $(1-t)\left|\beta\right|^2 \gg t\langle a^\dagger a\rangle$. In many experiments, it is advantageous to use a 50 : 50 beam splitter and to measure also the other output field of the beam splitter, $\langle d^\dagger d\rangle$, as shown in Fig. 7.4B. By subtracting the signals obtained by the two detectors, we have [49]

$$\langle c^\dagger c\rangle - \langle d^\dagger d\rangle = i\langle a^\dagger b - ab^\dagger\rangle \approx -2\left|\beta\right|\langle X\left(\phi+\pi/2\right)\rangle. \tag{7.27}$$

This method is called the balanced homodyne detection in the literature, which is found more robust than the single-detector case.

By choosing different values of the phase, ϕ, of the LO and repeat the measurement, one obtains the marginal probability density of the quadrature, $X\left(\phi+\pi/2\right)$, along different axis, as shown in Fig. 7.4C. More precisely, they obey the following relation [141, 204–206]

$$P_\phi\left(x_\phi\right) = \int dp_\phi W\left[\alpha - p_\phi\left(\sin\phi - i\cos\phi\right), \alpha^* - p_\phi\left(\sin\phi + i\cos\phi\right)\right]. \tag{7.28}$$

This formula projects the 2D Wigner function to a 1D histogram, which is similar to a CT (computer tomography) image in medical science [207]. To provide a better analogy, we write the above equation in a slightly different form

$$P_\phi\left(r\right) = \int dx \int dp W\left(x,p\right)\delta\left(x\cos\phi + p\sin\phi - r\right), \tag{7.29}$$

where $W\left(x,p\right) \equiv W\left(x+ip, x-ip\right)$. This function is known as the Radon transform of a 2D image. Taking the Fourier transform with regard to the variable r, we have

$$P_\phi\left(\omega\right) = \int dx \int dp W\left(x,p\right)\exp\left[-j2\pi\omega\left(x\cos\phi + p\sin\phi\right)\right] = W(\Omega_1,\Omega_2), \tag{7.30}$$

where $W(\Omega_1,\Omega_2)$ is the 2D Fourier transform of $W(x,p)$ with $\Omega_1 = \omega\cos\phi$ and $\Omega_2 = \omega\sin\phi$. The above equation is also called the central slice theorem in medical imaging [207]. Correspondingly, we have

$$\begin{aligned} W\left(x,p\right) &= \int d\Omega_1 \int d\Omega_2 W(\Omega_1,\Omega_2)\exp\left[j2\pi\left(x\Omega_1 + p\Omega_2\right)\right] \\ &= \int_0^{2\pi} d\phi \int_0^{\infty} d\omega\omega P_\phi(\omega)\exp\left[j2\pi\omega\left(x\cos\phi + p\sin\phi\right)\right] \\ &= \int_0^{\pi} d\phi \int_{-\infty}^{+\infty} d\omega|\omega| P_\phi(\omega)\exp\left[j2\pi\omega\left(x\cos\phi + p\sin\phi\right)\right] \\ &= \frac{1}{2\pi}\int_0^{\pi} d\phi \left(\frac{1}{\pi r} * \frac{\partial P_\phi(r)}{\partial r}\right)\Big|_{r=x\cos\phi+p\sin\phi}. \end{aligned} \tag{7.31}$$

Here, the convolution with $1/(\pi r)$ is also called the Hilbert transform.

For illustration, we apply this method to the same example as introduced in Sections 7.1 and 7.2. Here, we omit the gain and amplification noise for simplicity. The tomography results with different number of projection angles are shown in Fig. 7.5. Here, we choose $\phi = k\pi/N$ with $k = 0,\cdots,N-1$ and $N = 3, 9, 15$. As one may naively expect, the more angles we use to measure the marginal distributions, $P_\phi(r)$, the closer the reconstructed state is to the ideal state. For $N = 15$, one can hardly distinguish the Wigner functions of the exact and the reconstructed states. We note that one may also apply the compressed sensing technique [208–210] and use an even smaller number of

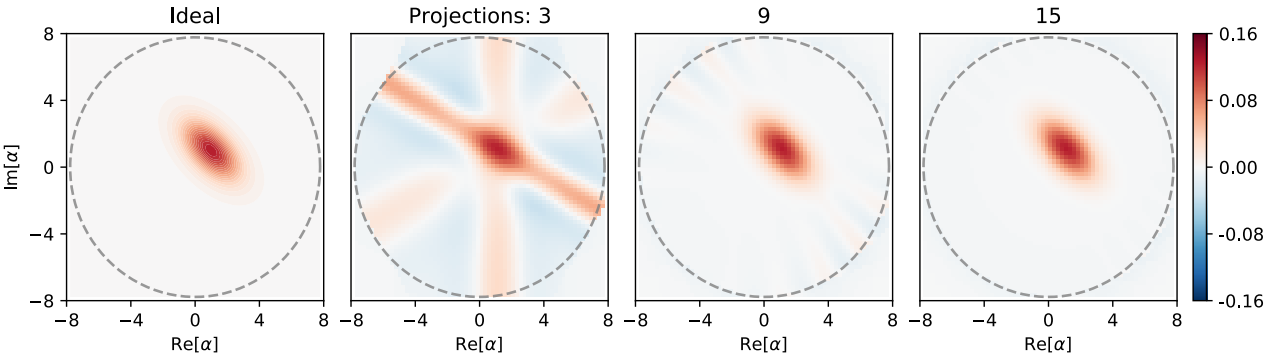

Figure 7.5. Tomography results with a power-law detector. With the increase of the measurement angles, the reconstructed Wigner function converges monotonically to the exact state. The reconstructed state is almost indistinguishable from the exact state with 15 projections.

projections for quantum state tomography [211–213]. These improvements should be considered in our future experiments.

Although the amplification noise has been omitted in our simulation, we comment that this is a reasonable assumption in practice. Because we are interested only in a single quadrature in the homodyne measurement, we can operate a parametric amplifier in the phase-sensitive mode where the amplification noise in the measured quadrature can be reduced to *zero* photon number [141]. This is the major advantage of the homodyne-based tomography over the heterodyne-based method, regardless of the difficulty in operating the parametric amplifier *in situ*. In addition, one may also consider using the single photon detectors, such as JPM (Josephson photomultiplier) [214–216] and others [217–225], which are operating at cryogenic temperatures to circumvent the amplification noise.

7.3.2 Tomography with a probe qubit

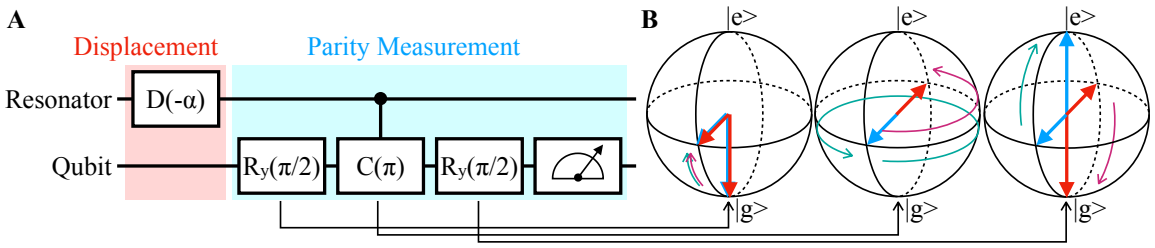

Figure 7.6. Schematic of the tomography process with a probe qubit. (A) To measure the Wigner function, $W(\alpha, \alpha^*)$, we first displace the resonator by $D(-\alpha)$ and then perform a parity measurement. The latter is implemented by using a probe qubit, which is initially prepared at the ground state and dispersively coupled to the resonator. After a Ramsey-type of measurement, i.e., a controlled phase gate, $C(\pi) = |g\rangle\langle g| + \exp\left(i\pi a^\dagger a\right)|e\rangle\langle e|$, sandwiched by two $\pi/2$-Y gates, $R_y(\pi/2) = \exp\left(-i\pi\sigma_y/4\right)$, the qubit is detected at the excited state if there is an even number of photons in the resonator. Otherwise, the qubit is in the ground state. This procedure is repeated by a large amount of times to obtain the parity. **(B)** Illustration of the three steps for the parity measurement on a Bloch sphere. Here, the blue (red) arrow indicates the evolution of the qubit state with an even (odd) number of photons in the resonator.

Instead of probing the microwave fields directly with the linear or power-law detectors, one may also use a qubit as the probe to measure the parity of the field [226–228], as shown in Fig. 7.6. This method originates from the observation that the characteristic function of the W representation, which

is introduced in Chapter 2, can be written in the form of the displacement operator [43, 44]

$$\chi_S(z, z^*) = \mathrm{tr}\left[\rho D\left(iz^*\right)\right], \tag{7.32}$$

such that the W representation is

$$W(\alpha, \alpha^*) = \mathrm{tr}\left[\frac{\rho}{\pi^2}\int d^2z e^{-iz^*\alpha^*} e^{-iz\alpha} D\left(iz^*\right)\right] = \mathrm{tr}\left[\frac{\rho}{\pi^2}\int d^2z e^{\alpha z^* - \alpha^* z} D\left(z\right)\right]. \tag{7.33}$$

To simplify the notation, we define $T(\alpha) = (1/\pi^2)\int d^2z e^{\alpha z^* - \alpha^* z} D(z)$, and thus $W(\alpha, \alpha^*) = \mathrm{tr}\left[\rho T(\alpha)\right]$. Recalling the properties of the displacement operator, we obtain

$$e^{\alpha z^* - \alpha^* z} D(z) = D(\alpha) D(z) D^\dagger(\alpha), \tag{7.34}$$

which indicates that $T(\alpha) = D(\alpha) T(0) D^\dagger(\alpha)$. On the other hand, one can verify that $T(0) = 2(-1)^{a^\dagger a}/\pi$. Thus, we have $T(\alpha) = 2D(\alpha)\exp\left(i\pi a^\dagger a\right) D^\dagger(\alpha)/\pi$, such that

$$W(\alpha, \alpha^*) = \frac{2}{\pi}\mathrm{tr}\left\{\left[D(-\alpha)\rho D^\dagger(-\alpha)\right]\exp\left(i\pi a^\dagger a\right)\right\}. \tag{7.35}$$

This result indicates that the Wigner function, $W(\alpha, \alpha^*)$, can be directly measured by first displacing the state by $D(-\alpha)$ and then measuring the parity, $\exp\left(i\pi a^\dagger a\right)$, of the photon number [226–234].

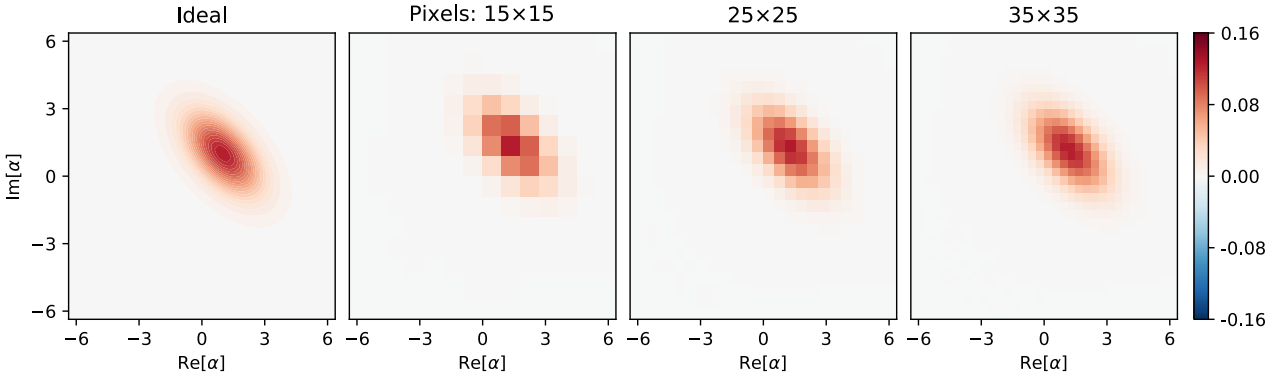

Figure 7.7. Tomography results with a probe qubit. With the increase of the pixel numbers, the resolution of the reconstructed Wigner function increases monotonically. The reconstructed state with 35×35 pixels is almost indistinguishable from the exact one.

We also apply the method to the same example as introduced in Section 7.1 and 7.2. Fig. 7.7 shows the tomography results with different number of displacement operations, which correspond to pixels in the tomography results and thus the resolution of the tomography results. By increasing the resolution, the reconstructed Wigner function shows more details and becomes closer to the exact result. In the particular example, the result with a pixel number of 35×35 has already reached a reasonably good state reconstruction. Despite the technical difficulty in coupling the resonator with the probe qubit and controlling the latter with high fidelity, one clear advantage of this method is that the amplification noise does not influence the tomography result. Moreover, it also requires no assumption on the state itself besides a rough estimation of the largest photon number. This property makes it particularly suitable for photonic state tomography in superconducting quantum circuits. However, we should also note that this method is generally only suitable for few-photon state reconstruction, because of the relatively large damping rate of a large photonic state [235, 236].

Part IV:
QUANTUM SIMULATION WITH NONLINEAR OSCILLATORS

*credit Metro-Goldwyn-Mayer

Chapter 8

QUANTUM BEHAVIOR OF DUFFING OSCILLATOR AT DISSIPATIVE PHASE TRANSITION

8.1 Introduction

The Duffing oscillator is a well-known model system in physics. It describes a driven oscillator with a cubic nonlinearity and a linear viscous damping [237]. In a certain parameter regime, classical mechanics predicts a double-well potential which allows two possible steady states (SSs) at the same parameter setting. This gives rise to hysteretic behavior when changing the system parameters, and the fact that the systems state depends on the starting conditions [238]. Thermal fluctuations may induce random jumps between the two potential wells and lead to the unpredictable phenomenon of bistability. The non-deterministic behavior of a Duffing oscillator has been observed in a considerable number of experiments, for example, in superconducting quantum circuits [239, 240]. The underlying double-well potential model has been successfully used to explain a variety of physical processes, such as optical bistability [241, 242], parametric amplification [3, 243], and self-oscillation [244, 245]. However, it has been revealed by Drummond and Walls already in the 1980s that a fully quantum-mechanical treatment of the Duffing oscillator yields only a single unique SS over the entire parameter space, which "does not exhibit bistability or hysteresis" [246]. The two perspectives indicate fundamentally different dynamics of a Duffing oscillator. However, only the classical behavior have been reported in the literature until recently. Important experimental milestones include observing intriguing phenomena in the transmission spectrum [247, 248], decay rate [249], and second-order optical correlation [250] at a specific parameter setting in a continuous-wave measurement setup.

Here, we study the quantum and non-equilibrium behavior of a Duffing oscillator with tunable nonlinearity in a pulsed heterodyne measurement setup. By our experiments we reconcile the seeming controversy between the classical and quantum treatments of the Duffing oscillator. In particular, we demonstrate that the two classical SSs are in fact metastable states (MSs), which emerge when the low-laying eigenvalues of the Liouvillian superoperator are separated from the rest of the spectrum [251]. In a certain parameter regime, the MSs have a lifetime much longer than any other time scales in the system but are not the exact SS solutions of the Schrödinger equation. An exceptional case occurs when the system approaches a thermodynamic limit with an infinite number of photons [252]. In this case, the MSs gain an increasingly long lifetime when approaching a critical point but, suddenly, cannot be properly defined at the exact point [253]. This non-analytical phenomenon is defined as a first-order dissipative phase transition (DPT), which originates from the interplay between a coherent drive and an incoherent dissipation in a driven-dissipative system.

8.2 Theory

8.2.1 Quantum and classical descriptions of a Duffing oscillator

As introduced in Chapter 3, we write the Hamiltonian of a nonlinear superconducting resonator as

$$H_{\mathrm{s}}/\hbar = \omega_{\mathrm{A}} a^{\dagger} a + U_{\mathrm{A}} a^{\dagger} a^{\dagger} a a. \tag{8.1}$$

Here, a and $a^{\dagger}$ are the annihilation and creation operators for the intracavity field with resonant frequency ω_{A} and nonlinearity U_{A}. Following the input-output formalism given in Chapter 5, we write the dynamics of the system in the rotating frame at the driving frequency, ω_{d}, as

$$\dot{a}(t) = -i\Delta a(t) - i2U_{\mathrm{A}} a^{\dagger}(t) a^{2}(t) - \frac{\gamma}{2} a(t) - \xi. \tag{8.2}$$

Here, $\Delta = \omega_{\mathrm{A}} - \omega_{\mathrm{d}}$ is the frequency detuning between the resonator and the driving field, γ is the total energy dissipation rate of the resonator mode. We have assumed that the input field, b_{in}, is a relatively strong coherent field such that we can use a complex number to represent the driving strength, $\xi = -i\sqrt{\kappa_{\mathrm{c}}}\langle b_{\mathrm{in}} \rangle$, where κ_{c} is the coupling rate between the resonator and the driving field. According to Ref. [246], all orders of optical moments of the SS can be written in a compact form

$$\langle a^{\dagger j} a^{k} \rangle = d^{*j} d^{k} \frac{\Gamma(c)\Gamma(c^{*}) {}_0\mathcal{F}_2 \left(k + c, j + c^{*}, 2\left|d\right|^2 \right)}{\Gamma(k + c)\Gamma(j + c^{*}) {}_0\mathcal{F}_2 \left(c, c^{*}, 2\left|d\right|^2 \right)}, \tag{8.3}$$

where $c = \left(\Delta - i\gamma/2\right)/U_{\mathrm{A}}$, $d = -\xi/U_{\mathrm{A}}$, ${}_0\mathcal{F}_2\left(x, y, z\right) = \sum_{n=0}^{\infty} \Gamma(x)\Gamma(y) z^{n} / \left[\Gamma(x + n)\Gamma(y + n) n!\right]$ is the generalized hypergeometric function, and $\Gamma(\,\cdot\,)$ is the gamma special function. This formula indicates that the optical moments are single valued in the entire parameter space, such that "(it) does not exhibit bistability or hysteresis" [246]. Theoretical calculations also indicate a rather compact form of the unique SS [254]

$$W\left(\alpha, \alpha^{*}\right) = \mathcal{N} e^{-2|\alpha|^2} \left| \frac{\mathcal{J}_{c-1}\left(\sqrt{-8d\alpha^{*}}\right)}{\left(\alpha^{*}\right)^{\frac{c-1}{2}}} \right|^2, \tag{8.4}$$

where $\mathcal{N}$ is a normalization factor, and $\mathcal{J}_{c-1}(\,\cdot\,)$ is a $(c-1)$th-order Bessel function of the first kind. This expression is equivalent to

$$W\left(\alpha, \alpha^{*}\right) = \mathcal{N}' e^{-2|\alpha|^2} \left| {}_0\mathcal{F}_1\left(c, 2d\alpha^{*}\right) \right|^2, \tag{8.5}$$

where $\mathcal{N}'$ is a different normalization factor, and ${}_0\mathcal{F}_1(x, z) = \sum_{n=0}^{\infty} \Gamma(x) z^{n} / \left[\Gamma(x + n) n!\right]$ is the hypergeometric function.

If we take the mean value of the Langevin equation and neglect the photon correlations in the third-order term, i.e., $\langle a^{\dagger}(t) a^{2}(t) \rangle \to \alpha^{*} \alpha^{2}$, we obtain the classical EOM of a Duffing oscillator

$$\dot{\alpha}(t) = -i\Delta\alpha(t) - i2U_{\mathrm{A}} \alpha^{*}(t) \alpha^{2}(t) - \frac{\gamma}{2}\alpha(t) - \xi(t). \tag{8.6}$$

Following the discussions in Appendix D, one can prove that this equation is equivalent to the so-called Duffing equation under a rotating wave approximation (RWA). The SS solution of the Duffing

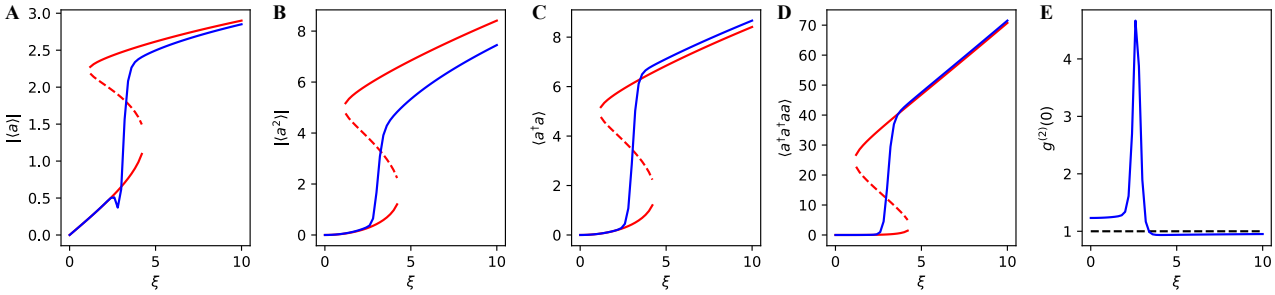

Figure 8.1. Comparison of the optical moments calculated by the quantum and classical theories. **(A)** – **(D)** Shown are the absolute value of $\langle a \rangle$ and $\langle a^2 \rangle$, and the value of $\langle a^\dagger a \rangle$ and $\langle a^\dagger a^\dagger a a \rangle$, respectively. The quantum-mechanical $|\langle a \rangle|$ curve shows a dip around the transition point, which has a quantum-mechanical origin. The $|\langle a^2 \rangle|$ curve shows a clear difference between the quantum and classical results, which indicates a squeezing effect. **(E)** The second-order correlation function, $g^{(2)}(0)$, is strongly peaked around the transition point. The value of $g^{(2)}(0)$ is slightly larger or smaller than 1 for a sufficiently small or large driving strength ξ, respectively. In all panels, the blue and red solid curves correspond to quantum and classical SS solutions, respectively. The red dashed line indicates the unstable classical SS solution, which is usually neglected in the literature because of its instability.

equation obeys the following form

$$4U_{\mathrm{A}}^2|\alpha|^6 + 4\Delta U_{\mathrm{A}}|\alpha|^4 + \left[\Delta^2 + \left(\frac{\gamma}{2}\right)^2\right]|\alpha|^2 - \xi^2 = 0. \tag{8.7}$$

Depending on different parameter settings, either one, two, and three solutions of $|\alpha|^2$ are allowed according to the classical theory (see Appendix D for detail). This observation is in stark contrast to the quantum mechanical analysis, where a single unique SS solution is predicted throughout the parameter space. The stability of the system can be verified by checking whether $\partial|\xi|^2/\partial|\alpha|^2 > 0$ [246]. At the boundaries of the bistability regime, we have

$$|\alpha|^2 = \frac{-2\Delta \pm \sqrt{\Delta^2 - 3\,(\gamma/2)^2}}{6U_{\mathrm{A}}}, \tag{8.8}$$

which, in combination with Eq. (8.6), can be used to draw the two boundaries of the bistability regime in the ξ-Δ space, as shown in Section 8.4. It indicates that the bistability exists only in the regime $\Delta^2 > 3\,(\gamma/2)^2$, where the system is described by a double-well potential [238]. Outside this parameter regime, the potential has only a single minimum and there exists only a single unique SS solution [238]. Depending on whether the driving strength is smaller or larger than either of the two bistability boundaries, the single well is approximately localized at one of the two minima of the double-well potential. This observation leads to the method of initial state preparation, as will be introduced in Section 8.3.

To illustrate the difference between the quantum and classical theories of the Duffing oscillator, we compare the resulting optical moments, as shown in Fig. 8.1A-D. The simulation parameters are chosen as $\Delta = 5$ and $U_{\mathrm{A}} = 0.5$ normalized by γ. Generally speaking, the moments predicted by the two theories qualitatively agree with each other. However, one major difference is that the quantum-mechanical results are single-valued functions of the control parameter ξ without hysteresis or bistability. Furthermore, the $|\langle a \rangle|$ curve as a function of ξ shows a clear dip around the transition, which is not observed in the other optical moments, such as the $|\langle a^\dagger a \rangle|$ curve. The origin of the dip

has been theoretically explained as the out-of-phase quantum fluctuations of two MSs, which is an indication of the quantum interference effects [246]. In addition, the quantum-mechanical prediction of $|\langle a^2\rangle|$ is well below the classical prediction. This indicates a squeezing effect that cannot be captured by the classical theory. Moreover, one can also calculate the *zero*-time second-order correlation function, $g^{(2)}(0) = \langle a^\dagger a^\dagger a a\rangle / \langle a^\dagger a\rangle^2$, from the two moments, $\langle a^\dagger a\rangle$ and $\langle a^\dagger a^\dagger a a\rangle$, as shown in Fig. 8.1E. The $g^{(2)}(0)$ curve is strongly peaked around the transition point, but approaches approximately unity at a large driving strength. A more careful calculation indicates that the system stays in a nonclassical state with $g^{(2)}(0)$ slightly smaller than *one* after the transition. These features can be used as evidences for distinguishing the quantum and classical mechanics of a Duffing oscillator, which are going to be measured in Section 8.4.

8.2.2 Liouvillian spectrum, metastability, and dissipative phase transition

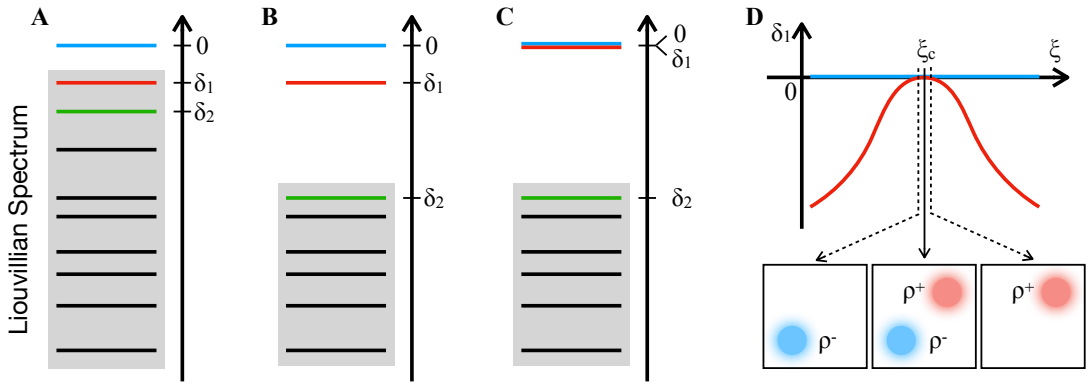

Figure 8.2. The Liouvillian spectrum and the sketch of a first-order DPT. (A) The Liouvillian spectrum of a normal system, where there exists a single eigenvalue *zero*. The smallest non-*zero* eigenvalue, corresponding to the Liouvillian gap δ_1, defines a characteristic time, $1/\delta_1$, of the system. **(B)** When $\delta_1 \ll \delta_2$, there exists a gap in the spectrum such that a quantum metastability phenomenon emerges. **(C)** The Liouvillian gap δ_1 can be made sufficiently small in finite systems and even *zero* at a thermodynamic limit. By definition, the closure of Liouvillian gap leads to a first-order DPT. **(D)** Sketch of a first-order DPT, where the Liouvillian gap closes at the critical point ξ^*. The system stays at $\rho^\mp$ right before or after the transition, where $\rho^+ \neq \rho^-$ correspond to the two phases of the system. For a finite system, the SS at the critical point is $(\rho^+ + \rho^-)/2$.

From the Langevin equation in Eq. (8.2), we extract the effective Hamiltonian as

$$H_{\text{eff}}/\hbar = \Delta a^\dagger a + U_{\text{A}} a^\dagger a^\dagger a a + \xi\left(a + a^\dagger\right). \tag{8.9}$$

In the Schrödinger picture, the dynamics of the system is described by the master equation in the Linblad form $\dot{\rho} = \mathcal{L}\rho$ (see Chapter 2 for detail). Here,

$$\mathcal{L}(\cdot) = -\frac{i}{\hbar}\left[H_{\text{eff}}, (\cdot)\right] + \frac{\gamma}{2}\mathcal{D}[a], \tag{8.10}$$

$$\mathcal{D}[a](\cdot) = 2a(\cdot)a^\dagger - a^\dagger a(\cdot) - (\cdot)a^\dagger a, \tag{8.11}$$

are called the Liouvillian and Lindblad superoperators, respectively.

When restricting our discussion to finite dimensions, the Liouvillian superoperator can be

decomposed into Jordan blocks that lead to the formal solution [251]

$$\rho(t) = \exp(t\mathcal{L})\rho(0) = \sum_n \exp(t\lambda_n) \left(\sum_m c_{n,m} r_{n,m} \right). \tag{8.12}$$

Here, $c_{n,m} = \mathrm{tr}\left[l_{n,m}\rho(0)\right]$, $l_{n,m}$ and $r_{n,m}$ are the left and right eigenmatrices of $\mathcal{L}$, which correspond to the nth eigenvalue with geometric multiplicity m, i.e., λ_n for $n = 0, 1, \cdots$. For convenience, we define $\delta_n = |\mathrm{Re}\,(\lambda_n)|$ and sort the eigenvalues according to $\delta_n < \delta_{n+1}$. All values of δ_n form a discrete spectrum called the Liouvillian spectrum [253], as schematically shown in Fig. 8.2A.

Under quite general conditions, there exists a single unique SS solution such that $\delta_0 = 0$, $\delta_1 > 0$ [255]. Thus, the smallest nonzero eigenvalue, forming the Liouvillian gap, δ_1, determines the time scale the system requires to relax back into the SS solution, and thereby results in a general exponential decay of the observables. However, an interesting two-stage relaxation phenomenon happens if the Liouvillian gap is well separated from the rest of the spectrum, $\delta_1 \ll \delta_2$, as schematically shown in Fig. 8.2B. Although the single exponential decay remains in the long-time limit, the system may quickly relax into the metastable manifold spanned by $r_{0,1}$ and $\{r_{1,m}\}$ within a time scale of $1/\delta_2$, and then stays almost invariant for a relatively large timescale, $1/\delta_1$, before a second relaxation to the unique SS solution [251]. This phenomenon is called quantum metastability, and the states of the system at $1/\delta_2 \ll t \ll 1/\delta_1$ are called the metastable states (MS). Depending on the value of the Liouvillian gap, the lifetime of the MSs may be remarkably larger than any other time scale in the system. However, the MSs evidently are not the exact SS solution of the system such that they must decay into the SS for $t \to \infty$.

If the system allows a single unique SS solution, the Liouvillian gap must be a non-zero value throughout the entire parameter space. However, this observation does not prohibit the gap from bring infinitesimally small. In particular, the Liouvillian gap may close at some specific value of the control parameter in the thermodynamical limit [253]. In this situation, as schematically shown in Fig. 8.2C, the eigenvalue *zero* has a geometric multiplicity of two but an algebraic multiplicity of one. The SS solution must undergo a sudden change on the two sides of the critical point and result into a phase transition [253]. This phenomenon is called a first-order DPT, which is a quantum and non-equilibrium phase transition in a driven-dissipative nonlinear system. For illustration, let us consider a system with no degeneracy in λ_1. The system around the phase transition point can be described as $\rho(\xi) = r_0(\xi) + e^{t\lambda_1} c_1 r_1(\xi)$ for $1/\delta_2 \ll t \ll 1/\delta_1$. We define the SS solution just before and after the transition point as $\rho(\xi^* \pm \delta) = \rho^{\pm}$, where δ is an infinitely small perturbation around ξ^*, as shown in Fig. 8.2D. On the one hand, for any non-*zero* δ, we have $r_0(\xi^* \pm \delta) = \rho^{\pm}$. One may infer that $r_0(\xi^*) = \left(\rho^+ + \rho^-\right)/2$ because of the continuity argument. On the other hand, the SS must be on the manifold spanned by $\rho^{\pm}$ at the exact transition point, $\xi = \xi^*$. According to the requirement $\mathrm{tr}\left[r_1(\xi)\right] = 0$, we have $r_1(\xi^*) \propto \rho^+ - \rho^-$ [253]. If we also assume $r_1(\xi)$ to be continuous around ξ^*, these two observations yield the remarkable result that $\rho^{\pm}$ are MSs around the transition point. The SS at the exact transition point is an equiprobable mixture of the two MSs, $\rho(\xi^*) = \left(\rho^+ + \rho^-\right)/2$, for any finite system size, which, however, cannot be properly defined in the exact thermodynamic limit.

8.2.3 Thermodynamic limit and the Bose-Hubbard lattice

For the Duffing oscillator, a well defined thermodynamic limit is obtained when $|\xi| \to \infty$ while $U_{\mathrm{A}}\xi^2$ remains a constant [252, 253]. We define $U_{\mathrm{A}} = U_0/N$ and $\xi = \sqrt{N}\xi_0$, where U_0 and ξ_0 are constants and

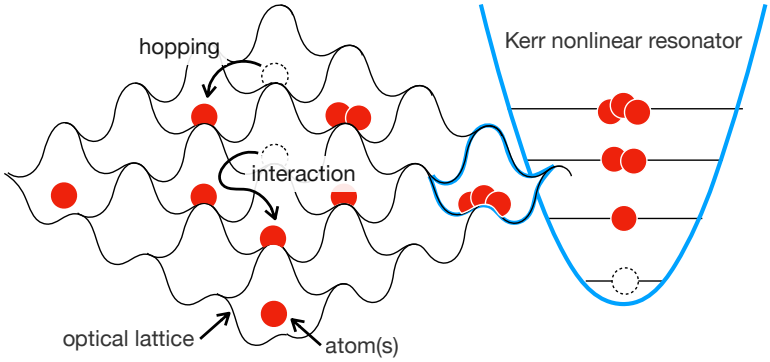

Figure 8.3. The schematic of a Bose-Hubbard lattice. The atoms are distributed over a photonic lattice. They can tunnel though the lattice barrier to the adjacent sites (hopping), or get repelled from one lattice site if there are already a finite number of atoms on one site (on-site interaction, repulsive or attractive). For each single lattice site (blue), the atomic field can be described by a Kerr nonlinear resonator. The latter can be further described as a Duffing oscillator if one considers also the drive and dissipation.

N is a scaling factor. Here, without loss of generality, we define $U_0 = \gamma$ for $N = 1$. With the increase of N, the system is increasingly close to a thermodynamic limit. This thermodynamic limit may be understood in two aspects. On the one hand, the Langivin equation, Eq. (8.2), is almost independent of N if we rescale the operators as $a \to a/\sqrt{N}$. For a sufficiently large N, the commutation relation $\left[a, a^\dagger\right] \to 1/N$ becomes negligible such that the field operators, a and $a^\dagger$, can be fairly regarded as classical complex variables, α and α^*. On the other hand, let us consider a Bose-Hubbard lattice, as shown in Fig. 8.3, with the following Hamiltonian

$$H/\hbar = \sum_{j=0}^{N-1} \omega_0 a_j^\dagger a_j + U_0 a_j^\dagger a_j^\dagger a_j a_j + \xi_0 \left(a_j + a_j^\dagger\right) + \sum_{(j,k)} g_0 \left(a_j^\dagger a_j + a_j a_k^\dagger\right). \tag{8.13}$$

Here, $a_j^\dagger$ is a bosonic creation operator which generates an atom on the jth site, ω_0 is the chemical potential on each lattice site, U_0 is the strength of the on-site interaction, g_0 is the hopping rate between nearest-neighbor sites (j, k), and ξ_0 is the strength of a global driving field that acts homogeneously at all the lattice sites. One can prove that the mean field of this manybody Hamiltonian is equivalent to that of the effective Hamiltonian given in Eq. (8.9), with the correspondence $\omega_\mathrm{A} = \omega_0 + 2g_0$, $U_\mathrm{A} = U_0/N$, and $\xi = \sqrt{N}\xi_0$. Here, we apply the transformation $\sum_{j=0}^{N-1} e^{-i2\pi kj/N} a_j/\sqrt{N} \to a_k$ and keep only the $k = 0$ term in the spirit of RWA [252]. In this regard, one may interpret the scaling factor N as the number of sites in a Bose-Hubbard lattice, and make a correspondence between a single Duffing oscillator and the mean field of an N-site Bose-Hubbard lattice in the driven-dissipation regime. In a thermodynamic limit, the quantum statistical properties of a single Duffing oscillator corresponds to the mean field statistics of an infinitely large Bose-Hubbard lattice, i.e., the Bose-Hubbard model, which is one of the most fundamental models in condensed matter physics with an extremely rich phase diagram [256–262].

8.3 Experimental methods

The schematic of the experimental procedure is shown in Fig. 8.4. We modulate the radio-frequency driving field by three different pulse shapes, which prepare the system in either of the two potential wells or in the SS at the initial time. Then, the driving strength is switched to ξ, and we trigger

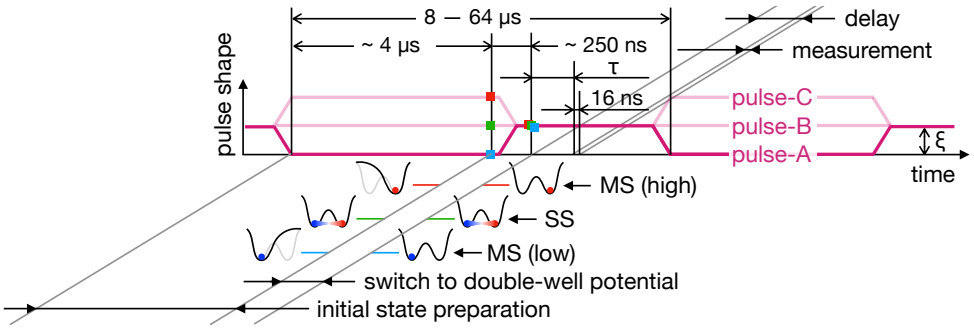

Figure 8.4. The schematic of the pulsed heterodyne measurement protocol . We prepare the initial state of system in either of the two potential wells by driving it with either a *zero*-amplitude (pulse-A) or a high-intensity field (pulse-C). Then, the driving strength is switched to ξ and lasts for a controllable time τ before performing a 16 ns quadrature measurement. This procedure is repeated for more than 10^6 times to accumulate a histogram of the field quadratures. In certain experiments, we also drive the system with a constant driving field with driving strength ξ (pulse-B), which prepares the system in the SS at the initial time.

a measurement after a time delay of τ. In each repetition, the measurement lasts for only 16 ns to capture the transient dynamics of the system. We repeat this procedure for approximately 10^6 – 10^9 times depending on different types of measurement, and concatenate the results into a long trace for further DSP. Eventually, we obtain the snapshots of the quasidistribution functions of the intra-resonator field for different initial states and also different control parameters, Δ, ξ, and τ.

The sample and the cryogenic setup have been introduced in Chapter 3. Moreover, the characterization of the closed-system parameters and the method of tuning the nonlinearity were introduced in Chapter 4. The characterization of the energy dissipation and the dephasing rates have been determined in Chapter 5. The room-temperature setup and the measurement method were described in Chapter 6, where we also characterize the intra-resonator photon number and the driving strength. Finally, a general recipe for quantum state tomography was summarized in Chapter 7.

8.4 Results and analysis

8.4.1 Quantum fluctuations in hysteresis

We first tune the system parameter to achieve a resonant frequency of $\omega_A/2\pi = 7.00\,\text{GHz}$ and a nonlinearity of $U_A/2\pi = -132\,\text{kHz}$. We drive the the system with a varying strength, ξ, and frequency with detuning, Δ. The measurement is delayed by $\tau = 3.25\,\mu\text{s}$, which is more than 10 times larger than the free-relaxation time of the resonator, $1/\gamma$ (the characterized value is $\gamma \approx 3.85\,\text{MHz}$, see Chapter 5). When the system is initially prepared in either of the two wells, the absolute mean field, $|\langle a\rangle|$, and the photon number, $\langle a^\dagger a\rangle$, show a transition at either of the two classical boundaries of the bistability regime, as shown in Fig. 8.5A. Within this regime, the measured values are also different for the same parameter setting, which can be attributed to the two classical SSs in a double-well potential. However, the transition occurs inside the bistability regime with a constant driving field, which corresponds to an infinitely large measurement delay in either of the former cases. Classically, this is explained by the presence of thermal fluctuations that induce random jumps between the two potential wells, and wash out the dependence on the initial-state for large τ. However, this interpretation fails in our experimental situation where the thermal noise is much smaller than half a photon and is thus not likely to cause a noticeable transition between the two wells. Similar phenomena are also observed at

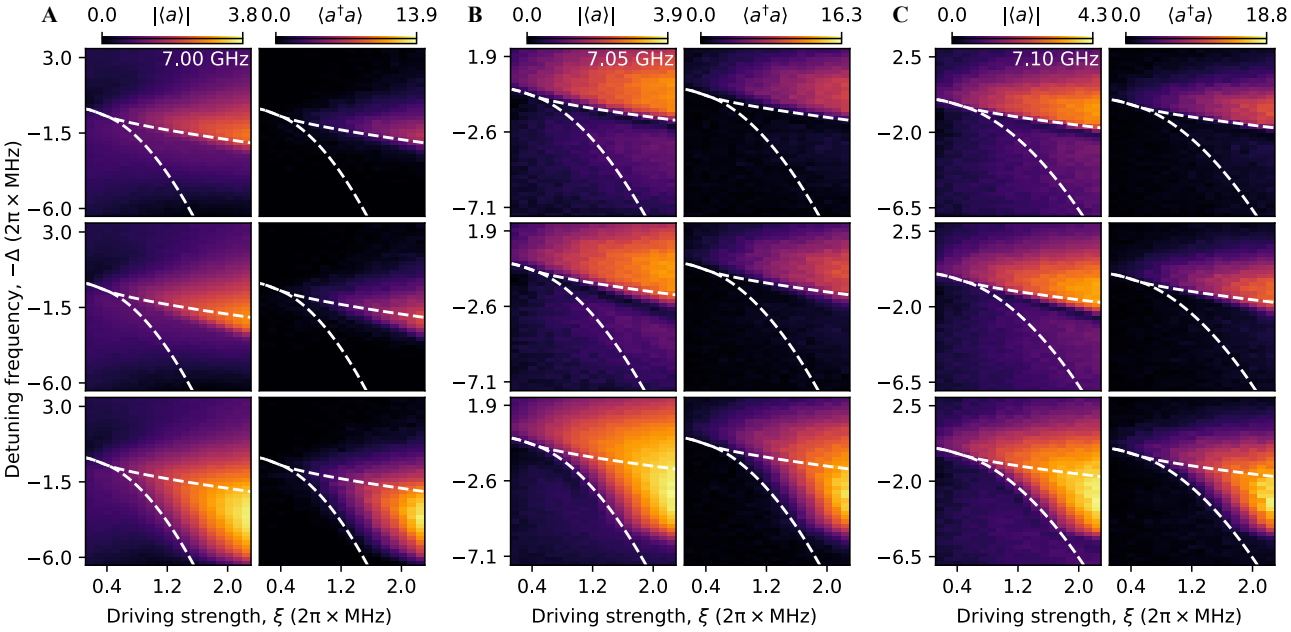

Figure 8.5. Power-frequency sweeps showing classical hysteretic behavior. Depending on the initial state, the absolute field mean, $|\langle a\rangle|$, and photon number, $\langle a^\dagger a\rangle$, show a clear difference in the bistability regime enclosed by the dashed lines. A drastic change happens at either of the two boundaries if the system is initially prepared in one well (upper and lower), while it resides inside the bistability regime for a constant driving field (middle). The boundaries are calculated from the classical theory with no fitting parameter. Panels **(A)-(C)** correspond to the measurement results at different resonant frequencies, $\omega_A/2\pi = 7.00\,\text{GHz}$, 7.05 GHz, and 7.10 GHz, respectively.

different resonant frequencies, as shown in Fig. 8.5B-C for $\omega_A/2\pi = 7.05\,\text{GHz}$ and 7.10 GHz.

Indeed, quantum fluctuations play a significant role in the transition process. This allows us to interpret the classical SSs as two MSs with a remarkably long lifetime around the transition point. The specific MS, in which the systems is staying, is determined by the initial condition. Fig. 8.6A shows the transition curves for different initial states at a fixed detuning frequency, $\Delta/2\pi = 1.86\,\text{MHz}$. Here, the resonant frequency is set as $\omega_A/2\pi = 7.00\,\text{GHz}$, which is the same as Fig. 8.5A. We observe a clear dip in the $|\langle a\rangle|$ curve around the ξ value marking the transition from a lower to a higher value, which originates from the out-of-phase quantum fluctuations between the two MSs [246–248]. By comparison, $\langle a^\dagger a\rangle$ is a monotonic function of ξ since it is insensitive to the phase of quantum fluctuations. Moreover, the normalized second-order correlation function, $g^{(2)}(0)$, is strongly peaked around the transition point and converges to the unity for large ξ. This correlation peak is a typical signature of a first-order DPT, resulting from the enhanced quantum fluctuations around the transition point [246, 250]. Similar phenomena are also observed at different detuning frequencies, as shown in Fig. 8.5B-C for $\Delta_A/2\pi = 2.36\,\text{MHz}$ and 2.86 MHz.

8.4.2 Two-stage relaxation of metastable states

According to the quantum theory, the MSs exist only in the time window $1/\delta_2 \ll \tau \leq 1/\delta_1$ and should eventually relax into the single unique SS for $\tau \gg 1/\delta_1$. We then fix the detuning frequency to $\Delta/2\pi = 2.01\,\text{MHz}$ and measure the reflection response, S_{22}, with a varying driving strength, ξ, and measurement delay, τ. Here, the nonlinearity is characterized as $U/2\pi = -71\,\text{kHz}$. Similar to the results in Fig. 8.6, the reflection coefficients, corresponding to the two MSs, form a closed loop in phase space for each fixed τ (Fig. 8.7A-B). However, the loop exists in a smaller range of ξ around the

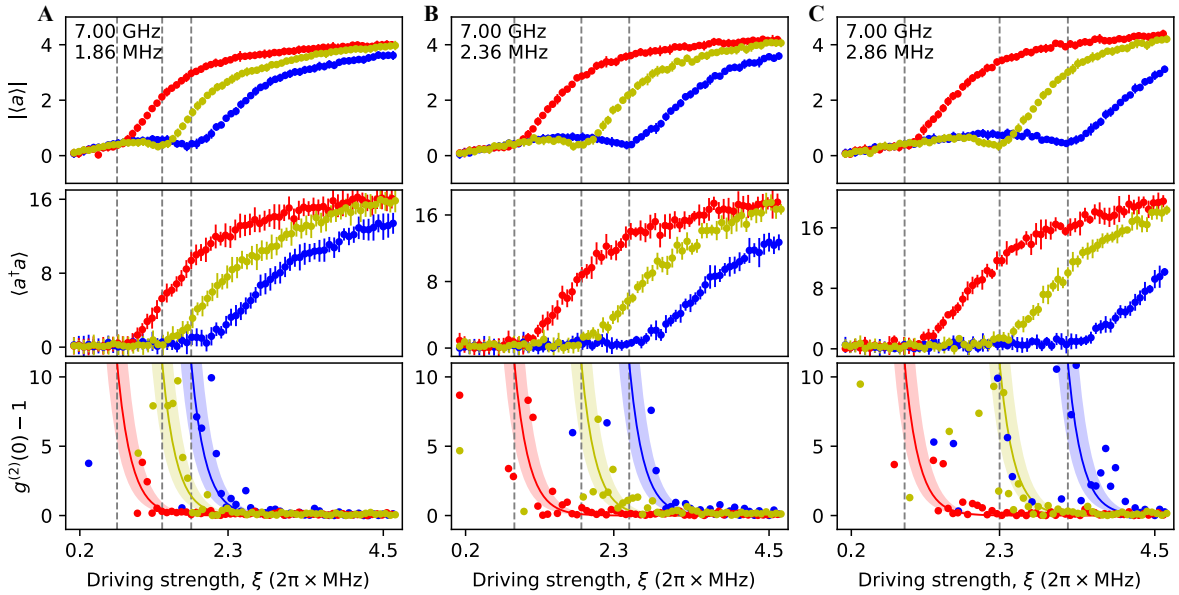

Figure 8.6. Power sweep reveals quantum fluctuations. At a fixed detuning frequency, the $|\langle a\rangle|$ curve as a function of ξ shows a dip around the transition point (dashed), while $\langle a^\dagger a\rangle$ is a monotonic function of ξ. The $g^{(2)}(0)$ is also strongly peaked around the transition point, which converges to 1.0 for large ξ. Here, the solid lines are drawn to guide the eye. Panels **(A)-(C)** correspond to the measurement results at different detuning frequencies, $\Delta/2\pi \approx 1.86\,\text{MHz}$, $2.36\,\text{MHz}$, and $2.86\,\text{MHz}$, respectively. In all the panels, the blue, yellow, and red colors correspond to the pulse shape A, B, and C, respectively, as shown in Fig. 8.4. The error bars represent the standard deviation over 8 independent experiments.

transition point, $\xi^*/2\pi \approx 1.5\,\text{MHz}$, with the increase of τ. The loop is expected to be fully closed after $55\,\mu\text{s}$, where the two MS branches converge to the single unique SS allowed by quantum mechanics. This observation provides a clear evidence for the validity of the quantum description of a Duffing oscillator. It predicts that the hysteretic behavior observed in Fig. 8.5 is the measurement outcome of two different MSs, while the system should eventually converge to the single unique SS for $\tau \to \infty$.

To quantify this convergence, we numerically calculate the loop area for different τ, as shown in Fig. 8.7C. The exponential fit of the data indicates two distinctively different decay rates at a small or large τ, respectively (fitted values $0.742\,\text{MHz}$ and $0.039\,\text{MHz}$, respectively). This two-stage relaxation process is qualitatively different from the classical prediction [263], but can be well understood from the quantum theory of the Liouvillian spectrum [249, 264]. Fig. 8.7D shows the Liouvillian gap, δ_1, as a function of the driving strength, ξ, which is extracted from the time-domain measurement, as shown in Fig. 8.7E-F. The gap is approximately $3.788\,\text{MHz}$ at a small or large ξ, which agrees with the energy decay rate γ. However, it decreases by more than two orders of magnitude around the critical point, ξ^*, and achieves a minimum of $0.023\,\text{MHz}$. This observation indicates a critical slowing down of the system dynamics when approaching a critical point where the Liouvillian gap almost closes. This is another typical signature of a first-order DPT [248]. For a sufficiently small τ, the decay rate of the loop area is determined by the mean of the Liouvillian gap over the bistability regime of ξ, that is, $1.216\,\text{MHz}$. However, it is dominated by the minimum gap when $\tau \to \infty$. In the time window between the two extreme cases, the decay rate decreases monotonically with τ and connects the two extremes, which shows a qualitative agreement with the two-stage relaxation, as shown in Fig. 8.7C.

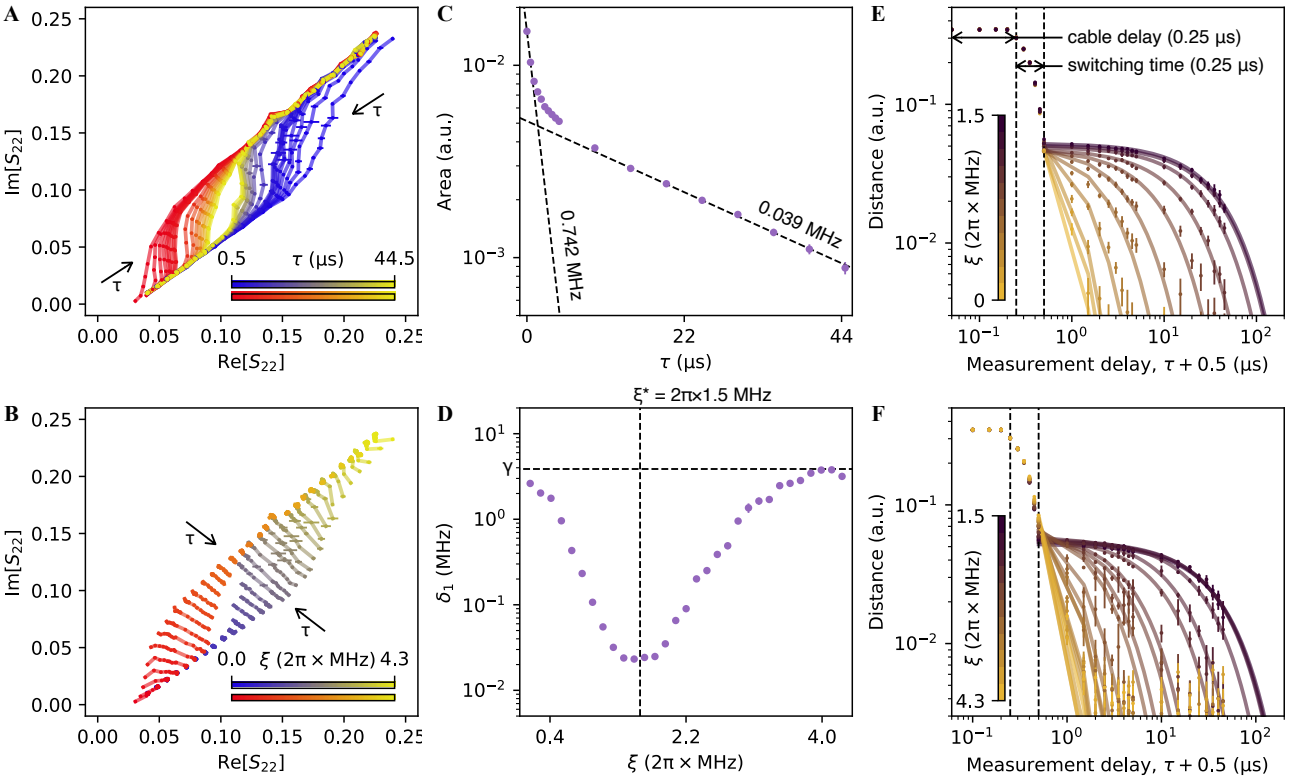

Figure 8.7. Two-stage relaxation of the MSs towards the single unique SS. (A) The reflection coefficients, S_{22}, corresponding to the two MS branches form a closed loop (blue and red), which converges to the unique SS solution with increasing τ. **(B)** The convergence of the two MSs at each fixed ξ. **(C)** The loop area decays with τ and shows two distinct time scales. The dashed lines show the exponential fits of the decay rate at either a small or large τ with fitted values 0.742 MHz and 0.039 MHz, respectively. **(D)** The Liouvillian gap, δ_1, is approximately equal to the total energy dissipation rate, γ, at a sufficiently small or large ξ (dashed). However, it decreases by more than two orders of magnitude when approaching the critical point, $\xi^*/2\pi = 1.5$ MHz, and achieves a minimum value of 0.023 MHz. **(E)-(F)** The raw data for extracting the Liouvillian gap, where the solid curves correspond to the exponential fits. In all the panels, the error bars represent the standard deviation over 16 independent experiments.

8.4.3 A first-order dissipative phase transition

It is then natural to ask whether the Liouvillian gap can be engineered to *zero* for a particular parameter setting, where the system dynamics becomes infinitely slow and the two MSs become also SSs. This expectation is in conflict with the uniqueness of the SS solution for a quantum-mechanical Duffing oscillator [246]. However, multiple SSs can exist in a driven-dissipative Bose-Hubbard model, where an infinite number of identical Duffing oscillators are coupled to each other and form an infinitely large lattice [265]. A bridge between the mean field description of an N-site Bose-Hubbard lattice and a single Duffing oscillator may be constructed by rescaling the nonlinearity and driving strength of the later as U_0/N and $\sqrt{N}\xi_0$ [252], as introduced in Section 8.2. Without loss of generality, we define $U_0 \equiv -\gamma$ for $N = 1$. a thermodynamic limit of the Duffing oscillator can be achieved at the limit $N \to \infty$, where the Liouvillian gap is closed at a critical point, ξ^*, and results into a first-order DPT.

In our experiment, we tune the resonant frequency from $\omega_A/2\pi = 6.80$ GHz to 7.15 GHz, and measure the absolute mean field, $|\langle a \rangle|$, and photon number, $\langle a^\dagger a \rangle$, of the SS with a varying driving strength, ξ, and detuning frequency, Δ. Correspondingly, the nonlinearity varies from $U/2\pi = -295$ kHz to -58 kHz. The measurement results are summarized in Fig 8.8A-H. This setup

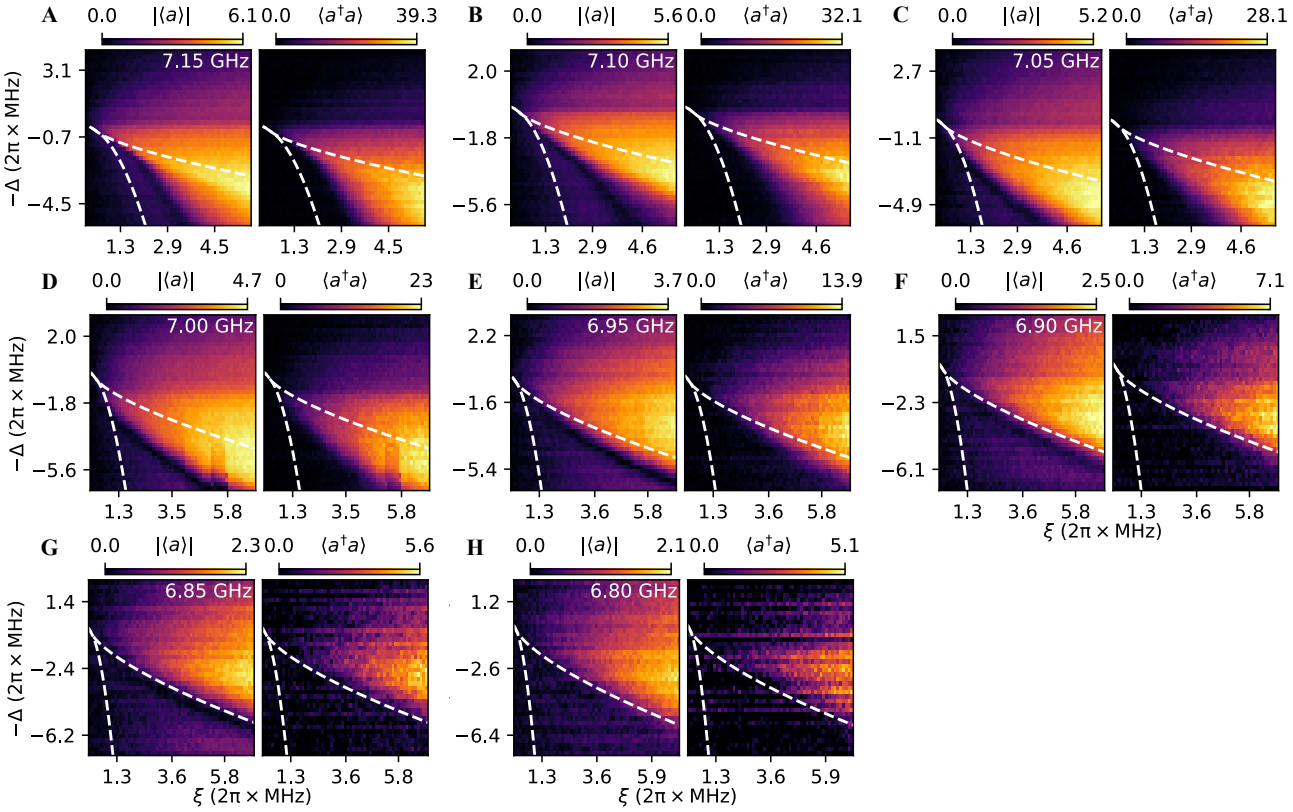

Figure 8.8. Absolute mean field, $|\langle a\rangle|$, and photon number, $\langle a^\dagger a\rangle$, plotted versus the detuning and the driving strength at different resonant frequencies. By tuning the resonant frequency to different values, and correspondingly the nonlinearity, we engineer the scaling factor N from 1.9 to 10.6 and approach a thermodynamic limit. Panels **(A)**-**(H)** correspond to the measurement results at different resonant frequencies, $\omega_A/2\pi = 7.15\,\text{GHz}$, $7.10\,\text{GHz}$, $\cdots$, $6.80\,\text{GHz}$, respectively.

allows the quantum simulation of a Bose-Hubbard lattice from approximately 2 to 11 sites.

To reveal the first order DPT, we fix the detuning at $\Delta = 3.0\gamma$, and compare the photon number transition curves as a function of the rescaled driving strength, ξ_0, (Fig. 8.9B). For different N, the transition happens at the same rescaled critical driving strength, $\xi_0^*/2\pi = 0.58\,\text{MHz}$, and the photon density also saturates at a similar value of around $\langle a^\dagger a\rangle/N = 3.1$. However, the transition becomes increasingly sharp with N, which indicates a sudden jump for $N \to \infty$. In this limit, the lifetime of the MSs diverges at the critical point, and results into a sudden change of the SS on the two sides of ξ^* [253]. The system thus explores two separate phases around the critical point. This observed tendency exists only in the quantum mechanical description. Most importantly, it is a direct proof of a first-order DPT. Similar phenomena are also observed at different detuning frequencies, as shown in Fig. 8.9A and C for $\Delta = 2.5\gamma$ and 3.5γ.

8.4.4 Microscopic picture of the phase transition

To understand the underlying physics of the phase transition, we reconstruct the Wigner quasidistribution function of the intra-resonator field. On the one hand, theoretical model presented in Section 8.2 yields the exact Wigner function as

$$W(\alpha, \alpha^*) = \mathcal{N}' e^{-2|\alpha|^2} \left|{}_0\mathcal{F}_1\left(c, 2d\alpha^*\right)\right|^2, \tag{8.14}$$

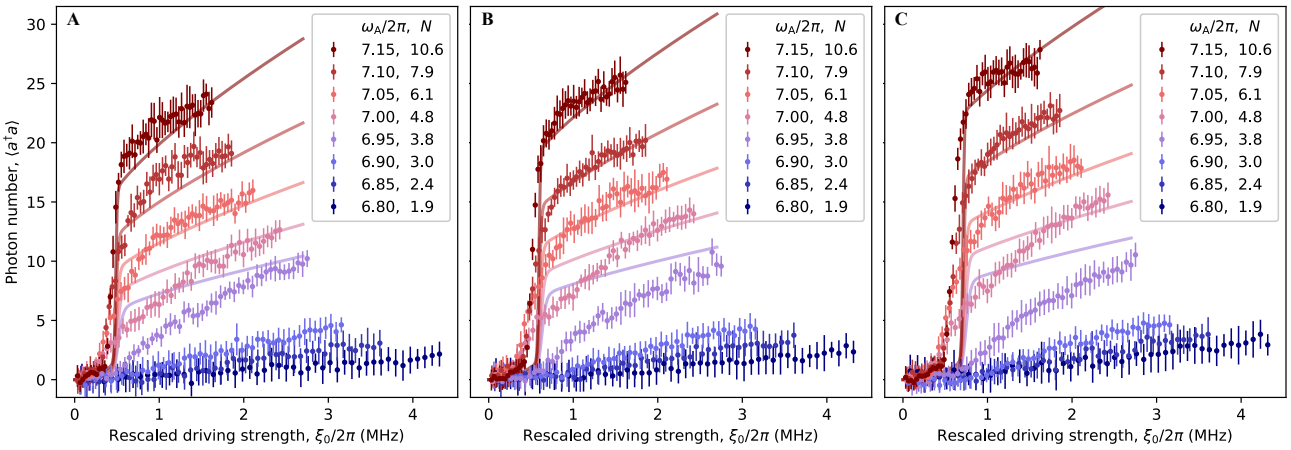

Figure 8.9. Plots of the photon number versus the rescaled driving strength showing an increasingly sharp photon number transition with the scaling factor N. When approaching to a thermodynamic limit, the observed step of the $\langle a^\dagger a \rangle$ becomes increasingly sharp, indicating a first-order DPT. Panels **(A)-(C)** correspond to the measurement results at different detuning frequencies, $\Delta = 2.5\gamma$, 3.0γ, and 3.5γ, respectively. In all panels, the error bars represent the standard deviation over 8 independent experiments. The solid lines are calculated from the quantum theory with no fitting parameter. The deviation between theory and experiment becomes increasingly large at lower resonant frequencies, which we attribute to the increasingly large dephasing rate when tuning the DC flux of the SQUID away from its sweet spot.

where $\mathcal{N}'$ is a normalization factor, ${}_0\mathcal{F}_1(x,z) = \sum_{n=0}^{\infty}\Gamma(x)z^n/\left[\Gamma(x+n)n!\right]$ is a hypergeometric function, and $\Gamma(\,\cdot\,)$ is the gamma special function. The Wigner function can be fully determined by determining the value of the two parameters $c = (\Delta - i\gamma/2)/U_\mathrm{A}$ and $d = -\xi/U_\mathrm{A}$. On the other hand, these two parameters can be determined by measuring the optical moments (see also Section 8.2)

$$\langle a^{\dagger j} a^k \rangle = d^{*j} d^k \frac{\Gamma(c)\Gamma(c^*)\,{}_0\mathcal{F}_2\left(k+c, j+c^*, 2\left|d\right|^2\right)}{\Gamma(k+c)\Gamma(j+c^*)\,{}_0\mathcal{F}_2\left(c, c^*, 2\left|d\right|^2\right)}, \tag{8.15}$$

where ${}_0\mathcal{F}_2\left(x,y,z\right) = \sum_{n=0}^{\infty}\Gamma(x)\Gamma(y)z^n/\left[\Gamma(x+n)\Gamma(y+n)n!\right]$ is a generalized hypergeometric function. We thus combine Eqs. (8.14) and (8.15) to find the best fit of the Wigner function according to the first two orders of optical moments, $\langle a \rangle$, $\langle a^\dagger a \rangle$, and $\langle a^2 \rangle$. We would like to point out that the described procedure relies on a priori knowledge of the SS and thus lacks general objectivity. Alternative methods, such as coupling a probe qubit to the resonator [231, 232] as introduced in Chapter 7, may provide a more objective tomography result than ours. However, we see that we are able to reveal the non-classical feature of the SS during the transition with a simple physical model, and obtain a consistent agreement between theory and experiment among independent measurements.

To minimize the influence of the dephasing effect, we operate the SQUID at its sweep spot by tuning the resonant frequency to $\omega_\mathrm{A}/2\pi = 7.15\,\mathrm{GHz}$ with a nonlinearity of $U/2\pi = -295\,\mathrm{kHz}$. The detuning is fixed at $\Delta = 3\gamma$. The first three orders of optical moments are shown in Fig. 8.10A-F. The experimental results agree excellently with the analytical predictions of Eq. (8.15) without using any fitting parameter. It thus allows us to extract the values of c and d from the measured optical moments, and reconstruct the Wigner function of the system by inserting the fitted values into Eq. (8.14). Because c is a complex number and d is real, one needs at least the information of the two moments, $\langle a \rangle$ and $\langle a^\dagger a \rangle$, to unambiguously determine the two parameters. Here, we take also the value of $\langle a^2 \rangle$ into account, what makes the fitting problem overdetermined and thus increases the

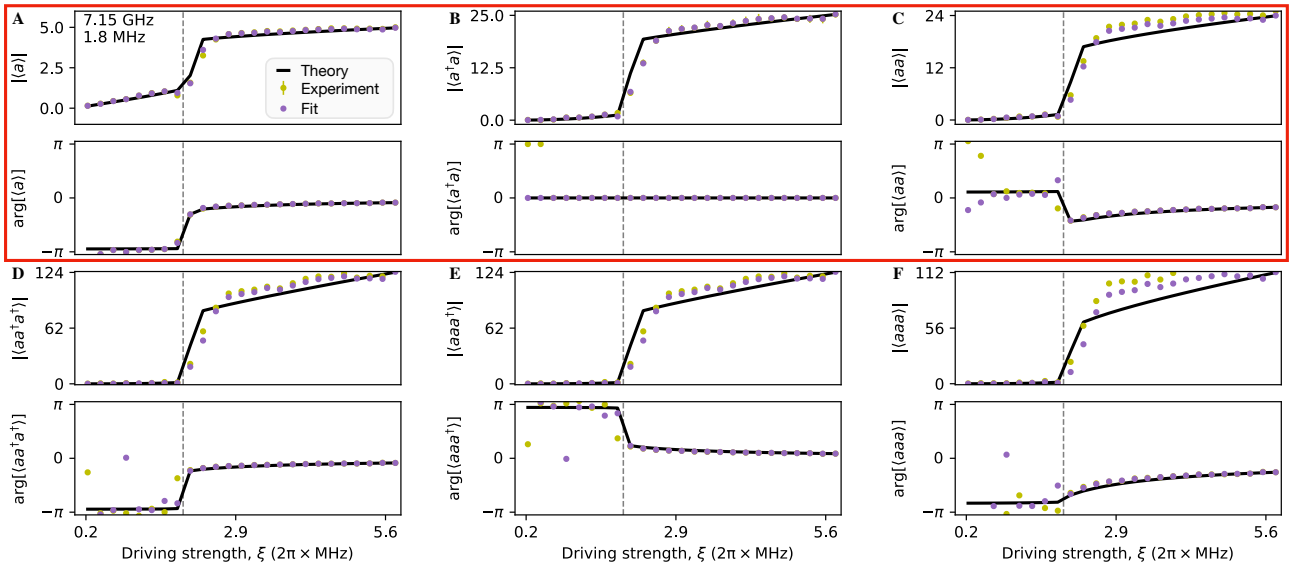

Figure 8.10. The first three orders of optical moments plotted versus the driving strength. The measured amplitude and phase of the optical moments show an excellent agreement to the theoretical prediction in Eq. (8.3), which guarantees the correctness of quantum state tomography. Panels **(A)-(F)** correspond to the optical moments, $\langle a\rangle$, $\langle a^\dagger a\rangle$, $\langle a^2\rangle$, $\langle aa^{\dagger 2}\rangle$, $\langle a^2a^\dagger\rangle$, $\langle a^3\rangle$, respectively. The error bars in (A) and (B) represent the standard deviation over 8 independent experiments, while it is not recorded in other panels. The first two orders of moments, enclosed by the red boxed, will be used for quantum state tomography.

reliability of the tomography result.

Figure 8.11 shows the tomography result. The reconstructed SS is approximately a coherent or a squeezed state in the two phases of the Duffing oscillator [266], while their field mean coincides with the two classical SSs in a double-well potential [252]. In each individual phase, the SS remains almost invariant with respect to the rescaled driving strength, ξ_0. However, the system undergoes a drastic change in a relatively small range around the critical point, $0.52\,\mathrm{MHz} \leq \xi_0/2\pi \leq 0.64\,\mathrm{MHz}$, which results into the rapid photon number transition as shown in Fig. 3. In this regime, the Wigner function consists of two parts which are separate in phase space and correspond, respectively, to the two phases. The probability of being in the coherent phase changes continuously to that of being in the squeezed phase with increasing ξ_0. It reaches a equiprobable mixture of the two phases at the exact critical point, ξ_0^* [253].

8.4.5 The two phases of phase transition

Because the SSs in the two phases are approximately coherent and squeezed states [266], as shown in Fig. 8.11, we use a Gaussian function to describe them and calculate the corresponding squeezing levels. As introduced in Chapter 2, a Gaussian state is a rotated, squeezed, and displaced thermal state

$$\rho_{\mathrm{G}} = D(\alpha)S(\zeta)R(\phi)\rho_T R^\dagger(\phi)S^\dagger(\zeta)D^\dagger(\alpha), \tag{8.16}$$

where $D(\alpha)$, $S(\zeta)$, and $R(\phi)$ are the displacement, squeeze, and rotation operators, respectively. The squeezing level can be defined as [267]

$$S = -20\,|\zeta|\log_{10}(e). \tag{8.17}$$

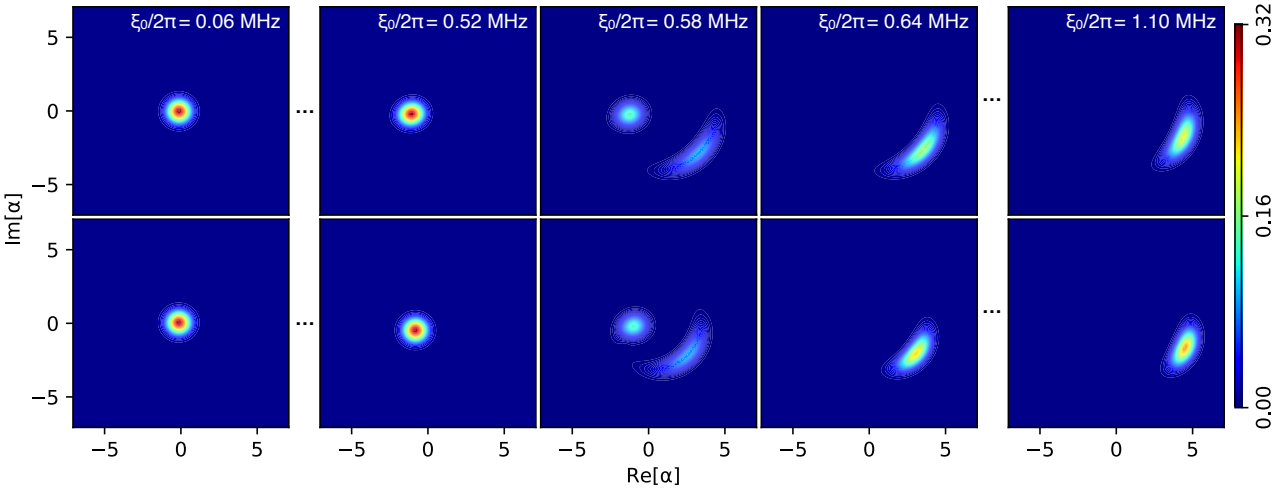

Figure 8.11. Wigner function of the SS during the phase transition. Shown are theory (top) with no fitting parameter and experiment (bottom) measured at $\omega_A/2\pi = 7.15\,\mathrm{GHz}$, where the dephasing rate is negligible small. The SS is approximately a coherent (squeezed) state before (after) the phase transition, which defines the two phases of a Duffing oscillator. The transition between the two phases happens in a relatively small range, $0.52\,\mathrm{MHz} \leq \xi_0/2\pi \leq 0.64\,\mathrm{MHz}$, during which the SS has two separate parts in the phase space and is a mixture of the two phases. It reaches a equiprobable mixture of the two phases at the exact critical point, $\xi_0^*/2\pi = 0.58\,\mathrm{MHz}$.

Following the derivations in Chapter 7, we have

$$\tanh\left(2\left|\zeta\right|\right) = \frac{\langle a^2\rangle - \langle a\rangle^2}{\langle a^\dagger a\rangle + 1/2 - \left|\langle a\rangle\right|^2}. \tag{8.18}$$

One can thus calculate the squeezing level of the two phases according to the first two orders of optical moments, $\langle a\rangle$, $\langle a^\dagger a\rangle$, and $\langle a^2\rangle$.

Fig. 8.12 shows the squeezing level of the system as a function of the driving strength. The critical point, ξ^*, separates the system into two different phases with drastically different squeezing levels. The value of S is approximately *zero* before the phase transition, but jumps to approximately 3 dB after the transition. This observation defines the two phases of the system and supports the existence of a first-order DPT. We note that the Gaussian-state approximation breaks down around the critical point, where the SS is a mixture of the two phases, as shown in Fig. 8.11. One can thus understand the dip of $|\langle a\rangle|$ and also the peak of $g^{(2)}(0)$ around the critical point, as shown in Fig. 8.6A-C, as a result of the interference between the coherent and squeezed parts. With the increase of N, the photon number approaches to the infinity and the system behaves more and more classically. The SS thus must jump at ξ^* in a thermodynamic limit, because only one potential well can be occupied at the same time in a classical system. This observation explains the increasingly steep transition of $\langle a^\dagger a\rangle$ with N, as shown in Fig. 8.9A-C, and reveals the origin of the first-order DPT.

8.4.6 Discussion of dephasing effects

So far, we have neglected dephasing effect in the discussion. This is feasible because the determined dephasing rate, γ_ϕ, is smaller than the energy dissipation rate, γ, in the frequency range of interest (see Chapter 5 for the characterization results). It is also justified by the fact that we obtain excellent agreement between theory and experiment for all the first three orders of optical moments, as shown in Fig. 8.10. However, this agreement exists only at high resonant frequencies. As can be observed in

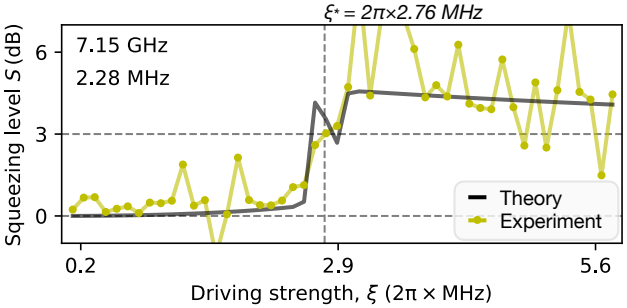

Figure 8.12. The squeezing level as a function of the driving strength. The critical point, $\xi^*/2\pi = 2.76\,\mathrm{MHz}$, separates the system into two different phases with drastically different squeezing levels S. The value of S is approximately *zero* before the transition, indicating a coherent phase of the system. After the transition, the squeezing level is approximately 3 dB, corresponding to a squeezed phase. Here, we fine-tune the estimated resonant frequency to $\omega_\mathrm{A}/2\pi = 7.148\,\mathrm{GHz}$, and the detuning frequency is $\Delta/2\pi = 2.76\,\mathrm{MHz}$. We correct the power gain, G, by $-1.2\,\mathrm{dB}$ according to the photon number difference between theory and experiment.

Fig. 8.9, the experimentally observed transition curve is less steep than that predicted by the model at lower frequencies. As discussed in Section 3.3, we attribute the reduced steepness to the dephasing effect, since the dephasing rate increases when going to lower frequencies.

To achieve a quantitive understanding of the experimental data, we add a dephasing term in the master equation, i.e., Eq. (8.11), and consider also a finite temperature of the bath

$$\partial_t \rho(t) = -\frac{i}{\hbar}\left[H_\mathrm{eff}, \rho(t)\right] + \frac{\gamma}{2}\left(n_\mathrm{T}+1\right)\mathcal{D}\left[a\right]\rho(t) + \frac{\gamma}{2} n_\mathrm{T}\mathcal{D}\left[a\right]\rho(t) + \frac{\gamma_\phi}{2}\mathcal{D}\left[a^\dagger a\right]\rho(t). \tag{8.19}$$

Here, the Lindbladian superoperator $\mathcal{D}\left[a^\dagger a\right]$ describes the dephasing effect. The value of the energy relaxation and the dephasing rates, γ and γ_ϕ, have been determined in Chapter 5.

Figure 8.13 compares the measured optical moments with the simulation results. Compared with the ideal Duffing model, where $\gamma_\phi \equiv 0$, a finite dephasing rate, γ_ϕ, successfully captures the observed smaller steepness of the transition. Here, we have considered a small thermal photon occupation number of the environment, $\bar{n}_T = 0.1$. However, a closer inspection on the second-order moment, $|\langle a^2\rangle|$, indicates that γ_ϕ also leads to a significantly smaller saturation value of this quantity. To achieve a better fitting between the simulation and the experiments, one may consider adding the second-order processes into the simulation. Here, we consider the two-photon drive, $\xi_2\left(a^2 + a^{\dagger 2}\right)$, and corresponding loss, $(\gamma_2/2)\,D\left[a^2\right]$. These higher-order processes should be weak, such that the parameters, ξ_2 and γ_2, are assumed to be smaller than ξ and γ, respectively. We achieve a quantitive agreement between theory and experiment for $\xi_2 = 0.3\xi$ and $\gamma_2 = 0.1\gamma$. These results demonstrate that we are able to achieve a consistent understanding of our experimental results with a simple physical model. We emphasize that the conclusions are either insensitive to the dephasing rate, such as the hysteretic behavior in Fig. 8.5, or drawn from the high-frequency measurements where the dephasing rate is negligibly small, such as the tomography results in Fig. 8.11.

8.5 Conclusions

The observed quantum behavior of the Duffing oscillator promote the view that the observed hysteresis and bistability originate from a non-classical SS around a critical point, which consists of two separate parts in phase space. These two parts correspond to the two phases of the system, which are identified

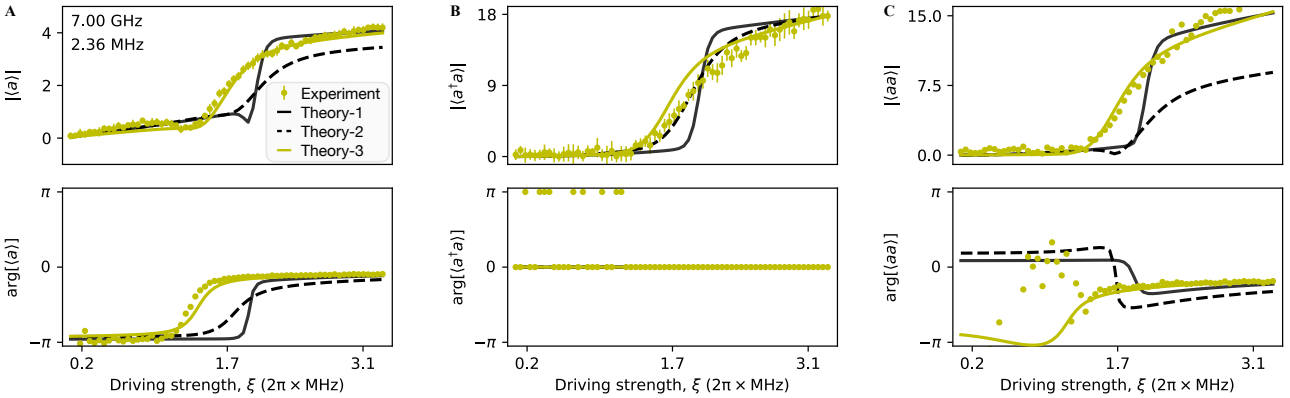

Figure 8.13. Comparison between experimental and numerical results for the first two orders of optical moments. The yellow dots represent the experimental results, which are identical to the curve shown in Fig. 8.6B. The error bars represent the standard deviation over 8 independent experiments. The black solid curves show the analytical result in Eq. (8.3), where only energy dissipation is considered (Theory-1). The dashed black line shows the master equation simulation results, including dephasing effect and a finite thermal photon number of the environment. It captures the the slower transition rate observed in experiment (Theory-2). We also consider a weak two-photon drive and loss process in the model (Theory-3, yellow solid), which provides a good agreement with the experimental results.

as MSs with a remarkably long lifetime. Their lifetime diverges when approaching a thermodynamic limit and results in a first-order DPT, which mimics a sudden change of the mean field in the Bose-Hubbard model. The tunable superconducting resonator investigated in this thesis is a versatile building block for quantum simulation [268–270], and the pulsed measurement plays an indispensable role in revealing the non-equilibrium dynamics. We expect this toolbox serves as a stepping stone for understanding the non-equilibrium physics in a general driven-dissipative system and unveiling the mystery of the "butterfly effect" from a quantum-mechanical perspective.

Chapter 9

TOWARDS A SUPERCONDUCTING BOSE-HUBBARD QUANTUM SIMULATOR

With the knowledge of the quantum statistical properties of a single Duffing oscillator, a natural continuation of this thesis is to coupled two or even more Duffing oscillators together and explore the quantum statistical properties of microwave radiation in a lattice. In the literature, such system implements a N-site Bose-Hubbard lattice [261, 262] which contains extremely rich physics, such as boson crystallization [271], gas-liquid phase transition [272], and fermionized photons [273]. As can be seen in Chapters 3 and 4, our sample consists two coupled nonlinear resonators with in-situ tunability, and thus provides a minimum realization of the Bose-Hubbard lattice, also known as the Bose-Hubbard dimer. Besides the aforementioned proposals, a large number of experiments focused on the Bose-Hubbard dimer can also be arranged. However, as is revealed in Chapter 5, the Q-factor of the first resonator is way smaller than the second one as we have used in Chapter 8 for quantum simulation. Moreover, as is revealed in Chapter 6, the relatively huge amplification noise of the HEMT amplifier in the output path, OUT 1, makes it difficult to reveal the quantum statistical properties of the first resonator. Moreover, our test experiments with two-coupled resonators (not shown) request a fundamental improvement of both the sample quality and the stability of the cryostat. Furthermore, adding more resonators in the system may also require a change of the method for revealing the photon statistics, as discussed in Chapter 7. To this end, here we summarize several research proposals for the two-resonator system with simulation results, which may be experimentally studied in the future.

9.1 Unconventional photon blockade

The photon blockade is a non-classical phenomenon in quantum optics, where a particular system can accommodate only a single photon at the same time. Appropriate systems rely on a strongly nonlinear medium such that the transition from the first to the second excited states, $|1\rangle \rightarrow |2\rangle$, is forbidden if the driving field is resonant with the transition between the energy levels, $|0\rangle$ and $|1\rangle$ [156, 157, 274–280], as shown in Fig. 9.1A (left). This effect has been experimentally observed in various platforms and leads to the invention of a single-photon source [281–285]. However, it remains a technical challenge to further improve the blockade efficiency, which requires a remarkably large nonlinearity. By comparison, unconventional photon blockade takes advantage of the hopping between two cavities to suppress the photon accumulation, which requires only a negligibly small nonlinearity [286–291], as shown in Fig. 9.1A (right). For example, if one drives only the first cavity, the two feasible transitions paths, $|1,0\rangle \rightarrow |2,0\rangle$ and $|1,0\rangle \rightarrow |0,1\rangle \rightarrow |1,1\rangle \rightarrow |2,0\rangle$, can destructively interfere with each other in a certain parameter regime such that the population in $|2,0\rangle$ can be completely suppressed. This phenomenon has been observed in recent experiments in quantum dots [292] and also in superconducting quantum circuits in an indirect way [145]. Our goal is to reveal the microscopic picture of the unconventional blockade effect by full quantum state tomography, and use the Bose-Hubbard dimer to generate single microwave photons.

Here, we simulate the *zero*-time second-order correlation function, $g_{11}^{(2)}(0)$, of the driven resonator

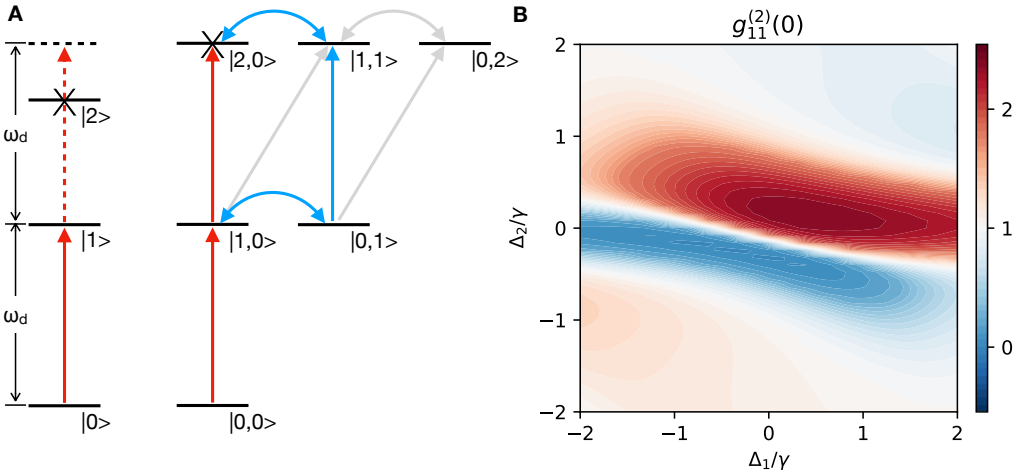

Figure 9.1. Unconventional photon blockade. **(A)** Comparison of conventional and unconventional photon blockade. Conventional photon blockade (left) relies on a strong nonlinearity to prohibit the generation of a second photon in the system. By comparison, unconventional photon blockade (right) uses the destructive interference between the two state transition paths (red and blue) to blockade the second photon. The grey arrows indicate the second order transition processes that can be fairly neglected. **(B)** Simulation of the second-order correlation function, $g_{11}^{(2)}(0)$, for unconventional photon blockade. The photons in the driven resonator can be strongly bunched or antibunched in certain parameter regimes.

with different detuning frequencies, Δ_1 and Δ_2, as shown in Fig. 9.1. The simulation parameters are chosen as $g = 2.0$, $U = -0.1$, $\xi_1 = 0.1$, and $\xi_2 = 0$ normalized by γ, and the Hilbert space is truncated to 5×5 dimensions. The $g_{11}^{(2)}(0)$ reaches a minimum value of 3.6×10^{-4} at $\Delta_1 = 0.00$ and $\Delta_2 = -0.32$, and a maximum value of 5.2 at $\Delta_1 = 0.40$ and $\Delta_2 = 0.16$. In other words, strong photon bunching and antibunching can happen in the same system depending on the parameter settings. The average photon over the chosen parameter range is found to be 6.1×10^{-6} with a standard variance of 1.5×10^{-5}. It reveals that single microwave photons may be emitted one by one and thus have a good time distinguishability [284]. These observations indicate that a Bose-Hubbard dimer can be a promising candidate to implement a single photon source. However, we did not achieve a numerical stability when calculating the time-delayed correlation function, $g_{11}^{(2)}(\tau)$, at the optimal antibunching point, such that the result is not shown here. A more detailed study, regarding time-delayed self- or cross-correlation functions and the wavefunctions of the two modes, and also an experimental demonstration should be performed elsewhere in the future.

9.2 Quantum cups and balls

The ancient trick "cups and balls" relies on a professional degree of sleight of hand that transfers a ball deceptively between two cups without opening the covers. However, this process can naturally happen in the context of quantum mechanics due to the wave-particle duality, i.e., the so-called tunneling effects [293]. If one treats photons as balls and resonators as cups in a Bose-Hubbard dimer, the initial process of "putting a ball in the cup" can be understood as detecting one photon in the resonator. By applying some "magic", the final location of the ball is determined by the self- and cross-correlation functions of the two resonators, $g_{11}^{(2)}(0)$ and $g_{12}^{(2)}(0)$. Depending on whether the correlation function is larger or smaller than unity, there are four possible combinations of $g_{11}^{(2)}(0)$ and $g_{12}^{(2)}(0)$, which correspond to the four outcomes of the trick, as shown in Fig. 9.2A. Our second proposal aims

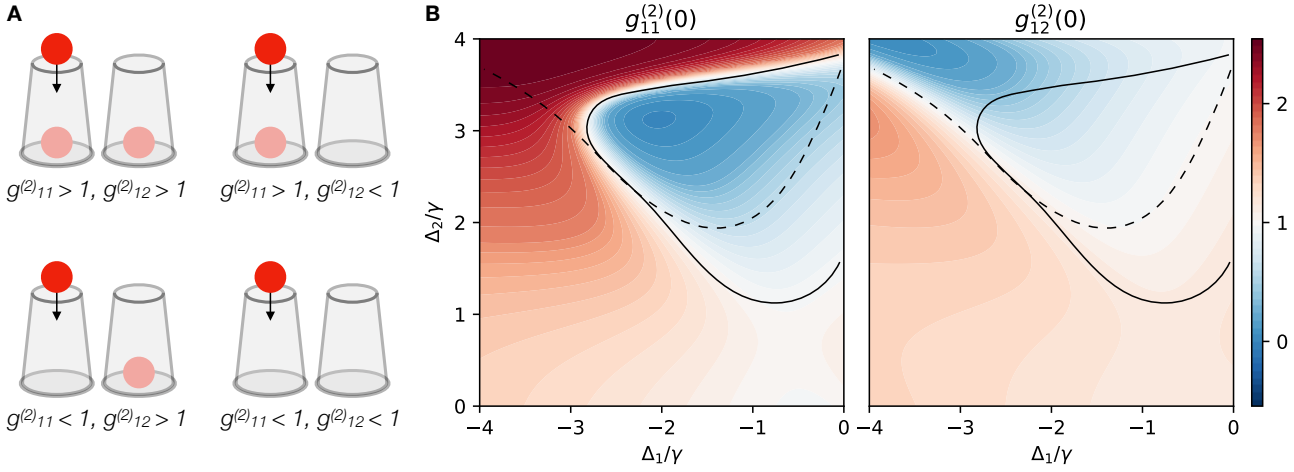

Figure 9.2. The quantum "cups and balls" game. (A) The quantum "cups and balls" trick. After detecting a photon in the first resonator, the probability of the second photon is determined by the self- and cross-correlation functions of the two resonator modes. **(B)** Simulation of the correlation functions $g^{(2)}_{11}(0)$ and $g^{(2)}_{12}(0)$. One can achieve all the four combinations of $g^{(2)}_{11}(0) \gtrless 1$ and $g^{(2)}_{12}(0) \gtrless 1$ by changing the detuning frequency, Δ_1 and Δ_2, of the driving field. The areas enclosed by the dashed (solid) curve indicate the regions where $g^{(2)}_{11}(0) < 1$ ($g^{(2)}_{12}(0) < 1$).

at tailoring the correlation functions, $g^{(2)}_{11}(0)$ and $g^{(2)}_{12}(0)$, in-situ and playing the "cups and balls" trick in a Bose-Hubbard dimer.

Here, we simulate the second-order correlation functions of the two oscillating modes, $g^{(2)}_{11}(0)$ and $g^{(2)}_{12}(0)$, with different detuning frequencies, Δ_1 and Δ_2, as shown in Fig. 9.2B. The simulation parameters are chosen as $g = 2.0$, $U = -0.1$, $\xi_1 = 0.1$, and $\xi_2 = 0.2$ normalized by γ, and the Hilbert space is truncated to 5×5 dimensions. By tuning Δ_1 and Δ_2, we observe all four combinations of $g^{(2)}_{11}(0)$ and $g^{(2)}_{12}(0)$. For example, for $\Delta_1 = -3.84$ and $\Delta_2 = 4.00$, photons in the first resonator are strongly bunched with $g^{(2)}_{11} = 58.8$, while a second photon is not likely to be observed in the second resonator because $g^{(2)}_{12} = 0.06$. At a different parameter setting with $\Delta_1 = -4.00$ and $\Delta_2 = 3.12$, we have $g^{(2)}_{12} = 3.72$ and $g^{(2)}_{12} = 1.46$ such that the second photon is to be detected by measuring either of the two resonators. These observations indicate that a quantum version of the "cups and balls" trick can be performed in a Bose-Hubbard dimer. However, we should note that the photon bunching and antibunching effects seem to be very weak in the $g^{(2)}_{11}(0) < 1$, $g^{(2)}_{12}(0) > 1$ regime. We expect to solve this potential issue by including more degrees of freedom, such as the driving strengths ξ_1 and ξ_2. A more detailed study and also an experimental demonstration should be performed elsewhere in the future.

9.3 Boundary time crystal

A time crystal is a novel phase of matter which predicts a time-dependent steady state for a time-independent Hamiltonian [294]. After years of debate on the existence of such a phenomenon [295–303], the current focus of this field is to search for examples that may circumvent the so-called no-go theorem [304–306]. A Floquet time-crystal, which breaks the discrete time-translational symmetry of time, $H(t) = H(t + T)$, has been found in theory [307–315], and demonstrated in recent experiments [316–322]. This type of time-crystal oscillates at a discrete, integer multiple of the driving period (usually, two), and is thus called the discrete time-crystal. The so-called boundary time-crystal is a potentially new member of the family, where the system undergoes an eternal oscillation in the presence

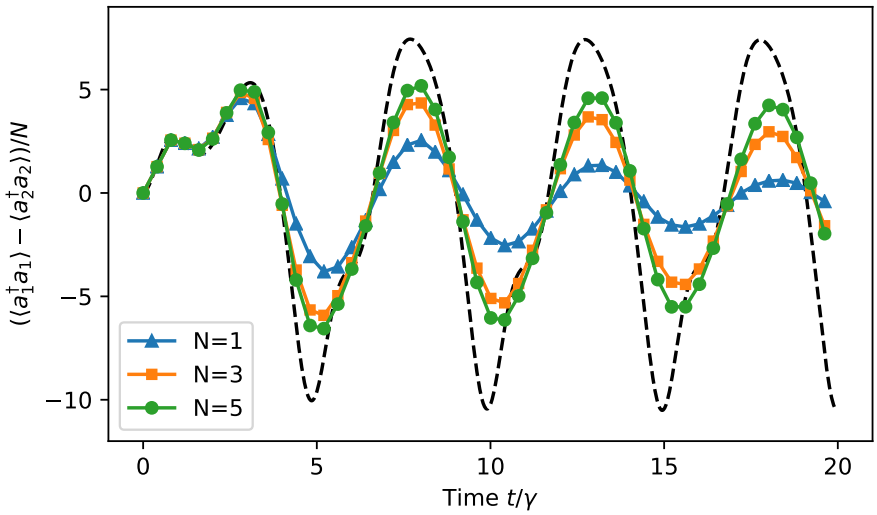

Figure 9.3. Boundary time-crystal. The system shows a long-time oscillation at the time scale of several multiples of the energy relaxation time $1/\gamma$. With the increase of N, the system approaches a thermodynamic limit such that the oscillation lasts increasingly longer. In the limit $N \to \infty$, the dynamics converges to an eternal oscillation (dashed), which is the numerical solution of the classical counterpart.

of both driving and dissipation at a frequency that is incommensurate with the driving period [323–326]. The effective Hamiltonian of the composite system can be written in a time-invariant form in a certain frame, such that it breaks the time-translational symmetry. Recent theories predict that the Bose-Hubbard dimer may be a potential system allowing to realize such a continuous time-crystal [327–331], which is fundamentally different from the discrete time-crystals reported in the literature.

Here, we simulate the normalized photon number difference $\left(\langle a_1^\dagger a_1\rangle - \langle a_2^\dagger a_2\rangle\right)/N$, between the two resonator fields, a_1 and a_2, as shown in Fig. 9.3. The integer number N is an artificial scaling factor, which rescales $U \equiv U_0/N$ and $\xi_{1/2} \equiv \sqrt{N}\xi_{1/2,0}$ as we did in Chapter 8. In this way, the thermodynamic limit can be achieved for $N \to \infty$. Here, the simulation parameters are chosen as $\Delta = 2.0$, $g_0 = 1.2$, $U_0 = -0.1$, $\xi_{1,0} = 3.4$, and $\xi_{2,0} = 0.0$ normalized by γ. The Hilbert space is truncated to 90×90 dimensions for achieving the numerical convergence. We observe an increasing oscillation lifetime of the observable with N, which converges to the classical result and lasts forever for $N \to \infty$. This observation indicates the existence of a boundary time-crystal at the thermodynamic limit ($N \to \infty$), as predicted by Refs. [328–330]. However, we can hardly increase N further in our simulation, which is strongly limited by the numerical efficiency. We hope to solve this problem by employing the truncated Wigner approximation (TWA) method [330, 332–335], and observe the long-time oscillation in a Bose-Hubbard dimer in experiments in the future.

Part V:
APPENDICES

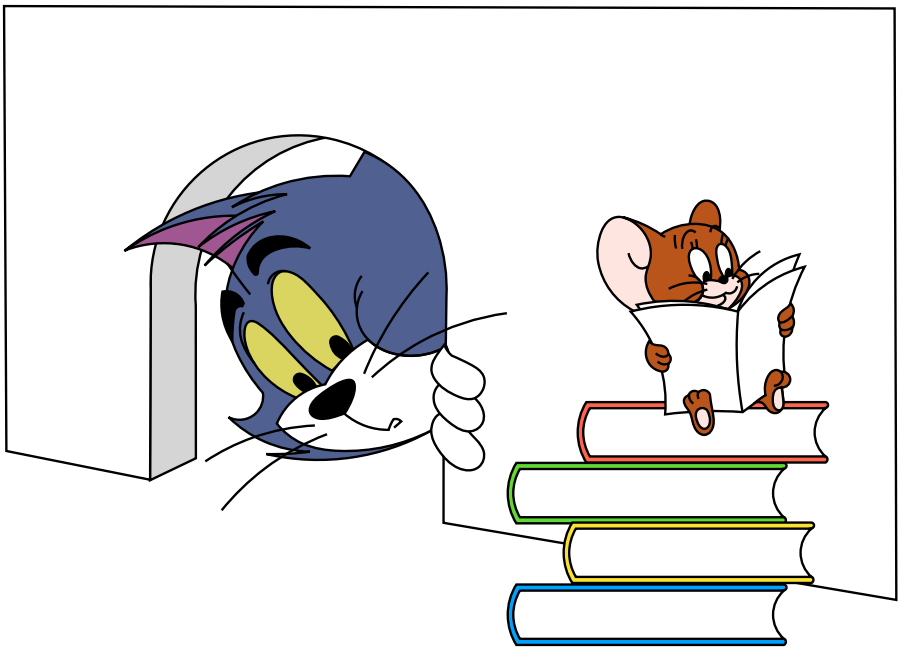

*credit Metro-Goldwyn-Mayer

Appendix A

QUASI-DISTRIBUTION FUNCTIONS OF GAUSSIAN STATES

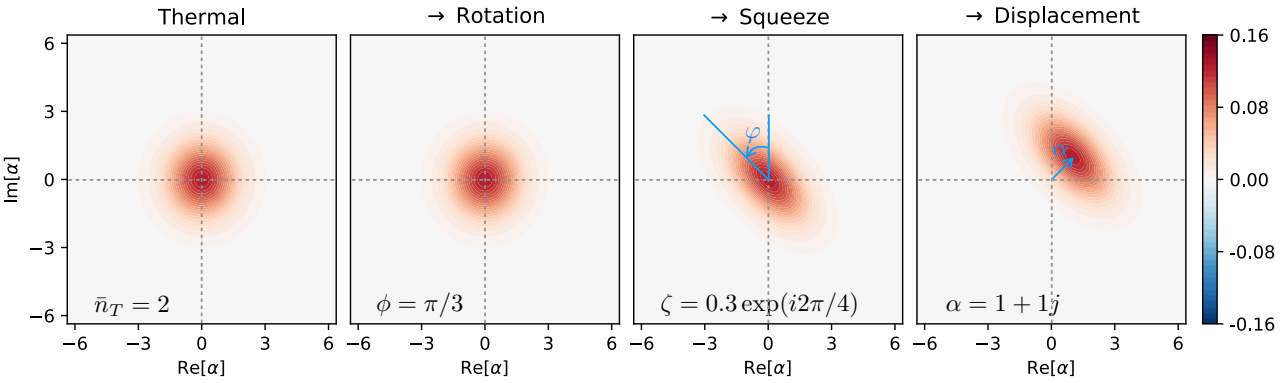

Figure A.1. Sequence of operations for generating a Gaussian state. From left to right, we apply the rotation, squeeze, and displacement operators sequentially to a thermal state, and plot the Wigner functions of the state after each operation.

The Gaussian states introduced in Chapter 2 are probably the most favorable states in quantum optics since they are robust to noise and easy to be prepared and characterized [33–36], as shown in Fig. A.1. To describe a Gaussian state in the P, Q, and W representations, we first derive the characteristic functions of them. The characteristic function in the P representation is

$$\begin{aligned}
\chi_{\mathrm{N}}(z,z^*) =& \mathrm{tr}\left[D(\beta)S(\zeta)R(\phi)\rho_T R^\dagger(\phi)S^\dagger(\zeta)D^\dagger(\beta)e^{iz^*a^\dagger}e^{iza}\right] \\
=& \mathrm{tr}\left[\rho_T R^\dagger(\phi)S^\dagger(\zeta)D^\dagger(\beta)e^{iz^*a^\dagger}D(\beta)S(\zeta)R(\phi)R^\dagger(\phi)S^\dagger(\zeta)D^\dagger(\beta)e^{iza}D(\beta)S(\zeta)R(\phi)\right] \\
=& e^{iz^*\beta^*}e^{iz\beta}\mathrm{tr}\left[\rho_T R^\dagger(\phi)S^\dagger(\zeta)e^{iz^*a^\dagger}S(\zeta)R(\phi)R^\dagger(\phi)S^\dagger(\zeta)e^{iza}S(\zeta)R(\phi)\right] \\
=& e^{iz^*\beta^*}e^{iz\beta}\mathrm{tr}\left\{\rho_T R^\dagger(\phi)\exp\left[iz^*\left(a^\dagger\cosh r - ae^{-i2\varphi}\sinh r\right)\right]R(\phi)\right. \\
&\left.\times R^\dagger(\phi)\exp\left[iz\left(a\cosh r - a^\dagger e^{i2\varphi}\sinh r\right)\right]R(\phi)\right\} \\
=& e^{iz^*\beta^*}e^{iz\beta}\mathrm{tr}\left\{\rho_T \exp\left[iz^*\left(a^\dagger e^{i\phi}\cosh r - ae^{-i(\phi+2\varphi)}\sinh r\right)\right]\right. \\
&\left.\times\exp\left[iz\left(ae^{-i\phi}\cosh r - a^\dagger e^{i(\phi+2\varphi)}\sinh r\right)\right]\right\},
\end{aligned} \tag{A.1}$$

where $\zeta = re^{i2\varphi}$. To proceed, we calculate the commutator

$$\begin{aligned}
&\left[iz^*\left(a^\dagger e^{i\phi}\cosh r - ae^{-i(\phi+2\varphi)}\sinh r\right), iz\left(ae^{-i\phi}\cosh r - a^\dagger e^{i(\phi+2\varphi)}\sinh r\right)\right] \\
=& -|z|^2\left[a^\dagger a\cosh^2(r) + aa^\dagger\sinh^2(r) - aa^\dagger\cosh^2(r) - a^\dagger a\sinh^2(r)\right] \\
=& |z|^2 .
\end{aligned} \tag{A.2}$$

Recalling the Baker-Hausdorff theorem: If O_1 and O_2 are operators that commute with their commutator, $[O_1, O_2]$, then $e^{O_1+O_2} = e^{O_1}e^{O_2}e^{-[O_1,O_2]/2} = e^{O_2}e^{O_1}e^{[O_1,O_2]/2}$ [42], the characteristic

function can be rewritten as

$$\begin{aligned}\chi_{\mathrm{N}}(z,z^*) =& e^{\frac{|z|^2}{2}} e^{iz^*\beta^*} e^{iz\beta} \mathrm{tr}\left\{\rho_T \exp\left[iz^*\left(a^\dagger e^{i\phi}\cosh r - a e^{-i(\phi+2\varphi)}\sinh r\right)\right.\right.\\ &\left.\left.+iz\left(a e^{-i\phi}\cosh r - a^\dagger e^{i(\phi+2\varphi)}\sinh r\right)\right]\right\}\\ =& e^{\frac{|z|^2}{2}} e^{iz^*\beta^*} e^{iz\beta} \mathrm{tr}\left\{\rho_T \exp\left[i\left(z^*\cosh r - z e^{i2\varphi}\sinh r\right)e^{i\phi}a^\dagger\right.\right.\\ &\left.\left.+i\left(z\cosh r - z^* e^{-i2\varphi}\sinh r\right)e^{-i\phi}a\right]\right\}\\ =& e^{\frac{|z|^2}{2}} e^{iz^*\beta^*} e^{iz\beta}\int d\alpha^2 \frac{e^{-\frac{|\alpha|^2}{\bar{n}_T}}}{\pi\bar{n}_T}\left\langle\alpha\left|\exp\left[i\left(z^*\cosh r - z e^{i2\varphi}\sinh r\right)e^{i\phi}a^\dagger\right.\right.\right.\\ &\left.\left.\left.+i\left(z\cosh r - z^* e^{-i2\varphi}\sinh r\right)e^{-i\phi}a\right]\right|\alpha\right\rangle. \end{aligned} \tag{A.3}$$

We use the Baker-Hausdorff theorem again with the commutator

$$\begin{aligned}&\left[i\left(z^*\cosh r - z e^{i2\varphi}\sinh r\right)e^{i\phi}a^\dagger, i\left(z\cosh r - z^* e^{-i2\varphi}\sinh r\right)e^{-i\phi}a\right]\\ &= -\left|z^*\cosh r - z e^{i2\varphi}\sinh r\right|^2\left(a^\dagger a - a a^\dagger\right)\\ &= \left|z^*\cosh r - z e^{i2\varphi}\sinh r\right|^2, \end{aligned} \tag{A.4}$$

which leads to the result

$$\begin{aligned}\chi_{\mathrm{N}}(z,z^*) =& e^{\frac{|z|^2}{2}} e^{iz^*\beta^*} e^{iz\beta}\exp\left(-\frac{\left|z^*\cosh r - z e^{i2\varphi}\sinh r\right|^2}{2}\right)\\ &\times\int d\alpha^2 \frac{e^{-\frac{|\alpha|^2}{\bar{n}_T}}}{\pi\bar{n}_T}\exp\left[i\left(z^*\cosh r - z e^{i2\varphi}\sinh r\right)e^{i\phi}\alpha^* + i\left(z\cosh r - z^* e^{-i2\varphi}\sinh r\right)e^{-i\phi}\alpha\right] \end{aligned} \tag{A.5}$$

Pure Gaussian states

For the simplest case, we consider a Gaussian state which is a rotated, squeezed, and displaced *vacuum* state. The integral of Eq. (A.5) equals *one*, such that the characteristic function is

$$\begin{aligned}\chi_{\mathrm{N}}(z,z^*) =& e^{iz^*\beta^*} e^{iz\beta}\exp\left(-\frac{\left|z^*\cosh r - z e^{i2\varphi}\sinh r\right|^2 - |z|^2}{2}\right)\\ =& \exp\left[i2\left(\mu x_0 - \nu y_0\right)\right]\\ &\times\exp\left\{-\frac{1}{2}\left[\left|(\mu - i\nu)\cosh r - (\mu + i\nu)\left(\cos 2\varphi + i\sin 2\varphi\right)\sinh r\right|^2 - (\mu^2+\nu^2)\right]\right\}\\ =& \exp\left[i2\left(\mu x_0 - \nu y_0\right)\right]\\ &\times\exp\left\{-\frac{1}{2}\left[\left(\mu\cos\varphi - \nu\sin\varphi\right)^2\left(e^{-2r}-1\right) + \left(\mu\sin\varphi + \nu\cos\varphi\right)^2\left(e^{2r}-1\right)\right]\right\}, \end{aligned} \tag{A.6}$$

where $z = \mu + i\nu$, $\beta = x_0 + iy_0$. Consequently, the other two characteristic functions can be obtained as

$$\begin{aligned}\chi_{\mathrm{A}}(z,z^*) =& \exp\left[i2\left(\mu x_0 - \nu y_0\right)\right] \\ &\times \exp\left\{-\frac{1}{2}\left[\left(\mu\cos\varphi - \nu\sin\varphi\right)^2\left(e^{-2r}+1\right) + \left(\mu\sin\varphi + \nu\cos\varphi\right)^2\left(e^{2r}+1\right)\right]\right\}, \qquad \text{(A.7)} \\ \chi_{\mathrm{S}}(z,z^*) =& \exp\left[i2\left(\mu x_0 - \nu y_0\right)\right] \\ &\times \exp\left\{-\frac{1}{2}\left[\left(\mu\cos\varphi - \nu\sin\varphi\right)^2 e^{-2r} + \left(\mu\sin\varphi + \nu\cos\varphi\right)^2 e^{2r}\right]\right\}, \qquad \text{(A.8)}\end{aligned}$$

Hence, the quasi-distribution functions can be directly obtained by taking the Fourier transform. For example, we may write

$$\begin{aligned}P(\alpha,\alpha^*) =& \frac{1}{\pi^2}\int d\mu \int d\nu e^{-i2[\mu(x-x_0)-\nu(y-y_0)]} \\ &\times \exp\left\{-\frac{1}{2}\left[\left(\mu\cos\varphi - \nu\sin\varphi\right)^2\left(e^{-2r}-1\right) + \left(\mu\sin\varphi + \nu\cos\varphi\right)^2\left(e^{2r}-1\right)\right]\right\}, \\ =& \sqrt{\frac{2}{\pi(e^{-2r}-1)}}\exp\left\{2\frac{[(x-x_0)\cos\varphi + (y-y_0)\sin\varphi]^2}{e^{-2r}-1}\right\} \\ &\times \sqrt{\frac{2}{\pi(e^{2r}-1)}}\exp\left\{2\frac{[-(x-x_0)\sin\varphi + (y-y_0)\cos\varphi]^2}{e^{2r}-1}\right\}, \qquad \text{(A.9)}\end{aligned}$$

where $\alpha = x + iy$. However, this is not an ordinary function since it diverges at infinity. In fact, the characteristic function $\chi_{\mathrm{N}}(z,z^*)$ shown in Eq. (A.6) already diverges. This is the reason we claim in Chapter 2 that a squeezed state does not have a P representation. By comparison, the other two quasi-distribution functions are well defined [45]

$$\begin{aligned}Q(\alpha,\alpha^*) =& \sqrt{\frac{2}{\pi(1+e^{-2r})}}\exp\left\{-2\frac{[(x-x_0)\cos\varphi + (y-y_0)\sin\varphi]^2}{1+e^{-2r}}\right\} \\ &\times \sqrt{\frac{2}{\pi(1+e^{2r})}}\exp\left\{-2\frac{[-(x-x_0)\sin\varphi + (y-y_0)\cos\varphi]^2}{1+e^{2r}}\right\}, \qquad \text{(A.10)} \\ W(\alpha,\alpha^*) =& \sqrt{\frac{2}{\pi e^{-2r}}}\exp\left\{-2\frac{[(x-x_0)\cos\varphi + (y-y_0)\sin\varphi]^2}{e^{-2r}}\right\} \\ &\times \sqrt{\frac{2}{\pi e^{2r}}}\exp\left\{-2\frac{[-(x-x_0)\sin\varphi + (y-y_0)\cos\varphi]^2}{e^{2r}}\right\}. \qquad \text{(A.11)}\end{aligned}$$

Mixed Gaussian states

For a more general case, we define $c + id = \left(z\cosh r - z^* e^{-i2\varphi}\sinh r\right)e^{-i\phi}$. The integral in Eq. (A.5) can be calculated by replacement of variables, which gives

$$\begin{aligned}&\frac{1}{\pi\bar{n}_T}\int dx \exp\left(-\frac{x^2}{\bar{n}_T} + i2cx\right)\int dy \exp\left(-\frac{y^2}{\bar{n}_T} - i2dy\right) \\ =& \exp\left[-\left(c^2+d^2\right)\bar{n}_T\right] \\ =& \exp\left\{-\left[\left(\mu\cos\varphi - \nu\sin\varphi\right)^2 e^{-2r} + \left(\mu\sin\varphi - \nu\cos\varphi\right)^2 e^{2r}\right]\bar{n}_T\right\}. \qquad \text{(A.12)}\end{aligned}$$

Thus, the characteristic functions can be obtained as

$$\chi_{\mathrm{N}}(z,z^*) = \exp\left[i2\left(\mu x_0 - \nu y_0\right)\right] \exp\left\{-\frac{1}{2}\left[\left(\mu\cos\varphi - \nu\sin\varphi\right)^2\left((2\bar{n}_T+1)e^{-2r}-1\right) + \left(\mu\sin\varphi + \nu\cos\varphi\right)^2\left((2\bar{n}_T+1)e^{2r}-1\right)\right]\right\}, \tag{A.13}$$

$$\chi_{\mathrm{A}}(z,z^*) = \exp\left[i2\left(\mu x_0 - \nu y_0\right)\right] \exp\left\{-\frac{1}{2}\left[\left(\mu\cos\varphi - \nu\sin\varphi\right)^2\left((2\bar{n}_T+1)e^{-2r}+1\right) + \left(\mu\sin\varphi + \nu\cos\varphi\right)^2\left((2\bar{n}_T+1)e^{2r}+1\right)\right]\right\}, \tag{A.14}$$

$$\chi_{\mathrm{S}}(z,z^*) = \exp\left[i2\left(\mu x_0 - \nu y_0\right)\right] \exp\left\{-\frac{1}{2}\left[\left(\mu\cos\varphi - \nu\sin\varphi\right)^2(2\bar{n}_T+1)e^{-2r} + \left(\mu\sin\varphi + \nu\cos\varphi\right)^2(2\bar{n}_T+1)e^{2r}\right]\right\}. \tag{A.15}$$

Correspondingly, the Q and W functions read

$$\begin{aligned} Q(\alpha,\alpha^*) =& \sqrt{\frac{2}{\pi[1+(2\bar{n}_T+1)e^{-2r}]}}\exp\left\{-2\frac{[(x-x_0)\cos\varphi+(y-y_0)\sin\varphi]^2}{1+(2\bar{n}_T+1)e^{-2r}}\right\} \\ &\times\sqrt{\frac{2}{\pi[1+(2\bar{n}_T+1)e^{2r}]}}\exp\left\{-2\frac{[-(x-x_0)\sin\varphi+(y-y_0)\cos\varphi]^2}{1+(2\bar{n}_T+1)e^{2r}}\right\}, \end{aligned} \tag{A.16}$$

$$\begin{aligned} W(\alpha,\alpha^*) =& \sqrt{\frac{2}{\pi(2\bar{n}_T+1)e^{-2r}}}\exp\left\{-2\frac{[(x-x_0)\cos\varphi+(y-y_0)\sin\varphi]^2}{(2\bar{n}_T+1)e^{-2r}}\right\} \\ &\times\sqrt{\frac{2}{\pi(2\bar{n}_T+1)e^{2r}}}\exp\left\{-2\frac{[-(x-x_0)\sin\varphi+(y-y_0)\cos\varphi]^2}{(2\bar{n}_T+1)e^{2r}}\right\}. \end{aligned} \tag{A.17}$$

Appendix B

GENERAL FORM OF THE INPUT-OUTPUT FORMALISM

We consider a general model where a multi-mode system interacts with several environments [42, 48, 336]

$$H_{\mathrm{s}} = \sum_{n} \hbar\omega_n a_n^\dagger a_n, \tag{B.1}$$

$$H_{\mathrm{b}} = \sum_{m} \hbar \int_{-\infty}^{+\infty} d\omega \omega b_{m,\omega}^\dagger b_{m,\omega}, \tag{B.2}$$

$$H_{\mathrm{sb}} = \sum_{m,n} \hbar \int_{-\infty}^{+\infty} d\omega \left[\kappa_{m,n}^* a_n b_{m,\omega}^\dagger + \kappa_{m,n} a_n^\dagger b_{m,\omega}\right]. \tag{B.3}$$

Following the Heisenberg equation, the time evolution of the intra-resonator field, a_n, as well as the bath field, $b_{m,\omega}$, can be readily written as

$$\dot{a}_n = -i\omega_n a_n - i\sum_{m} \int_{-\infty}^{+\infty} d\omega \kappa_{m,n} b_{m,\omega}, \tag{B.4}$$

$$\dot{b}_{m,\omega} = -i\omega b_{m,\omega} - i\sum_{n} \kappa_{m,n}^* a_n. \tag{B.5}$$

By inserting the formal solution of Eq. (B.5),

$$b_{m,\omega}(t) = e^{-i\omega(t-t_0)} b_{m,\omega}(t_0) - i\sum_{n} \kappa_{m,n'}^* \int_{t_0}^{t} dt' e^{-i\omega(t-t')} a_{n'}(t'). \tag{B.6}$$

into Eq. (B.4), we obtain

$$\dot{a}_n = -i\omega_n a_n - i\sum_{m} \kappa_{m,n} \int_{-\infty}^{+\infty} d\omega e^{-i\omega(t-t_0)} b_{m,\omega}(t_0) - \sum_{m,n'} \kappa_{m,n}\kappa_{m,n'}^* \int_{-\infty}^{+\infty} d\omega \int_{t_0}^{t} dt' e^{-i\omega(t-t')} a_{n'}(t'). \tag{B.7}$$

We recall the property

$$\int_{-\infty}^{+\infty} d\omega e^{-i\omega(t-t_0)} = 2\pi\delta\left(t - t_0\right) \tag{B.8}$$

and define the input field, i.e., the noise operator in quantum Langevin equation, as

$$b_{m,\mathrm{in}} = \frac{1}{\sqrt{2\pi}} \int_{-\infty}^{+\infty} d\omega e^{-i\omega(t-t_0)} b_{m,\omega}(t_0). \tag{B.9}$$

Then, the dynamics of the system, i.e., Eq (B.7), can be simplified as

$$\dot{a}_n = -i\omega_n a_n - i\sum_m \sqrt{2\pi}\kappa_{m,n} b_{m,\text{in}} - \sum_{m,n'} \pi\kappa_{m,n}\kappa^*_{m,n'} a_{n'}. \tag{B.10}$$

Alternatively, the formal solution of Eq. (B.5) may be written as

$$b_{m,\omega}(t) = e^{-i\omega(t-t_1)} b_{m,\omega}(t_1) + i\sum_n \kappa^*_{m,n'} \int_t^{t_1} dt' e^{-i\omega(t-t')} a_{n'}(t'). \tag{B.11}$$

We have

$$\dot{a}_n = -i\omega_n a_n - i\sum_m \kappa_{m,n} \int_{-\infty}^{+\infty} d\omega e^{-i\omega(t-t_1)} b_{m,\omega}(t_1) + \sum_{m,n'} \kappa_{m,n}\kappa^*_{m,n'} \int_{-\infty}^{+\infty} d\omega \int_t^{t_1} dt' e^{-i\omega(t-t')} a_{n'}. \tag{B.12}$$

We define the output field as

$$b_{m,\text{out}} = \frac{1}{\sqrt{2\pi}} \int_{-\infty}^{+\infty} d\omega e^{-i\omega(t-t_1)} b_{m,\omega}(t_0), \tag{B.13}$$

such that Eq. (B.12) can be simplified as

$$\dot{a}_n = -i\omega_n a_n - i\sum_m \sqrt{2\pi}\kappa_{m,n} b_{m,\text{out}} + \sum_{m,n'} \pi\kappa_{m,n}\kappa^*_{m,n'} a_{n'}. \tag{B.14}$$

Combining Eqs. (B.9)-(B.10) and (B.13)-(B.14), we obtain the so-called input-output formalism

$$\dot{a}_n = -i\omega_n a_n - \sum_m \sqrt{\gamma_{m,n}} b_{m,\text{in}} - \frac{1}{2}\sum_{m,n'} \sqrt{\gamma_{m,n}} \left(\sqrt{\gamma_{m,n'}}\right)^* a_{n'} - \frac{\gamma_{a_n}}{2} a_n, \tag{B.15}$$

$$b_{m,\text{out}} = b_{m,\text{in}} + \sum_{n'} \left(\sqrt{\gamma_{m,n'}}\right)^* a_{n'}., \tag{B.16}$$

Here, we have defined $\sqrt{\gamma_{m,n}} = i\sqrt{2\pi}\kappa_{m,n}$ and $\left(\sqrt{\gamma_{m,n}}\right)^* = -i\sqrt{2\pi}\kappa^*_{m,n}$ and added the intrinsic damping of the modes, $\gamma_n/2$, by hand.

Appendix C

THE Z-TRANSFORM AND THE TRANSFER FUNCTION

The Z-transform converts a digitized signal in the time domain into a function in the so-called Z-domain. This transform is closely related to the Laplace transform but works on digitally sampled signals. Assuming that a continuous function, $x(t)$, is sampled at a rate of f_S, the sampled signal is a sequence of values, $\{x_k | k = 0, 1, \cdots\}$, that are defined only at the time instances k/f_S. To reveal the frequency properties of the sampled signal sequence, the idea of the Z-transform is to write it as a continuous function

$$x'(t) = x(t) \sum_{k=0}^{\infty} \delta\left(t - \frac{k}{f_S}\right), \tag{C.1}$$

where $\delta(\,\cdot\,)$ is the delta function. Applying the Laplace transform to $x'(t)$, we have

$$x'(s) = \sum_{k=0}^{\infty} x(k/f_S) e^{-sk/f_S}. \tag{C.2}$$

The Z-transform is readily obtained by replacing $x(k/f_S)$ and $\exp(s/f_S)$ by the discrete variables x_k and z, that is

$$x'(z) = \sum_{k=0}^{\infty} x_k z^{-k}. \tag{C.3}$$

The Z-transform contains lots of information on the function $x'(t)$, such as the convergence of the signal at $t \to \infty$. The Fourier transform is obtained by simply replacing z by $\exp(i\omega t)$,

$$x'(\omega) = \sum_{k=0}^{\infty} x_k e^{-ik\omega t}. \tag{C.4}$$

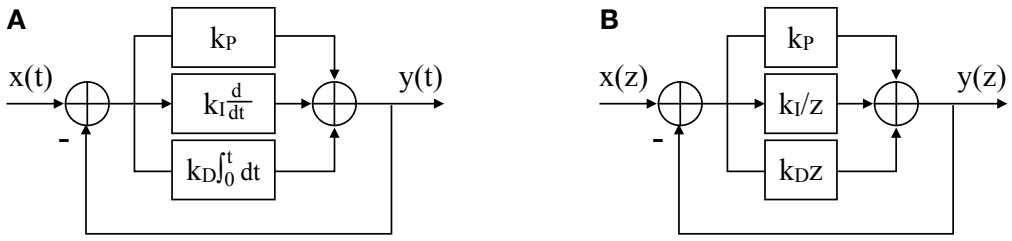

Figure C.1. The input-output relation of a PID controller. (A), (B) Schematics of the controller in the time or Z-domain, respectively.

The convenience of the Z-transform lies in synthesizing discrete-time systems, for example, a computer-based controller. The so-called transfer function is a useful tool for the analysis, which describes the the input-output relation of a system. It can be a very complicated function with a combination of time derivatives, integrals, and scalings. However, one can significantly simplify the

problem by transferring it to the Laplace-domain. For discrete-time systems, the transfer function is written in the Z-domain. Supposing that the Z-domain input and output signals are $x(z)$ and $y(z)$, respectively, the transfer function of a discrete-time system can be simply expressed as

$$H(z) = \frac{y(z)}{x(z)}. \tag{C.5}$$

Let us consider a typical feedback control protocol called the PID controller, as shown in Fig. C.1. The input-output relation in the time domain is

$$y(t) = k_{\mathrm{P}}\left[y(t) - x(t)\right] + k_{\mathrm{I}}\int_0^t \left[y(t') - x(t')\right] dt' + k_{\mathrm{D}}\frac{d\left[y(t) - x(t)\right]}{dt}. \tag{C.6}$$

Here, k_{P}, k_{I}, and k_{D} denote the coefficients for the proportional, integral, and derivative terms, respectively, which give rise to the name PID controller. By comparison, the transfer function in the Z-domain can be written in a rather compact form. That is

$$H(z) = \frac{(k_{\mathrm{P}} + k_{\mathrm{I}}/z + k_{\mathrm{D}}z)}{1 + (k_{\mathrm{P}} + k_{\mathrm{I}}/z + k_{\mathrm{D}}z)}. \tag{C.7}$$

We note that such a PID controller is used to control the local temperature of the attenuator for output characterization, as introduced in Chapter 3. We have also used the Z-transform to analyze the performance of the FIR and CIC filters, as introduced in Chapter 6.

Appendix D

CLASSICAL THEORY OF DUFFING OSCILLATOR

The Duffing oscillator is a general model system in physics that describes the driven motion of an oscillator with a cubic nonlinearity and a linear viscous damping [237]. The EOM of a Duffing oscillator reads

$$\ddot{x} + \omega_0^2 x = -\gamma\dot{x} - \beta x^3 + f\cos(\omega t), \tag{D.1}$$

where ω_0 and ω_d are the resonant and driving frequencies, γ the energy relaxation rate, β the nonlinear coefficient, and f the driving strength. To describe the system in the Hamiltonian's form, we neglect the energy dissipation for temporary and obtain

$$H = \frac{p^2}{2} + \frac{\omega_0^2 x^2}{2} + \frac{\beta x^4}{4} + xf\cos(\omega_\mathrm{d} t), \tag{D.2}$$

where $p = \dot{x}$ is the conjugate variable of the coordinate x, i.e., the momentum.

To understand the dynamics of the system, it is convenient to move to a rotating frame at the driving frequency. For convenience, we define $x = \sqrt{1/(2\omega_0)}\,(\alpha^* + \alpha)$ and $p = i\sqrt{\omega_0/2}\,(\alpha^* - \alpha)$, such that the required transform reads $\alpha \to \alpha e^{-i\omega_\mathrm{d} t}$, $\alpha^* \to \alpha^* e^{+i\omega_\mathrm{d} t}$, and $H \to H - \omega_\mathrm{d}\alpha^* a$ [337–339]. Finally, it results in the following Hamiltonian under the rotating wave approximation (RWA)

$$H = \Delta\alpha^*\alpha + U(\alpha^*\alpha)^2 + \xi(\alpha^* + \alpha), \tag{D.3}$$

where $\Delta = \omega_0 - \omega_\mathrm{d}$, $U = 3\beta/\left(8\omega_0^2\right)$, and $\xi = f/\left(\sqrt{2\omega_0}\right)$. The corresponding first-order Hamiltonian equation is thus

$$\dot{\alpha} = -i\delta\omega_0\alpha - i2U\alpha^*\alpha^2 - i\xi - \frac{\gamma}{2}\alpha, \tag{D.4}$$

where we have added the previously omitted damping term by hand. This equation is equivalent to the Duffing equation, i.e., Eq. (D.1), assuming that the RWA is valid.

The steady state of a Duffing oscillator can be obtained by solving the following equation

$$4U^2|\alpha|^6 + 4\Delta U|\alpha|^4 + \left[\Delta^2 + \left(\frac{\gamma}{2}\right)^2\right]|\alpha|^2 - \xi^2 = 0, \tag{D.5}$$

which is a third-order polynomial of $|\alpha|^2$. However, because $|\alpha|^2$ is real and positive by definition, either one, two, and three solutions are allowed depending on different parameter settings. The stability of the system can be verified by checking whether $\partial|\xi|^2/\partial|\alpha|^2 > 0$ [246]. The so-called bistability regime of the Duffing oscillator exists only if $\Delta^2 > 3(\gamma/2)^2$, where the system is described by a double-well potential. Correspondingly, there exist two stable solutions located in the two minima of the double-well potential and one unstable solution at the maximum between the two wells [238]. Outside this parameter regime, the potential has only a single minimum and there exists only a single unique SS

solution [238]. At the boundaries of the bistability regimes, we have two solutions

$$|\alpha|^2 = \frac{-2\Delta \pm \sqrt{\Delta^2 - 3\left(\gamma/2\right)^2}}{6U}, \tag{D.6}$$

which, in combination with Eq. (D.4), determines the boundaries of the bistability regime.

Bibliography

[1] A. J. Leggett, *Macroscopic Quantum Systems and the Quantum Theory of Measurement*, Prog. Theor. Phys. Supp. **69**, 80 (1980). [Cited on page 3.]

[2] A. Caldeira and A. Leggett, *Quantum tunnelling in a dissipative system*, Ann. Phys. **149**, 374 (1983). [Cited on page 3.]

[3] B. Yurke and J. S. Denker, *Quantum network theory*, Phys. Rev. A **29**, 1419 (1984). [Cited on pages 3, 5, and 97.]

[4] P. A. M. Dirac, *The principles of quantum mechanics*, Oxford university press, 3rd edition, 1948. [Cited on page 3.]

[5] W. J. Elion, M. Matters, U. Geigenmüller, and J. E. Mooij, *Direct demonstration of Heisenberg's uncertainty principle in a superconductor*, Nature **371**, 594 (1994). [Cited on page 3.]

[6] M. H. Devoret, Quantum fluctuations in electrical circuits, in *Quantum Fluctuations: Proceedings of the Les Houches Summer School, Session LXIII*, edited by S. Reynaud, S. Giacobino, and J. Zinn-Justin, pages 351–386, 1995. [Cited on pages 3, 4, 5, and 6.]

[7] V. E. Manucharyan, E. Boaknin, M. Metcalfe, R. Vijay, I. Siddiqi, and M. Devoret, *Microwave bifurcation of a Josephson junction: Embedding-circuit requirements*, Phys. Rev. B **76**, 014524 (2007). [Cited on pages 4, 25, and 28.]

[8] D. B. Haviland, L. S. Kuzmin, P. Delsing, and T. Claeson, *Observation of the Coulomb Blockade of Cooper Pair Tunnelling in Single Josephson Junctions*, Euro. Phys. Lett. **16**, 103 (1991). [Cited on page 5.]

[9] P. Joyez, P. Lafarge, A. Filipe, D. Esteve, and M. H. Devoret, *Observation of parity-induced suppression of Josephson tunneling in the superconducting single electron transistor*, Phys. Rev. Lett. **72**, 2458 (1994). [Cited on page 5.]

[10] M. H. Devoret, D. Esteve, and C. Urbina, Single electron phenomena in metallic nanostructures, in *Mesoscopic Quantum Physics: Proceedings of the Les Houches Summer School, Session LXI*, edited by E. Akkermans, J.-L. Montambaux, and J. Zinn-Justin, pages 605–658, 1994. [Cited on page 5.]

[11] A. Schmid, *Diffusion and Localization in a Dissipative Quantum System*, Phys. Rev. Lett. **51**, 1506 (1983). [Cited on page 5.]

[12] K. K. Likharev and A. B. Zorin, *Theory of the Bloch-wave oscillations in small Josephson junctions*, J. Low Temp. Phys. **59**, 347 (1985). [Cited on page 5.]

[13] L. S. Kuzmin and D. B. Haviland, *Observation of the Bloch oscillations in an ultrasmall Josephson junction*, Phys. Rev. Lett. **67**, 2890 (1991). [Cited on page 5.]

[14] S. E. Nigg, H. Paik, B. Vlastakis, G. Kirchmair, S. Shankar, L. Frunzio, M. H. Devoret, R. J. Schoelkopf, and S. M. Girvin, *Black-Box Superconducting Circuit Quantization*, Phys. Rev. Lett. **108**, 240502 (2012). [Cited on page 5.]

[15] F. Solgun, D. W. Abraham, and D. P. DiVincenzo, *Blackbox quantization of superconducting circuits using exact impedance synthesis*, Phys. Rev. B **90**, 134504 (2014). [Cited on page 5.]

[16] J. Koch, V. Manucharyan, M. H. Devoret, and L. I. Glazman, *Charging Effects in the Inductively Shunted Josephson Junction*, Phys. Rev. Lett. **103**, 217004 (2009). [Cited on page 6.]

[17] I. V. Pechenezhskiy, R. A. Mencia, L. B. Nguyen, Y.-H. Lin, and V. E. Manucharyan, *The superconducting quasicharge qubit*, Nature **585**, 368 (2020). [Cited on page 6.]

[18] R. C. Jaklevic, J. Lambe, A. H. Silver, and J. E. Mercereau, *Quantum Interference Effects in Josephson Tunneling*, Phys. Rev. Lett. **12**, 159 (1964). [Cited on page 7.]

[19] J. Lambe, A. Silver, J. Mercereau, and R. Jaklevic, *Microwave observation of quantum interference effects in superconductors*, Phys. Lett. **11**, 16 (1964). [Cited on page 7.]

[20] J. E. Zimmerman and A. H. Silver, *Macroscopic Quantum Interference Effects through Superconducting Point Contacts*, Phys. Rev. **141**, 367 (1966). [Cited on page 7.]

[21] A. B. Zorin, *Josephson Traveling-Wave Parametric Amplifier with Three-Wave Mixing*, Phys. Rev. Appl. **6**, 034006 (2016). [Cited on page 7.]

[22] N. E. Frattini, U. Vool, S. Shankar, A. Narla, K. M. Sliwa, and M. H. Devoret, *3-wave mixing Josephson dipole element*, Appl. Phys. Lett. **110**, 222603 (2017). [Cited on page 7.]

[23] N. E. Frattini, V. V. Sivak, A. Lingenfelter, S. Shankar, and M. H. Devoret, *Optimizing the Nonlinearity and Dissipation of a SNAIL Parametric Amplifier for Dynamic Range*, Phys. Rev. Appl. **10**, 054020 (2018). [Cited on page 7.]

[24] V. V. Sivak, N. E. Frattini, V. R. Joshi, A. Lingenfelter, S. Shankar, and M. H. Devoret, *Kerr-Free Three-Wave Mixing in Superconducting Quantum Circuits*, Phys. Rev. Appl. **11**, 054060 (2019). [Cited on page 7.]

[25] P. Coleman, *Introduction to many-body physics*, Cambridge University Press, 2015. [Cited on pages 8 and 11.]

[26] D. J. Griffiths and D. F. Schroeter, *Introduction to quantum mechanics*, Cambridge University Press, 2018. [Cited on page 11.]

[27] E. C. G. Sudarshan, *Equivalence of Semiclassical and Quantum Mechanical Descriptions of Statistical Light Beams*, Phys. Rev. Lett. **10**, 277 (1963). [Cited on pages 12 and 15.]

[28] R. J. Glauber, *Coherent and Incoherent States of the Radiation Field*, Phys. Rev. **131**, 2766 (1963). [Cited on pages 12 and 15.]

[29] D. F. Walls and G. J. Milburn, *Quantum optics*, Springer Science & Business Media, 2007. [Cited on page 13.]

[30] J. J. Gong and P. K. Aravind, *Expansion coefficients of a squeezed coherent state in the number state basis*, Am. J. Phys. **58**, 1003 (1990). [Cited on page 13.]

[31] C. Gerry, P. Knight, and P. L. Knight, *Introductory quantum optics*, Cambridge university press, 2005. [Cited on page 13.]

[32] P. Kok and B. W. Lovett, *Introduction to optical quantum information processing*, Cambridge university press, 2010. [Cited on page 14.]

[33] M. M. Wolf, G. Giedke, and J. I. Cirac, *Extremality of Gaussian Quantum States*, Phys. Rev. Lett. **96**, 080502 (2006). [Cited on pages 14 and 119.]

[34] X.-B. Wang, T. Hiroshima, A. Tomita, and M. Hayashi, *Quantum information with Gaussian states*, Phys. Rep. **448**, 1 (2007). [Cited on pages 14 and 119.]

[35] C. Weedbrook, S. Pirandola, R. García-Patrón, N. J. Cerf, T. C. Ralph, J. H. Shapiro, and S. Lloyd, *Gaussian quantum information*, Rev. Mod. Phys. **84**, 621 (2012). [Cited on pages 14 and 119.]

[36] H.-A. Bachor and T. C. Ralph, *A guide to experiments in quantum optics*, Wiley Online Library, 3rd edition, 2019. [Cited on pages 14, 30, 85, and 119.]

[37] A. Vourdas, *Superposition of squeezed coherent states with thermal light*, Phys. Rev. A **34**, 3466 (1986). [Cited on page 14.]

[38] G. S. Agarwal and G. Adam, *Photon-number distributions for quantum fields generated in nonlinear optical processes*, Phys. Rev. A **38**, 750 (1988). [Cited on page 14.]

[39] G. S. Agarwal and G. Adam, *Photon distributions for nonclassical fields with coherent components*, Phys. Rev. A **39**, 6259 (1989). [Cited on page 14.]

[40] S. Chaturvedi and V. Srinivasan, *Photon-number distributions for fields with Gaussian Wigner functions*, Phys. Rev. A **40**, 6095 (1989). [Cited on page 14.]

[41] G. Adam, *Density Matrix Elements and Moments for Generalized Gaussian State Fields*, J. Mod. Opt. **42**, 1311 (1995). [Cited on pages 14 and 85.]

[42] H. J. Carmichael, *Statistical Methods in Quantum Optics 1: Master Equations and Fokker-Planck Equations*, Springer-Verlag Berlin Heidelberg, 1999. [Cited on pages 15, 16, 17, 18, 19, 21, 22, 119, and 123.]

[43] K. E. Cahill and R. J. Glauber, *Ordered Expansions in Boson Amplitude Operators*, Phys. Rev. **177**, 1857 (1969). [Cited on pages 15 and 93.]

[44] K. E. Cahill and R. J. Glauber, *Density Operators and Quasiprobability Distributions*, Phys. Rev. **177**, 1882 (1969). [Cited on pages 15 and 93.]

[45] H. J. Carmichael, *Statistical Methods in Quantum Optics 2: Non-Classical Fields*, Springer-Verlag Berlin Heidelberg, 1999. [Cited on pages 17, 18, and 121.]

[46] G. Nogues, A. Rauschenbeutel, S. Osnaghi, P. Bertet, M. Brune, J. M. Raimond, S. Haroche, L. G. Lutterbach, and L. Davidovich, *Measurement of a negative value for the Wigner function of radiation*, Phys. Rev. A **62**, 054101 (2000). [Cited on page 18.]

[47] L. D. Landau and E. M. Lifshitz, *Mechanics*, volume 1 of *Course of Theoretical Physics*, Butterworth-Heinemann, 3rd edition, 1976. [Cited on page 19.]

[48] C. W. Gardiner and M. J. Collett, *Input and output in damped quantum systems: Quantum stochastic differential equations and the master equation*, Phys. Rev. A **31**, 3761 (1985). [Cited on pages 20, 21, 55, and 123.]

[49] M. O. Scully and M. S. Zubairy, *Quantum Optics*, Cambridge University Press, 1997. [Cited on pages 20, 22, 90, and 91.]

[50] C. W. Gardiner and P. Zoller, *Quantum noise: a handbook of Markovian and non-Markovian quantum stochastic methods with applications to quantum optics*, Springer, second enlarged edition, 2000. [Cited on pages 20, 22, and 60.]

[51] D. F. Walls and G. J. Milburn, *Effect of dissipation on quantum coherence*, Phys. Rev. A **31**, 2403 (1985). [Cited on pages 20, 22, and 60.]

[52] C. J. Myatt, B. E. King, Q. A. Turchette, C. A. Sackett, D. Kielpinski, W. M. Itano, C. Monroe,

and D. J. Wineland, *Decoherence of quantum superpositions through coupling to engineered reservoirs*, Nature **403**, 269 (2000). [Cited on pages 20, 22, and 60.]

[53] Q. A. Turchette, C. J. Myatt, B. E. King, C. A. Sackett, D. Kielpinski, W. M. Itano, C. Monroe, and D. J. Wineland, *Decoherence and decay of motional quantum states of a trapped atom coupled to engineered reservoirs*, Phys. Rev. A **62**, 053807 (2000). [Cited on pages 20, 22, and 60.]

[54] Y.-x. Liu, Ş. K. Özdemir, A. Miranowicz, and N. Imoto, *Kraus representation of a damped harmonic oscillator and its application*, Phys. Rev. A **70**, 042308 (2004). [Cited on pages 20, 22, and 60.]

[55] G. S. Agarwal, *Rotating-Wave Approximation and Spontaneous Emission*, Phys. Rev. A **4**, 1778 (1971). [Cited on page 22.]

[56] G. S. Agarwal, *Rotating-Wave Approximation and Spontaneous Emission*, Phys. Rev. A **7**, 1195 (1973). [Cited on page 22.]

[57] R. M. Angelo, E. S. Cardoso, and K. Furuya, *Decoherence induced by a phase-damping reservoir*, Phys. Rev. A **73**, 062107 (2006). [Cited on page 22.]

[58] C. W. Gardiner, *Inhibition of Atomic Phase Decays by Squeezed Light: A Direct Effect of Squeezing*, Phys. Rev. Lett. **56**, 1917 (1986). [Cited on page 22.]

[59] N. P. Georgiades, E. S. Polzik, K. Edamatsu, H. J. Kimble, and A. S. Parkins, *Nonclassical Excitation for Atoms in a Squeezed Vacuum*, Phys. Rev. Lett. **75**, 3426 (1995). [Cited on page 22.]

[60] M. Fischer, Q.-M. Chen, C. Besson, P. Eder, J. Goetz, S. Pogorzalek, M. Renger, E. Xie, M. J. Hartmann, K. G. Fedorov, A. Marx, F. Deppe, and R. Gross, *In situ tunable nonlinearity and competing signal paths in coupled superconducting resonators*, Phys. Rev. B **103**, 094515 (2021). [Cited on pages 25, 33, 34, and 64.]

[61] M. Metcalfe, *A new microwave readout for superconducting qubits*, PhD thesis, Yale University, 2008. [Cited on pages 25 and 27.]

[62] R. Vijayaraghavan, *Josephson Bifurcation Amplifier:Amplifying quantum signals using a dynamical bifurcation*, PhD thesis, Yale University, 2008. [Cited on page 25.]

[63] M. Watanabe, K. Inomata, T. Yamamoto, and J.-S. Tsai, *Power-dependent internal loss in Josephson bifurcation amplifiers*, Phys. Rev. B **80**, 174502 (2009). [Cited on pages 25, 28, 39, and 64.]

[64] R. Vijay, M. H. Devoret, and I. Siddiqi, *Invited Review Article: The Josephson bifurcation amplifier*, Rev. Sci. Instrum. **80**, 111101 (2009). [Cited on page 25.]

[65] D. M. Pozar, *Microwave Engineering (4th Edition)*, Wiley, 2011. [Cited on pages 26, 27, 28, 29, 47, 48, 49, 50, 52, 54, and 55.]

[66] J. Bourassa, J. M. Gambetta, A. A. Abdumalikov, O. Astafiev, Y. Nakamura, and A. Blais, *Ultrastrong coupling regime of cavity QED with phase-biased flux qubits*, Phys. Rev. A **80**, 032109 (2009). [Cited on page 29.]

[67] T. Niemczyk, F. Deppe, H. Huebl, E. P. Menzel, F. Hocke, M. J. Schwarz, J. J. Garcia-Ripoll, D. Zueco, T. Hümmer, E. Solano, A. Marx, and R. Gross, *Circuit quantum electrodynamics in the ultrastrong-coupling regime*, Nat. Phys. **6**, 772 (2010). [Cited on page 29.]

[68] M. Leib, F. Deppe, A. Marx, R. Gross, and M. J. Hartmann, *Networks of nonlinear superconducting transmission line resonators*, New J. Phys. **14**, 075024 (2012). [Cited on pages 29 and 32.]

[69] J. Bourassa, F. Beaudoin, J. M. Gambetta, and A. Blais, *Josephson-junction-embedded transmission-line resonators: From Kerr medium to in-line transmon*, Phys. Rev. A **86**, 013814 (2012). [Cited on pages 29 and 32.]

[70] D. Zueco, J. J. Mazo, E. Solano, and J. J. García-Ripoll, *Microwave photonics with Josephson junction arrays: Negative refraction index and entanglement through disorder*, Phys. Rev. B **86**, 024503 (2012). [Cited on page 29.]

[71] C. K. Andersen, G. Oelsner, E. Il'ichev, and K. Mølmer, *Quantized resonator field coupled to a current-biased Josephson junction in circuit QED*, Phys. Rev. A **89**, 033853 (2014). [Cited on page 29.]

[72] C. K. Andersen and K. Mølmer, *Multifrequency modes in superconducting resonators: Bridging frequency gaps in off-resonant couplings*, Phys. Rev. A **91**, 023828 (2015). [Cited on page 29.]

[73] H. L. Mortensen, K. Mølmer, and C. K. Andersen, *Normal modes of a superconducting transmission-line resonator with embedded lumped element circuit components*, Phys. Rev. A **94**, 053817 (2016). [Cited on page 29.]

[74] C. Fabre and N. Treps, *Modes and states in quantum optics*, Rev. Mod. Phys. **92**, 035005 (2020). [Cited on page 30.]

[75] S. M. Girvin, *Circuit QED: superconducting qubits coupled to microwave photons*, in *Quantum Machines: Measurement and Control of Engineered Quantum Systems*, edited by M. Devoret, B. Huard, R. Schoelkopf, and L. F. Cugliandolo, pages 113–256, Oxford University Press, 2011. [Cited on pages 32, 47, 57, and 80.]

[76] S. Krinner, S. Storz, P. Kurpiers, P. Magnard, J. Heinsoo, R. Keller, J. Lütolf, C. Eichler, and A. Wallraff, *Engineering cryogenic setups for 100-qubit scale superconducting circuit systems*, EPJ Quantum Technol. **6**, 2 (2019). [Cited on pages 36, 37, and 80.]

[77] Q.-M. Chen, M. Fischer, Y. Nojiri, M. Renger, S. Pogorzalek, M. Partanen, K. G. Fedorov, A. Marx, F. Deppe, and R. Gross, *Automated calibration and control of superconducting resonators with tunable nonlinearity*, in *WMI Annual Report*, pages 53–54, 2020. [Cited on page 39.]

[78] R. Harris, M. W. Johnson, T. Lanting, A. J. Berkley, J. Johansson, P. Bunyk, E. Tolkacheva, E. Ladizinsky, N. Ladizinsky, T. Oh, F. Cioata, I. Perminov, P. Spear, C. Enderud, C. Rich, S. Uchaikin, M. C. Thom, E. M. Chapple, J. Wang, B. Wilson, M. H. S. Amin, N. Dickson, K. Karimi, B. Macready, C. J. S. Truncik, and G. Rose, *Experimental investigation of an eight-qubit unit cell in a superconducting optimization processor*, Phys. Rev. B **82**, 024511 (2010). [Cited on page 39.]

[79] S. J. Weber, G. O. Samach, D. Hover, S. Gustavsson, D. K. Kim, A. Melville, D. Rosenberg, A. P. Sears, F. Yan, J. L. Yoder, W. D. Oliver, and A. J. Kerman, *Coherent Coupled Qubits for Quantum Annealing*, Phys. Rev. Appl. **8**, 014004 (2017). [Cited on page 39.]

[80] P. Yang, J. D. Brehm, J. Leppäkangas, L. Guo, M. Marthaler, I. Boventer, A. Stehli, T. Wolz,

A. V. Ustinov, and M. Weides, *Probing the Tavis-Cummings Level Splitting with Intermediate-Scale Superconducting Circuits*, Phys. Rev. Appl. **14**, 024025 (2020). [Cited on page 39.]

[81] J. D. Brehm, A. N. Poddubny, A. Stehli, T. Wolz, H. Rotzinger, and A. V. Ustinov, *Waveguide bandgap engineering with an array of superconducting qubits*, npj Quantum Mater. **6**, 10 (2021). [Cited on page 39.]

[82] T. A. Baart, P. T. Eendebak, C. Reichl, W. Wegscheider, and L. M. K. Vandersypen, *Computer-automated tuning of semiconductor double quantum dots into the single-electron regime*, Appl. Phys. Lett. **108**, 213104 (2016). [Cited on page 41.]

[83] C. J. van Diepen, P. T. Eendebak, B. T. Buijtendorp, U. Mukhopadhyay, T. Fujita, C. Reichl, W. Wegscheider, and L. M. K. Vandersypen, *Automated tuning of inter-dot tunnel coupling in double quantum dots*, Appl. Phys. Lett. **113**, 033101 (2018). [Cited on page 41.]

[84] U. Mukhopadhyay, J. P. Dehollain, C. Reichl, W. Wegscheider, and L. M. K. Vandersypen, *A* 2×2 *quantum dot array with controllable inter-dot tunnel couplings*, Appl. Phys. Lett. **112**, 183505 (2018). [Cited on page 41.]

[85] T. Botzem, M. D. Shulman, S. Foletti, S. P. Harvey, O. E. Dial, P. Bethke, P. Cerfontaine, R. P. G. McNeil, D. Mahalu, V. Umansky, A. Ludwig, A. Wieck, D. Schuh, D. Bougeard, A. Yacoby, and H. Bluhm, *Tuning Methods for Semiconductor Spin Qubits*, Phys. Rev. Appl. **10**, 054026 (2018). [Cited on page 41.]

[86] J. D. Teske, S. S. Humpohl, R. Otten, P. Bethke, P. Cerfontaine, J. Dedden, A. Ludwig, A. D. Wieck, and H. Bluhm, *A machine learning approach for automated fine-tuning of semiconductor spin qubits*, Appl. Phys. Lett. **114**, 133102 (2019). [Cited on page 41.]

[87] A. R. Mills, M. M. Feldman, C. Monical, P. J. Lewis, K. W. Larson, A. M. Mounce, and J. R. Petta, *Computer-automated tuning procedures for semiconductor quantum dot arrays*, Appl. Phys. Lett. **115**, 113501 (2019). [Cited on page 41.]

[88] C. R. Harris, K. J. Millman, S. J. van der Walt, R. Gommers, P. Virtanen, D. Cournapeau, E. Wieser, J. Taylor, S. Berg, N. J. Smith, R. Kern, M. Picus, S. Hoyer, M. H. van Kerkwijk, M. Brett, A. Haldane, J. F. del Río, M. Wiebe, P. Peterson, P. Gérard-Marchant, K. Sheppard, T. Reddy, W. Weckesser, H. Abbasi, C. Gohlke, and T. E. Oliphant, *Array programming with NumPy*, Nature **585**, 357 (2020). [Cited on page 43.]

[89] Q.-M. Chen, M. Pfeiffer, M. Partanen, F. Fesquet, K. E. Honasoge, F. Kronowetter, Y. Nojiri, M. Renger, K. G. Fedorov, A. Marx, F. Deppe, and R. Gross, *The scattering coefficients of superconducting microwave resonators: I. Transfer-matrix approach*, arXiv:2109.07762 (2021). [Cited on pages 47, 49, 50, 52, 53, and 54.]

[90] Q.-M. Chen, M. Partanen, F. Fesquet, K. E. Honasoge, F. Kronowetter, Y. Nojiri, M. Renger, K. G. Fedorov, A. Marx, F. Deppe, and R. Gross, *The scattering coefficients of superconducting microwave resonators: II. System-bath approach*, arXiv:2109.07766 (2021). [Cited on pages 47 and 57.]

[91] H. Paik, D. I. Schuster, L. S. Bishop, G. Kirchmair, G. Catelani, A. P. Sears, B. R. Johnson, M. J. Reagor, L. Frunzio, L. I. Glazman, S. M. Girvin, M. H. Devoret, and R. J. Schoelkopf, *Observation of High Coherence in Josephson Junction Qubits Measured in a Three-Dimensional Circuit QED Architecture*, Phys. Rev. Lett. **107**, 240501 (2011). [Cited on page 48.]

[92] C. Rigetti, J. M. Gambetta, S. Poletto, B. L. T. Plourde, J. M. Chow, A. D. Córcoles, J. A. Smolin, S. T. Merkel, J. R. Rozen, G. A. Keefe, M. B. Rothwell, M. B. Ketchen, and M. Steffen, *Superconducting qubit in a waveguide cavity with a coherence time approaching 0.1 ms*, Phys. Rev. B **86**, 100506 (2012). [Cited on page 48.]

[93] T. Brecht, M. Reagor, Y. Chu, W. Pfaff, C. Wang, L. Frunzio, M. H. Devoret, and R. J. Schoelkopf, *Demonstration of superconducting micromachined cavities*, Appl. Phys. Lett. **107**, 192603 (2015). [Cited on page 48.]

[94] T. Brecht, W. Pfaff, C. Wang, Y. Chu, L. Frunzio, M. H. Devoret, and R. J. Schoelkopf, *Multilayer microwave integrated quantum circuits for scalable quantum computing*, npj Quantum Inf. **2**, 1 (2016). [Cited on page 48.]

[95] T. Brecht, Y. Chu, C. Axline, W. Pfaff, J. Z. Blumoff, K. Chou, L. Krayzman, L. Frunzio, and R. J. Schoelkopf, *Micromachined Integrated Quantum Circuit Containing a Superconducting Qubit*, Phys. Rev. Appl. **7**, 044018 (2017). [Cited on page 48.]

[96] E. Xie, F. Deppe, M. Renger, D. Repp, P. Eder, M. Fischer, J. Goetz, S. Pogorzalek, K. G. Fedorov, A. Marx, and R. Gross, *Compact 3D quantum memory*, Appl. Phys. Lett. **112**, 202601 (2018). [Cited on page 48.]

[97] L. V. Abdurakhimov, I. Mahboob, H. Toida, K. Kakuyanagi, and S. Saito, *A long-lived capacitively shunted flux qubit embedded in a 3D cavity*, Appl. Phys. Lett. **115**, 262601 (2019). [Cited on page 48.]

[98] A. Romanenko, A. Grassellino, A. C. Crawford, D. A. Sergatskov, and O. Melnychuk, *Ultra-high quality factors in superconducting niobium cavities in ambient magnetic fields up to 190 mG*, Appl. Phys. Lett. **105**, 234103 (2014). [Cited on page 48.]

[99] A. Romanenko, R. Pilipenko, S. Zorzetti, D. Frolov, M. Awida, S. Belomestnykh, S. Posen, and A. Grassellino, *Three-Dimensional Superconducting Resonators at $T < 20$ mK with Photon Lifetimes up to $\tau = 2$ s*, Phys. Rev. Appl. **13**, 034032 (2020). [Cited on page 48.]

[100] C. U. Lei, L. Krayzman, S. Ganjam, L. Frunzio, and R. J. Schoelkopf, *High coherence superconducting microwave cavities with indium bump bonding*, Appl. Phys. Lett. **116**, 154002 (2020). [Cited on page 48.]

[101] S. Chakram, A. E. Oriani, R. K. Naik, A. V. Dixit, K. He, A. Agrawal, H. Kwon, and D. I. Schuster, *Seamless High-Q Microwave Cavities for Multimode Circuit Quantum Electrodynamics*, Phys. Rev. Lett. **127**, 107701 (2021). [Cited on page 48.]

[102] M. Reagor, H. Paik, G. Catelani, L. Sun, C. Axline, E. Holland, I. M. Pop, N. A. Masluk, T. Brecht, L. Frunzio, M. H. Devoret, L. Glazman, and R. J. Schoelkopf, *Reaching 10 ms single photon lifetimes for superconducting aluminum cavities*, Appl. Phys. Lett. **102**, 192604 (2013). [Cited on page 48.]

[103] M. Reagor, W. Pfaff, C. Axline, R. W. Heeres, N. Ofek, K. Sliwa, E. Holland, C. Wang, J. Blumoff, K. Chou, M. J. Hatridge, L. Frunzio, M. H. Devoret, L. Jiang, and R. J. Schoelkopf, *Quantum memory with millisecond coherence in circuit QED*, Phys. Rev. B **94**, 014506 (2016). [Cited on page 48.]

[104] M. Kudra, J. Biznárová, A. F. Roudsari, J. J. Burnett, D. Niepce, S. Gasparinetti, B. Wickman,

and P. Delsing, *High quality three-dimensional aluminum microwave cavities*, Appl. Phys. Lett. **117**, 070601 (2020). [Cited on page 48.]

[105] X. Wang, T. Liu, A. F. Kockum, H.-R. Li, and F. Nori, *Tunable Chiral Bound States with Giant Atoms*, Phys. Rev. Lett. **126**, 043602 (2021). [Cited on page 48.]

[106] Z. K. Minev, I. M. Pop, and M. H. Devoret, *Planar superconducting whispering gallery mode resonators*, Appl. Phys. Lett. **103**, 142604 (2013). [Cited on page 48.]

[107] Z. K. Minev, K. Serniak, I. M. Pop, Z. Leghtas, K. Sliwa, M. Hatridge, L. Frunzio, R. J. Schoelkopf, and M. H. Devoret, *Planar Multilayer Circuit Quantum Electrodynamics*, Phys. Rev. Appl. **5**, 044021 (2016). [Cited on page 48.]

[108] B. Mazin, *Microwave Kinetic Inductance Detectors*, PhD thesis, California Institute of Technology, 2004. [Cited on page 49.]

[109] M. Jerger, *Experiments on Superconducting Qubits Coupled to Resonators*, PhD thesis, KIT, 2013. [Cited on page 49.]

[110] K. Geerlings, *Improving Coherence of Superconducting Qubits and Resonators*, PhD thesis, Yale University, 2013. [Cited on page 49.]

[111] D. Schuster, *Circuit Quantum Electrodynamics*, PhD thesis, Yale Univeristy, 2007. [Cited on pages 51 and 74.]

[112] L. Frunzio, A. Wallraff, D. Schuster, J. Majer, and R. Schoelkopf, *Fabrication and characterization of superconducting circuit QED devices for quantum computation*, IEEE Trans. Appl. Supercond. **15**, 860 (2004). [Cited on pages 51 and 52.]

[113] M. Göppl, A. Fragner, M. Baur, R. Bianchetti, S. Filipp, J. M. Fink, P. J. Leek, G. Puebla, L. Steffen, and A. Wallraff, *Coplanar waveguide resonators for circuit quantum electrodynamics*, J. Appl. Phys. **104**, 113904 (2008). [Cited on pages 51 and 52.]

[114] J.-H. Yeh and S. M. Anlage, *In situ broadband cryogenic calibration for two-port superconducting microwave resonators*, Rev. Sci. Instrum. **84**, 034706 (2013). [Cited on page 52.]

[115] L. Ranzani, L. Spietz, Z. Popovic, and J. Aumentado, *Two-port microwave calibration at millikelvin temperatures*, Rev. Sci. Instrum. **84**, 034704 (2013). [Cited on page 52.]

[116] G. Cataldo, E. J. Wollack, E. M. Barrentine, A. D. Brown, S. H. Moseley, and K. U-Yen, *Analysis and calibration techniques for superconducting resonators*, Rev. Sci. Instrum. **86**, 013103 (2015). [Cited on page 52.]

[117] H. Wang, A. Zhuravel, S. Indrajeet, B. Taketani, M. Hutchings, Y. Hao, F. Rouxinol, F. Wilhelm, M. LaHaye, A. Ustinov, and B. Plourde, *Mode Structure in Superconducting Metamaterial Transmission-Line Resonators*, Phys. Rev. Appl. **11**, 054062 (2019). [Cited on page 52.]

[118] M. S. Khalil, M. J. A. Stoutimore, F. C. Wellstood, and K. D. Osborn, *An analysis method for asymmetric resonator transmission applied to superconducting devices*, J. Appl. Phys. **111**, 054510 (2012). [Cited on pages 53 and 63.]

[119] C. Deng, M. Otto, and A. Lupascu, *An analysis method for transmission measurements of superconducting resonators with applications to quantum-regime dielectric-loss measurements*, J. Appl. Phys. **114**, 054504 (2013). [Cited on page 53.]

[120] J. Leppäkangas, J. D. Brehm, P. Yang, L. Guo, M. Marthaler, A. V. Ustinov, and M. Weides,

Resonance inversion in a superconducting cavity coupled to artificial atoms and a microwave background, Phys. Rev. A **99**, 063804 (2019). [Cited on pages 53 and 60.]

[121] M. J. Collett and C. W. Gardiner, *Squeezing of intracavity and traveling-wave light fields produced in parametric amplification*, Phys. Rev. A **30**, 1386 (1984). [Cited on page 55.]

[122] P. Chak, S. Pereira, and J. E. Sipe, *Coupled-mode theory for periodic side-coupled microcavity and photonic crystal structures*, Phys. Rev. B **73**, 035105 (2006). [Cited on pages 56 and 60.]

[123] S. Fan, i. m. c. E. Kocabaş, and J.-T. Shen, *Input-output formalism for few-photon transport in one-dimensional nanophotonic waveguides coupled to a qubit*, Phys. Rev. A **82**, 063821 (2010). [Cited on page 57.]

[124] S. Xu and S. Fan, *Input-output formalism for few-photon transport: A systematic treatment beyond two photons*, Phys. Rev. A **91**, 043845 (2015). [Cited on page 57.]

[125] M. Pierre, S. R. Sathyamoorthy, I.-M. Svensson, G. Johansson, and P. Delsing, *Resonant and off-resonant microwave signal manipulation in coupled superconducting resonators*, Phys. Rev. B **99**, 094518 (2019). [Cited on page 60.]

[126] P. J. Petersan and S. M. Anlage, *Measurement of resonant frequency and quality factor of microwave resonators: Comparison of methods*, J. Appl. Phys. **84**, 3392 (1998). [Cited on page 62.]

[127] S. Probst, F. B. Song, P. A. Bushev, A. V. Ustinov, and M. Weides, *Efficient and robust analysis of complex scattering data under noise in microwave resonators*, Rev. Sci. Instrum. **86**, 024706 (2014). [Cited on page 62.]

[128] N. Chernov and C. Lesort, *Least Squares Fitting of Circles*, J. Math. Imaging Vis. **23**, 239 (2005). [Cited on page 62.]

[129] A. Palacios-Laloy, F. Nguyen, F. Mallet, P. Bertet, D. Vion, and D. Esteve, *Tunable Resonators for Quantum Circuits*, J. Low Temp. Phys. **151**, 1034 (2008). [Cited on page 64.]

[130] M. Sandberg, C. M. Wilson, F. Persson, T. Bauch, G. Johansson, V. Shumeiko, T. Duty, and P. Delsing, *Tuning the field in a microwave resonator faster than the photon lifetime*, Appl. Phys. Lett. **92**, 203501 (2008). [Cited on page 64.]

[131] H. A. Haus and J. A. Mullen, *Quantum Noise in Linear Amplifiers*, Phys. Rev. **128**, 2407 (1962). [Cited on page 69.]

[132] C. M. Caves, *Quantum limits on noise in linear amplifiers*, Phys. Rev. D **26**, 1817 (1982). [Cited on page 69.]

[133] A. A. Clerk, M. H. Devoret, S. M. Girvin, F. Marquardt, and R. J. Schoelkopf, *Introduction to quantum noise, measurement, and amplification*, Rev. Mod. Phys. **82**, 1155 (2010). [Cited on page 69.]

[134] C. M. Caves and B. L. Schumaker, *New formalism for two-photon quantum optics. I. Quadrature phases and squeezed states*, Phys. Rev. A **31**, 3068 (1985). [Cited on pages 69 and 71.]

[135] B. L. Schumaker and C. M. Caves, *New formalism for two-photon quantum optics. II. Mathematical foundation and compact notation*, Phys. Rev. A **31**, 3093 (1985). [Cited on pages 69 and 71.]

[136] S. Barnett and P. Knight, *Squeezing in Correlated Quantum Systems*, J. Mod. Opt. **34**, 841 (1987). [Cited on pages 69 and 71.]

[137] M. S. Kim and N. Imoto, *Phase-sensitive reservoir modeled by beam splitters*, Phys. Rev. A **52**, 2401 (1995). [Cited on pages 69 and 72.]

[138] M. S. Kim, *Quasiprobability functions measured by photon statistics of amplified signal fields*, Phys. Rev. A **56**, 3175 (1997). [Cited on pages 69 and 72.]

[139] C. Eichler, D. Bozyigit, and A. Wallraff, *Characterizing quantum microwave radiation and its entanglement with superconducting qubits using linear detectors*, Phys. Rev. A **86**, 032106 (2012). [Cited on pages 70, 77, 79, and 89.]

[140] M. A. Castellanos-Beltran, K. D. Irwin, G. C. Hilton, L. R. Vale, and K. W. Lehnert, *Amplification and squeezing of quantum noise with a tunable Josephson metamaterial*, Nat. Phys. **4**, 929 (2008). [Cited on page 74.]

[141] F. Mallet, M. A. Castellanos-Beltran, H. S. Ku, S. Glancy, E. Knill, K. D. Irwin, G. C. Hilton, L. R. Vale, and K. W. Lehnert, *Quantum State Tomography of an Itinerant Squeezed Microwave Field*, Phys. Rev. Lett. **106**, 220502 (2011). [Cited on pages 74, 91, and 92.]

[142] M. Hofheinz, F. Portier, Q. Baudouin, P. Joyez, D. Vion, P. Bertet, P. Roche, and D. Esteve, *Bright Side of the Coulomb Blockade*, Phys. Rev. Lett. **106**, 217005 (2011). [Cited on page 74.]

[143] C. Altimiras, O. Parlavecchio, P. Joyez, D. Vion, P. Roche, D. Esteve, and F. Portier, *Dynamical Coulomb Blockade of Shot Noise*, Phys. Rev. Lett. **112**, 236803 (2014). [Cited on page 74.]

[144] M. Westig, B. Kubala, O. Parlavecchio, Y. Mukharsky, C. Altimiras, P. Joyez, D. Vion, P. Roche, D. Esteve, M. Hofheinz, M. Trif, P. Simon, J. Ankerhold, and F. Portier, *Emission of Nonclassical Radiation by Inelastic Cooper Pair Tunneling*, Phys. Rev. Lett. **119**, 137001 (2017). [Cited on page 74.]

[145] C. Vaneph, A. Morvan, G. Aiello, M. Féchant, M. Aprili, J. Gabelli, and J. Estève, *Observation of the Unconventional Photon Blockade in the Microwave Domain*, Phys. Rev. Lett. **121**, 043602 (2018). [Cited on pages 74 and 113.]

[146] M. Mariantoni, E. P. Menzel, F. Deppe, M. A. Araque Caballero, A. Baust, T. Niemczyk, E. Hoffmann, E. Solano, A. Marx, and R. Gross, *Planck Spectroscopy and Quantum Noise of Microwave Beam Splitters*, Phys. Rev. Lett. **105**, 133601 (2010). [Cited on pages 74 and 79.]

[147] E. P. Menzel, F. Deppe, M. Mariantoni, M. A. Araque Caballero, A. Baust, T. Niemczyk, E. Hoffmann, A. Marx, E. Solano, and R. Gross, *Dual-Path State Reconstruction Scheme for Propagating Quantum Microwaves and Detector Noise Tomography*, Phys. Rev. Lett. **105**, 100401 (2010). [Cited on pages 74 and 77.]

[148] E. P. Menzel, R. Di Candia, F. Deppe, P. Eder, L. Zhong, M. Ihmig, M. Haeberlein, A. Baust, E. Hoffmann, D. Ballester, K. Inomata, T. Yamamoto, Y. Nakamura, E. Solano, A. Marx, and R. Gross, *Path Entanglement of Continuous-Variable Quantum Microwaves*, Phys. Rev. Lett. **109**, 250502 (2012). [Cited on pages 74 and 77.]

[149] L. Zhong, E. P. Menzel, R. D. Candia, P. Eder, M. Ihmig, A. Baust, M. Haeberlein, E. Hoffmann, K. Inomata, T. Yamamoto, Y. Nakamura, E. Solano, F. Deppe, A. Marx, and R. Gross, *Squeezing with a flux-driven Josephson parametric amplifier*, New J. Phys. **15**, 125013 (2013). [Cited on pages 74 and 77.]

[150] K. G. Fedorov, L. Zhong, S. Pogorzalek, P. Eder, M. Fischer, J. Goetz, E. Xie, F. Wulschner, K. Inomata, T. Yamamoto, Y. Nakamura, R. Di Candia, U. Las Heras, M. Sanz, E. Solano, E. P. Menzel, F. Deppe, A. Marx, and R. Gross, *Displacement of Propagating Squeezed Microwave States*, Phys. Rev. Lett. **117**, 020502 (2016). [Cited on pages 74 and 77.]

[151] J. Goetz, S. Pogorzalek, F. Deppe, K. G. Fedorov, P. Eder, M. Fischer, F. Wulschner, E. Xie, A. Marx, and R. Gross, *Photon Statistics of Propagating Thermal Microwaves*, Phys. Rev. Lett. **118**, 103602 (2017). [Cited on pages 74 and 77.]

[152] K. G. Fedorov, S. Pogorzalek, U. L. Heras, M. Sanz, P. Yard, P. Eder, M. Fischer, J. Goetz, E. Xie, K. Inomata, Y. Nakamura, R. D. Candia, E. Solano, A. Marx, F. Deppe, and R. Gross, *Finite-time quantum entanglement in propagating squeezed microwaves*, Sci. Rep. **8**, 6416 (2018). [Cited on pages 74 and 77.]

[153] S. Pogorzalek, K. G. Fedorov, M. Xu, A. Parra-Rodriguez, M. Sanz, M. Fischer, E. Xie, K. Inomata, Y. Nakamura, E. Solano, A. Marx, F. Deppe, and R. Gross, *Secure quantum remote state preparation of squeezed microwave states*, Nat. Commun. **10**, 1604 (2019). [Cited on pages 74 and 77.]

[154] M. Renger, S. Pogorzalek, Q. Chen, Y. Nojiri, K. Inomata, Y. Nakamura, M. Partanen, A. Marx, R. Gross, F. Deppe, and K. G. Fedorov, *Beyond the standard quantum limit for parametric amplification of broadband signals*, npj Quantum Inf. **7**, 1 (2021). [Cited on pages 74 and 77.]

[155] K. G. Fedorov, M. Renger, S. Pogorzalek, R. D. Candia, Q.-M. Chen, Y. Nojiri, K. Inomata, Y. Nakamura, M. Partanen, A. Marx, R. Gross, and F. Deppe, *Experimental quantum teleportation of propagating microwaves*, Sci. Adv. **7**, eabk0891 (2021). [Cited on pages 74 and 77.]

[156] D. Bozyigit, C. Lang, L. Steffen, J. M. Fink, C. Eichler, M. Baur, R. Bianchetti, P. J. Leek, S. Filipp, M. P. da Silva, A. Blais, and A. Wallraff, *Antibunching of microwave-frequency photons observed in correlation measurements using linear detectors*, Nat. Phys. **7**, 154 (2010). [Cited on pages 74, 77, and 113.]

[157] C. Lang, D. Bozyigit, C. Eichler, L. Steffen, J. M. Fink, A. A. Abdumalikov, M. Baur, S. Filipp, M. P. da Silva, A. Blais, and A. Wallraff, *Observation of Resonant Photon Blockade at Microwave Frequencies Using Correlation Function Measurements*, Phys. Rev. Lett. **106**, 243601 (2011). [Cited on pages 74, 77, 85, and 113.]

[158] C. Lang, C. Eichler, L. Steffen, J. M. Fink, M. J. Woolley, A. Blais, and A. Wallraff, *Correlations, indistinguishability and entanglement in Hong–Ou–Mandel experiments at microwave frequencies*, Nat. Phys. **9**, 345 (2013). [Cited on pages 74, 77, and 85.]

[159] S. Gasparinetti, M. Pechal, J.-C. Besse, M. Mondal, C. Eichler, and A. Wallraff, *Correlations and Entanglement of Microwave Photons Emitted in a Cascade Decay*, Phys. Rev. Lett. **119**, 140504 (2017). [Cited on pages 74, 77, and 85.]

[160] M. C. Collodo, A. Potočnik, S. Gasparinetti, J.-C. Besse, M. Pechal, M. Sameti, M. J. Hartmann, A. Wallraff, and C. Eichler, *Observation of the Crossover from Photon Ordering to Delocalization in Tunably Coupled Resonators*, Phys. Rev. Lett. **122**, 183601 (2019). [Cited on pages 74, 77, and 85.]

[161] C. Rolland, A. Peugeot, S. Dambach, M. Westig, B. Kubala, Y. Mukharsky, C. Altimiras,

H. le Sueur, P. Joyez, D. Vion, P. Roche, D. Esteve, J. Ankerhold, and F. Portier, *Antibunched Photons Emitted by a dc-Biased Josephson Junction*, Phys. Rev. Lett. **122**, 186804 (2019). [Cited on pages 74 and 77.]

[162] A. Peugeot, G. Ménard, S. Dambach, M. Westig, B. Kubala, Y. Mukharsky, C. Altimiras, P. Joyez, D. Vion, P. Roche, D. Esteve, P. Milman, J. Leppäkangas, G. Johansson, M. Hofheinz, J. Ankerhold, and F. Portier, *Generating Two Continuous Entangled Microwave Beams Using a dc-Biased Josephson Junction*, Phys. Rev. X **11**, 031008 (2021). [Cited on pages 74 and 77.]

[163] E. Menzel, *Propagating Quantum Microwaves: Dual-path State Reconstruction and Path Entanglement*, PhD thesis, WMI, 2013. [Cited on pages 74, 76, and 80.]

[164] J. Goetz, *The Interplay of Superconducting Quantum Circuits andPropagating Microwave States*, PhD thesis, WMI, 2017. [Cited on page 74.]

[165] T. Schilcher, Rf applications in digital signal processing, in *CERN Accelerator School Digital Signal Processing*, edited by D. Brandt, pages 249–283, 2007. [Cited on pages 75 and 76.]

[166] C. L. Phillips, A. J. Brash, D. P. S. McCutcheon, J. Iles-Smith, E. Clarke, B. Royall, M. S. Skolnick, A. M. Fox, and A. Nazir, *Photon Statistics of Filtered Resonance Fluorescence*, Phys. Rev. Lett. **125**, 043603 (2020). [Cited on page 75.]

[167] L. Hanschke, L. Schweickert, J. C. L. Carreño, E. Schöll, K. D. Zeuner, T. Lettner, E. Z. Casalengua, M. Reindl, S. F. C. da Silva, R. Trotta, J. J. Finley, A. Rastelli, E. del Valle, F. P. Laussy, V. Zwiller, K. Müller, and K. D. Jöns, *Origin of Antibunching in Resonance Fluorescence*, Phys. Rev. Lett. **125**, 170402 (2020). [Cited on page 75.]

[168] C. Lang, *Quantum Microwave Radiation and its Interference Characterized by Correlation Function Measurements in Circuit Quantum Electrodynamics*, PhD thesis, ETH Zurich, 2014. [Cited on page 76.]

[169] C. Eichler, *Experimental Characterization of Quantum Microwave Radiation and its Entanglement with a Superconducting Qubit*, PhD thesis, ETH Zurich, 2013. [Cited on pages 77, 88, and 89.]

[170] B. Yurke, L. R. Corruccini, P. G. Kaminsky, L. W. Rupp, A. D. Smith, A. H. Silver, R. W. Simon, and E. A. Whittaker, *Observation of parametric amplification and deamplification in a Josephson parametric amplifier*, Phys. Rev. A **39**, 2519 (1989). [Cited on page 77.]

[171] T. Yamamoto, K. Inomata, M. Watanabe, K. Matsuba, T. Miyazaki, W. D. Oliver, Y. Nakamura, and J. S. Tsai, *Flux-driven Josephson parametric amplifier*, Appl. Phys. Lett. **93**, 042510 (2008). [Cited on page 77.]

[172] C. Eichler, Y. Salathe, J. Mlynek, S. Schmidt, and A. Wallraff, *Quantum-Limited Amplification and Entanglement in Coupled Nonlinear Resonators*, Phys. Rev. Lett. **113**, 110502 (2014). [Cited on page 77.]

[173] C. Eichler and A. Wallraff, *Controlling the dynamic range of a Josephson parametric amplifier*, EPJ Quantum Technol. **1** (2014). [Cited on page 77.]

[174] T. Roy, S. Kundu, M. Chand, A. M. Vadiraj, A. Ranadive, N. Nehra, M. P. Patankar, J. Aumentado, A. A. Clerk, and R. Vijay, *Broadband parametric amplification with impedance engineering: Beyond the gain-bandwidth product*, Appl. Phys. Lett. **107**, 262601 (2015). [Cited on page 77.]

[175] P. Krantz, A. Bengtsson, M. Simoen, S. Gustavsson, V. Shumeiko, W. D. Oliver, C. M. Wilson, P. Delsing, and J. Bylander, *Single-shot read-out of a superconducting qubit using a Josephson parametric oscillator*, Nat. Commun. **7** (2016). [Cited on page 77.]

[176] S. Pogorzalek, K. G. Fedorov, L. Zhong, J. Goetz, F. Wulschner, M. Fischer, P. Eder, E. Xie, K. Inomata, T. Yamamoto, Y. Nakamura, A. Marx, F. Deppe, and R. Gross, *Hysteretic Flux Response and Nondegenerate Gain of Flux-Driven Josephson Parametric Amplifiers*, Phys. Rev. Appl. **8**, 024012 (2017). [Cited on page 77.]

[177] J. Grebel, A. Bienfait, É. Dumur, H.-S. Chang, M.-H. Chou, C. R. Conner, G. A. Peairs, R. G. Povey, Y. P. Zhong, and A. N. Cleland, *Flux-pumped impedance-engineered broadband Josephson parametric amplifier*, Appl. Phys. Lett. **118**, 142601 (2021). [Cited on page 77.]

[178] O. Yaakobi, L. Friedland, C. Macklin, and I. Siddiqi, *Parametric amplification in Josephson junction embedded transmission lines*, Phys. Rev. B **87**, 144301 (2013). [Cited on page 77.]

[179] K. O'Brien, C. Macklin, I. Siddiqi, and X. Zhang, *Resonant Phase Matching of Josephson Junction Traveling Wave Parametric Amplifiers*, Phys. Rev. Lett. **113**, 157001 (2014). [Cited on page 77.]

[180] C. Macklin, K. O'Brien, D. Hover, M. E. Schwartz, V. Bolkhovsky, X. Zhang, W. D. Oliver, and I. Siddiqi, *A near–quantum-limited Josephson traveling-wave parametric amplifier*, Science **350**, 307 (2015). [Cited on page 77.]

[181] T. C. White, J. Y. Mutus, I.-C. Hoi, R. Barends, B. Campbell, Y. Chen, Z. Chen, B. Chiaro, A. Dunsworth, E. Jeffrey, J. Kelly, A. Megrant, C. Neill, P. J. J. O'Malley, P. Roushan, D. Sank, A. Vainsencher, J. Wenner, S. Chaudhuri, J. Gao, and J. M. Martinis, *Traveling wave parametric amplifier with Josephson junctions using minimal resonator phase matching*, Appl. Phys. Lett. **106**, 242601 (2015). [Cited on page 77.]

[182] V. V. Sivak, S. Shankar, G. Liu, J. Aumentado, and M. H. Devoret, *Josephson Array-Mode Parametric Amplifier*, Phys. Rev. Appl. **13**, 024014 (2020). [Cited on page 77.]

[183] N. Bergeal, F. Schackert, M. Metcalfe, R. Vijay, V. E. Manucharyan, L. Frunzio, D. E. Prober, R. J. Schoelkopf, S. M. Girvin, and M. H. Devoret, *Phase-preserving amplification near the quantum limit with a Josephson ring modulator*, Nature **465**, 64 (2010). [Cited on page 77.]

[184] N. Bergeal, R. Vijay, V. E. Manucharyan, I. Siddiqi, R. J. Schoelkopf, S. M. Girvin, and M. H. Devoret, *Analog information processing at the quantum limit with a Josephson ring modulator*, Nat. Phys. **6**, 296 (2010). [Cited on page 77.]

[185] N. Roch, E. Flurin, F. Nguyen, P. Morfin, P. Campagne-Ibarcq, M. H. Devoret, and B. Huard, *Widely Tunable, Nondegenerate Three-Wave Mixing Microwave Device Operating near the Quantum Limit*, Phys. Rev. Lett. **108**, 147701 (2012). [Cited on page 77.]

[186] J.-D. Pillet, E. Flurin, F. Mallet, and B. Huard, *A compact design for the Josephson mixer: The lumped element circuit*, Appl. Phys. Lett. **106**, 222603 (2015). [Cited on page 77.]

[187] C. Eichler, D. Bozyigit, C. Lang, L. Steffen, J. Fink, and A. Wallraff, *Experimental State Tomography of Itinerant Single Microwave Photons*, Phys. Rev. Lett. **106**, 220503 (2011). [Cited on pages 77 and 85.]

[188] C. Eichler, D. Bozyigit, C. Lang, M. Baur, L. Steffen, J. M. Fink, S. Filipp, and A. Wallraff,

Observation of Two-Mode Squeezing in the Microwave Frequency Domain, Phys. Rev. Lett. **107**, 113601 (2011). [Cited on pages 77 and 85.]

[189] C. Eichler, C. Lang, J. M. Fink, J. Govenius, S. Filipp, and A. Wallraff, *Observation of Entanglement between Itinerant Microwave Photons and a Superconducting Qubit*, Phys. Rev. Lett. **109**, 240501 (2012). [Cited on pages 77 and 85.]

[190] F. R. Ong, M. Boissonneault, F. Mallet, A. Palacios-Laloy, A. Dewes, A. C. Doherty, A. Blais, P. Bertet, D. Vion, and D. Esteve, *Circuit QED with a Nonlinear Resonator: ac-Stark Shift and Dephasing*, Phys. Rev. Lett. **106**, 167002 (2011). [Cited on page 81.]

[191] S. Haroche and J.-M. Raimond, *Exploring the Quantum: Atoms, Cavities, and Photons*, Oxford University Press, 2006. [Cited on page 81.]

[192] Q.-M. Chen, F. Deppe, Y. Nojiri, M. Renger, S. Pogorzalek, M. Partanen, K. G. Fedorov, A. Marx, and R. Gross, *Measurement of the second-order correlation functions under different signal-to-noise ratios*, in *WMI Annual Report*, pages 51–52, 2019. [Cited on page 83.]

[193] D. F. V. James, P. G. Kwiat, W. J. Munro, and A. G. White, *Measurement of qubits*, Phys. Rev. A **64**, 052312 (2001). [Cited on page 84.]

[194] H. Häffner, W. Hänsel, C. F. Roos, J. Benhelm, D. C. al kar, M. Chwalla, T. Körber, U. D. Rapol, M. Riebe, P. O. Schmidt, C. Becher, O. Gühne, W. Dür, and R. Blatt, *Scalable multiparticle entanglement of trapped ions*, Nature **438**, 643 (2005). [Cited on page 85.]

[195] M. S. Kaznady and D. F. V. James, *Numerical strategies for quantum tomography: Alternatives to full optimization*, Phys. Rev. A **79**, 022109 (2009). [Cited on page 85.]

[196] J. M. Chow, A. D. Córcoles, J. M. Gambetta, C. Rigetti, B. R. Johnson, J. A. Smolin, J. R. Rozen, G. A. Keefe, M. B. Rothwell, M. B. Ketchen, and M. Steffen, *Simple All-Microwave Entangling Gate for Fixed-Frequency Superconducting Qubits*, Phys. Rev. Lett. **107**, 080502 (2011). [Cited on page 85.]

[197] J. A. Smolin, J. M. Gambetta, and G. Smith, *Efficient Method for Computing the Maximum-Likelihood Quantum State from Measurements with Additive Gaussian Noise*, Phys. Rev. Lett. **108**, 070502 (2012). [Cited on page 85.]

[198] A. Wunsche, *Displaced Fock states and their connection to quasiprobabilities*, Quantum Opt. **3**, 359 (1991). [Cited on page 89.]

[199] Z. Hradil, *Quantum-state estimation*, Phys. Rev. A **55**, R1561 (1997). [Cited on page 89.]

[200] J. Řeháček, Z. Hradil, and M. Ježek, *Iterative algorithm for reconstruction of entangled states*, Phys. Rev. A **63**, 040303 (2001). [Cited on page 89.]

[201] Z. Hradil, D. Mogilevtsev, and J. Řeháček, *Biased Tomography Schemes: An Objective Approach*, Phys. Rev. Lett. **96**, 230401 (2006). [Cited on page 89.]

[202] J. Řeháček, Z. Hradil, E. Knill, and A. I. Lvovsky, *Diluted maximum-likelihood algorithm for quantum tomography*, Phys. Rev. A **75**, 042108 (2007). [Cited on page 89.]

[203] D. Mogilevtsev, J. Řeháček, and Z. Hradil, *Objective approach to biased tomography schemes*, Phys. Rev. A **75**, 012112 (2007). [Cited on page 89.]

[204] A. I. Lvovsky and M. G. Raymer, *Continuous-variable optical quantum-state tomography*, Rev. Mod. Phys. **81**, 299 (2009). [Cited on pages 89 and 91.]

[205] K. Vogel and H. Risken, *Quasiprobability distributions in dispersive optical bistability*, Phys. Rev. A **39**, 4675 (1989). [Cited on page 91.]

[206] D. T. Smithey, M. Beck, M. G. Raymer, and A. Faridani, *Measurement of the Wigner distribution and the density matrix of a light mode using optical homodyne tomography: Application to squeezed states and the vacuum*, Phys. Rev. Lett. **70**, 1244 (1993). [Cited on page 91.]

[207] G. L. Zeng, *Medical Image Reconstruction: A Conceptual Tutorial*, Springer-Verlag Berlin Heidelberg, 2010. [Cited on page 91.]

[208] D. Donoho, *Compressed sensing*, IEEE Transactions on Information Theory **52**, 1289 (2006). [Cited on page 91.]

[209] E. J. Candes and T. Tao, *Near-Optimal Signal Recovery From Random Projections: Universal Encoding Strategies?*, IEEE Transactions on Information Theory **52**, 5406 (2006). [Cited on page 91.]

[210] E. J. Candes and M. B. Wakin, *An Introduction To Compressive Sampling*, IEEE Signal Processing Magazine **25**, 21 (2008). [Cited on page 91.]

[211] D. Gross, Y.-K. Liu, S. T. Flammia, S. Becker, and J. Eisert, *Quantum State Tomography via Compressed Sensing*, Phys. Rev. Lett. **105**, 150401 (2010). [Cited on page 92.]

[212] A. Shabani, R. L. Kosut, M. Mohseni, H. Rabitz, M. A. Broome, M. P. Almeida, A. Fedrizzi, and A. G. White, *Efficient Measurement of Quantum Dynamics via Compressive Sensing*, Phys. Rev. Lett. **106**, 100401 (2011). [Cited on page 92.]

[213] C. A. Riofrío, D. Gross, S. T. Flammia, T. Monz, D. Nigg, R. Blatt, and J. Eisert, *Experimental quantum compressed sensing for a seven-qubit system*, Nat. Commun. **8** (2017). [Cited on page 92.]

[214] Y.-F. Chen, D. Hover, S. Sendelbach, L. Maurer, S. T. Merkel, E. J. Pritchett, F. K. Wilhelm, and R. McDermott, *Microwave Photon Counter Based on Josephson Junctions*, Phys. Rev. Lett. **107**, 217401 (2011). [Cited on page 92.]

[215] L. C. G. Govia, E. J. Pritchett, C. Xu, B. L. T. Plourde, M. G. Vavilov, F. K. Wilhelm, and R. McDermott, *High-fidelity qubit measurement with a microwave-photon counter*, Phys. Rev. A **90**, 062307 (2014). [Cited on page 92.]

[216] A. Opremcak, I. V. Pechenezhskiy, C. Howington, B. G. Christensen, M. A. Beck, E. Leonard, J. Suttle, C. Wilen, K. N. Nesterov, G. J. Ribeill, T. Thorbeck, F. Schlenker, M. G. Vavilov, B. L. T. Plourde, and R. McDermott, *Measurement of a superconducting qubit with a microwave photon counter*, Science **361**, 1239 (2018). [Cited on page 92.]

[217] R. Aguado and L. P. Kouwenhoven, *Double Quantum Dots as Detectors of High-Frequency Quantum Noise in Mesoscopic Conductors*, Phys. Rev. Lett. **84**, 1986 (2000). [Cited on page 92.]

[218] C. W. J. Beenakker and H. Schomerus, *Counting Statistics of Photons Produced by Electronic Shot Noise*, Phys. Rev. Lett. **86**, 700 (2001). [Cited on page 92.]

[219] R. Deblock, E. Onac, L. Gurevich, and L. P. Kouwenhoven, *Detection of Quantum Noise from an Electrically Driven Two-Level System*, Science **301**, 203 (2003). [Cited on page 92.]

[220] E. Onac, F. Balestro, B. Trauzettel, C. F. J. Lodewijk, and L. P. Kouwenhoven, *Shot-Noise Detection in a Carbon Nanotube Quantum Dot*, Phys. Rev. Lett. **96**, 026803 (2006). [Cited on page 92.]

[221] S. Gustavsson, M. Studer, R. Leturcq, T. Ihn, K. Ensslin, D. C. Driscoll, and A. C. Gossard, *Frequency-Selective Single-Photon Detection Using a Double Quantum Dot*, Phys. Rev. Lett. **99**, 206804 (2007). [Cited on page 92.]

[222] G. Romero, J. J. García-Ripoll, and E. Solano, *Microwave Photon Detector in Circuit QED*, Phys. Rev. Lett. **102**, 173602 (2009). [Cited on page 92.]

[223] J.-C. Besse, S. Gasparinetti, M. C. Collodo, T. Walter, P. Kurpiers, M. Pechal, C. Eichler, and A. Wallraff, *Single-Shot Quantum Nondemolition Detection of Individual Itinerant Microwave Photons*, Phys. Rev. X **8**, 021003 (2018). [Cited on page 92.]

[224] R. Lescanne, S. Deléglise, E. Albertinale, U. Réglade, T. Capelle, E. Ivanov, T. Jacqmin, Z. Leghtas, and E. Flurin, *Irreversible Qubit-Photon Coupling for the Detection of Itinerant Microwave Photons*, Phys. Rev. X **10**, 021038 (2020). [Cited on page 92.]

[225] R. Dassonneville, R. Assouly, T. Peronnin, P. Rouchon, and B. Huard, *Number-Resolved Photocounter for Propagating Microwave Mode*, Phys. Rev. Appl. **14**, 044022 (2020). [Cited on page 92.]

[226] L. G. Lutterbach and L. Davidovich, *Method for Direct Measurement of the Wigner Function in Cavity QED and Ion Traps*, Phys. Rev. Lett. **78**, 2547 (1997). [Cited on pages 92 and 93.]

[227] M. S. Kim, G. Antesberger, C. T. Bodendorf, and H. Walther, *Scheme for direct observation of the Wigner characteristic function in cavity QED*, Phys. Rev. A **58** (1998). [Cited on pages 92 and 93.]

[228] P. Bertet, A. Auffeves, P. Maioli, S. Osnaghi, T. Meunier, M. Brune, J. M. Raimond, and S. Haroche, *Direct Measurement of the Wigner Function of a One-Photon Fock State in a Cavity*, Phys. Rev. Lett. **89**, 200402 (2002). [Cited on pages 92 and 93.]

[229] M. Hofheinz, E. M. Weig, M. Ansmann, R. C. Bialczak, E. Lucero, M. Neeley, A. D. O'Connell, H. Wang, J. M. Martinis, and A. N. Cleland, *Generation of Fock states in a superconducting quantum circuit*, Nature **454**, 310 (2008). [Cited on page 93.]

[230] M. Hofheinz, H. Wang, M. Ansmann, R. C. Bialczak, E. Lucero, M. Neeley, A. D. O'Connell, D. Sank, J. Wenner, J. M. Martinis, and A. N. Cleland, *Synthesizing arbitrary quantum states in a superconducting resonator*, Nature **459**, 546 (2009). [Cited on page 93.]

[231] G. Kirchmair, B. Vlastakis, Z. Leghtas, S. E. Nigg, H. Paik, E. Ginossar, M. Mirrahimi, L. Frunzio, S. M. Girvin, and R. J. Schoelkopf, *Observation of quantum state collapse and revival due to the single-photon Kerr effect*, Nature **495**, 205 (2013). [Cited on pages 93 and 108.]

[232] Y. Shalibo, R. Resh, O. Fogel, D. Shwa, R. Bialczak, J. M. Martinis, and N. Katz, *Direct Wigner Tomography of a Superconducting Anharmonic Oscillator*, Phys. Rev. Lett. **110**, 100404 (2013). [Cited on pages 93 and 108.]

[233] L. Sun, A. Petrenko, Z. Leghtas, B. Vlastakis, G. Kirchmair, K. M. Sliwa, A. Narla, M. Hatridge, S. Shankar, J. Blumoff, L. Frunzio, M. Mirrahimi, M. H. Devoret, and R. J. Schoelkopf, *Tracking photon jumps with repeated quantum non-demolition parity measurements*, Nature **511**, 444 (2014). [Cited on page 93.]

[234] J.-C. Besse, S. Gasparinetti, M. C. Collodo, T. Walter, A. Remm, J. Krause, C. Eichler, and A. Wallraff, *Parity Detection of Propagating Microwave Fields*, Phys. Rev. X **10**, 011046 (2020). [Cited on page 93.]

[235] N. Lu, *Effects of dissipation on photon statistics and the lifetime of a pure number state*, Phys. Rev. A **40**, 1707 (1989). [Cited on page 93.]

[236] H. Wang, M. Hofheinz, M. Ansmann, R. C. Bialczak, E. Lucero, M. Neeley, A. D. O'Connell, D. Sank, J. Wenner, A. N. Cleland, and J. M. Martinis, *Measurement of the Decay of Fock States in a Superconducting Quantum Circuit*, Phys. Rev. Lett. **101**, 240401 (2008). [Cited on page 93.]

[237] A. H. Nayfeh and D. T. Mook, *Nonlinear Oscillations*, John Wiley & Sons, Ltd, 1995. [Cited on pages 97 and 127.]

[238] N. S. Maslova, E. V. Anikin, N. A. Gippius, and I. M. Sokolov, *Effects of tunneling and multiphoton transitions on squeezed-state generation in bistable driven systems*, Phys. Rev. A **99**, 043802 (2019). [Cited on pages 97, 99, 127, and 128.]

[239] I. Siddiqi, R. Vijay, F. Pierre, C. M. Wilson, M. Metcalfe, C. Rigetti, L. Frunzio, and M. H. Devoret, *RF-Driven Josephson Bifurcation Amplifier for Quantum Measurement*, Phys. Rev. Lett. **93**, 207002 (2004). [Cited on page 97.]

[240] I. Siddiqi, R. Vijay, F. Pierre, C. M. Wilson, L. Frunzio, M. Metcalfe, C. Rigetti, R. J. Schoelkopf, M. H. Devoret, D. Vion, and D. Esteve, *Direct Observation of Dynamical Bifurcation between Two Driven Oscillation States of a Josephson Junction*, Phys. Rev. Lett. **94**, 027005 (2005). [Cited on page 97.]

[241] H. M. Gibbs, S. L. McCall, and T. N. C. Venkatesan, *Differential Gain and Bistability Using a Sodium-Filled Fabry-Perot Interferometer*, Phys. Rev. Lett. **36**, 1135 (1976). [Cited on page 97.]

[242] G. Rempe, R. J. Thompson, R. J. Brecha, W. D. Lee, and H. J. Kimble, *Optical bistability and photon statistics in cavity quantum electrodynamics*, Phys. Rev. Lett. **67**, 1727 (1991). [Cited on page 97.]

[243] Z. Lin, K. Inomata, K. Koshino, W. Oliver, Y. Nakamura, J. Tsai, and T. Yamamoto, *Josephson parametric phase-locked oscillator and its application to dispersive readout of superconducting qubits*, Nat. Commun. **5**, 4480 (2014). [Cited on page 97.]

[244] J. Fajans and L. Frièdland, *Autoresonant (nonstationary) excitation of pendulums, Plutinos, plasmas, and other nonlinear oscillators*, Am. J. Phys. **69**, 1096 (2001). [Cited on page 97.]

[245] K. W. Murch, R. Vijay, I. Barth, O. Naaman, J. Aumentado, L. Friedland, and I. Siddiqi, *Quantum fluctuations in the chirped pendulum*, Nat. Phys. **7**, 105 (2010). [Cited on page 97.]

[246] P. D. Drummond and D. F. Walls, *Quantum theory of optical bistability. I. Nonlinear polarisability model*, J. Phys. A: Math. Gen. **13**, 725 (1980). [Cited on pages 97, 98, 99, 100, 104, 106, and 127.]

[247] T. K. Mavrogordatos, G. Tancredi, M. Elliott, M. J. Peterer, A. Patterson, J. Rahamim, P. J. Leek, E. Ginossar, and M. H. Szymańska, *Simultaneous Bistability of a Qubit and Resonator in Circuit Quantum Electrodynamics*, Phys. Rev. Lett. **118**, 040402 (2017). [Cited on pages 97 and 104.]

[248] P. Brookes, G. Tancredi, A. D. Patterson, J. Rahamim, M. Esposito, T. K. Mavrogordatos, P. J. Leek, E. Ginossar, and M. H. Szymanska, *Critical slowing down in circuit quantum electrodynamics*, Sci. Adv. **7** (2021). [Cited on pages 97, 104, and 105.]

[249] S. R. K. Rodriguez, W. Casteels, F. Storme, N. Carlon Zambon, I. Sagnes, L. Le Gratiet,

E. Galopin, A. Lemaître, A. Amo, C. Ciuti, and J. Bloch, *Probing a Dissipative Phase Transition via Dynamical Optical Hysteresis*, Phys. Rev. Lett. **118**, 247402 (2017). [Cited on pages 97 and 105.]

[250] T. Fink, A. Schade, S. Höfling, C. Schneider, and A. Imamoglu, *Signatures of a dissipative phase transition in photon correlation measurements*, Nat. Phys. **14**, 365 (2017). [Cited on pages 97 and 104.]

[251] K. Macieszczak, M. Guţă, I. Lesanovsky, and J. P. Garrahan, *Towards a Theory of Metastability in Open Quantum Dynamics*, Phys. Rev. Lett. **116**, 240404 (2016). [Cited on pages 97 and 101.]

[252] W. Casteels, R. Fazio, and C. Ciuti, *Critical dynamical properties of a first-order dissipative phase transition*, Phys. Rev. A **95**, 012128 (2017). [Cited on pages 97, 101, 102, 106, and 109.]

[253] F. Minganti, A. Biella, N. Bartolo, and C. Ciuti, *Spectral theory of Liouvillians for dissipative phase transitions*, Phys. Rev. A **98**, 042118 (2018). [Cited on pages 97, 101, 107, and 109.]

[254] K. V. Kheruntsyan, *Wigner function for a driven anharmonic oscillator*, J. Opt. B: Quantum Semiclass. Opt. **1**, 225 (1999). [Cited on page 98.]

[255] V. V. Albert and L. Jiang, *Symmetries and conserved quantities in Lindblad master equations*, Phys. Rev. A **89**, 022118 (2014). [Cited on page 101.]

[256] M. P. A. Fisher, P. B. Weichman, G. Grinstein, and D. S. Fisher, *Boson localization and the superfluid-insulator transition*, Phys. Rev. B **40**, 546 (1989). [Cited on page 102.]

[257] D. Jaksch, C. Bruder, J. I. Cirac, C. W. Gardiner, and P. Zoller, *Cold Bosonic Atoms in Optical Lattices*, Phys. Rev. Lett. **81**, 3108 (1998). [Cited on page 102.]

[258] M. Greiner, O. Mandel, T. Esslinger, T. W. Hänsch, and I. Bloch, *Quantum phase transition from a superfluid to a Mott insulator in a gas of ultracold atoms*, Nature **415**, 39 (2002). [Cited on page 102.]

[259] I. Bloch, J. Dalibard, and W. Zwerger, *Many-body physics with ultracold gases*, Rev. Mod. Phys. **80**, 885 (2008). [Cited on page 102.]

[260] W. S. Bakr, A. Peng, M. E. Tai, R. Ma, J. Simon, J. I. Gillen, S. Fölling, L. Pollet, and M. Greiner, *Probing the Superfluid–to–Mott Insulator Transition at the Single-Atom Level*, Science **329**, 547 (2010). [Cited on page 102.]

[261] I. Carusotto and C. Ciuti, *Quantum fluids of light*, Rev. Mod. Phys. **85**, 299 (2013). [Cited on pages 102 and 113.]

[262] A. Le Boité, G. Orso, and C. Ciuti, *Bose-Hubbard model: Relation between driven-dissipative steady states and equilibrium quantum phases*, Phys. Rev. A **90**, 063821 (2014). [Cited on pages 102 and 113.]

[263] P. Jung, G. Gray, R. Roy, and P. Mandel, *Scaling law for dynamical hysteresis*, Phys. Rev. Lett. **65**, 1873 (1990). [Cited on page 105.]

[264] W. Casteels, F. Storme, A. Le Boité, and C. Ciuti, *Power laws in the dynamic hysteresis of quantum nonlinear photonic resonators*, Phys. Rev. A **93**, 033824 (2016). [Cited on page 105.]

[265] A. Le Boité, G. Orso, and C. Ciuti, *Steady-State Phases and Tunneling-Induced Instabilities in the Driven Dissipative Bose-Hubbard Model*, Phys. Rev. Lett. **110**, 233601 (2013). [Cited on page 106.]

[266] J. Bajer, A. Miranowicz, and M. Andrzejewski, *Quantum noise and mixedness of a pumped dissipative non-linear oscillator*, J. Opt. B: Quantum Semiclass. **6**, 387 (2004). [Cited on page 109.]

[267] S. Pogorzalek, *Remote State Preparation of Squeezed Microwave States*, PhD thesis, WMI, 2020. [Cited on page 109.]

[268] J. Raftery, D. Sadri, S. Schmidt, H. E. Türeci, and A. A. Houck, *Observation of a Dissipation-Induced Classical to Quantum Transition*, Phys. Rev. X **4**, 031043 (2014). [Cited on page 112.]

[269] M. Fitzpatrick, N. M. Sundaresan, A. C. Y. Li, J. Koch, and A. A. Houck, *Observation of a Dissipative Phase Transition in a One-Dimensional Circuit QED Lattice*, Phys. Rev. X **7**, 011016 (2017). [Cited on page 112.]

[270] R. Ma, B. Saxberg, C. Owens, N. Leung, Y. Lu, J. Simon, and D. I. Schuster, *A dissipatively stabilized Mott insulator of photons*, Nature **566**, 51 (2019). [Cited on page 112.]

[271] M. J. Hartmann, *Polariton Crystallization in Driven Arrays of Lossy Nonlinear Resonators*, Phys. Rev. Lett. **104**, 113601 (2010). [Cited on page 113.]

[272] M. Biondi, G. Blatter, H. E. Türeci, and S. Schmidt, *Nonequilibrium gas-liquid transition in the driven-dissipative photonic lattice*, Phys. Rev. A **96**, 043809 (2017). [Cited on page 113.]

[273] I. Carusotto, D. Gerace, H. E. Tureci, S. De Liberato, C. Ciuti, and A. Imamoğlu, *Fermionized Photons in an Array of Driven Dissipative Nonlinear Cavities*, Phys. Rev. Lett. **103**, 033601 (2009). [Cited on page 113.]

[274] L. Tian and H. J. Carmichael, *Quantum trajectory simulations of two-state behavior in an optical cavity containing one atom*, Phys. Rev. A **46**, R6801 (1992). [Cited on page 113.]

[275] W. Leoński and R. Tanaś, *Possibility of producing the one-photon state in a kicked cavity with a nonlinear Kerr medium*, Phys. Rev. A **49**, R20 (1994). [Cited on page 113.]

[276] A. Imamoğlu, H. Schmidt, G. Woods, and M. Deutsch, *Strongly Interacting Photons in a Nonlinear Cavity*, Phys. Rev. Lett. **79**, 1467 (1997). [Cited on page 113.]

[277] P. Grangier, D. F. Walls, and K. M. Gheri, *Comment on "Strongly Interacting Photons in a Nonlinear Cavity"*, Phys. Rev. Lett. **81**, 2833 (1998). [Cited on page 113.]

[278] K. M. Birnbaum, A. Boca, R. Miller, A. D. Boozer, T. E. Northup, and H. J. Kimble, *Photon blockade in an optical cavity with one trapped atom*, Nature **436**, 87 (2005). [Cited on page 113.]

[279] A. Faraon, I. Fushman, D. Englund, N. Stoltz, P. Petroff, and J. Vučković, *Coherent generation of non-classical light on a chip via photon-induced tunnelling and blockade*, Nat. Phys. **4**, 859 (2008). [Cited on page 113.]

[280] Y.-x. Liu, A. Miranowicz, Y. B. Gao, J. c. v. Bajer, C. P. Sun, and F. Nori, *Qubit-induced phonon blockade as a signature of quantum behavior in nanomechanical resonators*, Phys. Rev. A **82**, 032101 (2010). [Cited on page 113.]

[281] J. Kim, O. Benson, H. Kan, and Y. Yamamoto, *A single-photon turnstile device*, Nature **397**, 500 (1999). [Cited on page 113.]

[282] P. Michler, A. Kiraz, C. Becher, W. Schoenfeld, P. Petroff, L. Zhang, E. Hu, and A. Imamoglu, *A Quantum Dot Single-Photon Turnstile Device*, Science **290**, 2282 (2000). [Cited on page 113.]

[283] A. A. Houck, D. I. Schuster, J. M. Gambetta, J. A. Schreier, B. R. Johnson, J. M. Chow,

L. Frunzio, J. Majer, M. H. Devoret, S. M. Girvin, and R. J. Schoelkopf, *Generating single microwave photons in a circuit*, Nature **449**, 328 (2007). [Cited on page 113.]

[284] M. D. Eisaman, J. Fan, A. Migdall, and S. V. Polyakov, *Invited Review Article: Single-photon sources and detectors*, Rev. Sci. Instrum. **82**, 071101 (2011). [Cited on pages 113 and 114.]

[285] Y. Zhou, Z. Peng, Y. Horiuchi, O. Astafiev, and J. Tsai, *Tunable Microwave Single-Photon Source Based on Transmon Qubit with High Efficiency*, Phys. Rev. Appl. **13**, 034007 (2020). [Cited on page 113.]

[286] T. C. H. Liew and V. Savona, *Single Photons from Coupled Quantum Modes*, Phys. Rev. Lett. **104**, 183601 (2010). [Cited on page 113.]

[287] M. Bamba, A. Imamoğlu, I. Carusotto, and C. Ciuti, *Origin of strong photon antibunching in weakly nonlinear photonic molecules*, Phys. Rev. A **83**, 021802 (2011). [Cited on page 113.]

[288] M.-A. Lemonde, N. Didier, and A. A. Clerk, *Antibunching and unconventional photon blockade with Gaussian squeezed states*, Phys. Rev. A **90**, 063824 (2014). [Cited on page 113.]

[289] H. Flayac and V. Savona, *Single photons from dissipation in coupled cavities*, Phys. Rev. A **94**, 013815 (2016). [Cited on page 113.]

[290] H. Flayac and V. Savona, *Unconventional photon blockade*, Phys. Rev. A **96**, 053810 (2017). [Cited on page 113.]

[291] M. Radulaski, *A Double Take on Unconventional Photon Blockade*, Physics **11**, 74 (2018). [Cited on page 113.]

[292] H. J. Snijders, J. A. Frey, J. Norman, H. Flayac, V. Savona, A. C. Gossard, J. E. Bowers, M. P. van Exter, D. Bouwmeester, and W. Löffler, *Observation of the Unconventional Photon Blockade*, Phys. Rev. Lett. **121**, 043601 (2018). [Cited on page 113.]

[293] P.-M. Billangeon and Y. Nakamura, *Quantum cups and balls*, Nat. Phys. **7**, 594 (2011). [Cited on page 114.]

[294] P. Ball, *In search of time crystals*, Phys. World **31**, 29 (2018). [Cited on page 115.]

[295] A. Shapere and F. Wilczek, *Classical Time Crystals*, Phys. Rev. Lett. **109**, 160402 (2012). [Cited on page 115.]

[296] F. Wilczek, *Quantum Time Crystals*, Phys. Rev. Lett. **109**, 160401 (2012). [Cited on page 115.]

[297] J. Zakrzewski, *Crystals of time*, Physics **5**, 116 (2012). [Cited on page 115.]

[298] P. Bruno, *Comment on "Space-Time Crystals of Trapped Ions"*, Phys. Rev. Lett. **111**, 029301 (2013). [Cited on page 115.]

[299] T. Li, Z.-X. Gong, Z.-Q. Yin, H. T. Quan, X. Yin, P. Zhang, L.-M. Duan, and X. Zhang, *Space-Time Crystals of Trapped Ions*, Phys. Rev. Lett. **109**, 163001 (2012). [Cited on page 115.]

[300] F. Wilczek, *Wilczek Reply:*, Phys. Rev. Lett. **110**, 118902 (2013). [Cited on page 115.]

[301] F. Wilczek, *Superfluidity and Space-Time Translation Symmetry Breaking*, Phys. Rev. Lett. **111**, 250402 (2013). [Cited on page 115.]

[302] P. Bruno, *Comment on "Quantum Time Crystals"*, Phys. Rev. Lett. **110**, 118901 (2013). [Cited on page 115.]

[303] A. Syrwid, J. Zakrzewski, and K. Sacha, *Time Crystal Behavior of Excited Eigenstates*, Phys. Rev. Lett. **119**, 250602 (2017). [Cited on page 115.]

[304] P. Bruno, *Impossibility of Spontaneously Rotating Time Crystals: A No-Go Theorem*, Phys. Rev. Lett. **111**, 070402 (2013). [Cited on page 115.]

[305] H. Watanabe and M. Oshikawa, *Absence of Quantum Time Crystals*, Phys. Rev. Lett. **114**, 251603 (2015). [Cited on page 115.]

[306] K. Nakatsugawa, T. Fujii, A. Saxena, and S. Tanda, *Time operators and time crystals: self-adjointness by topology change*, J. Phys. A Math **53**, 025301 (2019). [Cited on page 115.]

[307] K. Sacha, *Modeling spontaneous breaking of time-translation symmetry*, Phys. Rev. A **91**, 033617 (2015). [Cited on page 115.]

[308] A. Chandran and S. L. Sondhi, *Interaction-stabilized steady states in the driven $O(N)$ model*, Phys. Rev. B **93**, 174305 (2016). [Cited on page 115.]

[309] C. W. von Keyserlingk, V. Khemani, and S. L. Sondhi, *Absolute stability and spatiotemporal long-range order in Floquet systems*, Phys. Rev. B **94**, 085112 (2016). [Cited on page 115.]

[310] V. Khemani, A. Lazarides, R. Moessner, and S. L. Sondhi, *Phase Structure of Driven Quantum Systems*, Phys. Rev. Lett. **116**, 250401 (2016). [Cited on page 115.]

[311] D. V. Else, B. Bauer, and C. Nayak, *Floquet Time Crystals*, Phys. Rev. Lett. **117**, 090402 (2016). [Cited on page 115.]

[312] D. V. Else, B. Bauer, and C. Nayak, *Prethermal Phases of Matter Protected by Time-Translation Symmetry*, Phys. Rev. X **7**, 011026 (2017). [Cited on page 115.]

[313] N. Y. Yao, A. C. Potter, I.-D. Potirniche, and A. Vishwanath, *Discrete Time Crystals: Rigidity, Criticality, and Realizations*, Phys. Rev. Lett. **118**, 030401 (2017). [Cited on page 115.]

[314] K. Giergiel, A. Kosior, P. Hannaford, and K. Sacha, *Time crystals: Analysis of experimental conditions*, Phys. Rev. A **98**, 013613 (2018). [Cited on page 115.]

[315] N. Y. Yao, C. Nayak, L. Balents, and M. P. Zaletel, *Classical discrete time crystals*, Nat. Phys. **16**, 438 (2020). [Cited on page 115.]

[316] J. Zhang, P. W. Hess, A. Kyprianidis, P. Becker, A. Lee, J. Smith, G. Pagano, I.-D. Potirniche, A. C. Potter, A. Vishwanath, N. Y. Yao, and C. Monroe, *Observation of a discrete time crystal*, Nature **543**, 217 (2017). [Cited on page 115.]

[317] S. Choi, J. Choi, R. Landig, G. Kucsko, H. Zhou, J. Isoya, F. Jelezko, S. Onoda, H. Sumiya, V. Khemani, C. von Keyserlingk, N. Y. Yao, E. Demler, and M. D. Lukin, *Observation of discrete time-crystalline order in a disordered dipolar many-body system*, Nature **543**, 221 (2017). [Cited on page 115.]

[318] S. Pal, N. Nishad, T. S. Mahesh, and G. J. Sreejith, *Temporal Order in Periodically Driven Spins in Star-Shaped Clusters*, Phys. Rev. Lett. **120**, 180602 (2018). [Cited on page 115.]

[319] J. Rovny, R. L. Blum, and S. E. Barrett, *Observation of Discrete-Time-Crystal Signatures in an Ordered Dipolar Many-Body System*, Phys. Rev. Lett. **120**, 180603 (2018). [Cited on page 115.]

[320] J. Rovny, R. L. Blum, and S. E. Barrett, ^{31}P *NMR study of discrete time-crystalline signatures in an ordered crystal of ammonium dihydrogen phosphate*, Phys. Rev. B **97**, 184301 (2018). [Cited on page 115.]

[321] J. Smits, L. Liao, H. T. C. Stoof, and P. van der Straten, *Observation of a Space-Time Crystal in a Superfluid Quantum Gas*, Phys. Rev. Lett. **121**, 185301 (2018). [Cited on page 115.]

[322] H. Keßler, P. Kongkhambut, C. Georges, L. Mathey, J. G. Cosme, and A. Hemmerich, *Observation of a Dissipative Time Crystal*, Phys. Rev. Lett. **127**, 043602 (2021). [Cited on page 115.]

[323] F. Iemini, A. Russomanno, J. Keeling, M. Schirò, M. Dalmonte, and R. Fazio, *Boundary Time Crystals*, Phys. Rev. Lett. **121**, 035301 (2018). [Cited on page 116.]

[324] P. Wang and R. Fazio, *Dissipative phase transitions in the fully connected Ising model with p-spin interaction*, Phys. Rev. A **103**, 013306 (2021). [Cited on page 116.]

[325] L. F. d. Prazeres, L. d. S. Souza, and F. Iemini, *Boundary time crystals in collective d-level systems*, Phys. Rev. B **103**, 184308 (2021). [Cited on page 116.]

[326] G. Piccitto, M. Wauters, F. Nori, and N. Shammah, *Symmetries and conserved quantities of boundary time crystals in generalized spin models*, Phys. Rev. B **104**, 014307 (2021). [Cited on page 116.]

[327] D. Sarchi, I. Carusotto, M. Wouters, and V. Savona, *Coherent dynamics and parametric instabilities of microcavity polaritons in double-well systems*, Phys. Rev. B **77**, 125324 (2008). [Cited on page 116.]

[328] C. Lledó, T. K. Mavrogordatos, and M. H. Szymańska, *Driven Bose-Hubbard dimer under nonlocal dissipation: A bistable time crystal*, Phys. Rev. B **100**, 054303 (2019). [Cited on page 116.]

[329] C. Lledó and M. H. Szymańska, *A dissipative time crystal with or without Z2 symmetry breaking*, New J. Phys. **22**, 075002 (2020). [Cited on page 116.]

[330] K. Seibold, R. Rota, and V. Savona, *Dissipative time crystal in an asymmetric nonlinear photonic dimer*, Phys. Rev. A **101**, 033839 (2020). [Cited on page 116.]

[331] N. Carlon Zambon, S. R. K. Rodriguez, A. Lemaître, A. Harouri, L. Le Gratiet, I. Sagnes, P. St-Jean, S. Ravets, A. Amo, and J. Bloch, *Parametric instability in coupled nonlinear microcavities*, Phys. Rev. A **102**, 023526 (2020). [Cited on page 116.]

[332] K. Vogel and H. Risken, *Determination of quasiprobability distributions in terms of probability distributions for the rotated quadrature phase*, Phys. Rev. A **40**, 2847 (1989). [Cited on page 116.]

[333] B. Opanchuk and P. D. Drummond, *Functional Wigner representation of quantum dynamics of Bose-Einstein condensate*, J. Math. Phys. **54**, 042107 (2013). [Cited on page 116.]

[334] M. Kunimi, K. Nagao, S. Goto, and I. Danshita, *Performance evaluation of the discrete truncated Wigner approximation for quench dynamics of quantum spin systems with long-range interactions*, Phys. Rev. Res. **3**, 013060 (2021). [Cited on page 116.]

[335] H. Lang, O. Vendrell, and P. Hauke, *Generalized discrete truncated Wigner approximation for nonadiabatic quantum-classical dynamics*, J. Chem. Phys. **155**, 024111 (2021). [Cited on page 116.]

[336] C. W. Gardiner, *Driving a quantum system with the output field from another driven quantum system*, Phys. Rev. Lett. **70**, 2269 (1993). [Cited on page 123.]

[337] M. I. Dykman, *Critical exponents in metastable decay via quantum activation*, Phys. Rev. E **75**, 011101 (2007). [Cited on page 127.]

[338] I. Serban, M. I. Dykman, and F. K. Wilhelm, *Relaxation of a qubit measured by a driven Duffing oscillator*, Phys. Rev. A **81**, 022305 (2010). [Cited on page 127.]

[339] L. Guo, Z. Zheng, X.-Q. Li, and Y. Yan, *Dynamic quantum tunneling in mesoscopic driven Duffing oscillators*, Phys. Rev. E **84**, 011144 (2011). [Cited on page 127.]

List of publications (2018.10-2022.04)

Qi-Ming Chen, Michael Fischer, Yuki Nojiri, Michael Renger, Edwar Xie, Matti Partanen, Stefan Pogorzalek, Kirill G. Fedorov, Achim Marx, Frank Deppe, and Rudolf Gross, *Quantum behavior of the Duffing oscillator at the dissipative phase transition*, arXiv:2206.06338 (2022)

Florian Fesquet, Fabian Kronowetter, Michael Renger, Qi-Ming Chen, Kedar Honasoge, Oscar Gargiulo, Yuki Nojiri, Achim Marx, Frank Deppe, Rudolf Gross, and Kirill G. Fedorov, *Perspectives of microwave quantum key distribution in open-air*, arXiv:2203.05530 (2022)

Qi-Ming Chen, Fabian Kronowetter, Florian Fesquet, Kedar E. Honasoge, Yuki Nojiri, Michael Renger, Kirill G. Fedorov, Achim Marx, Frank Deppe, and Rudolf Gross, *Tuning and amplifying the interactions in superconducting quantum circuits with subradiant qubits*, Phys. Rev. A **105**, 012405 (2022)

Qi-Ming Chen, Matti Partanen, Florian Fesquet, Kedar E. Honasoge, Fabian Kronowetter, Yuki Nojiri, Michael Renger, Kirill G. Fedorov, Achim Marx, Frank Deppe, and Rudolf Gross, *The scattering coefficients of superconducting microwave resonators: II. System-bath approach*, arXiv:2109.07766 (2021)

Qi-Ming Chen, Meike Pfeiffer, Matti Partanen, Florian Fesquet, Kedar E. Honasoge, Fabian Kronowetter, Yuki Nojiri, Michael Renger, Kirill G. Fedorov, Achim Marx, Frank Deppe, and Rudolf Gross, *The scattering coefficients of superconducting microwave resonators: I. Transfer-matrix approach*, arXiv:2109.07762 (2021)

Kirill G. Fedorov, Michael Renger, Stefan Pogorzalek, Roberto Di Candia, Qi-Ming Chen, Yuki Nojiri, Kunihiro Inomata, Yasunobu Nakamura, Matti Partanen, Achim Marx, Rudolf Gross, and Frank Deppe, *Experimental quantum teleportation of propagating microwaves*, Sci. Adv. 7 (52), eabk0891 (2021)

Michael Renger, Stefan Pogorzalek, Qi-Ming Chen, Yuki Nojiri, Kunihiro Inomata, Yasunobu Nakamura, Matti Partanen, Achim Marx, Rudolf Gross, Frank Deppe, and Kirill G. Fedorov, *Beyond the standard quantum limit for parametric amplification of broadband signals*, njp Quantum Inf. **7**, 160 (2021)

Michael Fischer, Qi-Ming Chen, Christian Besson, Peter Eder, Jan Goetz, Stefan Pogorzalek, Michael Renger, Edwar Xie, Michael J. Hartmann, Kirill G. Fedorov, Achim Marx, Frank Deppe, and Rudolf Gross, *In situ tunable nonlinearity and competing signal paths in coupled superconducting resonators*, Phys. Rev. B **103**, 094515 (2021)

Qi-Ming Chen, Michael Fischer, Yuki Nojiri, Stefan Pogorzalek, Michael Renger, Matti Partanen, Kirill G. Fedorov, Achim Marx, Frank Deppe, and Rudolf Gross, *Automated calibration and control of superconducting resonators with tunable nonlinearity*, in *WMI Annual Report*, pages 53–54, 2020.

Xiaodong Yang, Christian Arenz, Istvan Pelczer, Qi-Ming Chen, Re-Bing Wu, Xinhua Peng, and Herschel Rabitz, *Assessing three closed-loop learning algorithms by searching for high-quality quantum control pulses*, Phys. Rev. A **102**, 062605 (2020)

Qi-Ming Chen, Xiaodong Yang, Christian Arenz, Re-Bing Wu, Xinhua Peng, Istvan Pelczer, and Herschel Rabitz, *Combining the synergistic control capabilities of modeling and experiments: Illustration of finding a minimum time quantum objective*, Phys. Rev. A **98**, 042328 (2020)

Qi-Ming Chen, Frank Deppe, Yuki Nojiri, Stefan Pogorzalek, Michael Renger, Matti Partanen, Kirill G. Fedorov, Achim Marx, and Rudolf Gross, *Measurement of the second-order correlation functions*

under different signal-to-noise ratios, in *WMI Annual Report*, pages 51–52, 2019.

Qi-Ming Chen, Frank Deppe, Re-Bing Wu, Luyan Sun, Yu-xi Liu, Yuki Nojiri, Stefan Pogorzalek, Michael Renger, Matti Partanen, Kirill G. Fedorov, Achim Marx, and Rudolf Gross, *Quantum Fourier transform in oscillating modes*, arXiv:1912.09861 (2019)

Qi-Ming Chen, Yu-xi Liu, Luyan Sun, and Re-Bing Wu, *Tuning the coupling between superconducting resonators with collective qubits*, Phys. Rev. A **98**, 042328 (2018)

Acknowledgement

This thesis should credit not only the author but also many of our colleagues and friends. The whole story starts from an email I sent to Dr. Frank Deppe on June 16, 2018. He introduced me to Dr. Rudolf Gross, and they offered me a Ph.D. position at the Walther-Meißner-Institut (WMI). When I look back on these years, I do think that I learned a lot from both of you and I had a great time here. Thank you very much for giving me the opportunity to pursue a Ph.D. degree in Munich, teaching me a variety of things more than physics, and always covering me under your wings.

I would also like to thank all the scientists, postdocs, Ph.D. students, engineers, and technicians at WMI. You provide tremendous help to this thesis work. In particular, I appreciate Dr. Michael Fischer, Dr. Achim Marx, Dr. Stefan Pogorzalek, and Dr. Edwar Xie a lot for teaching me cryogenic techniques and microwave engineering; Yuki Nojiri, Dr. Daniel Schwienbacher, Dr. Tobias Wimmer, and Dr. Edwar Xie for fabrication training; Michael Renger, Dr. Matti Partanen, Dr. Kirill G. Fedorov, and Dr. Hans Hübl for many insightful discussions; and Sebastian Kammerer, Jan Naundorf, Andreas Russo, and Alexander Rößl for the continuous support on helium, electronics, and mechanical engineering.

Besides, I want to thank Dr. Stefan Filipp and his whole team for offering me the opportunity to join their qubit experiments; my officemates, Fabian Kronowetter, Dr. Luis Flacke, Dr. Daniel Schwienbacher, and Dr. Tobias Wimmer, for making a cozy atmosphere in room 134; those many friends sitting on the second floor: Florian Fesquet, Janine Gückelhorn, Kedar E. Honasoge, Leonhard Hölscher, Thomas Luschmann, Manuel Müller, Dr. Daniel Jost, Dr. Lukas Liensberger, Dr. Philip Schmidt, Dr. Natalie Segercrantz, and Dr. Stefan Weichselbaumer; and also Dr. Ge He for the many after-lunch walks alongside the Isar. In addition, I thank the Elite Network of Bavaria (Elitenetzwerk Bayern) for support via the international doctoral program Exploring Quantum Matter (ExQM).

最后感谢我的父母：陈旭功和黄英，以及我的妻子：谢喆。你们的信任与陪伴帮助我度过许多艰难的日子，我也有很多开心的时刻要与你们分享。